

MODEL-BASED ANALYSIS AND OPTIMIZATION OF MEMBRANE DISTILLATION

Ivaylo Hitsov, MSc

Thesis submitted in fulfilment of the requirements for the degree of

Doctor (Ph.D) in Applied Biological Sciences

Academic year 2016-2017

Supervisors: Prof. dr. ir. Ingmar Nopens
Department of Mathematical Modelling, Statistics and Bioinformatics
Ghent University, Belgium

Dr. ir. Chris Dotremont
Flemish Institute for Technological Research
VITO, Belgium

Dr. ir. Kristien De Sitter
Flemish Institute for Technological Research
VITO, Belgium

Dean: Prof. dr. ir. Marc Van Meirvenne

Rector: Prof. dr. Anne De Paepe

Ivaylo Hitsov, MSc

MODEL-BASED ANALYSIS AND OPTIMIZATION OF MEMBRANE DISTILLATION

Thesis submitted in fulfilment of the requirements for the degree of

Doctor (Ph.D) in Applied Biological Sciences

Academic year 2016-2017

Dutch translation of the title:

Modelgebaseerde analyse en optimalisatie van membraandestillatie

Please refer to this work as follows:

Ivaylo Hitsov (2017). *Model-based analysis and optimization of membrane distillation*, PhD Thesis, Department of Mathematical Modelling, Statistics and Bioinformatics, Ghent University, Ghent, Belgium.

ISBN: 978-94-6357-003-9

The author and the supervisors give the authorization to consult and to copy parts of this work for personal use only. Every other use is subject to the copyright laws. Permission to reproduce any material contained in this work should be obtained from the author.

Acknowledgments

When I first applied for this PhD I had no idea what membrane distillation was. Hmm, a heat exchanger, but with a membrane, could it really be that easy? Alright then, no problem, I can model this. Four years later, it turns out that MD is much more than just that and it still amazes me how such a simple system can behave in such a complex way.

But this section is about thanking people, so I better start doing it. First of all I have to thank my co-promoters Kris De Sitter and Chris Dotremont for trusting me over a Skype interview from Bulgaria and selecting me as a candidate for this position. But I have much more things to thank them. They were always there for me in these four years, giving me countless advices and discussing with me all of my sometimes crazy ideas. I always valued their opinions as great membrane specialists.

Then I would like to thank Ingmar for being the best promoter a PhD student could ask for. He left me be independent in my work, but always kept an eye on how I was doing. Although he is probably the busiest person on the planet, if I requested a meeting I would usually get one on the same day. Also, he was usually the first one to comment on my papers and his comments are so extensive that usually takes me more than a day to address them and this helps a lot. But most of all I would like to thank him for always supporting me and for stepping up for me when I needed it.

I would also like to thank Lies Eykens, my experimental equivalent PhD student in VITO. She produced tons of experimental data for me, helped me when I needed to make experiments myself and was always there when I needed to discuss something. Without her I could never brag that my models are thoroughly calibrated and validated.

I would like to gratefully acknowledge VITO - The Flemish institute for technological research for providing the PhD scholarship that funded this research. A warm thank you goes to all of the researchers and supporting personnel in

VITO for all the help and discussions.

I am also thankful to all the great people in the department and more specifically in BIOMATH. I was so happy to work in such a friendly atmosphere, where everyone is casual, helpful, cheerful and simply awesome! Special thanks go to my office mates throughout the years - Thomas, Katrijn, Vivek, Ashish, Youri, and more recently Dorien, Chaim, Sophie, Han and Roop. I will miss you guys, thank you for all of the funny stories we were telling each other, the discussions and simply for putting up with me and my 21 °C heating requirements. Even more special thanks go to Thomas for also being my daily supervisor during the first two years of my PhD, but also for being a good friend. Thank you also goes to all the rest of the BIOMATH crew over the years - Elena, Wouter, Niels and Andreia, Michael, Séverine, Daan, Lieven, Usman, Stijn, Timothy, David, Gurmeet, Yohannis, Giacomo, Bram, Wim and Jenna for all the friendly talks, BIOMATH weekends, "bier and plezier" evenings and all the biers we drank and made together (think Wouter, who is a part time researcher, full time brewer). Special thanks go to a special lady - Tinne the lab technician, but also the cake making magician.

I would also like to thank some other people from the department - Raul, José, Christina, Marc, Guillermo, Aisling, Steffie, Marlies, Timpe and Ruth for all the friendly talks, parties and lunches together.

A huge thank you goes out to my mom and dad Plamen and Anna. It was hard being separated these four years, but talking over Skype every weekend made it a bit easier. They are the greatest parents on earth, not many people decide to start a new life in their 50s, move to another country and buy a new house. I am immensely proud of them. I would also like to thank my sister Tina for all the sisterly love, smart advices, support and also visiting me here a couple of times here in Belgium. I also want to thank her for helping mom and dad settle in the US and overall for being such a great sister. I love you guys!

Finally, I would like to thank my best friend, the love of my life and also recently, my wife Irina! Wow it's been a roller coaster, right? Now it's your turn (she just started a PhD herself)! I love you babe, thank you for always being there for me when I needed it, for giving me motivation and joy in life!

Summary

Membrane distillation is a thermally driven separation process. Recent interest has been observed in the technology due to its unique features such as mild operating temperature, allowing the use of waste heat as driving force, ultimate rejection for non-volatile components, low operational pressure which allows the use of cheap, plastic modules, that do not suffer from corrosion. This thesis is dedicated almost exclusively to the modelling of the process. It covers the selection, development and calibration of lab-scale as well as full-scale models of the most popular membrane distillation configurations studied and used today.

In chapter 1 the general introduction to this thesis is done, starting with introduction to the topic, problem statements and the objectives of this research. Then an outline of the roadmap through this thesis is presented.

Chapter 2 deals with a literature overview on the current modelling approaches and practices concerning MD. Key lab- and full-scale studies are briefly discussed and the general gaps in the literature are outlined. The most used sub-models for heat and mass transfer inside the channels and membranes are discussed as well as their practical applicability, limitations and input parameters.

Chapter 3 deals with calibration and analysis of a typical lab-scale direct contact membrane distillation (DCMD) model. The chapter presents a methodology for the calibration of an arbitrary channel spacer in terms of heat and mass transfer. Further, different mass transfer models are compared in their predictive power for seven different membranes.

Chapter 4 describes a methodology for scaling up of a DCMD model from lab-scale and applying it to a full-scale module geometry, without using calibration parameters on full-scale. The chapter reveals a novel direct measurement as well as model extension dealing with the membrane compaction, which was demonstrated to have a large impact on the heat and mass transfer properties

of the membrane. Thorough validation reveals that the model has an excellent fit to the experimental data.

In chapter 5, the DCMD model from chapter 3 is extended to an air gap membrane distillation (AGMD). Novel, but simple measurement techniques are presented in order to measure for the first time the previously unknown parameters in the gap compartment. Experimental validation shows an excellent predictive power of the newly developed model. Further in this chapter an experimental comparison between DCMD and AGMD was performed for two modules with otherwise identical geometry and the same manufacturer. It was demonstrated that contrary to popular beliefs, AGMD modules can have higher fluxes on full-scale compared to DCMD.

Chapter 6 is dedicated to demonstrating the in-house tool developed in this thesis for process and module optimization of membrane distillation modules and systems. First, modules from the three major MD configurations are optimized in terms of geometry and operational conditions. The major limitation factors in each of the configurations is outlined. During the second part of this chapter, complete systems are designed for several cases and scenarios. A thorough economical analysis is performed and the economical aspects of MD are discussed.

In chapter 7 general conclusions are presented. The thesis is summarized and recommendations for future research are given.

Samenvatting

Membraandestillatie is een thermisch aangedreven scheidingsproces. De technologie wordt de laatste jaren uitgebreid bestudeerd vanwege zijn unieke kenmerken, zoals een milde operationele temperatuur, waardoor het gebruik van restwarmte als drijvende kracht mogelijk wordt, volledige retentie van niet-vluchtige componenten en een lage operationele druk, die het gebruik van goedkope, plastic modules die niet corrosiegevoelig zijn toestaat. Dit proefschrift is bijna uitsluitend gewijd aan het modelleren van het membraandestillatie proces. Er is aandacht besteed de selectie, ontwikkeling en kalibratie van zowel lab- als full-scale modellen van de meest gebruikte en onderzochte membraandestillatieconfiguraties.

Hoofdstuk 1, de algemene inleiding van dit proefschrift, bevat een inleiding tot het onderwerp en zijn probleemstelling en beschrijft de doelstellingen van het onderzoek. Vervolgens wordt aan de hand van een roadmap een overzicht van dit proefschrift gepresenteerd.

Hoofdstuk 2 bevat een literatuuroverzicht van de huidige modelleerbenaderingen en -praktijken met betrekking tot MD. Toonaangevende lab- en full-scale studies worden kort besproken en de grote hiaten in de literatuur worden beschreven. De meest gebruikte submodellen voor warmte- en massa-overdracht in kanalen en membranen worden besproken, evenals hun praktische toepasbaarheid, beperkingen en invoerparameters.

Hoofdstuk 3 beschrijft de kalibratie en analyse van een typisch laboratoriumschaal DCMD model. Het hoofdstuk presenteert een methodologie voor de kalibratie van een willekeurige kanaalspacer in termen van warmte en massa-overdracht. Verder worden verschillende massa-overdracht modellen vergeleken op hun voorspellende kracht voor zeven verschillende membranen.

Hoofdstuk 4 beschrijft een methode voor het opschalen van een DCMD model startend van laboratoriumschaal en past deze toe op een full-scale module geometrie, zonder gebruik te maken van kalibratieparameters op full-scale.

Het hoofdstuk onthult zowel een innovatieve directe meting als een modelextensie ter behandeling van de samendrukbaarheid van het membraan. Voor beiden wordt aangetoond dat ze een grote invloed hebben op de warmte- en massaoverdrachteigenschappen van het membraan. Uit een grondige validatie blijkt dat het model een uitstekende fit vertoont met de experimentele data.

In hoofdstuk 5 wordt het DCMD model uit hoofdstuk 3 uitgebreid naar een air gap membraan distillatie (AGMD). Daarvoor worden nieuwe, maar eenvoudige meettechnieken voorgesteld die de onbekende parameters in de air gap kunnen meten. Experimentele validatie toont een uitstekende voorspellende kracht van het ontwikkelde model. Verder bevat dit hoofdstuk een experimentele vergelijking tussen een DCMD en een AGMD module met identieke geometrie en van dezelfde fabrikant. In tegenstelling tot wat algemeen aangenomen wordt, blijkt dat AGMD modules op volle schaal hogere fluxen hebben dan DCMD.

Hoofdstuk 6 is gewijd aan het demonstreren van de in-house ontwikkelde tool die gebruikt kan worden voor proces- en module optimalisatie van membraan distillatiemodules en -systemen. Ten eerste worden modules uit de drie grote MD configuraties geoptimaliseerd in termen van geometrie en operationele omstandigheden. De belangrijkste beperkende factoren in elk van de configuraties worden geschetst. In het tweede deel van dit hoofdstuk worden volledige systemen ontworpen voor verschillende gevallen en scenarios. Een grondige economische analyse wordt uitgevoerd en de economische aspecten van MD worden besproken.

In hoofdstuk 7 worden de algemene conclusies gepresenteerd. Het proefschrift wordt samengevat en aanbevelingen voor toekomstig onderzoek worden gegeven.

Contents

Acknowledgments	i
English summary	iii
Nederlandse samenvatting	v
Contents	x
1 Problem statement	1
1.1 Introduction	1
1.2 Problem Statement	3
1.3 Objectives of this research	4
1.4 Outline: The roadmap through this dissertation	5
2 Literature review	9
2.1 Introduction	10
2.2 State of the art in membrane distillation modelling	13
2.2.1 Heat transfer models	13
2.2.2 Mass transfer (concentration polarization) inside the feed channel	20
2.2.3 Models for mass transfer inside the membrane	24
2.2.4 Empirical models	34
2.2.5 Computational Fluid Dynamics (CFD) models	37
2.3 Discussion and research gaps	42
2.3.1 Discussion	42
2.3.2 Research gaps	46
2.4 Conclusions	48
3 Lab-scale DCMD modelling	49

3.1	Introduction	51
3.1.1	Transport phenomena in the channels	51
3.1.2	Transport phenomena inside the membrane	52
3.2	Materials and Methods	54
3.2.1	Membranes and module	54
3.2.2	Channel heat and mass transfer calibration	56
3.2.3	Submodels for the thermal conductivity of the membrane	59
3.2.4	Submodels for mass transfer inside the membrane	59
3.2.5	Monte Carlo filtering method	62
3.3	Results and Discussion	65
3.3.1	Calibration of the heat and mass transfer inside the channels	65
3.3.2	Choice of calibration parameters	66
3.3.3	Calibration of the heat and mass transfer inside the membrane using Monte Carlo filtering	68
3.3.4	Simulation of single layer membranes	70
3.3.5	Simulation of supported membranes	74
3.3.6	Submodel selection for the mass transfer inside the membrane	76
3.3.7	Submodel selection for the thermal conductivity of the membrane	78
3.4	Conclusions	81
4	Full-scale DCMD modelling	83
4.1	Introduction	85
4.2	Materials and Methods	86
4.2.1	Lab-scale setup	86
4.2.2	Full-scale setup	88
4.3	Spacer characterization	89
4.3.1	Pressure drop measurement	89
4.3.2	Heat and mass transfer characterization	90
4.4	Lab-scale modelling	91
4.4.1	Heat and mass transfer inside the channels	91
4.4.2	Heat and mass transfer inside the membrane	91
4.4.3	Lab-scale model calibration	92
4.5	Model upscaling	92
4.5.1	Model discretization	92
4.5.2	Heat and mass balance in each section	94

4.5.3	Membrane compaction at full-scale	95
4.6	Results and discussion	98
4.6.1	Lab-scale model calibration	98
4.6.2	Full-scale experimental and modelling results	99
4.6.3	Influence of number of sections in which the model is discretized	107
4.6.4	Module optimization based on the validated model	107
4.7	Conclusions	109
5	Full-scale AGMD modelling	111
5.1	Introduction	113
5.2	Materials and Methods	114
5.2.1	Full-scale membrane distillation setup	114
5.2.2	Setup for measurement of the condensate layer thickness	116
5.2.3	Setup for measurement of the gap flooding	117
5.3	Air gap model structure	118
5.3.1	Model calibration at lab-scale	118
5.3.2	Module discretization and solution method	118
5.3.3	Heat and mass transfer in each section of the model . . .	120
5.3.4	Heat and mass transfer inside the membrane and the gap	121
5.4	Results and discussion	123
5.4.1	Air-gap condensation	123
5.4.2	Measurement of gap flooding	124
5.4.3	Experimental comparison between air gap and direct con- tact membrane distillation	126
5.4.4	Model validation	130
5.4.5	Module optimization based on the validated model	132
5.5	Conclusions	134
5.6	Acknowledgment	135
6	Process and module optimization	137
6.1	Introduction	138
6.2	Materials and Methods	139
6.2.1	GUI for module optimization	139
6.2.2	System design model	145
6.2.3	Pressure drop modelling	151
6.3	Results and discussion	153
6.3.1	Module design optimization	153

6.3.2	Full-scale system optimization	160
6.4	Conclusions	170
7	General conclusions and perspectives	171
7.1	General conclusions	171
7.1.1	Lab-scale modelling	171
7.1.2	Full-scale MD modelling	172
7.1.3	Process and module optimization of membrane distillation	174
7.2	Perspectives	175
7.2.1	Improvements and gaps in the experimental measurements	175
7.2.2	Process and module optimization gaps and promising re- search paths	177
8	Bibliography	179
9	Appendices	199
9.1	SEM crosssections of the membranes studied in Chapter 3	200
9.2	Equations used in Chapter 4	202
9.3	Equations used in Chapter 5	203
9.4	Case scenario 1, pilot scale 2 m ³ distillate per day, Chapter 6	206
9.5	Case scenario 2, small production scale, 10 m ³ distillate per day, Chapter 6	207
9.6	Case scenario 3, production scale, 100 m ³ distillate per day, Chapter 6	208
9.7	Case scenario 4, large production scale, 1000 m ³ distillate per day, Chapter 6	209
	Nomenclature	211
10	Curriculum Vitae	215

CHAPTER 1

Problem statement, research objectives and outline

1.1 Introduction

The increasing earth population puts ever increasing stress on the water availability. An estimated 1.2 B people globally suffer from inadequate access to clean drinking water. While 71 percent of the surface of the earth is covered with water [1], more than 97 percent of the water has a salinity that is unfit for direct human consumption. The increasing demand for fresh water leads to a large interest in desalination technologies that are able to access the previously untapped source of saline water. A breakthrough desalination technology was developed in the 1960 when scientists in UCLA developed a commercially viable, semi-permeable reverse osmosis (RO) membrane [2]. In reverse osmosis saline water is, under high pressure, pushed through a semi-permeable membrane, allowing for a cheap, accessible water desalination. In 2015, desalination plants are providing water for 300 million people worldwide [3] and more than 60 % of the desalination is being performed by means of reverse osmosis [4]. Reverse osmosis today is an extremely mature technology vastly optimized such that the state-of-the-art plants have a total energy consumption, including pretreatment, post treatment and water intake between 3 and 4 kW-h to desalinate one cubic meter of water [5]. If only the desalination step is considered, the modern plants approach a power consumption of less than 2 kW-h/m³, while the thermodynamic minimum required is 1.06 kW-h/m³ [5]. Yet, RO also suffers from a number of limitations. The capital investment of an RO plant requires expensive high pressure pumps, pressure recovery devices and

pressure vessels. But the biggest limitation is the inability of the technology to be applied on high salinity streams. At normal sea water concentrations, a minimum transmembrane pressure of 25 bars (also known as osmotic pressure) needs to be applied in order to achieve a positive flux. RO quickly approaches its application limit at fairly low salinities of about 6 wt %, while the saturation concentration of NaCl is 24 wt %.

In contrast to reverse osmosis, membrane distillation (MD) is a technology which only recently started to receive wide attention. In MD (Figure 1.1), a porous hydrophobic membrane creates an interface for the feed to evaporate at the interface, the vapors travel through the pores and condense on the cold side of the membrane.

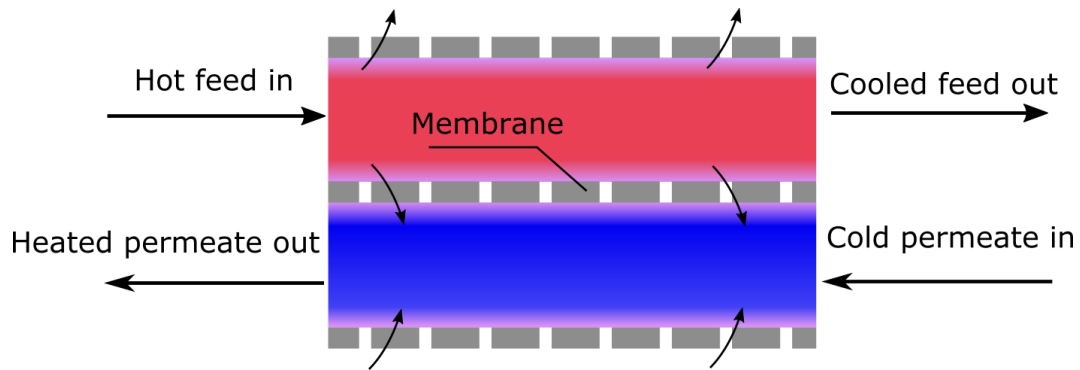


Figure 1.1: Membrane distillation principle

The process can be driven efficiently on low grade thermal sources (waste heat) and can reach extreme concentrations, while having an inherited potential for ultimate rejection of non-volatile components in the feed. Therefore, possible applications of membrane distillation include "difficult" cases with high salinity and streams with high fouling potential where waste heat is available. Example applications of MD include cases where the brine disposal is difficult or expensive, streams with extreme salinity where RO cannot be applied, concentration until saturation to recover chemicals, zero liquid discharge systems and other. Because of the low operational temperature and pressure, the technology can use cheap, plastic modules and piping, that do not suffer from corrosion.

Several of the most important full-scale systems available on the market today are summarized in Table 1.1

Table 1.1: The most important full-scale systems available on the market today are summarized. Adapted with permission from the PhD thesis of Lies Eykens [142]

Provider	Aquastill	SolarSpring (Fraunhofer)	Memstill (TNO)	Scarab	Memsys
Module type	Spiral wound		Plate and frame		
MD Configuration	AGMD	DCMD AGMD PGMD	AGMD	AGMD	V-AGMD
Membrane	PE (Ly-dall)	PTFE (Gore)	PTFE, PP, PE	PTFE (Gore)	PTFE (GE)
Capacity (Distillate) ($\text{m}^3 \cdot \text{day}^{-1}$)	24	10	-	2	100
Module size (m^2)	7.2 – 24	5-14	-	2.3	1.8-5
Flux ($\text{kg} \cdot \text{m}^{-2} \cdot \text{h}^{-1}$)	0.5-6	0.7-5		6.5 - 27	6.8-9.5
GOR	4-7	4.5	10-17		2.5-6
STEC ($\text{kW} \cdot \text{hT} \cdot \text{m}^{-3}$)	90-130	130-200	22-66	810	175-350
SEEC ($\text{kW} \cdot \text{hE} \cdot \text{m}^{-3}$)	0.1-0.4	<1	0.75	0.6-1.5	0.75-1.75
Production costs ($\text{€} \cdot \text{m}^{-3}$)	-	6	0.4-1.2	3-20	-

Where GOR, STEEC and SEEC are the gained output ration, the specific thermal energy consumption and the specific electrical energy consumption, claimed by the manufacturers. The main focus in this thesis is the simulation of the system provided by Aquastill.

1.2 Problem Statement

While membrane distillation has a tremendous potential as a separation technology for hard streams when waste heat is available, MD is still lacking widespread adoption. This could be due to a lack of major reference cases where MD is applied successfully for a significant amount of time. The uncertainty associated with the long term performance and cost of the technology is driving the industry away from MD. One possible way to reduce this uncertainty associated with the technology is to carefully model the process and gather process knowledge. The models can be used to predict the process perform-

ance across production scale and operational conditions. However, modelling of MD to date is mostly limited to lab-scale. Moreover, few authors in the literature discuss how their models are being calibrated and in fact almost no models are properly validated. Models with many calibration parameters are very common, where too many of them are simultaneously tuned just to achieve a good fit to the experimental data, possibly even outside of the realistic range of the parameter. This is not good modelling practice and one can question the added value of. Indeed, such model cannot be used reliably for studying the influence of each phenomena and is likely to fail when applied on larger or a smaller scale. In other words, it lacks predictive power.

MD modelling at full-scale is even more limited in the literature. Only a handful of models have been proposed for commercially available modules. By lacking full-scale models, the MD community cannot predict if MD would be a viable technology in a certain case and instead, expensive and time consuming pilot trials have to be performed.

Finally, reliable economic studies of MD are practically non-existent. Apart from the recent literature contributions by D. Winter [6], Ali et al. [7] and Al-Obaidani et al. [8], the price of membrane distillation is still largely unknown.

1.3 Objectives of this research

In view of the leaps in knowledge highlighted in section 1.2, this work aims at:

- Developing a soundly calibrated DCMD model that can be used to reliably study all of the heat and mass transfer phenomena in the system at lab-scale. In this way the bottlenecks in the system are identified and possible strategies for reduction of the limiting resistances are suggested.
- Scaling-up the DCMD model and applying it at full-scale including thorough validation using commercially available modules. The model scale-up in this work is done without including additional calibration parameters.
- Extending the full-scale model to other configurations, while still avoiding the use of calibration parameters. Instead of calibration, a novel methodology for measurement of the unknown parameters is developed.

- Studying the major heat and mass transfer bottlenecks of the system at full-scale and creating an optimal module design, starting from a commercially available module.
- Creating a graphical user interface tool that can be used as a decision support tool for system designs at different production scales. The tool can also be used for detailed and customized cost estimation of the system and the permeate prices.
- Creating a simplified model that can be used without prior modelling experience or simulation tools and be used to estimate the MD system and distillate price.

1.4 Outline: The roadmap through this dissertation

The roadmap of this thesis is provided in Figure 1.2.

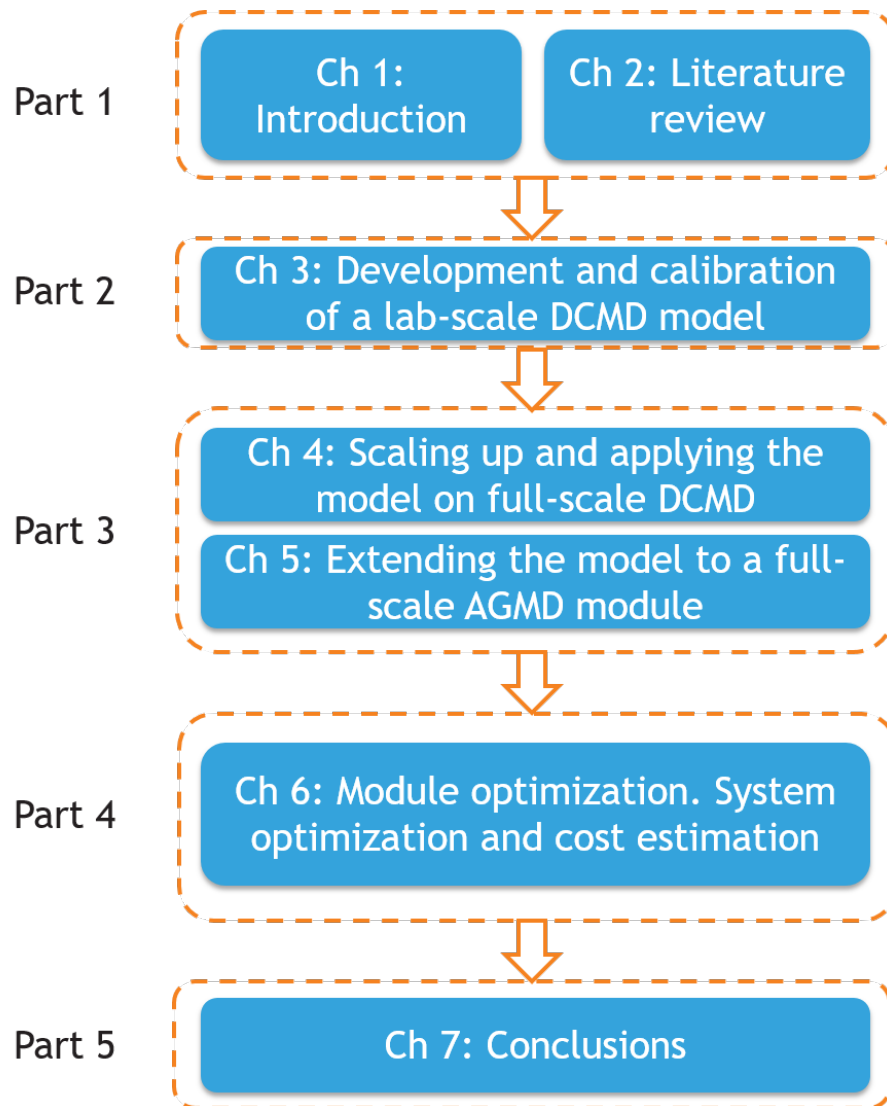


Figure 1.2: Outline of this thesis

In part 1 of this thesis the introduction and literature overview are given. In part 2 a methodology for calibration of a lab-scale model is presented. The model is built in a flexible, modular way, allowing the simulation of the system with another flow spacer or a membrane.

In part 3, the previously developed lab-scale model is applied and validated on full-scale for a DCMD module (Chapter 4) and later extended and validated on full-scale for two AGMD modules (Chapter 5). Particular care was taken to avoid the introduction of additional calibration parameters on full-scale.

In part 4 a graphical user interface is presented. All of the previously developed models are integrated into the interface in an intuitive way, allowing automated module optimization for three of the most popular membrane

distillation configurations. Further, this tool can be used for the automated designs of complete MD systems, including pumps, heat exchangers and other supporting equipment. The tool can quickly evaluate the price of the installation and the distillate in each case.

In part 5 of this thesis the general conclusions and recommendations for future research are given.

CHAPTER 2

Literature review

Redrafted from: I. Hitsov, T. Maere, K. De Sitter, C. Dotremont, I. Nopens, 2014. Modelling approaches in membrane distillation: A critical review, *Separation and Purification Technology* (142), 48-64

Abstract

Membrane distillation is a technique aimed at separating non-volatile components such as salts from aqueous feed streams. Mathematical modelling of a complex process like membrane distillation allows building further insight needed for effective analysis and optimization of the system, possibly leading to a breakthrough of the technology. Several models have been proposed in the literature for the heat and mass transport in the water channels of the module as well as inside the porous membranes. This chapter provides a critical review of these models and discusses the pros and cons of the different models to guide the reader into selecting the most suitable simulation approach. Moreover, research gaps in the literature are listed to indicate what is currently missing from a modelling as well as experimental data collection perspective. Areas for further research are suggested.

2.1 Introduction

Membrane distillation (MD) was first developed in 1963 by Bodel when he patented the vapor diffusion through silicone rubber for saline water distillation [9]. The most used and studied MD configuration is the direct contact membrane distillation where the hot feed and the cold permeate solutions are separated by a hydrophobic membrane. The feed solution comes into contact with the membrane and evaporates, the vapor travels through the pores and condenses on the cold permeate membrane interface (Fig. 2.1).

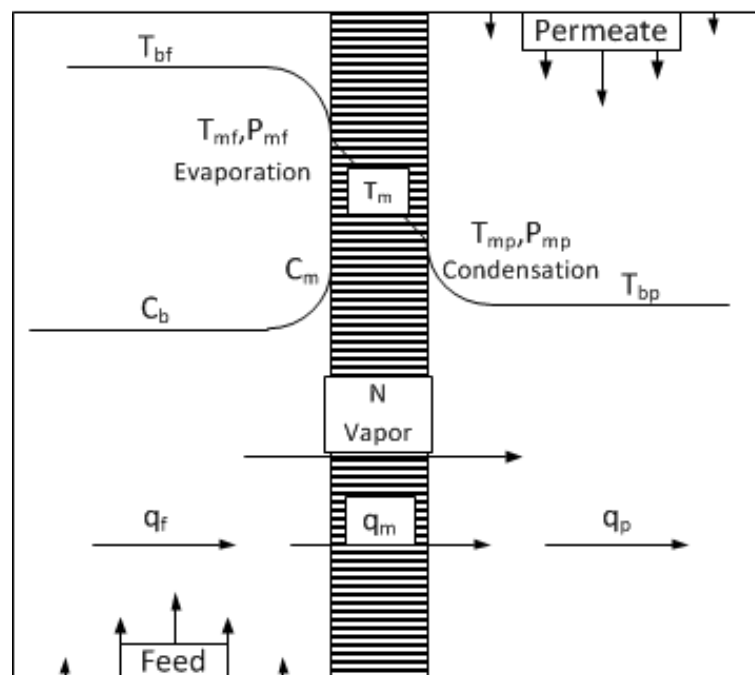


Figure 2.1: Operation of direct contact membrane distillation

The temperature difference across the membrane between the feed side (T_{mf}) and the permeate side (T_{mp}) as indicated in Fig. 2.1 results in different partial pressures of water vapor at the feed (P_{mf}) and the permeate side (P_{mp}). It is noteworthy that the actual driving force for the flux through the membrane is the vapor pressure difference and only the evaporated phase is transported across the membrane. The use of thin membranes creates large vapor pressure gradients, therefore allowing MD to be operated at relatively low feed temperatures, potentially allowing to reuse waste heat from other processes.

The heat and mass transfer in MD are interconnected and lead to a complex relationship. When water is evaporated on the feed side it takes away part of

the energy of the feed, which is carried away by the water vapor flux. This energy is transferred to the permeate during the condensation. Moreover, some of the energy is transferred through the membrane matrix itself via conduction in the form of sensible heat. The combined effect of the sensible heat and the heat due to evaporation creates thermal boundary layers near the interface of the membrane, leading to reduction of the intermembrane flux.

Recently, it was attempted to directly measure the interfacial temperature using miniature PT100 sensors [7], but this method has the disadvantage that a special cell must be designed and the assumption that the sensors will not interfere significantly with the thermal boundary layers should hold. Another recent study measured the temperatures inside an MD module using Thermochromic Liquid Crystals (TLCs) [10,11]. The TLCs can be used to quickly and relatively accurately measure the temperature of a stream by recording the color change [12]. Another approach is to model the system in order to predict the membrane temperatures. This could be done either using the semi-empirical Nusselt equations [13–16] which are frequently used in the design of heat exchangers, or by using the more physical approach of Computational Fluid Dynamics (CFD) [17–22], at the expense of larger computational power requirements. Both modelling approaches will be further discussed in this chapter and specific examples will be given.

There are four main contributions to the mass transfer inside the membrane pores: 1) molecular (ordinary) diffusion where the water vapors diffuse through the air trapped inside the larger pores of the membrane; 2) Knudsen diffusion occurs in the pores that have a size smaller than the length of the free path of the molecules for the given pressure and temperature; 3) viscous (poiseuille) flow is dominant in the larger pores in the cases where a total pressure difference across the pore exists; 4) surface diffusion is a mechanism of molecule transfer on the surface of the membrane polymer, but is neglected in MD modelling, because it is expected that due to the hydrophobic nature of the membranes the molecule-surface interaction will be low [23]. Depending on the operational mode and the used membrane type, one or more of the transport mechanisms can be neglected in order to simplify the system model. The main models that deal with the vapor flow through the membrane are the Dusty Gas Model (DGM) [24–27], the Schofield's model [28,29], some applications of the Kinetic Theory of Gasses (KTG) applied for each pore in a distribution [16], as well as models that are applied based on flow in a network of interconnected pores mimicking the membrane structure [30–33]. When real solutions

are used as feed instead of pure water the driving force will be lowered due to water activity reduction. Moreover, concentration polarization might occur, which additionally impairs the performance. This effect is strongest at high fluxes when the dissolved substance concentration near the membrane surface increases. The concentration polarization has not yet been directly measured but has been modelled either with a semi-empirical equation based on the Sherwood number or by CFD modelling.

An MD system allows for different operation modes such as feed temperatures, flow rates, concentrations, module configurations and membranes types to be incorporated. One could try to improve the performance of the system by varying the operational conditions in different modules, but this is an expensive and time-consuming job. Moreover, not fully understanding the transport mechanisms and phenomena occurring inside the system possibly results in one overlooking important parameters interactions. Therefore, it is crucial that MD is modelled in an accurate and physical way. A comparative table of the discussed models in this chapter is given in Table 2.1.

Table 2.1: Comparative table of models available for membrane distillation

Name	Region	Type	Output	Physical
Nusselt equation	Channels	HT	T_{mf} T_{mp} , TPC, EE	Semi
Sherwood equation	Feed Channel	MT	c_{mf}	Semi
Dusty gas model	Membrane	MT	N	Yes
Schofield's	Membrane	MT	N	Yes
Fick's	Membrane	MT	N	Yes
Structural network model	Membrane	MT	N	Yes
Kinetic theory of gasses	Membrane	MT	N	Yes
Ballistic transport model	Membrane	MT	N	Yes
Computational fluid dynamics	System	MT, HT	N, ∇T , ∇v , ∇c	Yes
Artificial neural networks	System	Black Box	N, EE	No
Design of Experiments toolbox	System	Statistical	System Optimization	No

This chapter first describes these models in detail (section 2.2). Section 2.3.1 then discusses and points out their pros and cons and finally section 2.3.2 highlights current research gaps. As can be seen there are numerous models in the literature allowing to describe the different phenomena that are occurring in MD and often there are multiple models that can be used to simulate the same phenomenon and all have their strengths and limitations. This chapter is intended to help the reader gain process knowledge on membrane distillation and assist in choosing the best model for their particular simulation.

2.2 State of the art in membrane distillation modeling

2.2.1 Heat transfer models

General Nusselt number-based approach

Heat transfer models are used to describe and quantify the heat transfer in the vicinity of the membrane and predict the temperatures on the membrane interface. Heat transfer models also serve as a backbone for the mass transfer models by predicting the average temperature inside the membrane and the vapor pressure at the interfaces, which are needed as inputs for calculating the mass transfer. There are four contributions to the heat transfer process - (1) the heat transfer from the feed bulk to the membrane interface, (2) the heat flux through the membrane via conduction in the air/polymer matrix, (3) the heat transfer due to the flux of evaporated water and (4) the heat transfer from the permeate membrane interface to the bulk of the permeate channel. In equilibrated MD modules the heat flux in the water channels and the membrane must be equal (Eq. 2.1).

$$\underbrace{h_f(T_{bf} - T_{mf})}_{(1)} = \underbrace{NH_v}_{(2)} + \underbrace{h_m(T_{mf} - T_{mp})}_{(3)} = \underbrace{h_p(T_{mp} - T_{bp})}_{(4)} \quad (2.1)$$

The symbols h_f, h_m and h_p represent the heat transfer coefficients of the feed, membrane and permeate, T, N and H_v the temperature, flux and specific heat of evaporation, respectively. The subscripts b, m, f and p represent the bulk, membrane interface, feed and permeate, respectively. Several heat transfer models have been developed in the literature for membrane distillation [7, 14–16, 34] but all are based on the calculation of the Nusselt number (Nu). In order to gain better understanding of these heat transfer models a schematic algorithm is given in Fig. 2.2. This algorithm is generic and the proposed models differ in the way certain steps are calculated. However, the used algorithm is always the same.

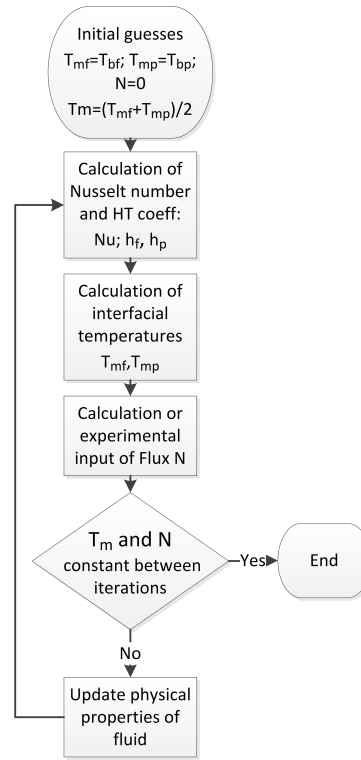


Figure 2.2: Typical algorithm for simulation of MD using Nusselt equations for the water channels

As a prerequisite for the calculation of Nusselt number, the Reynolds and Prandtl numbers must be calculated for the feed and the permeate channels. The mean membrane temperature is taken as an average of the bulk temperatures.

$$Re_{f,p} = \frac{vd\rho}{\mu} \quad (2.2)$$

$$Pr_{f,p} = \frac{\mu C_p}{\kappa} \quad (2.3)$$

In eq. 2.2 Re , the Reynolds dimensionless number, represents a ratio of the inertial to viscous forces and is used to describe the hydrodynamic conditions of the flow. Pr in eq. 2.3 stands for the Prandtl number, also dimensionless, representing the ratio of viscous to thermal diffusion rate. The symbols v , d , ρ , μ , C_p and κ represent the velocity, characteristic size of the geometry (diameter for a pipe and height for a channel), density, viscosity, specific heat capacity and thermal conductivity, respectively.

The next step is to evaluate the Nusselt number, a dimensionless number representing the ratio of the convective to diffusive heat transfer. Nusselt number

are computed for the feed and permeate channels using the following correlation (eq. 2.4) valid for laminar regimes, given by Gryta et al. [13]:

$$Nu_{f,p} = 0.097Re^{0.73}Pr_b^{0.13}(Pr_b/Pr_{wall})^{0.25} \quad (2.4)$$

The value of Pr_{wall} used in eq. 2.4 is evaluated for fluid properties at the interfacial temperature of the feed or the permeate. It should be noted that the form of the Nusselt equation is unique to the channel geometry and the flow regime. Once the Nusselt numbers for feed and permeate are evaluated, the heat transfer coefficients of the feed and the permeate h_f , h_p can be obtained using the relation in Eq. 2.5:

$$h_{f,p} = \frac{Nu_{f,p} \cdot \kappa}{d} \quad (2.5)$$

The last step is to calculate the interfacial temperatures of the membrane.

$$T_{mf} = \frac{T_{bf}h_f + T_{mp}h_m - NH_v}{h_f + h_m} \quad (2.6)$$

$$T_{mp} = \frac{T_{bp}h_p + T_{mf}h_m + NH_v}{h_p + h_m} \quad (2.7)$$

The above equations are derived from Eq. 2.1 assuming equality of heat flux in all compartments in steady state. The conductive heat transfer coefficient of the membrane h_m is determined as the ratio of the air/polymer matrix thermal conductivity κ_m and the thickness of the membrane δ

$$h_m = \frac{\kappa_m}{\delta_m} \quad (2.8)$$

It must be noted that the flux is included in the calculation of the interfacial temperatures (eq. 2.6 and 2.7). An initial guess for the first iteration and later the flux from the previous iteration is used for current iteration. The algorithm is then restarted using the newly calculated interfacial temperatures and repeated until the difference in two consecutive calculated interfacial temperatures or fluxes are within a user-defined accuracy.

If the heat transfer model is used for experimental analysis (estimation of temperature polarization and membrane permeability), the flux from the experiments should be used.

Considerations and extensions of Nusselt equations HT models

Most of the authors [7,13–15,34] pay special attention to the choice of the Nusselt number correlation. The Nusselt number is a semi-empirical correlation used for the estimation of heat transfer coefficient in the water compartments. A commonly used form, valid for laminar flow MD modules [13] is given in eq. 2.4. However, this form is not absolute and can greatly differ depending on the flow regime and module geometry. We must stress on the fact that the choice of Nu equation should be done very carefully. Usually, experimental data is collected and the experimental overall heat transfer coefficient is compared to the theoretical one in order to choose the best performing Nusselt equation. More information on the experimental validation of Nu number equations is given in section 2.2.1. Extensive lists of Nusselt equations for different geometries can be found elsewhere [7,13–15,35].

The Nusselt equation predicts solely a uniform interfacial temperature, however in some cases an iterative procedure can be applied as done by Zhang et al. [36] as well as by Winter et al. [6] where the geometry is split into a number of sections. The bulk temperature for each next segment is calculated by adjusting it with the exchanged energy of the previous elements using a heat balance. The procedure is stopped when the overall heat balance for the system is correct. By calculating the temperature for each section, the temperature profile along a MD module can be predicted. In order to validate the model, the flux is compared at different cell lengths and inlet temperatures. Excellent flux prediction was achieved in the validation. A similar approach was taken by Sirkar and Song [37], where a cross-flow, hollow fibre, direct contact MD module was simulated by splitting it into sections and adjusting the temperatures for each section using a heat balance. They also achieved good fit to experimental data. This is an alternative approach to using computational fluid dynamics (CFD) for determining the flux and temperature distribution inside a module, but cannot be used to develop a novel spacer or fibre designs. Another extension of HT models based on the Nusselt equation is proposed by Gryta et al. to create a model that is non-isenthalpic with a non-linear temperature distribution inside the membrane [14]. The authors, however, do not explicitly state the significance of this addition. Phattaranawik et al. on the other hand [15] show that even though the intermembrane temperature is an exponential function of thickness, the temperature profiles are nearly linear due to the very thin membranes used in MD.

Calculation of membrane thermal conductivity

The thermal conductivity of the membrane is not easy to model as the matrix is comprised of a mixture of water vapor, air and polymer in a complex structure. Mainly two models are used in the MD literature for the prediction of the thermal conductivity: the resistance in parallel model (Isostrain, eq. 2.9) [14, 16, 25, 33, 34, 36, 38, 39] and the much less often used resistance in series model (Isostress, eq. 2.10) [15, 40].

$$k_m = (1 - \epsilon)\kappa_s + \epsilon\kappa_g \quad (2.9)$$

$$k_m = \left[\frac{\epsilon}{\kappa_g} + \frac{1 - \epsilon}{\kappa_s} \right]^{-1} \quad (2.10)$$

In these equations κ_g and κ_s are the thermal conductivities of gas and polymer and ϵ is the porosity of the membrane.

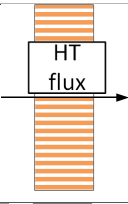
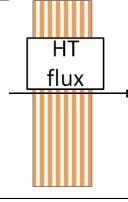
It is noteworthy that both the series and the parallel models are limiting cases for possible membrane structures. The parallel model assumes a membrane which is ordered in such way that the polymer is oriented in the direction of the heat flux, whereas the series model assumes the gas/polymer layers to be evenly spaced and oriented in series, perpendicular to the heat flux (Table 2.2). García-Payo et al. [40] performed an extensive evaluation of 9 different models for prediction of thermal conductivity of the membrane matrices of 2 PVDF, 2 PTFE and 2 supported PTFE membranes and compared them to experimental data. The authors concluded that the commonly used parallel model largely overestimates the thermal conductivity, whereas the series model slightly underestimates it. The best fit for all tested membranes and recommended to use for porosities higher than 60% was the Maxwell type I equation (eq. 2.11), where β is an intermediate factor.

$$\kappa_m = \frac{\kappa_g(1 + 2\beta(1 - \epsilon))}{1 - \beta(1 - \epsilon)} \quad (2.11)$$

$$\beta = (\kappa_s - \kappa_g) / (\kappa_s + 2\kappa_g) \quad (2.12)$$

Indicative κ_m predictions using these different modelling approaches are given in Table 2.2. This indicates that the resulting thermal conductivity very much depends on the choice of model, varying by a factor of 2 or more.

Table 2.2: Comparison of different models for the calculation of membrane thermal conductivity. Membrane parameters used: $\epsilon=0.8$, polymer conductivity $0.25W/(m.K)$, gas conductivity = $0.027W/(m.K)$

Model	Graphical representation	Calculated $\kappa_m, W/(m.K)$
Isostrain		0.072
Isostress		0.033
Maxwell I	N/A	0.041

Zhang et al. [36] also commented on the choice of the thermal conductivity model and stated that the experimental measurement of highly porous membranes can be compromised by the force of clamping when using the experimental equipment. The authors noted that if the clamping force of the measuring equipment is too large, the membrane can collapse and the thermal conductivity will be overestimated due to the reduced porosity. On the other hand if the clamping force is too small the contact with the membrane will be insufficient and the conductivity will be underestimated.

Because of this uncertainty it is not possible to directly recommend the best model for predicting thermal conductivity. Generally it would be a safe choice to use the Maxwell Type I model as it is not developed for a limiting geometric case. Nevertheless, if the structure resembles the parallel (isostrain) model for example for a membrane produced with track etching or with photo lithographic methods where the pores are much less tortuous and more ordered, the use of the parallel model could be advisable.

A laser flash technique was used by Dumée et al. [41] to measure the thermal conductivity of the membrane. In this technique a laser pulse is applied on one side of the membrane and the temperature response on the other side of the membrane is measured using an infrared detector. The authors coated both sides of the sample with thin gold and carbon layers. The gold layer was applied on the membrane to improve the surface thermal diffusivity and the carbon film was applied on top to minimize the laser reflection from the

golden surface. The total reported coating thickness was 10 μm . This method is interesting for validation of thermal conductivity models, however it needs extensive sample preparation and care should be taken that the coatings adhere well to the membrane and do not alter its structure. Dumée et al. [41] also point out that a lower surface energy of the membrane can facilitate the formation of an air film adjacent to the membrane that further lowers the total conductive losses across the membrane. This effect has not been taken into account by any model to date.

The thermal conductivity of the air and water vapor trapped inside the pores is very similar and could thus be treated as one component [15,42]. Their thermal conductivity can be estimated based on the equation given by Jonsson et al. [39] (eq. 2.13) or alternatively by the more recent expression given by Bahmanyar et al. [43] (eq. 2.14).

$$\kappa_g = 1.5 \times 10^{-3} \sqrt{T_m} \quad (2.13)$$

$$\kappa_g = 2.72 \times 10^{-3} + 7.77 \times 10^{-5} T_m \quad (2.14)$$

The thermal conductivity of crystalline polymers is assumed to be a weak function of temperature [15], and some example values at 23 and 75 $^{\circ}\text{C}$ are given by Phattaranawik [15] for PVDF, PTFE and PP. Additionally the thermal conductivity of PES can be graphically estimated from the work of Saleem et al. [44]. We derived an equation fit based on the assumption for linear change in conductivity as a function of temperature that could be used in modelling. A summary of the of the thermal conductivity of different polymers is given in Table 2.3.

Table 2.3: Thermal conductivity of some polymers and linear fit equation coefficients, temperature in K

Polymer	Therm. cond. , $W/(m.K)$ at 23 $^{\circ}\text{C}$	Therm. cond. , $W/(m.K)$ at 75 $^{\circ}\text{C}$	Linear fit equation $\kappa = A \times 10^{-4} T_m + B \times 10^{-2}$
PVDF	0.17-0.19 [15]	0.21 [15]	A=5.769 B=0.9144
PTFE	0.25-0.27 [15]	0.29 [15]	A=5.769 B=8.914
PP	0.11-0.16 [15]	0.20 [15]	A=12.50 B=-23.51
PES**	0.145* at 40 $^{\circ}\text{C}$ [44]	0.16* [44]	A=4.167 B=1.452

*Graphical estimation from [44]

**PES can be used in MD when modified to increase the hydrophobicity

Experimental validation of Nusselt equations HT model

In order to exclude the uncertainty the flux measurement and the uncertainty of the combined air and polymer thermal conductivity of the membrane (κ_m) some authors have proposed to use solid impermeable polymer sheets [14] or aluminium foil [15] in heat transfer experimental studies. The overall heat transfer coefficient U can be calculated from the measurement of inlet and outlet temperatures, flow rate F and the heat transfer area A .

$$Q = FC_p T_{in} - FC_p T_{out} \quad (2.15)$$

$$U = \frac{Q}{A \times LMTD} \quad (2.16)$$

Where $LMTD$ is the logarithmic mean temperature difference and Q is the heat flow calculated from the heat balance for one of the compartments. The experimental overall HT coefficient can be compared with the theoretical ones obtained by eq. 2.5 using different Nu number correlations. The theoretical overall HT coefficient can be calculated using eq. 2.17, and the advantage of using solid polymer or aluminium sheet instead of a membrane is the exact prediction of the term $\frac{\kappa_m}{\delta}$.

$$U = \frac{1}{\frac{1}{h_f} + \frac{\kappa_m}{\delta} + \frac{1}{h_p}} \quad (2.17)$$

2.2.2 Mass transfer (concentration polarization) inside the feed channel

As the salt is rejected at the membrane surface in the feed channel, the concentration near the membrane will increase. This phenomenon is known as concentration polarization. It is important to model this effect because it negatively influences the flux by reducing the water activity. Because MD achieves nearly 100% rejection for non-volatile components, the modelling is only required for the feed channel.

Concentration polarization estimation based on the Sherwood number

Similarly to the temperature polarisation that happens inside the MD channels, concentration polarization will also occur in the feed channels of a module. In

order to estimate the influence of this phenomenon Martínez-Díez al. [45] built a model for a flat sheet geometry that included the semi-empirical relations for the mass transfer in the channels based on the Graetz-Lévêque definition of the Sherwood number (Sh). The Sherwood number is a dimensionless number, the mass transfer equivalent of the Nusselt number representing the ratio of the convective to diffusive mass transfer:

$$c_{mf} = c_{bf} e^{Mw.N/\rho K} \quad (2.18)$$

$$K = \frac{ShD}{d_h} \quad (2.19)$$

$$Sh = 1.86(ReSc \frac{d_h}{L})^{0.33} \quad (2.20)$$

$$Sc = \frac{\mu}{\rho D} \quad (2.21)$$

Where Mw , c_{mf} , c_{bf} , K , D , Sc and L are the molar weight of water, concentrations at the membrane interface and bulk of the feed, the overall mass transfer coefficient, diffusion coefficient and the length of the geometry, respectively. Martínez-Díez et al. concluded that the interfacial salt concentration is as much as 4 percent higher compared to the bulk concentration [45] in the tested conditions with fluxes up to $10 \text{ kg}/(\text{m}^2.\text{h})$ and resulting driving force decrease of only 0.2%. In terms of driving force reduction, the concentration polarization in MD has a negligible contribution for low concentrations (see fig. 2.3). This is shown by Martínez et al. [27], where the heat and mass transfer resistances in a DCMD system are split and the resistance associated with concentration polarization becomes significant only for concentrations approaching saturation. Therefore, it would be safe to neglect the concentration polarization at low concentrations such as sea water. However, the concentration polarization is generally easy to model and does not add much computational burden and the models that include the concentration polarization phenomenon could be used to investigate the possibility of scaling on the membrane interface. Different modelling attempts for scaling [46], fouling [47–50] and biofouling [51] processes in MD exist in the literature, but are considered outside the scope of this review.

Similar to the Nusselt number, there is no universal form of the Sherwood eq. 2.20 and its form depends on the flow regime and the geometry of the system. Most MD authors assume the analogy between the heat and mass transfer in the channels [15,45,52] with Sh and Sc numbers being the mass transfer equivalents of Nu and Pr numbers respectively. This analogy could be used to

choose a Sherwood number equation after experimental validation of the Nusselt equation [45]. While there are attempts made to validate the interfacial temperatures with sensors [7] and thermochromic liquid crystals [10,11], no work is present in the literature that attempts to validate concentration polarization effects. An alternative to estimate the interfacial concentration is a study with CFD (see Section 2.2.5), although further validation would still be needed.

Calculation of water partial pressure and activity

To link the heat transfer models with the mass transfer model the partial pressure of water vapor must be calculated based on the interfacial temperatures. This can be done with the Antoine equation (eq.2.22) [53]:

$$p_0 = \exp \left(23.5377 - \frac{4016.3632}{T - 38.6339} \right) \quad (2.22)$$

The above equation calculates the vapor pressure for pure water p_0 in Pa based on temperature T in Kelvin. However, when real solutions are used as feed, the water vapor pressure on the feed side is lowered due to the reduced water activity. The actual vapor pressure p_i can be recalculated using either the activity a_w , or the activity coefficient γ_i and the water mole fraction x_w [54].

$$p_i = p_0 a_w = p_0 x_w \gamma_i \quad (2.23)$$

The activity and the activity coefficients of water are used to represent the non-ideality of the solution. It is generally accepted that the calculated vapor pressure using Antoine's equation only differs on the feed side, as the permeate of MD is usually pure water. In MD literature a fit to the experimental data derived by Schofield et al. [55] is cited in order to calculate the activity coefficient of the water-salt mixture [26,56].

$$\gamma_i = 1 - 0.5x_{NaCl} - 10x_{NaCl}^2 \quad (2.24)$$

Other references where the water activity could be obtained were compared to the one calculated with eq. 2.24 (Fig.2.3).

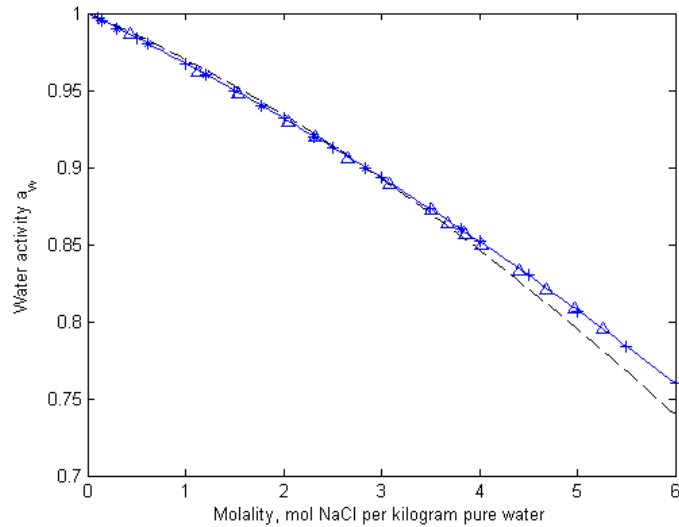


Figure 2.3: Water activity in salt solutions obtained from different sources. Legend: "+" [57] at 25°C, "*" [58] at 25°C, "Δ" adapted for molality from [59] at 35°C, dashed line adapted for activity and molality from - eq. 2.24, solid line fit using eq.2.25

As can be seen in Fig. 2.3, the activity obtained from the empirical equation of Schofield (eq. 2.24) [55] (seen as dashed line) slightly deviates from the referenced experimental data, in the sense that it underestimates the activity at high concentrations. Because of the discrepancies using eq. 2.24, we propose a second order polynomial fit to the data and the prediction of this new equation is seen as solid line (Fig. 2.3). The experimental data used to make the polynomial fit was taken from the latest water activity reference from 2007 [57] where the salt concentration was varied from 0 all the way until saturation. The newly proposed equation is given below:

$$a_w = 1 - 0.03112m - 0.001482m^2 \quad (2.25)$$

Where m is the NaCl molality (mol NaCl per kilogram pure water). The activity of water also depends on the temperature of the solution, although this effect is small [58]. In the article of Chirife et al. [60] the difference in activities of salty water between 25 and 60°C is less than 0.2%, indicating that there is no need for a temperature correction for salt solutions. More examples of equation fits for different solutes are given by Khayet et al. [56]. However, if a more complex mixture of ions is used as feed, more sophisticated and physical models such

as the Pitzer's equations [61] or the non-random two-liquid (NRTL) [62] model must be used to predict the water activity.

2.2.3 Models for mass transfer inside the membrane

Numerous models used to describe the mass transfer of water vapor inside the porous MD membrane exist in the literature. One of the simplest ways is to use Fick's law that treats the membrane as an empty space full of air in which the molecules of the water vapor are diffused. This approach does not consider the membrane structure such as the porosity, tortuosity and the pore size. These membrane parameters are taken into account for the much more widely used Dusty Gas Model and the Schofield's model. The latter models, however, do not take into account the effect of pore size distribution and an average pore size is used. Pore size distribution models have been developed based on the Kinetic Theory of Gasses (KTG) and extensions of the Dusty Gas Model. Finally, a three dimensional model based on the KTG has been developed in order to simulate the effect of the pore size distribution and interconnectivity. In this section the different models are presented and discussed giving their pros and cons.

Fick's law model

One of the simplest ways to describe the mass transfer through the membrane region is by using the Fick's law model. By representing the membrane region as a space full of stagnant air, Bahmanyar et al. [43] uses an expression for the flux of the water vapors diffusing through the air (eq. 2.26-2.29).

$$N_{calc} = \frac{PM_w D_{w-a}}{RT_m \delta} \ln \frac{P - p_{mp}}{P - p_{mf}} \quad (2.26)$$

$$D_{w-a} = \frac{2.634}{P} \left(\frac{T_m}{273.15} \right)^{1.5} \quad (2.27)$$

$$D_{eff} = \frac{N_{exp}}{N_{calc}} D_{w-a} \quad (2.28)$$

$$N_{eff} = \frac{PM_w D_{eff}}{RT_m \delta} \ln \frac{P - p_{mp}}{P - p_{mf}} \quad (2.29)$$

The author first obtains an initial theoretical flux N_{calc} (eq. 2.26) using the theoretically calculated diffusion coefficient D_{w-a} (eq. 2.27). To calibrate the model, the theoretical diffusion coefficient D_{w-a} is multiplied with the ratio of the experimental N_{exp} and initially calculated N_{calc} fluxes to find the effective diffusion D_{eff} (eq. 2.28), which is subsequently used to calculate the effective flux N_{eff} (eq. 2.29).

Dusty gas model

Another way to describe the mass flow inside the membrane is the Dusty Gas Model (DGM) [63]. It can be applied for a multi-component mixture of gases, where the pores of the medium are represented as stationary pseudo gas molecules with large size (dust) [64]. The effect of viscous (poiseuille) flow, as well as molecular and Knudsen diffusion are frequently modelled in porous media using the DGM [25,48,65]. Although theoretically the model can consider the effect of surface diffusion [24,66] it is generally considered negligible in the MD process [26] and has never been included in the MD modelling to our knowledge.

In its most general form the DGM equation used in membrane distillation is given by Lawson et al. [26]. This model accounts for the flux due to molecular and Knudsen diffusion as well as viscous flow, but neglects surface diffusion [23,25] (eq. 2.30-2.33).

$$\frac{N_i^D}{D_{ie}^K} + \sum_{j=1 \neq i}^n \frac{p_j N_i^D - p_i N_j^D}{D_{ije}^m} = \frac{-1}{RT} \nabla p_i \quad (2.30)$$

$$N_i^V = \frac{-p_i B_0}{RT \mu} \nabla P \quad (2.31)$$

$$N_i = N_i^D + N_i^V \quad (2.32)$$

$$D_{ij,e}^m = K_1 P D_{ij}, \quad D_{ie}^k = K_0 \sqrt{\frac{8RT}{\pi M_i}} \quad (2.33)$$

In the above equations N_i^D , N_i^V and N_i are the diffusive, viscous and total fluxes; P and μ are the total pressure and viscosity of the mixture while p_i is the partial pressure of component i , respectively. Finally, $D_{ij,e}^m$, D_{ie}^K represent the effective molecular and Knudsen diffusion coefficients and M_i is the molar weight of component i .

There are three constants (B_0 , K_0 , K_1) that depend on the membrane struc-

ture and are best determined experimentally due to the complex membrane structure [26]. As a quick approximation they can also be calculated using membrane parameters such as membrane pore radius, tortuosity and porosity (r, τ, ϵ) [26]:

$$B_0 = \frac{\epsilon r^2}{8\tau}, \quad K_0 = \frac{2\epsilon r}{3\tau}, \quad K_1 = \frac{\epsilon}{\tau} \quad (2.34)$$

It is generally accepted that during certain operational conditions some of the transport mechanisms can be excluded and some simplifications of the DGM are given in section 2.2.3.

Simplifications of the DGM - Ordinary, Knudsen and Transition regions

The first simplification of the dusty gas model is the exclusion of the term $p_i N_j^D$ from eq. 2.30, by assuming that the diffusive flux of air N_j^D is totally impaired by the low diffusion coefficient of air in water [26] and the low solubility of air in water [56].

An important characteristic of the vapor permeation process is the Knudsen number (Kn) which represents the relation of the mean free path that the molecule travels (λ) to the pore size of the membrane (d_p) expressed as $Kn = \lambda/d_p$. The mean free path of the molecule can be calculated using the equation:

$$\lambda_i = \frac{K_B T}{\sqrt{2\pi \bar{P}} \sigma_i^2} \quad (2.35)$$

In the equation above σ_i is the collision diameter, which is 0.2641nm for water vapors [67]. K_B , T and \bar{P} respectively stand for the Boltzmann constant, the absolute temperature and the mean pressure in the membrane pores [23].

There are three main mass transport regimes that can be distinguished based on the Knudsen number. If $Kn > 1$ the molecules will collide mainly with the pore walls and therefore the Knudsen diffusion mechanism will be prevailing for the membrane pores and equations 2.30-2.33 simplify to 2.36, by replacing the gradients of pressure ∇p_i with $\frac{\Delta p_i}{\delta}$ and neglecting the flux of air N_j . If the pore size is much larger than the mean free path of the water molecules ($Kn < 0.01$), the dominating transport mechanism will be molecular diffusion of water vapor through the stagnant air trapped inside the pore. This is described by eq. 2.37, where $|p_a|_{ln}$ is the log mean air pressure across the membrane [26]. Finally, a transition region exists for pore sizes characterized by $0.01 < Kn < 1$. Here, the transport will be governed by both molecular and Knudsen

diffusion (eq.2.38). The total flux equations for different permeation regimes as a function of the Kn number for a uniform pore size distribution are given by:

$$N^K = K_0 \frac{\bar{v}}{RT} \frac{p_{mf} - p_{mp}}{\delta}, \quad Kn > 1 \quad (2.36)$$

$$N^D = \frac{D_{ij,e}^m}{RT\delta} \frac{p_{mf} - p_{mp}}{|p_a| \ln}, \quad Kn < 0.01 \quad (2.37)$$

$$N^T = \frac{D_{ij,e}^m}{\delta RT} \ln \left(\frac{p_a^p D_{ie}^K + D_{ij,e}^m}{p_a^f D_{ie}^K + D_{ij,e}^m} \right), \quad 0.01 < Kn < 1 \quad (2.38)$$

Where \bar{v} is the mean molecular velocity, $\sqrt{\frac{8RT}{\pi M}}$. In case there is a total pressure difference across the membrane, the viscous flow could easily be added as the DGM considers the viscous flow as a linear addition to the flux from molecular and Knudsen diffusion fluxes (Fig. 2.4). Typical cases where the viscous flux is combined with Knudsen are the vacuum membrane distillation using a membrane with larger pores, gas permeation and deaerated DCMD distillation [35,68] as described by eq. 2.39:

$$N^{V-K} = \frac{1}{RT\delta} \left(D_{ie}^K + \frac{\bar{P}B_0}{\mu} \Delta P \right) \quad (2.39)$$

Gas permeation test for evaluation of DGM membrane parameters

Experimentally, the values of K_0 and B_0 can be estimated via gas permeation tests. Water vapors cannot be used because of condensation problems inside the test apparatus [26,69]. However, N_2 and CO_2 can be used successfully because the structural parameters as defined by DGM are independent of the used gas (eq. 2.40). The gas is pumped through the membrane and the pressures and fluxes are logged. The DGM equation for Knudsen-Poiseuille transition is rearranged in the form [26,53,70]:

$$\frac{NRT\delta}{\bar{v}\Delta P} = K_0 + B_0 \frac{\bar{P}}{\mu\bar{v}} \quad (2.40)$$

and the membrane structural parameters are evaluated from a linear fit of the experimental data, where K_0 is the intercept and B_0 is the slope. A simple mathematical transformation reveals the values of the pore radius and the coef-

ficient K_1 :

$$r = \frac{16B_0}{3K_0} \quad K_1 = \frac{3K_0}{2r} \quad (2.41)$$

A drawback of this type of gas permeation tests is that the membranes commonly used for membrane distillation are highly porous and the possibility exists that the membrane partially collapses at high transmembrane pressures [36]. An alternative gas permeation method for the determination of K_0 and B_0 is given by Lei et al. [71] and Zhang et al. [36,72], where the transmembrane pressure is kept constant at 1 kPa and the average pressure inside the membrane pores is varied. This alternative gas permeation experiment has the advantage of excluding the possibility of membrane compressibility due to the much lower applied transmembrane pressures.

Eq. 2.40 is derived for a flat sheet experiment. In case the tested membrane is cylindrical (hollow fibre or capillary) an equation derived for this geometry can be found in the work of Guijt et al. [69].

Zhang et al. also derived an experimental procedure for the evaluation of the permeability of hollow fibre membranes [73]. The authors used constant, low transmembrane pressure and varied the average pore pressure (by lowering or increasing the pressure simultaneously on both sides of the membrane). The obtained permeability parameters varied at different hollow fibre lengths which was explained by the pressure drop along the membrane lumen. Therefore, the permeability was measured at different membrane lengths and extrapolated to zero length. The obtained parameters were later used to simulate a vacuum MD and the model proved to have high predictive power.

Lawson et al. [74] and Zhang et al. [36] proposed that under certain operational conditions some of the membranes used for MD can be compacted. As the membrane compacts the thickness is reduced which should increase the flux. Meanwhile, the compaction also increases the tortuosity and decreases the porosity and pore size, which has negative impact on the flux [74]. Lawson et al. [74] derived an expression to compensate these changes and noted a region where the permeability is increased by compaction, followed by a region of reduced permeability at higher compaction for a PP membrane. Zhang et al. [36] on the other hand only notices a negative effect from the compaction of PTFE membrane used in DCMD as the flux is reduced in the compressed membranes. Moreover, Zhang et al. noticed an increase in the membrane thermal conductivity at higher flow rates, which was attributed to the reduced porosity [36]. The membrane compaction effects are not taken into account in

the majority of MD models and further investigation into these effects could be interesting for the community.

Limitations of the Dusty Gas Model

The DGM is in fact derived for isothermal conditions, whereas in reality the temperature throughout the membrane is not constant [26]. Nevertheless, it has been successfully applied in membrane distillation using an average temperature for the membrane [23,26].

Recently the schematic representation of resistances in DGM has been questioned by Field et al. [75]. The model considers a resistance in series approach to Knudsen and molecular diffusions, with viscous flow in parallel (Fig. 2.4).

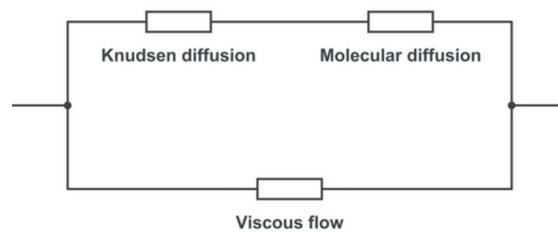


Figure 2.4: Schematic representation of DGM

Field et al. argue that it is not physically possible to have Knudsen and viscous flow occurring in the same pore (equation 2.39 in this work). The authors point out that viscous flow occurs differently when the pore size is comparable to the mean free path of the molecules. Moreover, a new equation for the addition of Knudsen and molecular diffusion is proposed for the transition region [75]. New modified equations to include these arguments were presented and tested against experimental work, but the model was not calibrated and the goodness-of-fit of the new model was not estimated. It would be interesting to see more work that further elaborates this approach.

Pore size distribution models

Models that take into account the pore size distribution for MD membranes have been developed by Phattaranawik et al. [76] and Khayet et al. [16]. The authors split the contribution of the Knudsen, molecular and transition mechan-

isms by proposing an equation for each region based on the calculated Knudsen number. Phattaranawik and co-workers propose an equation with average pore size in each region based on the Dusty gas model, while Khayet and co-workers calculated the flux for each pore in the size distribution based on the Kinetic Theory of Gasses (KTG) for straight cylindrical non-interconnected pores. The governing equations representing the permeability of a single pore with an area of πr^2 for these three regions is given by Khayet et al. [23]

$$B_i^K = \frac{2\pi \bar{v}}{3 RT \tau \delta} r_k^3 \quad Kn > 1 \quad (2.42)$$

$$B_i^D = \frac{\pi PD_i}{RT p_a} \frac{r_D^2}{\tau \delta} \quad Kn < 0.01 \quad (2.43)$$

$$B_i^T = \frac{\pi}{RT \tau \delta} \left[\left(\frac{2\bar{v}r_t^3}{3} \right)^{-1} + \left(\frac{PD_i}{p_a} r_t^2 \right)^{-1} \right]^{-1} \quad 0.01 < Kn < 1 \quad (2.44)$$

In eq. 2.42 r_k , M_i and δ represent the pore size in the Knudsen region, molecular weight of species i and thickness of the membrane respectively. In eq. 2.43 D_i is the diffusion coefficient, P and p_a the total and the air pressure inside the pore and r_D the pore size in the diffusion region. In eq. 2.44 r_t is the pore radius in the transition region. Because of the fact that most membranes have a pore size distribution this means that usually more than one transport mechanism will govern the process.

Based on eq. 2.42-2.44 Khayet et al. proposed an equation that could calculate the membrane flux for a distribution, instead of a uniform pore sizes [16]. In the resulting model the total membrane permeability is given by the following equations:

$$B_i^m = \frac{N}{\delta} \left[\sum_{j=1}^{m(r=0.5\lambda)} G_i^K f_j r_j^3 + \sum_{j=m(r=0.5\lambda)}^{p(r=50\lambda)} \left(\frac{1}{G_i^K r_j} + \frac{1}{G_i^D} \right)^{-1} f_j r_j^2 + \sum_{j=p(r=50\lambda)}^{n(r=r_{max})} G_i^D f_j r_j^2 \right] \quad (2.45)$$

$$G_i^K = \left(\frac{32\pi}{9M_i RT} \right)^{1/2} \quad (2.46)$$

$$G_i^D = \frac{\pi PD_i}{RT p_a} \quad (2.47)$$

$$N = \frac{\epsilon/\tau}{\sum_{j=1}^n f_j \pi r_j^2} \quad (2.48)$$

Where N, G, f are the number of pores per unit area, an intermediate term, and fraction of pores in this particular size class. The symbols m, n and p denote the largest pore size within each of the classes, i.e. Knudsen diffusion, Knudsen-molecular transition and the maximum pore size, respectively.

The authors of both pore size distribution models conclude that the influence of pore size distribution is not large and a single average pore size is an adequate representation [16,76]. Khayet and co-workers however state that this is due to the uniform pore size distribution of commercial membranes but potential discrepancies with the traditional method (mean pore size models) can be observed for membranes with a large standard deviation of pore size [16].

Schofield's model

Schofield and co-workers [28, 29, 77] proposed the following semi-empirical approximation of the flux in the viscous-Knudsen transition region.

$$N = a\eta^b \Delta P \quad (2.49)$$

With η a dimensionless pressure equal to P/P_{ref} . The reference pressure is chosen as a typical pressure for the operation range, in order for η to be close to 1. Parameter a is the membrane permeation constant and b the contribution of viscous flow to the total flux (0: Knudsen controlled, 1: fully viscous flow) [29]. Equation 2.49 is valid for deaerated systems and in order to account for the diffusive flux of water vapor in the air trapped inside the membrane pores, Schofield et al. proposed the following equation [29]

$$N = \left(\frac{1}{a\eta^b} + \frac{p_a}{d} \right)^{-1} \Delta P \quad (2.50)$$

$$d = \frac{\epsilon DPM}{\tau \delta RT} \quad (2.51)$$

As a first approximation of the coefficients a and b the following equations are proposed [28]:

$$a = M\bar{v}(A + BP_{ref}/L)/\delta \quad (2.52)$$

$$b = (BP_{ref}/L)/(A + BP_{ref}/L) \quad (2.53)$$

$$A = \frac{2r\epsilon}{3\tau RT} \quad (2.54)$$

$$B = \frac{\pi r^2 \epsilon}{32\tau RT} \quad (2.55)$$

A disadvantage of the Schofield's model, as pointed out by Lawson et al. [26] and Fernández [53] et al. is the dependency on the gas used to perform the permeability tests and the large experimental error that is associated with the determination of the coefficients a and b in eq. 2.49. An extensive comparison between the Schofield's model and the Dusty gas model was performed by Fernández et al. [53] and concluded that the DGM is superior to the Schofield's model and DGM was recommended as "the more physical" approach.

Structural network models (Monte Carlo)

In essence, what is characteristic to these models is the 3D network of pores and nodes used to represent the membrane structure. The first structural model for membrane distillation was published by Imdakm et al. [30] in 2004, where the authors applied the model to simulate 3 hypothetical membranes. A Monte Carlo method was applied to map the pore size distribution to a structure of nodes interconnected with pores, making the authors refer to them as Monte Carlo Models. However, we would like to point out that Monte Carlo is a general term for a methodology for system simulation where samples are taken randomly from a defined input distribution, solved through a model function which results in an output distribution of solutions [78].

Hence, the term Monte Carlo should not be used to represent a class of models. We therefore propose to more correctly refer to these models as Structural Network Models (SNM). A building block (single node) of these models is shown in Fig. 2.5.

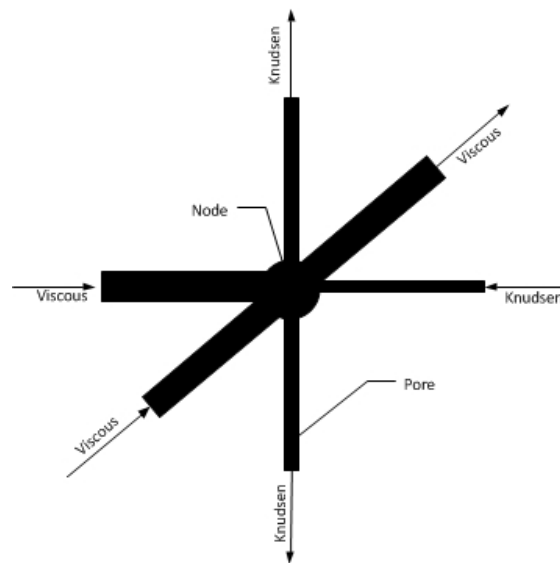


Figure 2.5: Representation of a single node with pores in structural network models (figure reproduced from Imdakm et al. [32])

In order to represent the membrane pore structure, a network of 12 nodes in the x, y and z direction was built [30–32] and an average, constant pore length was assumed [30–33]. To simulate changes in the membrane thickness the authors changed the number of nodes in the direction of the flux, z [31].

The structural network models use the kinetic theory of gasses in order to describe the flux in the system. The fundamental difference in these models is the ability to simulate the topology of the membrane, as well as to apply the proper transport mechanism for each pore, depending on the operating conditions and the pore size. Using the pore size probability density of a real [33] or hypothetical [30–32] membrane and an average pore length, the models are able to map the pore size distribution of the membrane to a 3D network of pores, that connect to each other forming nodes. In order to determine what the governing mass transport mechanism is, the Knudsen number is calculated for each pore based on the temperature, pressure and pore size. If the Knudsen number is larger than one, only Knudsen diffusion would take place. However, if the Knudsen number is smaller than unity, viscous flow would be used to calculate the flux through the pore. To evaluate the pressure drop that drives the viscous flow mechanism, Imdakm et al. [30] assume that the solutions are thoroughly degassed implying that the difference in partial pressure of the water vapor, calculated with the Antoine equation is in fact the total pressure difference.

The SNM models could in theory include molecular diffusion and surface dif-

fusion if needed, however in all of the related articles to date [30–33] the contribution of these transport mechanisms has not been included.

Ballistic transport model

The ballistic transport model is typically used to simulate the motion of electrons in media which has a characteristic size that is smaller than the mean free path of electrons. Soukane et al. [79] used the fact that under the low pressures applied in vacuum membrane distillation, the mean free path of the molecule is also much larger than the pore size (Knudsen type of flow, $Kn > 1$) and applied the ballistic transport model to simulate the fluxes in 8 PVDF membranes. What is unique to this model is that it can split and predict the direct flux contribution of molecules travelling from the pore inlet to the pore outlet without a collision and indirect contribution fluxes where the molecules collide with the pore walls during the transport. Moreover, the model is aimed at predicting the flux at extremely high and extremely low pore length to diameter ratios. The simulation could not predict the flux accurately for all of the membranes and in some cases the relative error of measured and predicted flux was as high as 73%. However, it should be noted that the Knudsen equation prediction was even worse and overall the ballistic transport model was able to fit the data for most of the membranes much better. This model is more complex, but also scientifically significant due to the fact that the flux in a Knudsen type of flow can be predicted in more physical way.

2.2.4 Empirical models

These models are completely data driven and the underlying equations represent only the final model output and not the actual physical phenomena that occur in the system. Two types of empirical models have been applied to membrane distillation - artificial neural networks and models derived from the design of experiments toolbox. The empirical models need large amount of data in order to be calibrated, and the output that they generate can only be applied for optimization of the operational conditions, for control strategies and for visualization of the operational space only for the experimental equipment that was used for the model calibration. These models cannot extrapolate outside of the calibration range and cannot be applied to other systems.

Artificial neural network (ANN) models

ANN are designed in a way that mimics the behavior of biological neural networks. They are organized in a layered structure, where the first and the last layers are the input and output layers and the layers in between are called hidden layers because they are not directly visible to the user. An example layout of an artificial neural network is shown in Fig. 2.6.

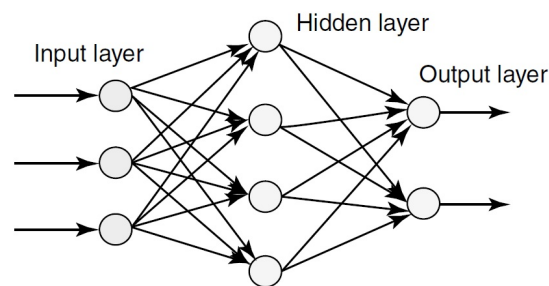


Figure 2.6: Multilayered artificial neural network with a single input, output and hidden layer (Ajith et al. [80])

Each circle in Fig. 2.6 represents a neuron, also called a node which is the building block of the network. The neurons are the basic processing units and each of them consists of a sum and a transfer function.

The configuration of an ANN network can vary greatly, but mostly the model performance is tuned by altering the number of layers and neurons in the hidden layer. By setting a large number of neurons in the hidden layer, the model will likely be able to represent the training data well, however a possibility exists that it will become unable to represent data outside of the training range [80], similarly to a conventional model which is overparameterized. A small number of neurons in the hidden layer will likely not be able to achieve the desired accuracy [80]. Once the ANN network is built it must be trained to represent a given data set. The training process could be supervised, unsupervised or by reinforcement learning. More detailed information about ANN models is available elsewhere [80].

Artificial neural networks are considered as completely black box models, because the mathematical equations in these models are hidden to the modeller and have no physical meaning. They can be used as universal function approximators, even for piecewise and non-linear functions [81]. Khayet and Cojocarú [82, 83] published two papers using artificial neural network models

for MD.

The first model in 2012 simulated air gap MD and is based on a total of 72 experiments split into 54 for training, 12 for validation and 6 for testing using a network with 10 neurons in the hidden layer [82]. The training and validation points are used during the learning process, whereas the testing points are used to evaluate the model's predictive power subsequent to the learning process. It was concluded that the maximal flux was at the smallest air gap distance, highest feed temperature and flow rate and lowest coolant temperature. The model's predictive power was evaluated based on statistical tests and proved to be high.

The second model using ANN is based on 53 sweep gas MD experiments in total, that were split in the ratio of 41:6:6 for training, validation and testing [83]. The model had 9 neurons in the hidden layer. Similar to the previous model, the optimal operation conditions (maximal flux) were found at the extremes with maximum air and feed flow rates, with the exception of the optimal feed temperature which was 1 degree less than the maximum tested. This model also revealed an interaction between the air gap thickness and the feed flow rate - at large gap thickness the increase of flow rate improved the performance index, while at small gap thickness it had the opposite effect [82]. A similar behavior was found for the flux as a function of the gap thickness and the inlet temperature of the coolant. The model developed for the sweep gas system also revealed interaction between the sweep gas velocity and the feed inlet velocity [83]. In both models the system optimum was found using the Monte Carlo method [82,83].

Empirical models based on tools from Design of Experiments (DoE)

In conventional experiments one of the degrees of freedom is changed, while the other parameters are kept constant in order to evaluate the impact on the system performance. In a design of experiments the input parameters are changed simultaneously, which reduces the number of experiments and often reveals complex interaction between the system parameters, which are kept hidden using conventional experiments.

Factorial design is a technique where each input parameter is changed in steps, called levels and a low order polynomial is fit as an approximation of the relation of the experimental response and the independent variables [84]. These statistical models are not mechanistic in nature, however the resulting equa-

tions can be examined mathematically, so they are not completely black box models as the ANN. A commonly used visualization technique is the Response Surface Methodology (RSM), where the predicted response is plotted in 3D as a function of two of the inputs, that allows to visualize interactions between them. It should be noted that the polynomial fit needs to be an adequate representation of the experimental response in order to have a useful RSM model [84].

Factorial design and RSM models were applied for DCMD by Khayet et al. [85] to optimize the flux by changing the flow rates, mean temperature and initial salt concentrations. The simulations were performed for four different membranes and the model predictions were evaluated as satisfactory when compared to the experimental ones using the coefficient of determination R^2 .

Onsekizoglu et al. applied factorial design and RSM to model the behavior of flux and dissolved solid content after membrane distillation and osmotic membrane distillation [86] as a function of osmotic agent concentration, flow rates and temperature differences between the feed and the permeate.

Mohammadi et al. [87] used the Taguchi method to optimize the performance of vacuum membrane distillation. The Taguchi method is an advanced DoE technique that minimizes the amount of experiments needed for the modeling. The parameters chosen for flux optimization were the different feed flow rates and temperatures, vacuum pressures and inlet concentrations.

Khayet et al. [88] applied factorial design and RSM to optimize the flux of a sweep gas MD system. The operational parameters that were changed are the water and sweep gas inlet temperatures and circulation velocities.

2.2.5 *Computational Fluid Dynamics (CFD) models*

Traditionally, the Nusselt and Sherwood equations are used to predict the temperature and concentration at the membrane surface. This approach is semi-empirical and the predicted temperatures and concentrations are uniform. Moreover, these equations are designed for a certain geometry and flow rate regime and the models cannot be reliably used for geometry optimizations.

Computational fluid dynamics uses a numerical approach to simulate a fluid flow. The development of CFD models began in the early 1950s mainly driven by aeronautic problems [89]. The CFD models can be used for virtual geometry prototyping [89]. Moreover, the CFD models for MD can predict the temper-

atures and concentrations locally throughout the module and can be used for identification of "performance bottlenecks". These models are discussed in more detail, because currently only a few CFD articles exist in the literature and we believe that the MD community will benefit from more CFD studies. This section is split in three parts. In section 2.2.5 the models are focusing only on improving the hydrodynamics and heat transfer in the channels of MD. The models in section 2.2.5 are aimed at improving the flux of the system, but the mass transfer through the membrane is not directly simulated - instead a constant mass transfer coefficient is given for the membrane across the whole geometry. In the last section 2.2.5 the models are also simulating the mass transfer across the membrane based on a semi-empirical model.

CFD models for heat transfer optimization in the channels

These types of models focus only on the heat transfer in the channels of the MD module. In order to simulate the process a constant heat flux is imposed at the inner boundaries of a single channel [90,91], or a membrane with a constant thermal conductivity is placed between two flow channels [22]. These models do not account for the flux in the system and are only focused on improving the hydrodynamic conditions and heat transfer in the module channels. Concentration polarization effects are neglected.

Al-Sharif [90] created a 3D model in the open source CFD package Open Foam. Three types of spacers - 90°, 45° and 3 layer double ladder shaped non-woven spacers were simulated and the model was set up assuming a constant heat flux through the membrane in a single channel. Interesting results were obtained concerning the heat transfer improvement by the 3 layer, double ladder spacer. It proved to be the best performing spacer with the least pressure drop. The authors explained that the good performance was due to the flow being forced to go around the middle filament and towards the membrane, thus improving the heat transfer. The heat transfer in the polymer fibres of the spacers was neglected, which could have an impact due to the different heat conductivities of water and polymer. The model was not validated with experimental data.

A three dimensional study of a single feed channel with a 45 degree non-woven spacer was published by Cipollina et al. [91]. A constant negative heat flux was imposed in order to simulate $5 \text{ kg}/(\text{m}^2 \cdot \text{h})$ vapor flux through the membrane. The simulation was done at a Reynolds number of 91 and the conductivity of

the spacer material was neglected. The model was tested for mesh dependency, but was not validated with experimental data.

A two dimensional CFD model was simulated by Shakaib et al. [22] in the commercial CFD software Fluent (Ansys). The model was set up with two channels (feed and permeate) that were flowing around a single flat sheet membrane in counter current fashion. The thermal conductivity of the membrane material was set to a constant value of $0.2 \text{ W}/(\text{m}^2\cdot\text{K})$. The conductive heat transfer in the spacer material was included in the calculation. The authors state that when the maximum velocity in the channels exceeded 0.15 m/s (Re number 350) the model failed to converge with Navier-Stokes equations and they used the Spalart-Allmaras turbulence model. Different 90° spacer arrangements were tested with the spacer filaments adjacent to the membrane, away from the membrane and a staggered (alternating) configuration. The performance of the spacers was evaluated based on the temperature polarization coefficient and the pressure drop in the channels. The model was tested for grid size dependency and there was no change of the simulated results with a higher number of grid cells. The Nusselt numbers that described the heat transfer in the simulation were compared to those obtained in the experimental work of Phattaranawik et al. [15]. The general trend was the same between the results from different arrangements and spacer channels and conventional Nusselt equation, but a direct comparison could not be made due to insufficient information on the exact experimental details.

CFD models for heat and mass transfer optimization in the channels

A series of articles was published by Yu et. al. [19,20] and Yang et al. [17,18] focusing on the simulation of heat flow and hydrodynamics inside a hollow fibre module with a single membrane. The simulations focused on module design and a constant membrane distillation coefficient was used to estimate the flux. The MD coefficient is usually expressed in units $\text{kg}/(\text{m}^2\cdot\text{s}\cdot\text{bar})$ and has the physical meaning of flux per intermembrane water vapor pressure difference. The models were set up with laminar flow when Reynolds numbers were ranging were 200-2000 and with $k-\epsilon$ turbulence model when this range was exceeded or turbulence promoters were used [17,18]. The flux influence on the heat transfer was included in the form of latent heat of evaporation but was neglected hydrodynamically [17,19,20], because of being 3 orders of magnitude lower than the feed flow rate [19]. The group published 3 articles

arranged in 2D [17,19,20] and one article in 3D [18]. The first article by Yu et al. [19] studied a single straight hollow fibre membrane and cylindrical shell side of the module. The study was focused on local fluxes, and heat flows, energy efficiencies and temperature polarization coefficients. The outlet temperatures were compared to experimental data at different module lengths in order to validate the model, revealing less than 1 percent error in the prediction.

The second article in the sequence by Yu et al. [20], extended the previous one by including baffles on the sides of the hollow fibre module. This simulation was again performed with a constant membrane MD coefficient. The influence of the MD coefficient on the temperature polarization coefficient was studied. It was concluded that turbulence promoters are an important tool for flux increase especially when membranes with a high MD coefficient were used. It was found that at high operating temperatures the energy efficiency of the process is substantially increased, even at small temperature differences between the feed and permeate. The obtained fluxes were compared to experimental results and showed excellent correlation.

The work of Yu et al. [19,20] was extended by Yang et al. [17] by including different spacers attached to a single hollow fibre membrane in combination with baffles on the shell side of the module. The effect of turbulence promoters on energy efficiency improvement was found to be less than 5 percent in the tested conditions. The best compromise between hydraulic energy consumption and flux improvement was achieved with the floating round spacers and with the attached quad (square shaped) spacers. The model was validated by comparing simulated fluxes with the experimental ones at fixed inlet temperatures with the different geometries. The validation showed an excellent correlation with errors in the mass fluxes being less than 5 percent.

The last article in the sequence by Yang et al. [18] used a 3D geometry, further expanding the previous 2D models. The tested geometries included hollow fibre membranes with wavy and gear-shaped outer surfaces. The constant MD coefficient assumption was maintained. Only the gear-shaped membrane was given a slightly lower MD coefficient to account for the cross sections that had a higher thickness. The model was not validated, based on the concept that the previous 2D based models are valid.

CFD system models including the mass transfer inside the membrane

Charfi et al. [92] developed a two dimensional numerical model for the simulation of sweeping gas membrane distillation. This MD configuration uses a sweeping gas to lower the partial pressure of water vapors on the permeate side and later the gas is regenerated in an external condenser. The geometry was limited to a flat sheet membrane with empty channels (without spacers). The system was based on the Navier-Stokes equation coupled with the Darcy-Brinkman-Forchheimer formulation in transient regime for the porous partition. The model was able to simulate different changes in water and sweep gas velocities and compared the results to experimental data with a relatively good fit.

Another CFD study by Xu et al. [93] incorporated the Knudsen-viscous transition of the DGM to simulate an air-gap MD system. The authors set up a two-dimensional axisymmetric model of a single hollow fibre. The effect of vapor pressure reduction due to activity was taken into account, however the feed concentration of NaCl was set quite low at 0.2 wt%. The concentration polarization as well as thermal conduction through the membrane were neglected. The $k-\epsilon$ turbulence model was chosen to simulate the water flowing inside the module at Reynolds numbers between 3400 and 10200. The model dependency on the feed temperature and flow rate was validated by comparison with experimental fluxes and showed excellent correlation. However, we must state that the validation of the feed flow rate was done in a region where the flux was nearly independent on the flow rate and was almost constant. Exact details on how the simulation was set up are missing.

Hwang et al. [94] developed a model that included the mass transfer inside the membrane using the commercial CFD software COMSOL. The geometry of a single flat sheet PTFE membrane was modelled for a lab-scale (0.06 m^2) rectangular module and fluid velocities of 0.17 to 0.55 m/s. The authors calculated a local flux via the local vapor pressure difference and the membrane MD coefficient. The MD coefficient was also calculated locally using the dusty gas model throughout the membrane length. Attention was given to the choice of flow configuration (short or long side) of the module in co- and countercurrent operation. The average and local vapor pressure was studied, and also the feed concentration of NaCl was varied from 1 to 6%. The model was validated by comparison of the experimental and simulated fluxes, as well as outlet temper-

ature comparison, showing excellent prediction of the model. Exact details on how the simulations were set up are missing.

2.3 Discussion and research gaps

There are different models and submodels that could be used in MD and in order to orient the reader what information could be reliably delivered from each type of model, we are classifying them into 4 categories: Process understanding and optimization, module design, process control and membrane synthesis.

The process understanding and optimization models are usually based on a combination between the Nusselt and Sherwood equations for the heat and mass transfer in the channels together with a mass transfer model for the membrane (see table 2.4). In order to simulate the mass transfer for the membrane, we would recommend the use of the dusty gas model, because of the more physical approach compared to the Schofield's.

CFD could be used for module design in order to investigate the local temperature and concentration polarization, flux and pressure drop in lab-scale modules. CFD can also aid the design of novel spacers that lead to a better mixing performance and lower pressure drop.

The empirical models based on ANN and RSM could be used to visualize the operational space and help understand the system behavior. These models can be implemented in process control models, but cannot be used to explain the physical phenomena or to extrapolate the results to another system.

The dusty gas model using the extension for pore size distribution, the structural network models and the ballistic transport models can be used for better understanding of the mass transfer inside the membrane and to apply the knowledge for better membrane synthesis.

A summary of the models is given in table 2.4.

2.3.1 Discussion

Most of the modelling efforts of heat transfer in MD literature is based on various Nusselt equations. They can predict the average interfacial temperatures with satisfactory accuracy as recently shown by Ali et al. and Tamburini et al. [7, 10, 11]. However, special care should be taken when choosing the

Table 2.4: Overview of the different models available in the literature

System definition	Model type	Strengths	Weaknesses	Remarks and gaps
Heat transfer in the channels	Nusselt-based	Simple, low computational burden	Single, uniform interfacial temperature is predicted	In some studies the calibration is not properly performed
	Computational fluid dynamics	Mechanistic approach. Temperature field is predicted	High computational burden	Commonly the geometry is over-simplified, HT in spacer material often excluded; Turbulence models are used for very low (laminar) flow velocities
Mass transfer in the channels	Sherwood-based	Simple, low computational burden	Single uniform interfacial concentration is predicted	Validation is missing
	Computational fluid dynamics	Mechanistic approach, concentration field is predicted	High computational burden	No models exist so far
Heat transfer in the membrane	Isostress, Isostrain, other	Simple, low computational burden		Validation is missing; unclear which model works best
Mass transfer in membrane	Dusty gas model	Good prediction, low computational burden	Lumped membrane properties	Accepted by the community, regarded as mechanistic
	Schofield's	Simple, low computational burden	Difficult to evaluate membrane parameters experimentally	Not widely used; Sometimes referred "less physical" than the DGM
	Pore size distribution models	More mechanistic	Complexity	Pore size distribution effect is assumed small; few articles in the literature
	Structural network model	Mechanistic; Simulates membrane structure	Complexity, high computational burden	Only used by one group; Excludes molecular diffusion, constant pore size and membrane thickness; Too small structure to be representative
	Ballistic transport model	Mechanistic; Can predict the flux in extremely short or long pores	High complexity and computational burden	Only one article; not fully tested
	Surface diffusion			Not included in any membrane model so far
Overall system models	Artificial neural network	Can behave similarly to real system; Low computational burden	Black-box models; Large amount of experimental data needed	Cannot be used for extrapolation beyond the calibration range
	Design of experiments-based	Simple, low computational burden	Non-mechanistic models	Cannot be used for extrapolation beyond the calibration range
	Nusselt and Sherwood eqns. and membrane MT model	Simple, low computational burden	Semi-empirical	Uniform prediction for temperature and concentration, not suitable for proper module design
	Computational fluid dynamics	The most mechanistic approach	High computational burden	Commonly oversimplified in terms of physics and geometry; Validation sometimes missing

appropriate Nusselt equation for the given geometry and flow regime. When modelling the system, it is important to first perform heat transfer experiments to validate the choice of Nusselt equation (as described in section 2.2.1), otherwise the heat transfer could be over or underestimated by orders of magnitude. Often the heat transfer models are not validated separately, but the performance of the whole model (heat and mass transfer) is validated by comparison of the predicted and measured fluxes. This could lead to an error of the mass transfer model being compensated by the error of the heat transfer model and an overall predictive power for only a very small range of temperatures and flow rates.

CFD has also been used to simulate the temperature polarization effect in the channels of MD [22,90]. The advantage of CFD simulations over Nusselt equation type models is that a field of temperature can be predicted, and therefore the performance of different spacers and module configurations can be accessed. However, CFD models are associated with very large computational burden.

The concentration polarization effects are commonly simulated with the Sherwood equation. By recognizing the analogy between heat and mass transfer, most MD authors use the same form of the Sherwood equation as the Nusselt equation they used for the heat transfer model. This approach has not been validated by direct experiments.

Numerous models have been developed based on the DGM to describe the mass transfer inside the membrane. It has been widely accepted in the MD community and describes the system with satisfactory accuracy. Recent critique of the DGM was published by Field et al. [75], concerning the parallel addition of Knudsen and viscous flux and some modifications have been proposed by the authors for the flux calculation in the Knudsen-molecular transition region. However, more work is needed to test the validity of this new extension.

The model proposed by Schofield et al. [28,29] could also be used to simulate the mass transfer in the membrane, however it is not widely used in the MD community. It has been criticized by Lawson [26] and Fernandez et al. [53] for having large experimental error associated with the gas permeation calibration experiments. Fernandez et al. [53] concluded that the DGM is more physically sound compared to Schofield's model.

Pore size distribution models have been developed based on the KTG for cylindrical pores by Khayet et al. [16] and the DGM by Phattaranawik et al. [76].

The models were able to estimate the effect of pore size distribution on MD performance. Both authors concluded that this influence is relatively small, especially for commercial membranes [16], where the pore size distribution is usually very narrow.

A series of structural pore network models has been published by Imdakm [30–32] and Khayet et al. [33]. The approach of the authors represents a network of nodes interconnected by pores and a combination of viscous and Knudsen flow is used to calculate the flux based on the Knudsen number. The key aspect of these models is the ability to simulate the effect of membrane structure. Although the authors claim that molecular diffusion could be included in the model structure, so far such model does not exist. These models are computationally intensive and complex, and have not yet been further used by the MD community.

The ballistic transport model was applied to simulate Knudsen flow by Soukane et al. [79]. This model has the advantage that it can predict the flux of water vapor at very high and very low pore length to diameter ratios. It is burdened with high complexity and computational requirements, but it is scientifically significant due to its novel and mechanistic approach.

Artificial neural network models were used to simulate different configurations of MD [82, 83]. The models could represent the behavior of the system and reveal complex interactions between the input parameters. The ANN models have the disadvantage that a large number of experimental runs must be performed for training, validation and testing and are only applicable to the experimental system that they are trained for. Moreover, these types of models are considered as a complete black box and non-mechanistic.

Models from the Design of Experiments toolbox were used to simulate various MD configurations by Khayet et al. and Onsekizoglu et al. [85, 86, 88]. These models were able to reveal interactions between the input parameters of the system similarly to ANN. They are non-mechanistic in their nature but can help building the mechanistic knowledge base. They also have the benefit of allowing statistical assessments. Care should be taken that the predictions of these models are properly tested for statistical significance before they are used to optimize the system.

Most authors of CFD system models assume that the MD coefficient is constant for a narrow temperature range as commonly quoted in the MD literature [19, 55, 75, 77]. Although the change of membrane permeability with temperature is small (estimated to be within 3 percent for every 10°C [55]), the

calculation of the local permeability coefficient is not computationally intensive and therefore a better approach to use in the CFD model, which is done so far only by a few authors [92–94].

Many authors use turbulent models in their CFD simulations [17, 18, 22, 95]. Turbulence models are needed in order to approximate the behavior of turbulent flows, which is otherwise prohibitively expensive to solve directly in terms of computational power. The flow inside spacer filled channels (commonly used in MD) is rarely fully turbulent [96] and the simulation of the transition between laminar and fully turbulent flow is extremely challenging as Nichols et al. points out [97]. Fimbres-Weihs et al. [96] reports in their review that the Reynolds numbers typically encountered in spacer filled channels are between 1,000 and 3,000. Moreover, the authors state that turbulence models can only be properly used at Re numbers above 30,000 when the flow is fully turbulent [96]. We therefore believe that if turbulent models are used, they must always be checked for validity against experimental data. The work of Tamburini et al. [10, 11] could be used for CFD model calibration and validation of heat transfer in spacer filled channels.

2.3.2 *Research gaps*

Although a lot of good models exist in the literature, more work needs to be done in the area of module design. Until recently, MD modules only have been modelled based on the semi-empirical Nusselt and Sherwood equations. Recent attempts on module design have been made to simulate the system with CFD, however often times either the geometry, or the physical phenomena are oversimplified. We believe that proper CFD based module design is key in order to make MD a competitive separation technology and more effort has to be put into the design of modules specifically optimized for MD.

The advantage of CFD studies over Sherwood equation mass transfer models is that the "hot spots" of concentration polarization can be identified and optimized in order to minimize the concentration polarization effects and possibly avoid membrane scaling in complex geometries such as spacer filled channels. However, so far such studies do not exist in the literature. Moreover, no study to date includes the influence of the convective flow near the membrane driven by the flux. Although this convective flow is expected to be several orders of magnitude smaller than the bulk flow [19], it is located in the stagnant boundary layer near the membrane surface and could have a significant interaction

with the other phenomena that occur in the module. In fact, this flow is the sole driving force of the concentration polarization.

The CFD studies regarding the heat transfer in MD have received more attention. However, the studies on spacer-filled channels are oversimplified and only take into account the heat transfer of the system. In the current CFD models of hollow fibre modules the geometry is simplified to a single membrane inside a shell [17–20,95]. The interaction effects between randomly packed hollow fibres could be tackled analytically [98,99] by drawing straight lines at equal distances between each randomly packed membrane, forming a polygonal structure around the fibre [8] called Voronoi tessellation. However, the interaction effect between the fibres so far has not been studied via CFD modelling.

The energy efficiency is an important parameter, essential to the industrial application of MD, but it is not always included in experimental and modelling articles. In order to calculate the energy efficiency, the thermal conductivity of the membrane matrix must be calculated, but it is still unclear which is the best performing equation. The experimental evaluation of this parameter is not trivial because it is based on clamping the material between solid discs [40], and some authors argue that the porous membrane can be compressed during these tests [36]. An evaluation of the thermal conductivity with a less invasive experimental method could be very beneficial for modelling purposes.

Multiple models exist in the literature to calculate the mass transfer for the membrane region, but some gaps still exist in this field. The structural network models that can be used in MD for flux evaluation includes 12 nodes in each axis direction [30–32] and uses pore lengths of $1\ \mu\text{m}$. Accounting for the fact that each node has two pores in each direction the resulting membrane thickness is $24\ \mu\text{m}$ [30–32]. It would be interesting to see the effect of changing the membrane pore length, which is not shown in any of the structural network models - and possibly to use a pore length distribution rather than a uniform, constant length of $1\ \mu\text{m}$. Moreover, the studies so far account for only 12 nodes in each direction, resulting in only about 5200 pores. It would be beneficial to show models with more pores and evaluate if this has an effect on the system performance. The current SNM models for MD exclude the influence of molecular diffusion and instead it is replaced by viscous flow. A SNM model which includes the influence of molecular diffusion would be valuable to the MD community.

The surface diffusion transport mechanism inside the membrane has always

been neglected in MD modelling, relying on the assumption that the membranes are hydrophobic and the interaction between the water vapor molecules and the surface of the membrane will be low. However, many membranes used in MD are only slightly hydrophobic (e.g. PVDF) and the contribution of this transport mechanism might not be negligible. Hence, the simulation results could be beneficial for membrane synthesis.

Most of the studies have not been extensively calibrated. In many of the models the tortuosity is manually adjusted and used as a tuning parameter and the use of special calibration tools applied to a MD model is lacking. Moreover, sensitivity analyses for the model parameters as well as the operational conditions is performed on only a few models [8,77,100,101] and should be explored in more detail.

2.4 Conclusions

Membrane distillation has been discovered 50 years ago, but so far lacks significant industrial applications. In order to optimize the technology and make it competitive to alternative separation techniques the MD community must have an in-depth understanding of the processes that occur inside the modules and the membranes.

The mass transfer modelling of the membrane region has been covered by many different mechanistic and statistical models that can predict the flux with varying accuracy. More recent models such as the ballistic transport model and the structural network models are innovative and interesting to the community, but have not yet been thoroughly tested and validated. Moreover, some of the physical phenomena that occur inside the membrane such as the surface diffusion has always been neglected in MD modelling which can prove to be important for membrane synthesis studies.

We believe that the lack of significant industrial applications of the technology is also due to the lack of proper module design, for which CFD can be helpful. Some of the recent CFD studies have focused on this task, however in most of the cases either the physical phenomena or the geometry have been severely oversimplified, leaving a room for further research.

CHAPTER 3

Model choice and calibration of lab-scale direct contact membrane distillation (DCMD) model

Redrafted from: I. Hitsov, L. Eykens, K. De Sitter, C. Dotremont, L. Pinoy, B. Van der Bruggen, I. Nopens, 2016. Calibration and analysis of a direct contact membrane distillation model using Monte Carlo filtering, *Journal of Membrane Science* (515), 63-78

Abstract

Membrane distillation is an emerging technology to separate non-volatile components from an aqueous feed stream. Mathematical models have proven useful to pursue breakthrough in the economics of the technology and for further improvement through module design and operational optimization. However, before this can be done, all of the resistances in the system must be identified correctly and the model must be carefully calibrated to ensure its predictive power.

In this chapter the typical structure of a direct contact membrane distillation (DCMD) model is studied, where the mass transfer inside the membrane is simulated using the Dusty Gas Model and Nusselt type equations are used to simulate the heat transfer inside the channels. We demonstrate that an off-the-shelf Nusselt equation cannot directly be applied to simulate the heat transfer in the spacer filled channels. Instead, the equations should be calibrated to

match the behavior of the particular spacer.

A Monte Carlo filtering method was applied to calibrate and study the structure of the DCMD model for the membrane region. The method proved useful to identify which parameters need to be included in the calibration as it highlighted parameter correlations. Additionally, a submodel selection was performed for the heat and mass transfer inside the membrane.

A simple, yet physical method for the simulation of supported membranes was tested and validated on 3 supported membranes, resulting in an excellent fit.

3.1 Introduction

Membrane distillation is a thermally driven separation process in which the volatile components are transported through a porous hydrophobic membrane due to a vapor pressure gradient [102]. Meanwhile the non-volatile components exhibit almost absolute rejection [103,104].

In order to optimize the system, thorough knowledge is required. Process modelling is a powerful tool often used to build this system knowledge and can highly contribute to optimize these systems. Membrane distillation modelling can be found in many papers [23,105,106], but how the model was calibrated is rarely discussed. In our view, proper calibration, followed by a validation is key to good modelling practice and is often getting too little attention. If a model is not calibrated correctly and for example the mass transfer is overcompensating for the heat transfer, just to achieve a good fit of the experimental data, the predictive power of the model could be sufficient. However, such an overfitted model cannot be used to study what is the limiting resistance in the system and is very likely to fail if the model is scaled up beyond lab-scale dimensions. Therefore it is crucial that all the heat (HT) and mass (MT) resistances in the system (Figure 3.1) are calibrated properly.

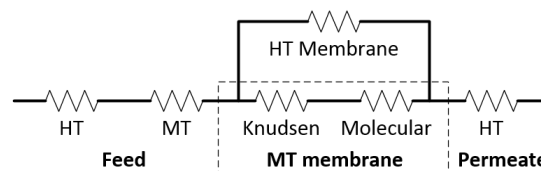


Figure 3.1: Heat (HT) and mass transfer (MT) resistances in the DCMD system

3.1.1 Transport phenomena in the channels

Nusselt equations are commonly used in membrane distillation modelling to simulate the heat transfer inside the fluid-filled channels [16,107]. The Nusselt equations are semi-empirical mathematical equations that were initially developed for heat transfer simulation in heat exchangers. The drawback of the Nusselt equations is that they are dependent on the flow regime and the geometry of the heat transfer surface. This results in hundreds of different relations specific for each case. However, in MD modelling these equations have rarely been validated [13,15] and instead a generic, off-the-shelf form is

commonly used, but as shown by Tamburini et al. [10,108] each specific spacer has a Nusselt equation that describes its behavior best. Hence, a generic form does not work for all spacers. In this chapter we utilize the methodology for spacer characterization of Phattaranawik et al. [15] where the membrane is replaced by an aluminium foil and the system is operated as heat exchanger at different flow velocities. Phattaranawik et al. then chose the best performing Nusselt equations from the literature. In this chapter, we take this approach a step further and calibrate a Nusselt equation to match the specific heat transfer behavior of a spacer, instead of just choosing an expression "off-the-shelf".

Similar to the temperature polarization that occurs inside the MD channels, concentration polarization will also occur in the feed channels of a module - i.e. the salt concentration on the membrane surface will be increased due to the flux. It is commonly regarded that the concentration polarization in membrane distillation is not as important as thermal polarization [109], yet the research of Martínez et al. [27] demonstrates that at high salinities the concentration polarization resistance becomes important and should not be neglected. This resistance is calculated using the Sherwood number (Sh), a dimensionless number which is the mass transfer equivalent of the Nusselt number. However, these equations face the same applicability problem as the Nusselt equations since they are also specific to the geometry and flow regime [110]. In this work the similarity between heat and mass transfer is recognized, also known as the Chilton-Colburn analogy [111], which allows for a Sherwood type equation to be derived in complete analogy with the Nusselt equation based on the calibration of the heat transfer experiments.

3.1.2 *Transport phenomena inside the membrane*

The calculation of the heat transfer inside the membrane depends on the thermal conductivity of the membrane matrix. The conductivity of the membrane matrix is important for the calculation of the Energy Efficiency (EE), but it also affects the flux due to the additional temperature polarization that the membrane conductivity is introducing. This parameter however is difficult to measure, due to the possibility of membrane compression during the measurement [72]. Moreover, the thermal conductivity of the membrane matrix κ_m can be calculated using different models [40], but these are all developed for a certain pore orientation and membrane morphology [105]. Due to the large uncertainty of both measurement and calculation, possibly the thermal conductivity of the

membrane κ_m can potentially be used as a calibration parameter in the model, but this has not been attempted before in the literature.

The Dusty Gas model (DGM) has been commonly applied in order to simulate the flux of vapors inside the porous membrane [16,24–27,76]. This model can predict the permeability of the membrane, based on the structural parameters such as porosity (ϵ), tortuosity (τ) and mean pore radius (R_p).

However, the DGM does not differentiate where exactly in the Knudsen-molecular transitional region a certain pore size is. To tackle this problem a model was recently introduced by Field et al. [75], which amends the DGM for the transition zone in order to correct the transitional DGM behavior based on the Knudsen number, but this model has not been previously compared to the traditional DGM. The mass transfer inside the membrane can also be modelled using the Knudsen diffusion, molecular diffusion as well as a simple permeability constant. Therefore in this study a proper model selection was performed to evaluate the goodness-of-fit of these models.

Another common practice is to use the tortuosity of the membrane as a single calibration parameter for the membrane permeability [105]. However, a proper model structure analysis has not been performed thus far in the literature, to show if the other parameters in the DGM also require adjustments in order to obtain a good-fitting model.

To address the abovementioned problems, a rigorous Monte Carlo filtering method was applied for the first time to the model structure for the membrane region. Monte Carlo simulations are commonly used in many fields of science and engineering e.g. hydrology and wastewater treatment, to study model uncertainty and analyse the model structure [112–115]. In this work a goal function was defined to evaluate the quality of fit of the model to both the flux and the energy efficiency, which has not been done before in the literature but is common practice when a model is fitted to multiple experimental datasets, commonly known as multicriteria analysis [116]. The method was then applied according to good modelling practice principles and in order to:

- Study if the tortuosity is sufficient as a single calibration parameter for the membrane permeability or the other morphological parameters of the membrane also need to be included in the calibration
- Investigate possible interactions between calibration parameters, i.e. parameters that counteract each other and multiple (infinite) combinations of their values result in the same quality of fit

- Investigate whether the thermal conductivity of the membrane should be included in the calibration of the model
- Perform a model selection for the sub-models that calculate the heat and mass transfer inside the membrane
- Investigate the feasibility of a newly proposed method for simulation of supported membranes

Furthermore, the method can later be used as a tool for automatic calibration and validation of the model. Following the presented method one can arrive at a model, where all of the resistances are identified correctly.

The applicability of the calibration method was demonstrated on 4 single layer and 3 supported membranes. Based on the Knudsen number all 7 membranes fall in the transitional regime between Knudsen and molecular diffusion.

3.2 Materials and Methods

3.2.1 *Membranes and module*

The experimental data used for calibration were obtained in a flat sheet lab-scale MD setup (6x18 cm). Two channels with thickness of 2 mm each are formed by compressing two 60° spacers (Figure 3.2) around a single membrane. The feed and the permeate were operated in a counter-current fashion using peristaltic pumps (Watson-Marlow, 520DuN/R2, Zwijnaarde, Belgium). The temperature was controlled using two heating bath thermostats (Huber, Ministat 230w-cc-NR, Offenburg, Germany) and measured using four thermocouples (Thermo Electric Company, PT100 TF, Balen, Belgium). The flux was measured by evaluating the weight change of the feed and distillate tank, using analytical balances (Sartorius GmbH, ED 8201-CW, Goettingen, Germany). The electrical conductivity at the feed and permeate side were measured using portable conductivity meters (WTW GmbH, pH/Cond 340i, Weilheim, Germany).

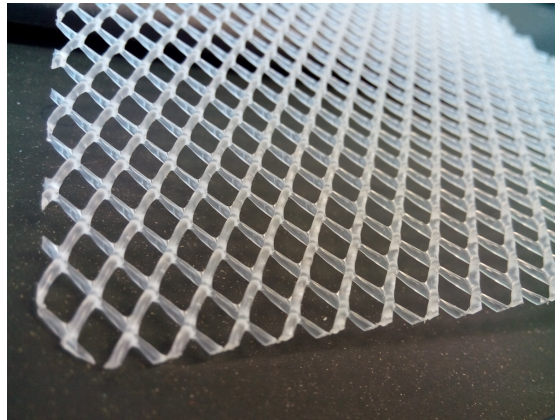


Figure 3.2: The spacer used in this study. Mesh size 4.5 mm, total thickness 2 mm, strand thickness 1 mm, strand angle of 60° in the general direction of the flow. Spacer porosity $\epsilon_s=0.79$.

A series of experiments was performed with 7 commercially and semi-commercially available membranes made of ultra high molecular weight polyethylene (UHMW PE), polypropylene (PP), polyvinylidene fluoride (PVDF), polyethersulfone (PES), electrospun PVDF membranes (ePVDF) and two supported polytetrafluoroethylene (PTFE) - Table 3.1.

Table 3.1: Membrane characterization

Material	Pore radius, R_p μm	Porosity, ϵ %	Active layer thickness, μm	Support thickness, μm
PP	0.27 ± 0.05	83 ± 2	180 ± 4	-
PE (UHMW)	0.15 ± 0.008	76 ± 1	92 ± 7	-
PVDF	0.22 ± 0.005	66 ± 1	109 ± 2	-
PES*	0.26 ± 0.02	58 ± 3	71 ± 3	-
ePVDF	0.30 ± 0.03	$79 \pm 1^*$	17 ± 5	74 ± 4 PP non-woven
PTFE1	0.24 ± 0.02	80^{**}	65 ± 3	261 ± 2 PP scrim
PTFE2	0.095 ± 0.001	80^{**}	20 ± 1	216 ± 2 PP non-woven

*The PES membrane has a PET spacer integrated inside the active layer in order to improve the mechanical strength

**Manufacturer supplied data

The pore size of the membranes was measured via capillary porometry using a Porolux 1000 device (Porometer, Eke, Belgium) based on the wet/dry method.

Porefil with a liquid surface tension of 16 mN/m was used as wetting liquid and the shape factor is assumed to be 1. The porosity of the membranes was measured via helium pycnometry [117]. The thickness of the supported membranes was measured via scanning electron microscopy (5keV, JEOL, Tokyo, Japan), whereas the thickness of the unsupported membranes was measured using a digital micrometer. The mean feed and permeate temperature were varied from 40 to 60 °C and 25 to 55 °C, respectively. The empty channel velocity was varied from 2 to 28 cm/s. More detailed information regarding the methodology of membrane characterization and setup can be found in our previous work by Eykens et al. [117].

3.2.2 Channel heat and mass transfer calibration

Aluminium foil experiments used for heat transfer calibration

The heat transfer experiments are performed in counter-current with 23 μm thick aluminium foil and equal flow rates in order to reliably measure the overall heat transfer coefficient. The experimental conditions are summarized in Table 3.2.

Table 3.2: Heat transfer experimental conditions

Conditions	Exp 1	Exp 2	Exp 3	Exp 4	Exp 5
$T_{f,in}$, °C	59.9	60.1	65.3	68.7	76.4
$T_{f,out}$, °C	54.9	54.0	57.2	57.5	58.2
$T_{p,in}$, °C	45.3	42.8	43.3	40.7	36.7
$T_{p,out}$, °C	49.9	48.4	51.2	51.6	54.0
Empty channel velocity v_{ch} , m/s	0.23	0.20	0.15	0.10	0.05
Reynolds number Re	1114	958	731	494	252

The average heat duty Q of the channels is calculated by making a heat balance:

$$Q = T_{in}Cp_{in}M_{in} - T_{out}Cp_{out}M_{out} \quad (3.1)$$

Where M is mass flow rate of the fluid in the channel and Cp is the specific heat capacity. The experimental overall heat transfer coefficient is then equal to

$$U = \frac{Q}{A.LMTD} \quad (3.2)$$

Where A is the heat transfer area, in our case measured to be 0.0108 m^2 . It should be noted that the classical formula for the Logarithmic Mean Temperature Difference (LMTD) in counter current flow $\text{LMTD}=(\Delta 1-\Delta 2)/\ln(\Delta 1/\Delta 2)$, where $\Delta 1=T_{f,in}-T_{p,out}$ and $\Delta 2=T_{f,out}-T_{p,in}$ is not applicable. This is because in all of the points $\Delta 1$ is nearly equal to $\Delta 2$ and leads to division by zero in the denominator. Therefore, in this case the LMTD was calculated as the average of the two deltas $\text{LMTD}=(\Delta 1+\Delta 2)/2$.

In order to calibrate the heat transfer, the interfacial temperatures $T_{m,f}$ and $T_{m,p}$, given by Khayet et al. [16] need to be calculated. An iterative loop was created that calculated the overall heat transfer using different Nusselt equations. The iterative approach is needed, because of the reciprocal dependency between the Prandtl number for the wall of the foil (Pr_w) and the interfacial temperatures.

$$Re = \frac{(v_{ch}/\epsilon_s)D_{ch}\rho}{\mu} \quad (3.3)$$

$$Pr = \mu C_p / \kappa \quad (3.4)$$

$$Nu_{f,p} = a(Re_{f,p})^b (Pr_{b,f,p})^c (Pr_{b,f,p}/Pr_{w,f,p})^d \quad (3.5)$$

$$h_{f,p} = Nu_{f,p} \kappa_{f,p} / D_{ch,f,p} \quad (3.6)$$

$$h_m = \kappa_m / \delta \quad (3.7)$$

$$T_{m,f} = \frac{T_{b,f} h_f + T_{m,p} h_m - NH_v}{h_f + h_m} \quad (3.8)$$

$$T_{m,p} = \frac{T_{b,p} h_p + T_{m,f} h_m + NH_v}{h_p + h_m} \quad (3.9)$$

$$U_{calc} = (1/h_f + 1/h_p + 1/h_m)^{-1} \quad (3.10)$$

The Reynolds number is calculated using the channel velocity v_{ch} adjusted for the porosity of the spacer ϵ_s , which was measured to be 0.79 by submerging the spacer and measuring the displaced volume. D_{ch} , ρ and μ are the thickness of the channel, density and viscosity of the fluid, calculated based on correlations given in the work of Sharqawy et al. [118].

The form of eq. 3.5 is a commonly used correlation for the calculation of the Nusselt number in laminar flow with different sources having different coefficients **a** and **b**, **c** and **d**. In eq. 3.6 κ_m and δ are the thermal conductivity and the thickness of the aluminium foil. The terms h_f , h_p and h_m are the local heat transfer coefficients for the feed, permeate channel and the membrane. N , H_v and U_{calc} are the water flux, specific heat of evaporation of water and the cal-

culated overall heat transfer coefficient, respectively. Equations 3.8 and 3.9 [16] can be used for the calculation of the interfacial temperature in the aluminium foil experiments as well as in the normal membrane distillation experiments, however in the case of aluminium foil experiments the flux term N is set to zero.

Different Nu number correlations listed in the works of Phattaranawik et al. [15] and Gryta et al. [13] were tested. The sum of squared errors between the calculated and experimental overall heat transfer coefficients are used as a goodness-of-fit indicator while adjusting the linear correction \mathbf{a} and the Reynolds exponent \mathbf{b} in eq. 3.5 to achieve good fit and the inlet and outlet flow rates of the channels are equal.

Concentration polarization in the feed channel

Similar to the temperature polarization that occurs inside the MD channels, concentration polarization will also occur in the feed channels of a module - i.e. the salt concentration on the membrane surface will be increased due to the flux. Based on the similarity between heat and mass transfer [111] a Sherwood type equation with the same form as the Nusselt equation was used:

$$c_{m,f} = c_{b,f} e^{MwN/\rho K} \quad (3.11)$$

$$K = \frac{ShD}{d_h} \quad (3.12)$$

$$Sh = a(Re_f)^b (Sc_{b,f})^c (Sc_{b,f}/Sc_{wf})^d \quad (3.13)$$

$$Sc = \frac{\mu}{\rho D} \quad (3.14)$$

Where Mw , $c_{m,f}$, $c_{b,f}$, K , d_h and D are the molar mass of water, concentrations at the membrane interface and bulk of the feed, the overall mass transfer coefficient, channel thickness and the diffusion coefficient, respectively. The Schmidt number (Sc) is the mass transfer equivalent of the Prandtl number. The coefficients in the Sh equation need to be calibrated, based on the heat transfer experiments.

3.2.3 Submodels for the thermal conductivity of the membrane

The initial value of the thermal conductivity (κ_m) can be calculated using Maxwell type I equation 3.17. This was the main model because this equation has been recommended in a dedicated study done by García-Payo et al. [40], (eq. 3.17).

$$\kappa_g = 2.72 \times 10^{-3} + 7.77 \times 10^{-5} T_m \quad (3.15)$$

$$\beta = (\kappa_s - \kappa_g) / (\kappa_s + 2\kappa_g) \quad (3.16)$$

$$\kappa_m = \frac{\kappa_g(1 + 2\beta(1 - \epsilon))}{1 - \beta(1 - \epsilon)} \quad (3.17)$$

Where κ_g is the thermal conductivity of the water vapors at the current membrane temperature [43] and κ_s is the thermal conductivity of the membrane polymer and β is an intermediate coefficient.

For the purposes of submodel selection analysis, two other models for the calculation of thermal conductivity of the membrane are investigated. These models were not used in the model calibration, but only for submodel comparison at a later stage. The first model is very often used in MD modelling [14, 16, 25, 33, 34, 36, 38, 39], known as the parallel model (eq. 3.18). A much less often used model is the resistance in series model [15,40], where the resistance of the air and polymer occur in series - eq. 3.19.

$$k_m = (1 - \epsilon)\kappa_s + \epsilon\kappa_g \quad (3.18)$$

$$k_m = \left[\frac{\epsilon}{\kappa_g} + \frac{1 - \epsilon}{\kappa_s} \right]^{-1} \quad (3.19)$$

3.2.4 Submodels for mass transfer inside the membrane

In order to calculate the flux through the membrane, the membrane interfacial temperatures should be converted to partial pressures p_0 using the Antoine equation [53]. When NaCl solutions are used, the water vapor pressure on the feed side is lowered due to the reduced water activity. The actual vapor pressure p_i can be recalculated using the activity a_w [54].

$$p_i = p_0 a_w \quad (3.20)$$

A polynomial fit for the water activity as a function of molality is given in Chapter 3.

The choice for Knudsen, molecular or combined Knudsen-molecular diffusion mechanism is made based on the value of the Knudsen number, which represents the relation of the mean free path that the molecule travels (λ) to the pore size of the membrane ($2R_p$) expressed as $Kn = \lambda/d_p$. The mean free path of the molecule can be calculated using the following equation [16]:

$$\lambda_i = \frac{K_B T_m}{\sqrt{2\pi P \sigma_i^2}} \quad (3.21)$$

In the equation above σ_i is the collision diameter, which is 0.2641 nm for water vapors [67]. K_B , T_m and P respectively represent the Boltzmann constant, the average temperature in the membrane in Kelvin and the mean pressure in the membrane pores. The total pressure inside the pores in DCMD is equal to the atmospheric pressure [25]. The Knudsen number was calculated for all membranes at a typical average membrane temperature of 50 °C and atmospheric pressure (Table 3.3).

Table 3.3: Pore size and Knudsen numbers for the used membranes at 50°C

Membrane	PP	PVDF	PES	ePVDF	PE	PTFE1	PTFE2
Kn number	0.27	0.33	0.28	0.24	0.48	0.30	0.77

Because the Knudsen number for all membranes is between 0.01 and 1, the mass transfer mechanism is expected to be in the transition region, governed by both molecular and Knudsen diffusions.

Dusty Gas Model (DGM)

The dusty gas model can take into account the Knudsen diffusion, molecular diffusion, viscous flow and a combination of the three as a flow mechanism inside porous media. The viscous flow does not occur in direct contact membrane distillation, because there is no total gaseous pressure difference across the membrane unless the system is degassed [25,56,105], therefore this mechanism was excluded from the study. The equations relevant for Knudsen-

molecular flow in the DGM are given by Lawson and Lloyd [25]

$$p_a^f = P - P_{m,f} \quad (3.22)$$

$$p_a^p = P - P_{m,p} \quad (3.23)$$

$$K_0 = \frac{2\epsilon R_p}{3\tau} \quad (3.24)$$

$$K_1 = \epsilon/\tau \quad (3.25)$$

$$D_{aw,e} = 4.46 \times 10^{-6} T_m^{2.334} K_1 \quad (3.26)$$

$$\bar{v} = \sqrt{\frac{8RT}{\pi M}} \quad (3.27)$$

$$D_e^K = K_0 \bar{v} \quad (3.28)$$

$$N = \frac{D_{aw,e}}{\delta RT_m} \ln \left(\frac{p_a^p D_e^K + D_{aw,e}}{p_a^f D_e^K + D_{aw,e}} \right) \quad (3.29)$$

In these equations p_a^p , p_a^f , $P_{m,p}$, $P_{m,f}$ and P are respectively the partial pressure of air on the permeate and feed side, the vapor pressure of water at the membrane and the atmospheric pressure. $D_{aw,e}$, D_e^K , \bar{v} are the effective molecular, Knudsen diffusion coefficient, the mean molecular velocity and the molar mass of water in kg/mol, respectively. All the symbols are expressed in SI units and the resulting molar flux is in units $\frac{\text{mol}}{\text{m}^2\text{s}}$.

DGM corrected with the Kn number

Field et al. [75] proposed a new equation (eq. 3.33) for the Kn-molecular transition, which weighs the degree of Knudsen and molecular resistances in the transitional region based on the Knudsen number. This expression was used as the default membrane mass transfer submodel in this study.

$$y_{af} = (P - p_{m,f})/P \quad (3.30)$$

$$y_{ap} = (P - p_{m,p})/P \quad (3.31)$$

$$D_{aw} = 1.895 \times 10^{-5} T_m^{2.072} K_1/P \quad (3.32)$$

$$N = \frac{K_1 P D_{aw} (1 + Kn)}{\delta RT_m} \ln \left(\frac{D_e^K y_{ap} + D_{aw} (1 + Kn)}{D_e^K y_{af} + D_{aw} (1 + Kn)} \right) \quad (3.33)$$

Here, y_{af} and y_{ap} are the molar fractions of air in the feed and permeate side of the membrane and D_{aw} is the molecular diffusion coefficient.

Knudsen diffusion

Based on the definition of the Knudsen number this type of diffusion will occur in those pores that are smaller than the free molecular path in the current conditions, calculated by Phattaranawik et al. [76] to be $0.11 \mu\text{m}$ under typical MD conditions. The relevant equation is given by Lawson and Lloyd [25]:

$$N = \frac{K_0 \bar{v} (p_{m,f} - p_{m,p})}{\delta RT_m} \quad (3.34)$$

Molecular diffusion

Molecular diffusion occurs in the larger pores of the membrane with pore size 100 times or larger the size of the mean molecular path or $11 \mu\text{m}$ [76]. The relevant equation is given by Lawson and Lloyd [25]:

$$N = \frac{D_{aw,e}}{\delta RT_m} \ln \left(\frac{P - p_{m,p}}{P - p_{m,f}} \right) \quad (3.35)$$

Membrane permeability constant

The most simple way to model the flux through the membrane is to use a constant permeability for the membrane (C), considered to be only a weak function of the temperature and estimated to change less than 3% for every 10°C [55].

$$N = C(p_{m,f} - p_{m,p}) \quad (3.36)$$

The membrane permeability constant C in this form has the unit of $\frac{\text{mol}}{\text{m}^2 \text{s Pa}}$.

3.2.5 Monte Carlo filtering method

As many parameters occur in the entire model and many of them can be considered as parameters to be calibrated, a thorough investigation of the parameter space is required. This cannot be achieved by using a local optimization method (e.g. gradient descent), but a global "brute force" method such as Monte Carlo filtering [114, 119] is more appropriate. Fig. 3.3 illustrates how the method works. First, a sampling range needs to be chosen for the parameters of interest. Next, a shot is taken from the parameter ranges using

quasi-random Sobol sampling [120] and the model is simulated using the given parameters set for all of the experiments of a given membrane. The prediction performance of the model is evaluated using the weighted sum of squared errors (wSSE) - eq. 3.39 [112]. In this way it is estimated how well a simulation based on a certain parameter set fits all of the available experimental data. This process is executed 36,000 times (meaning that 36,000 parameter combinations are sampled and each time the model is simulated for all experiments performed with the membrane), and subsequently a scatter (dotty) plot of wSSE for each simulation is plotted as a function of the parameter range. This allows to transparently visualize whether and where a minimum in wSSE occurs. The horizontal red line represents a user defined cut-off value, below which the solutions are considered as "behavioral" (good), whereas simulations resulting in points above this line are considered as non-behavioral (i.e. leading to a poor fit). The choice of this cut-off value is set to be 20 % higher than the minimum wSSE value. The latter value can be regarded as subjective, however it does not affect the final outcome of the model calibration, since it is only used for the visualization of trends of the behavioral solutions. One needs to make sure that sufficient behavioral solutions are retained in order to study these trends. The selected threshold was chosen quite narrow - if we consider a typical wSSE range from 10 to 10 000, only the solutions having wSSE between 10 and 12 are considered as behavioral

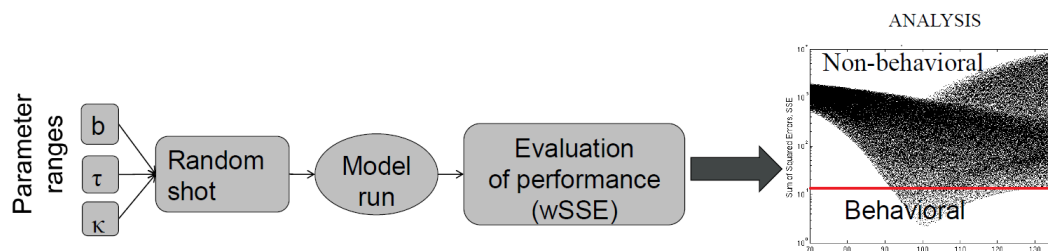


Figure 3.3: Schematic representation of the Monte Carlo filtering method. 36,000 parameter combinations are sampled and each time the model is simulated for all experiments performed with the membrane, followed by analysis of each parameter combination (resulting in a dot) based on the wSSE.

The experimental flux and energy efficiency were used as variables for estimating the wSSE (eq. 3.39). This is a classical way of setting up a multicriteria evaluation based on multiple datasets [121]. Note that the difference in units is not problematic here. We merely define a "distance" measure between ex-

perimental data points and several experimental datasets. Because the setup had a weighting balances measuring the weight of the feed and the permeate, the experimental flux was calculated for both channels and the difference was used to calculate the weight for each point - $W_{i,N}$. Similarly, the energy efficiency was also calculated in percent (eq. 3.40) using a heat balance for both channels and the difference, being a measure of the quality of the observation, was used as weight $W_{i,EE}$. In this way, the experimental data with lower quality will have less weight in the model calibration. Weights can also be used if datasets are in different orders of magnitude to bring these contributions in a similar order of magnitude, having them equally contribute to the value of $wSSE$.

$$W_{i,N} = 1 - \frac{|N_{exp,f} - N_{exp,p}|}{(N_{exp,f} + N_{exp,p})/2} \quad (3.37)$$

$$W_{i,EE} = 1 - \frac{|EE_{exp,f} - EE_{exp,p}|}{(EE_{exp,f} + EE_{exp,p})/2} \quad (3.38)$$

$$wSSE = \sum_{i=1}^n \left(((N_{i,calc} - N_{i,exp})W_{i,N})^2 + 0.01((EE_{i,calc} - EE_{i,exp})W_{i,EE})^2 \right) \quad (3.39)$$

A weighting factor of 0.01 was used for the squared error of the energy efficiency, because the value of energy efficiency is usually 1 or 2 orders of magnitude larger than the flux and generally a much higher experimental error is associated with its measurement. The choice of this value is subjective, but a coefficient should always be used when multiple criteria are evaluated and it would be equally subjective if this coefficient is equal to 1. The measurement error is particularly large in the experiments with higher flow rates and at low fluxes, where the temperature drops along the channels is small. This comes from the way energy efficiency is measured:

$$EE_{exp} = \frac{100N_{exp}H}{T_{in}Cp_{in}M_{in} - T_{out}Cp_{out}M_{out}}, \% \quad (3.40)$$

Where H , Cp and M are the latent heat of evaporation of water in J/mol, specific heat capacity and the mass flow rates. The energy efficiency is the ratio of the energy exchanged due to flux over the energy exchanged due to flux and conduction losses (i.e. the total energy exchanged through the membrane). In some of the experiments, the difference between inlet T_{in} and outlet T_{out} temperature is as low as 1 °C and this is very close to the accuracy of the temperature sensors, rated to be ± 0.2 °C. Hence, when the temperature difference

along the channels is small, the experimental error of EE can become quite large.

Summarized, the evaluation using wSSE allows to account for measurement uncertainty and the information present in multiple datasets and is therefore superior to just using one dataset based on flux, as is traditionally used.

3.3 Results and Discussion

3.3.1 Calibration of the heat and mass transfer inside the channels

Using the aluminium foil calibration method described in Section 3.2.2 an existing Nusselt equation was calibrated to match the behavior of the particular spacer. The best fit of calculated to experimental overall heat transfer coefficient is achieved with the following Nusselt equation:

$$Nu_{f,p} = 0.223(Re_{f,p})^{0.69}(Pr_{b,f,p})^{0.13}(Pr_{b,f,p}/Pr_{wf,p})^{0.25} \quad (3.41)$$

The basis of this equation is taken from the work of Gryta et al. [13], however the linear correction (**a**) is increased from 0.14 to 0.223 and the Reynolds exponent (**b**) is lowered from 0.73 to 0.69. The coefficients **c** and **d** were not calibrated (eq. 3.5) and were left at their original values of 0.13 and 0.25, since the Pr number is only dependent on the fluid properties. The values of **a** and **b** were obtained automatically using `fminsearch` (a local optimization function in Matlab based on the Nelder-Mead simplex algorithm [122]), while minimizing the sum of squared errors between the experimental and simulated overall heat transfer coefficients. The coefficients need to be changed, because this Nusselt equation was developed for an empty channel, while in our case a 60 degree non-woven spacer is used. In fact, it is allowed to tune the parameters **a** and **b** in eq. 3.5, because they are calibration parameters even in the original form of the Nusselt equation [110,123]. Using eq. 3.41 an excellent fit between the calculated and measured heat transfer coefficients is obtained - Figure 3.4.

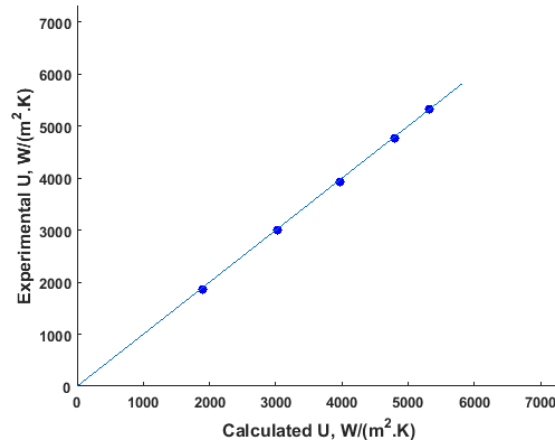


Figure 3.4: Simulated versus measured overall heat transfer coefficients.

Using the Chilton-Colburn analogy [111] between heat and mass transfer as done in other works [124,125], the Sherwood equation form and coefficients were taken the same as the ones obtained in the heat transfer calibration.

$$Sh = 0.223(Re_f)^{0.69}(Sc_{b,f})^{0.13}(Sc_{b,f}/Sc_{wf})^{0.25} \quad (3.42)$$

The calibration of the Nusselt equation was initially performed using a thin polymeric sheet instead of the aluminium foil as described by Gryta et al. [14]. However, we obtained better results with the aluminium foil, because the thermal conductivity of aluminium is exactly known and not a function of temperature or orientation of the polymer molecule [126]. Additionally, the local heat transfer coefficient of the aluminium foil is extremely high and its resistance is not limiting for the system, which is not the case when using polymeric sheet.

3.3.2 Choice of calibration parameters

In order to tackle the heat and mass transfer resistances inside the membrane, a Global Sensitivity Analysis (GSA) was applied to a subset of the model parameters. Table 3.4 summarizes the parameters that are studied, their range and whether it was decided based on the analysis to use them in the calibration.

Table 3.4: Parameters and their ranges used in the analysis

Parameter	Measured value	Sampling range	Used in the calibration
Mean pore radius R_p , μm	0.27*	$\pm 20\%$	No: Not Sensitive, Interactions
Membrane porosity ϵ	0.83*	[0.5-0.95]	No: Interactions
Tortuosity τ	-	[1-2.5]	Yes
Thermal conductivity of the membrane matrix κ_m	Calculated in eq. 3.17	-50 to 200%	Yes
Membrane thickness δ , μm	180*	$\pm 20\%$	No: Not sensitive
Diffusion coefficient, D_{aw}	Calculated in eq. 3.26	$\pm 20\%$	No: Not sensitive
Kn diffusion coefficient, D_e^K	Calculated in eq. 3.28	$\pm 20\%$	No: Not sensitive

*Values specific to the PP membrane

The mean pore radius was given a measurement uncertainty range of 20 %. The porosity was taken in a broad range from 0.5 to 0.95 in order to study its behavior using the Monte Carlo filtering. There is no available data for the tortuosity, therefore also a broad range of values from 1 to 2.5 was taken. The resistance of the heat transfer through the membrane needs to be addressed (Figure 3.1). The thermal conductivity of the membrane κ_m was calculated with eq. 3.17 and then sampled in a range from - 50 to +200 percent of the this value. The sampling range for the thermal conductivity was taken quite wide because this parameter is very uncertain as mentioned earlier in section 3.2.3, due to the irregular structure of the membranes. Additionally, an uncertainty of 20 % was set to the membrane thickness measurement δ and the calculated diffusion coefficients $D_{aw,e}$ and D_e^K , because they are calculated using semi-empirical correlations and could carry some uncertainty.

A variance based GSA was performed for the parameters in Table 3.4 using Sobol sampling and the design proposed by Saltelli et al. [127]. A total of 10 000 samples were taken with the ranges given in Table 3.4, using the Field's corrected DGM (eq. 3.33), PP membrane, bulk temperatures of 60 and 45 °C for the feed and the permeate, 0.15 m/s empty channel velocity and 40 g/l salinity. More details on the method implementation are described by Mortier et al. [128]. The total effect indices for the flux and the energy efficiency can be found in Table 3.5.

Table 3.5: Total effect indices calculated from the GSA

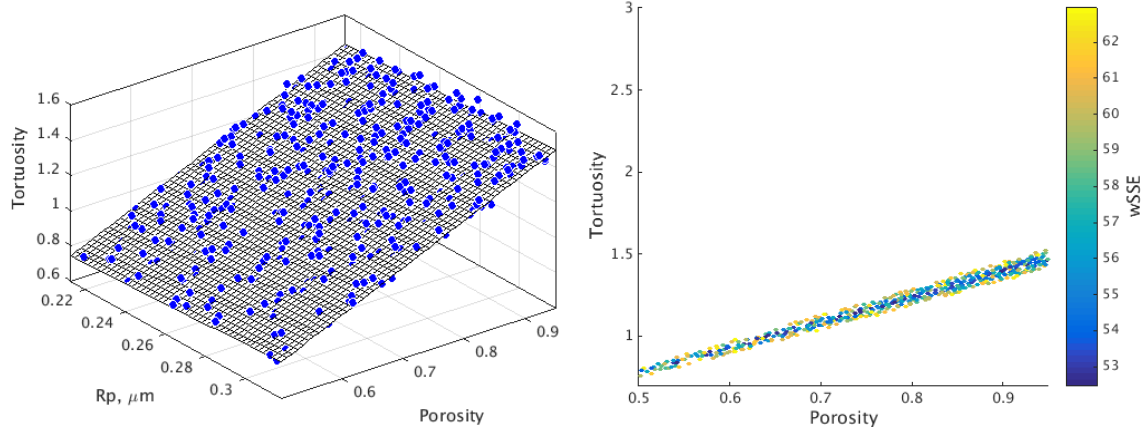
	τ	ϵ	κ_m	δ	$D_{aw,e}$	D_e^K	R_p
Flux S_{Ti}	0.543	0.310	0.007	0.090	0.054	0.009	0.002
EE S_{Ti}	0.173	0.450	0.372	0.000	0.018	0.003	0.008

The GSA study reveals that almost all of the variance of the flux can be described by the tortuosity and the porosity, while for the energy efficiency the most important parameters are the porosity, thermal conductivity of the membrane and the tortuosity. The membrane thickness δ , mean pore radius R_p and the calculated diffusion coefficients $D_{aw,e}$ and D_e^K are not sensitive parameters for the flux and the energy efficiency and are therefore excluded in the subsequent calibration. It is noteworthy that the membrane thicknesses is not a sensitive parameter for the energy efficiency at low salinities and thick membranes as also shown in our previous work [117].

The flux is not sensitive to the thermal conductivity of the membrane κ_m , whereas it is the second most important parameter for the energy efficiency. This suggests, that by having a goal function that includes both flux and energy efficiency (eq. 3.39), instead of the more traditional calibration efforts where only flux is accounted for, the value of the thermal conductivity of the membrane can be estimated from the EE data.

3.3.3 Calibration of the heat and mass transfer inside the membrane using Monte Carlo filtering

Figure 3.5a illustrates the Monte Carlo filtering for tortuosity and porosity. The mean pore radius was included for illustrative purposes. It clearly shows the correlation between the tortuosity and porosity and the irrelevance of R_p .



(a) Three dimensional dotted plot of the behavioral (acceptable) solutions of the membrane parameters. A plane is fitted through the solutions (dots) to visualize the trend. The three parameters clearly have interactions and if all three are calibrated simultaneously no unique calibration set can be obtained as infinite number of behavioral solutions exist on this plane.

(b) Behavioral solutions as a function of porosity and tortuosity. Pore radius is fixed at its measured value. The colorbar signifies the wSSE. The tortuosity and the porosity show clear interaction as and no unique calibration set can be obtained. When both parameters are included in the calibration, physically impossible calibration sets such as tortuosity lower than 1 can be obtained.

Figure 3.5: Behavioral solutions as a function of the membrane morphological parameters. The plots are specific to the PP membrane

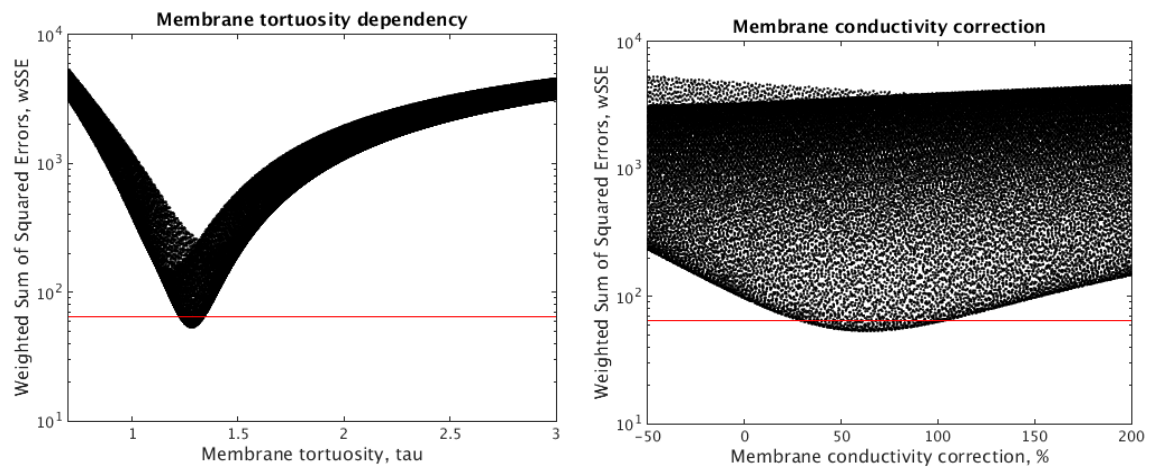
In this 3D figure the behavioral solutions form a plane in space, meaning that for example a certain pore radius value could be compensated by another combination of the other two membrane parameters. This means that if all 3 parameters are adjusted simultaneously, there would be an infinite number of combinations lying in this plane, which lead to the same quality of fit (similar value of goal function). In fact when the mean pore radius is fixed to its measured value (Figure 3.5b), the strong correlation between porosity and tortuosity is apparent. Indeed, an equally good wSSE can be achieved in the low and the high values of the porosity. This confirms that by adjusting simultaneously both parameters, one does not arrive at a better fit. This problem is related to the identifiability of the model, given a structure, a dataset and a set of parameters to be estimated [129,130]. Increased porosity and pore size lead to increased permeability, while increased tortuosity decreases the permeability [117], therefore it could be expected that these parameters are correlated, which is now clearly shown in Figure 3.5a.

Since there is no combination that is more favorable, calibrating all of the mem-

brane morphological parameters simultaneously does not lead to an improved fit. It is noteworthy that a local optimization method would not be able to detect this parameter correlation and would just provide a "solution" that is related to the optimization algorithm and constraints selected by the user with regard to aborting the search. Because the behavioral solutions lie in the whole range of the mean pore radius and porosity values (Figure 3.5a) and these properties can easily and accurately be measured, it was decided to leave them out of the calibration and use the measured values instead. The tortuosity is the most uncertain parameter, because there is no clearly defined methodology to characterize it, therefore it is justified to retain this as a calibration parameter.

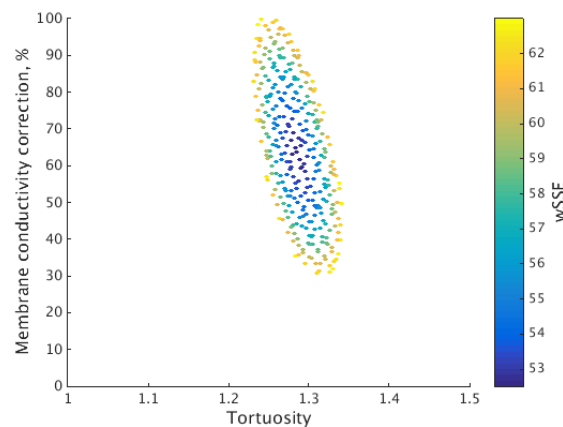
3.3.4 *Simulation of single layer membranes*

In order to calibrate the DCMD system using a single-layer membrane only 2 parameters are needed - the tortuosity to calibrate the mass transfer through the membrane and similarly the thermal conductivity of the membrane matrix can be used as an adjustable parameter for the heat transfer inside the membrane. These parameters can now be calibrated either by finding the parameter set which leads to the best solution from the Monte Carlo filtering study or by employing a local optimization algorithm. In our case we decided to re-use the Monte Carlo simulations, in order to avoid additional software implementation. The dotted plots specific for the calibration of the PP membrane can be seen in Figure 3.6.



(a) Weighted sum of squared errors as a function of membrane tortuosity

(b) Weighted sum of squared errors as a function of membrane thermal conductivity correction



(c) Zoomed in figure of the behavioral (good) solutions as a function of the membrane conductivity correction and the tortuosity. A clear optimum can be observed.

Figure 3.6: Dotted plots of the calibration parameters and the resulting sum of squared errors, eq. 3.39. The dots below the horizontal red line in (a) and (b) indicate the behavioral solutions. Pore radius and porosity fixed at the measured values of $0.27 \mu\text{m}$ and 83 percent. The optimum combination of the two parameters can be seen in (c)

For the PP membrane, the tortuosity values must lie within 1.25 and 1.35 and the predicted thermal conductivity of the membrane matrix using eq. 3.17 has to be increased by 60 %. Including the thermal conductivity of the membrane in the calibration improves the fit almost twice in terms of wSSE (Figure 3.6b) for this particular membrane. In order to demonstrate that a unique combin-

ation of the two parameters can be identified that leads to the best fit, the behavioral solutions are plotted as a function of the thermal conductivity and tortuosity (Figure 3.6c). The resulting fit for the flux after calibration can be seen in Figure 3.7.

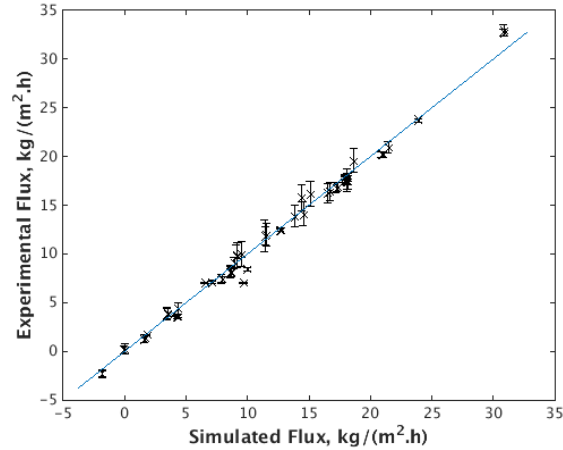


Figure 3.7: The simulated versus predicted flux for the PP membrane, eq. 3.33. Experimental conditions: $T_{b,f}$ 53 to 61 °C, $T_{b,p}$ 25 to 54 °C, salinity 0-327 g/l and channel velocity 2 to 28 cm/s

Using the Monte Carlo filtering method and a calibration set with only 2 parameters, an excellent fit for all of the experiments performed with the PP membrane could be achieved - Figure 3.7. This method can be completely automated and can derive a calibration for any other membrane within minutes, based on the available experimental data for flux and energy efficiency. It should be noted that the experimental conditions for the membrane varied in a wide range of feed temperatures from 53 to 61 °C, permeate temperatures from 25 to 54 °C channel velocities from 2 to 28 cm/s and salinity from 0 to 327 g/l - Table 3.6. Hence, the calibrated model is valid for all these operational conditions.

The error bars on Figure 3.7 represent the difference between the measurement of the feed and permeate channels. However, according to the specifications, the scales have an absolute error of 0.1 g in the measured range, therefore it is possible that a hidden error exists in the special case where both scales are simultaneously displaying 0.1 g higher or lower than the actual weight. To study the effect of such error, one should consider that the flux is calculated

using the following equation:

$$N = \frac{\Delta m \pm \sigma}{\Delta t A} \quad (3.43)$$

Where Δm , σ , Δt and A are the measured weight change (kg), the absolute error of the scales (kg), the measurement time (hr) and the area of the module (m^2), respectively. Considering a typical measurement time of 0.5 hr and module area of 0.0108 m^2 , the error of the flux, introduced by the absolute error of the scales can be visualized (Figure 3.8):

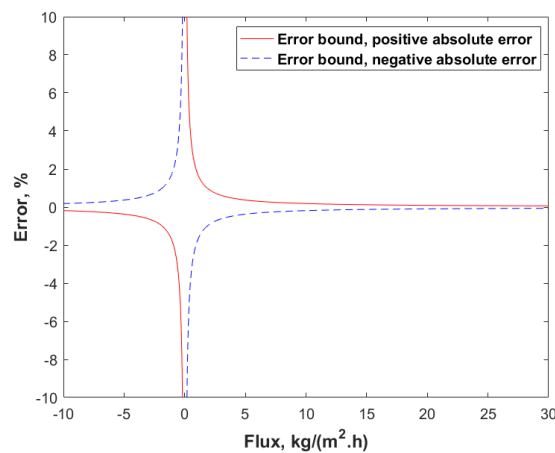


Figure 3.8: Error of the flux measurement introduced by the absolute error of the scales.

As seen in Figure 3.8 the error introduced by the scales is only significant at conditions resulting in fluxes between -2 and $2 \text{ kg}/(\text{m}^2.\text{h})$. At low flux conditions, the measured weight m is relatively small and the influence of the absolute error σ in equation 3.43 becomes significant. In such cases the error can be reduced by performing the experiments for a longer time, which will increase the measured weight change Δm .

Another possible source of measurement error would be due to air bubbles dynamically traveling as well as being entrapped inside the lab-scale system. This error can be mitigated by monitoring the weight evolution for both scales, which is likely to highlight the existence of such error.

3.3.5 Simulation of supported membranes

In order to simulate the supported membranes used in this study, a simple, yet physical approach was taken. Two of the supported membranes have a non-woven support (ePVDF and PTFE2) and one used a spacer-like scrim support (PTFE1). In all of the experiments the support was placed on the permeate side. The resistances in the system are illustrated in Figure 3.9.

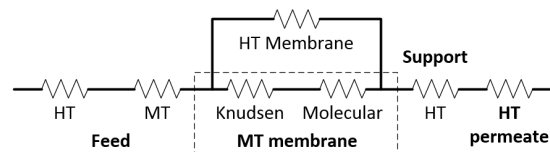
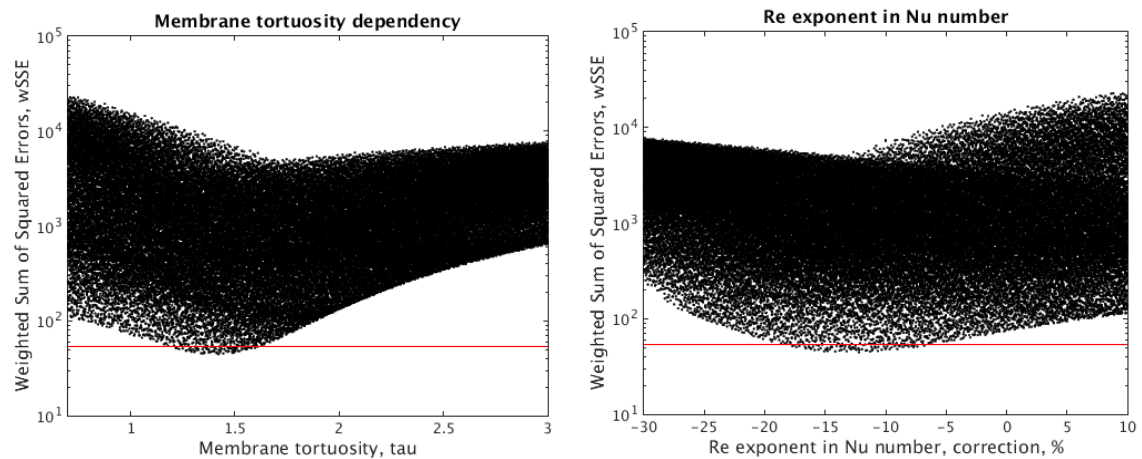


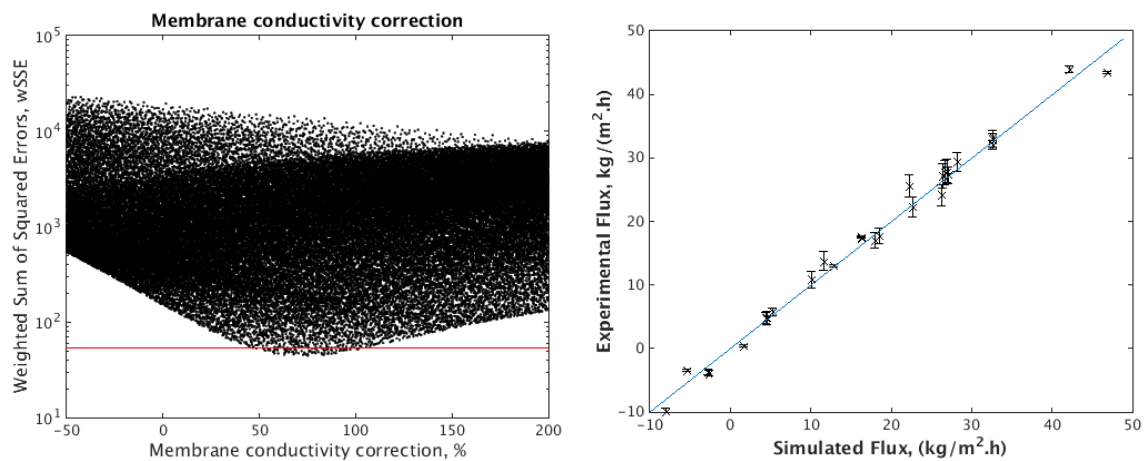
Figure 3.9: Resistances in the system when the support of the membrane is placed at the permeate side

The water flowing through the permeate channel does not experience concentration polarization because it has a uniform concentration and in most of the cases is almost pure water. Therefore, the membrane support can simply be modelled as an additional heat transfer resistance in the permeate channel. It was decided to attempt to merge the heat transfer resistances in the permeate channel and the support material and model them by adjusting the Reynolds exponent (parameter **b**) in eq. 3.5 for the permeate channel - Figure 3.10b.



(a) Weighted sum of squared errors as a function of membrane tortuosity

(b) Weighted sum of squared errors as a function of Reynolds exponent correction (**b** in eq. 3.41) for the permeate channel



(c) Weighted sum of squared errors as a function of membrane conductivity correction

(d) Simulated versus experimental flux for the ePVDF.

Figure 3.10: Dotty plots of the calibration for the supported ePVDF membrane. The dots below the horizontal red line in (a) and (b) and (c) indicate the behavioural solutions. Pore radius and porosity fixed at the measured values of $0.30\mu\text{m}$ and 79 percent

Using this approach the behavior of supported membranes can be predicted successfully (Figure 3.10d), without including additional equations to the model. Although the Reynolds exponent on the permeate side is an extra parameter that is added to the calibration, a unique combination can be identified (i.e. the minima of the behavioural solutions in the dotty plots are clearly defined), therefore they can be calibrated simultaneously.

3.3.6 Submodel selection for the mass transfer inside the membrane

In the previous sections the Field's Kn corrected DGM relation (eq. 3.33) was used to calculate the mass transfer in the membrane, because it estimates the degree of Knudsen flow in the transitional region and good results were obtained with it in previous work [117]. However, in order to compare and choose the best mass transfer model inside the membrane the Monte Carlo filtering method was applied with all of the previously listed membrane mass transfer models - Table 3.6. Hence, with this analysis, we aim to select the model of a series of candidate models that best describes the experimental data.

Table 3.6: Predictive performance of the different models available in the literature, calibrated values for tortuosity τ , thermal conductivity of the membrane κ_m and Reynolds exponent \mathbf{b} in eq. 3.5.

Description			Goodness-of-fit			Calibrated values		
Membrane	Conditions	Model type	wSSE	RMSD, $kg/(m^2h)$	R ² EE	τ	κ_m , W/(m.K)	Re expo- nent, \mathbf{b} in eq. 3.5
PP 70 Experiments Phase inversion Kn=0.27	$T_{b,f}=53-61$ °C $T_{b,p}=25-54$ °C Sal=0-327 g/l $v=2-28$ cm/s	DGM, eq. 3.29	54.2	0.08	0.91	1.13	0.06	Pre- calibrated value 0.69
		Field's correction, eq. 3.33	53.2	0.08	0.96	1.28	0.06	
		Knudsen, eq. 3.34	27.6	0.05	0.91	4.51	0.06	
		Molecular eq. 3.35	60.4	0.08	0.92	1.51	0.06	
		Permeability constant eq. 3.36	30.0	0.06	0.91	-	0.06	
PE (UHMW) 36 Experiments Stretching Kn=0.48	$T_{b,f}=38-59$ °C $T_{b,p}=23-49$ °C Sal=0-312 g/l $v=4-16$ cm/s	DGM, eq. 3.29	13.9	0.10	0.96	1.77	0.05	Pre- calibrated value 0.69
		Field's correction eq. 3.33	12.8	0.09	0.96	2.12	0.05	
		Knudsen, eq. 3.34	6.5	0.06	0.97	4.84	0.05	
		Molecular eq. 3.35	21.4	0.12	0.96	2.78	0.05	
		Permeability constant eq. 3.36	7.5	0.07	0.97	-	0.05	
PVDF 10 Experiments Phase inversion Kn=0.35	$T_{b,f}=58-59$ °C $T_{b,p}=44-54$ °C Sal=0-309 g/l $v=16$ cm/s	DGM, eq. 3.29	0.7	0.05	0.98	2.05	0.07	Pre- calibrated value 0.69
		Field's correction eq. 3.33	0.7	0.05	0.98	2.36	0.07	
		Knudsen, eq. 3.34	0.6	0.05	0.98	7.01	0.07	
		Molecular eq. 3.35	0.8	0.08	0.98	2.89	0.07	
		Permeability constant eq. 3.36	0.6	0.05	0.98	-	0.07	
PES 45 Experiments Phase inversion Kn=0.28	$T_{b,f}=58-59$ °C $T_{b,p}=43-54$ °C Sal=0-370 g/l $v=6-26$ cm/s	DGM, eq. 3.29	89.0	0.13	0.89	1.11	0.15	Pre- calibrated value 0.69
		Field's correction eq. 3.33	89.0	0.13	0.87	1.25	0.15	
		Knudsen, eq. 3.34	88.1	0.13	0.88	4.23	0.16	
		Molecular eq. 3.35	88.6	0.13	0.89	1.49	0.16	
		Permeability constant eq. 3.36	57.1	0.13	0.88	-	0.16	
Supported membranes								
ePVDF 28 Experiments Electrospinning Kn=0.24	$T_{b,f}=54-59$ °C $T_{b,p}=39-49$ °C Sal=0-347 g/l $v=4-28$ cm/s	DGM, eq. 3.29	45.6	0.22	0.99	1.55	0.07	0.61
		Field's correction eq. 3.33	45.4	0.21	0.98	1.60	0.07	0.59
		Knudsen, eq. 3.34	43.5	0.21	0.98	6.38	0.07	0.60
		Molecular eq. 3.35	46.5	0.21	0.98	1.87	0.07	0.59
		Permeability constant eq. 3.36	43.8	0.21	0.98	-	0.07	0.60
PTFE1 33 Experiments Stretching Kn=0.30	$T_{b,f}=58.5$ °C $T_{b,p}=44.0$ °C Sal=0-302 g/l $v=14$ cm/s	DGM, eq. 3.29	5.30	0.07	0.98	1.27	0.08	0.52
		Field's correction eq. 3.33	5.30	0.07	0.98	1.38	0.08	0.51
		Knudsen, eq. 3.34	5.30	0.07	0.97	4.24	0.08	0.51
		Molecular eq. 3.35	5.20	0.07	0.98	1.68	0.08	0.52
		Permeability constant eq. 3.36	5.30	0.07	0.98	-	0.08	0.52
PTFE2 38 Experiments Stretching Kn=0.77	$T_{b,f}=58-62$ °C $T_{b,p}=35-54$ °C Sal=0-319 g/l $v=14$ cm/s	DGM, eq. 3.29	129.6	0.29	0.94	1.33	0.04	0.55
		Field's correction eq. 3.33	129.1	0.29	0.94	1.61	0.04	0.55
		Knudsen, eq. 3.34	128.4	0.28	0.94	2.68	0.04	0.55
		Molecular eq. 3.35	131.3	0.29	0.94	2.65	0.04	0.56
		Permeability constant eq. 3.36	128.9	0.28	0.94	-	0.04	0.55

While the wSSE was used in the calibration and model structure analysis, it does not result in intuitive value for the fit quality. Hence, the Root Mean Square Deviation (RMSD) was adopted in order to intuitively describe the flux errors for each membrane, where only the normalized flux errors are included - eq. 3.44.

$$RMSD = \frac{\sqrt{\sum_1^n (\hat{N} - N)^2}}{n} \quad (3.44)$$

Above, \hat{N} , N and n are the predicted flux, the measured flux and the number of experiments performed with the membrane, respectively. Similarly, the R^2 values of the energy efficiency (R^2EE) in Table 3.6 are listed only as a goodness-of-fit indicator for the reader, but were not used to actually calibrate the model, because unlike wSSE, the R^2 calculation does not take into account the weights of each point.

To test whether the difference of fit between the models for the different membranes is statistically significant, the Friedman's test [131] was applied. The Friedman's test is a non-parametric statistical test for two-way analysis of variance. The test works by ranking the data points, in this case wSSE, from the smallest (rank=1) to the largest (rank=N). The result of this analysis can be seen in Figure 3.11.

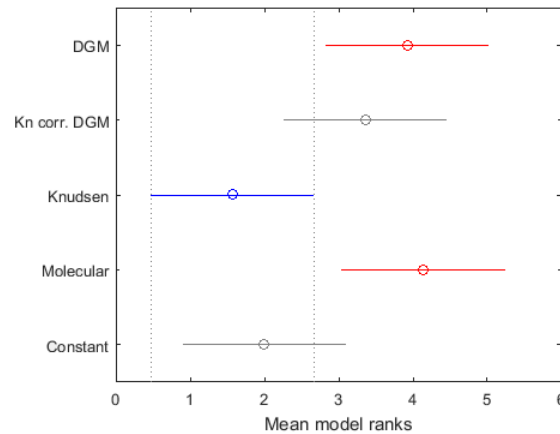


Figure 3.11: Analysis of the statistical significance of the difference in fit of the vapor flux models

According to the test, the models with overlapping bars around their rank means statistically perform the same. This means that the Knudsen model (blue) statistically performs better than the molecular diffusion and the DGM (red) and has the same performance as the Knudsen corrected DGM and the

permeability constant. However, from the perspective of the permeability constant and the Kn corrected DGM, they perform equally well to all other models. Therefore, all of the models perform very similar and the choice of model depends on the purpose of the modelling.

If the purpose is to be used as a scenario analysis for different flow rate conditions, temperatures and salinities, the use of the permeability constant is recommended, because it results in excellent performance for all membranes, while being the simplest way to model the system.

However, if the purpose of the model is to study the influence of the membrane properties such as porosity, tortuosity and pore size, one of the more physical models needs to be used. The molecular diffusion model does not result in better fit and should not be used, because as calculated by Phattaranawik et al. [76], the pore size needs to be larger than $11 \mu\text{m}$ to justify its use. The Knudsen diffusion model eq. 3.34, while statistically working better than the traditional DGM and the molecular diffusion, would also be theoretically incorrectly used since the pore size of the membranes is too large. The use of this model could only be acceptable for the PTFE2 membrane, because the Kn number is close to 1 and the predicted tortuosity seems acceptable, having a value of 2.65.

Although the advantage of the Kn corrected DGM over the traditional DGM is not statistically significant, this model has more realistic prediction for tortuosity of the PP and PES membranes and can therefore be recommended. The calibrated values of tortuosity using the Kn corrected DGM is 1.28 (PP) and 1.25 (PES) compared to the predicted 1.13 (PP) and 1.11 (PES) by the traditional DGM, which points to an underestimation of the permeability, that is counteracted by calibrating the tortuosity to an unrealistically low value. In fact, Field et al. [75] expressed an opinion that, while an improvement, the newly proposed eq. 3.33 is still underestimating the permeability in the transitional region.

3.3.7 *Submodel selection for the thermal conductivity of the membrane*

The calibration approach in this chapter takes into account both the errors in flux and the energy efficiency in the evaluation of the wSSE (eq. 3.39). This enables us to predict the thermal conductivity of the membrane matrix. It is

interesting to note that the thermal conductivity of the membrane κ_m calibrates to the same value and is not affected by the choice of membrane mass transfer model (Table 3.6). This confirms that the heat and mass transfer inside the membrane can be calibrated simultaneously as long as the weighted sum of squared errors (wSSE) of both the flux and the energy efficiency are used in the goal function (eq. 3.39).

The range of predicted thermal conductivity for the different membranes is between 0.04 and 0.08 $W/(m.K)$, with the exception of the predicted thermal conductivity of the PES membrane of 0.15-0.16 $W/(m.K)$, which is significantly higher than the rest. This can be explained by the PET support embedded inside the active layer of this membrane. PET has very high thermal conductivity of 0.15-0.4 $W/(m.K)$ [132] and probably a large part of the heat losses are caused by the heat transfer via the fibres of the PET support, resulting in higher overall thermal conductivity of the PES membrane.

Based on the calibrated values for the thermal conductivity (Table 3.7), the membrane manufacturing technology that produced the lowest membrane matrix conductivity is stretching at 0.04 and 0.05 $W/(m.K)$ for the PTFE2 and PE membrane, respectively. The PTFE1 membrane is also prepared by stretching, but the thermal conductivity is relatively high at 0.08 $W/(m.K)$, which can be due to partial embedding of the scrim support into the active layer, as observed by Zhang et al. [72].

Table 3.7: Calibrated thermal conductivity of the membranes and the base polymers and the corresponding porosity

Membrane	Technology, comment	Thermal conductivity of the base polymer, κ_s $W/(m.K)$	Porosity, %	Calibrated thermal conductivity κ_m , $W/(m.K)$	Deviation from predicted κ_m %		
					Series eq. 3.19	Maxwell eq. 3.17	Parallel eq. 3.18
PP	Phase inversion	0.11-0.20 [15]	83	0.06	+93	+62	+21
PE (UHMW)	Stretching	0.42-0.50 [133]	76	0.05	+36	0	-62
PVDF	Phase inversion	0.17-0.21 [15]	66	0.07	+85	+38	-14
PES	Phase inversion (Internal support)	0.15 - 0.16 [44]	58	0.15-0.16	+269	+180	+93
Supported membranes							
ePVDF	Electrospinning (NW support)	0.17-0.21 [15]	79	0.07	+103	+69	+8
PTFE1	Stretching (Scrim support)	0.25-0.29 [15]	80	0.08	+152	+95	+14
PTFE2	Stretching (NW support)	0.25-0.29 [15]	80	0.04	+16	-6	-46

In Table 3.7, the different submodels for the thermal conductivity of the membrane are compared. For the example of the PP membrane, the value obtained by the models needs to be increased by 93, 62 and 21 percent, respectively in order to arrive at the calibrated value. The best fitting model for the phase inverted as well as the electrospun membrane is the parallel model (eq. 3.18) with average underestimation of 27% and standard deviation (σ) of 40%. The structure of the stretched membranes seems to be better predicted by the Maxwell's lower bound equation 3.17 (average underestimation of 30%, $\sigma=46\%$), while the series model (eq. 3.19) severely underestimates the thermal conductivity of all membranes (average underestimation for the phase inverted and the electrospun membranes of 138%, $\sigma=76\%$, while the stretched membranes are underestimated by 68%, $\sigma=60\%$).

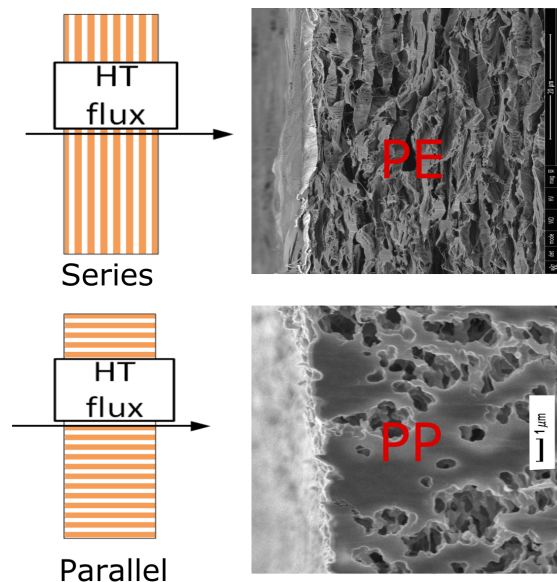


Figure 3.12: Left: Structure assumed by the series (eq. 3.19) and the parallel (eq. 3.18) models. Right: SEM micrographs of the stretched PE and the phase inverted PP membranes

The series (eq. 3.19) and the parallel (eq. 3.18) models are limiting cases of the membrane structure, where the pores are oriented perpendicularly or in parallel to the heat flux. The Maxwell's lower bound (eq. 3.17) is a case in between and cannot be described with an exact structure. Since the 3 submodels used for the simulation of the thermal conductivity of the membrane are developed for different ideal pore structures (Figure 3.12), it can be expected that one model represents better the structure of a certain membrane and none

of the models fits all of them, because the pores are oriented differently due to the manufacturing technology (phase inversion, stretching and electrospinning). In Figure 3.12 it appears that the series model is more representative for the structure of the PE membrane, while the parallel one represents better the PP membrane. SEM micrographs for all of the membranes can be seen in 9.1. The model predicts that the PE membrane matrix has a lower thermal conductivity than the PP membrane matrix (0.5 and $0.6 \text{ W}/(\text{m.K})$, respectively). This is interesting to notice, since the PE membrane has a lower porosity and more than twice higher thermal conductivity of the base polymer than the PP membrane. This suggests that the thermal conductivity of the base polymer is of minor significance for the thermal conductivity of the membrane and probably the structure is what dictates its overall thermal conductivity.

3.4 Conclusions

A series of supported and unsupported membranes were simulated and the model structure was examined using a Monte Carlo filtering method which was for the first time applied in the field of membrane technology to the best of our knowledge. The study yielded the following conclusions:

- The Nusselt equations can predict the system behavior with satisfactory accuracy, however the equations need to be calibrated for the particular membrane spacer.
- A 3D interaction between the pore size, tortuosity and porosity was found in the dusty gas model. The fit is not improved, moreover unique calibration set cannot be produced if all 3 are adjusted simultaneously. Since the tortuosity is the most uncertain of the 3, it was left as the only calibration parameter for the membrane permeability. This approach is widespread in the MD modelling, but a proper model analysis has not been performed so far to confirm it.
- The choice of mass transfer model for the membrane permeability is of little importance for the predictive power. The permeability constant has the same quality of fit as the most sophisticated models and is therefore recommended. Yet, this model it cannot be used to study the importance of the structural parameters of the membrane and in this case case a more

sophisticated model such as the newly proposed Kn corrected DGM equation by Field et al. (eq. 3.33) should be used. This model also predicts more realistically the membrane tortuosity and is therefore recommended over the traditional DGM model.

- By simply adjusting the Reynolds exponent for the Nusselt equation on the permeate side, the model can account for the additional heat transfer resistance of the support instead of adding equations and parameters to the model. This approach was demonstrated to work satisfactory, regardless of its simplicity.
- The thermal conductivity of the membrane proved to be a very important calibration parameter, but its value can be identified only if the goal function includes both the flux and the energy efficiency, unlike the traditional approach where only the flux error is evaluated.

CHAPTER 4

Full-scale Direct Contact Membrane Distillation (DCMD) model including membrane compaction effects

Redrafted from: I. Hitsov, W. De Schepper, K. De Sitter, C. Dotremont, I. Nopens, 2016. Full-scale Direct Contact Membrane Distillation (DCMD) model including membrane compaction effects, *Journal of Membrane Science* (524), 245-256

Abstract

While many models exist in the literature for description of lab-scale direct contact membrane distillation (DCMD) performance, only a handful of modelling attempts at full-scale have been described. In this chapter, a method is presented for the simulation of the flux and energy efficiency of a full-scale, counter-currently operated, spiral-wound DCMD module. The model is based on a previously calibrated lab-scale model. The geometry of the full-scale, spiral-wound module is discretized into small sections and the lab-scale model is applied in each section. It was found that the membrane used in this module compacts significantly under the operational conditions. This effect cannot be neglected, therefore the model had to be extended to account for it. It is noteworthy that, apart from this extension, no additional model calibration at full-scale was needed. Given its validity at full-scale the model can be safely used for extended scenario analysis with regard to the optimization of the

module design. The developed model and methodology are powerful tools to decide on system design and operation.

4.1 Introduction

Membrane distillation (MD) is an advancing thermal separation technology, whereby an aqueous solution is distilled through a porous, hydrophobic membrane, allowing for complete rejection of the non-volatile components in the feed such as salts. The process can be operated at relatively low temperatures (below 80 °C) and can therefore utilize sustainable thermal sources such as solar energy or even potentially free sources such as waste heat streams from factories. Membrane distillation is considered to have less problems with membrane fouling in comparison with pressure driven processes such as RO and NF [134, 135]. The low operational pressure, combined with mild temperatures allow the modules to be built from cheap, plastic materials. Yet, MD is still slow in its acceptance, which is possibly due to the lack of major reference cases, where MD is demonstrated successfully for several years on large production scale.

Modelling can be used to gain process knowledge, however the majority of models developed for membrane distillation today are only considering lab-scale module dimensions [105] and only a handful of models are applied on full-scale. Gustafson et al. [136] and Zhang et al. [36] developed step-wise models and validated them against series of flat sheet lab-scale modules, aiming to replicate full-scale conditions. Sirkar et al. [37] used a similar modelling approach and validated it against series of hollow fibre modules. The PhD thesis of D. Winter demonstrated a vast collection of full-scale models [6] that are also solved step-wise and validated against the commercial modules of SolarSpring, but did not look into the membrane compaction effect.

When sufficient hydrostatic pressure is applied on both sides of the membrane, the water cannot enter the hydrophobic membrane matrix and the membrane will compact. Membrane compaction has been discussed in only a few other articles for membrane distillation [36, 74, 137] and is rarely modelled or discussed in the literature. In fact, only the work of Zhang et al. [36] employs modelling of membrane compaction in modules with relatively long channels (0.75 m), however it was not validated by data from a commercially available module.

In a previous chapter we demonstrated how to calibrate and to properly identify all of the heat and mass transfer resistances in a lab-scale direct contact membrane distillation (DCMD) model (Chapter 3) using a Monte Carlo filtering methodology. The methodology maximized the fit to both the flux and the en-

ergy efficiency, instead of the traditional approach where only the flux is being modelled.

In this chapter, the lab-scale model that was previously developed in chapter 3 is being scaled up. The aim is to demonstrate how to model a full-scale DCMD module using a model that was calibrated only at lab-scale. A direct measurement of a membrane sample as a function of applied mechanical pressure is done allowing to correct the membrane properties as a function of the membrane compaction due to hydrostatic pressure. It is the first model to date that includes membrane compaction and is validated on full-scale against commercially available membrane distillation module. It is noteworthy, that the full-scale model presented here does not have any calibration parameters, the calibration is done only on lab-scale.

Since the model can be scaled up without the use of additional calibration parameters, it can later be utilized to predict how another membrane, spacer or module geometry would perform, starting from quick and cheap lab-scale experiments. Since the model does not need additional calibration, it is likely that all of the full-scale effects and resistances are identified correctly. This allows the model to be used with confidence to identify the bottlenecks in the system and improve its performance.

4.2 Materials and Methods

4.2.1 *Lab-scale setup*

The experimental data used for calibration were obtained in a flat sheet lab MD setup (6x18 cm). Two channels with thickness of 2 mm each are formed by compressing two spacers around a single membrane in a polycarbonate flow cell - Fig. 4.1.

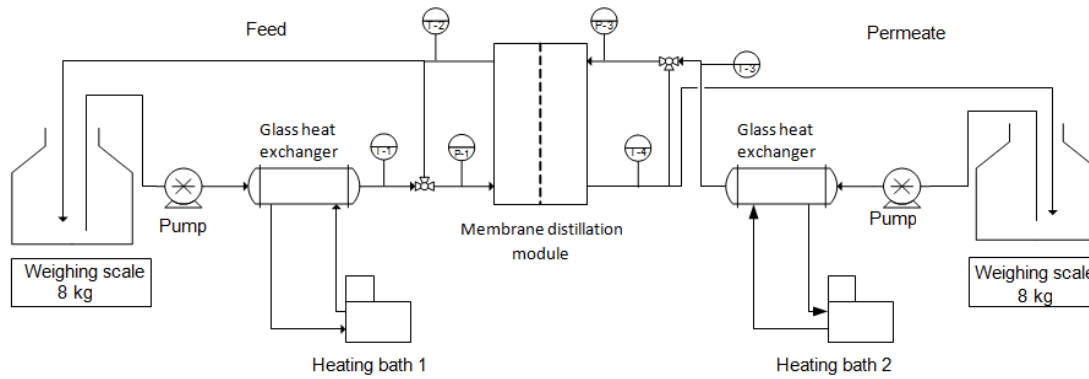


Figure 4.1: The lab-scale setup used in this study [117,138].

The flat-sheet module has an effective membrane surface of 0.0108 m^2 (6 cm by 18 cm). The feed and distillate were circulated counter-currently on the long side of the module using peristaltic pumps (Watson-Marlow, 520DuN/R2, Zwijnaarde, Belgium). The channel flow velocities were equal on the feed and permeate side and can be ranged from 0.04 to 0.28 m/s. The temperature is kept constant using two heating baths (Huber, Ministat 230w-cc-NR, Offen- burg, Germany) and monitored using four resistance temperature detectors (Thermo Electric Company, PT100 TF, Balen, Belgium), placed immediately after the inlet and outlet connections of the module. The flux was measured by evaluating the weight variations in the feed and distillate tank, using an analytical balance (Sartorius GmbH, ED8801-CW, Goettingen, Germany). The average flux over at least 30 minutes is reported. The electrical conductivity at the feed and permeate side was monitored by portable conductivity meters (WTW GmbH, pH/Cond 340i, Weilheim, Germany). The pressure drop was measured using a differential pressure drop meter with a resolution of 1 mbar and range of 0 to 1000 mbar (Endress Hauser, Deltabar PMD 130).

The lab- and full-scale experiments were performed with a commercially avail- able membrane made of ultra high molecular weight polyethylene, supplied by Aquastill. The pore radius, R_p is $0.15 \mu\text{m}$, porosity ϵ is 76 % and the thickness δ is $92 \pm 7 \mu\text{m}$. The minimum, average and maximum pore diameter and pore size distribution were measured using a Porolux 1000 (Porometer, Eke, Bel- gium) based on the wet/dry flow method. Porefil with a liquid surface tension of 16 mN/m was used as wetting liquid. The shape factor is assumed to be 1. The thickness was measured using a scanning electron microscope (SEM). More detailed information regarding the methodology of membrane charac-

terization is listed in Eykens et al. [117].

The spacer used in this study has a nominal thickness of 2 mm, a strand thickness of 1 mm, strand angle of 60° , a mesh size of 4.5 mm and a 30° flow-to-strand angle [139].

Load and compression were applied on the membrane and measured using a Tinius Olsen 5ST tensile/compression testing machine with a 100 N load cell, while the compressed membrane thickness was measured using the built-in extensometer. Incremental load was applied to reach 10, 25, 75 and 100 N, on a disk sample with area of 707 cm^2 . The first test was done only with the dead weight of the upper sample holder of 325 g (3.19 N), the resulting pressures were 0.05, 0.14, 0.35, 0.71, 1.06, 1.41 bar respectively.

4.2.2 Full-scale setup

The full-scale installation was supplied by Aquastill BV (The Netherlands) - Figure 4.2.

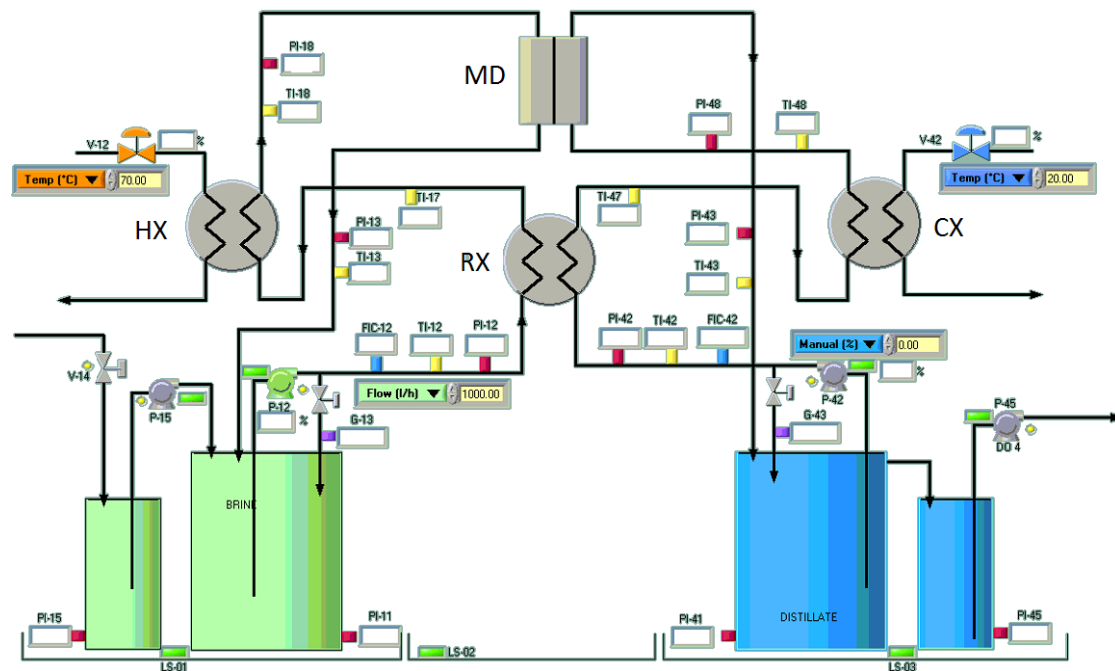


Figure 4.2: The full-scale system used in this study

The MD pilot system is equipped with a single 7.2 m^2 direct contact MD module also supplied by Aquastill. The module has 6 hot and 6 cold parallel

channels arranged in counter current flow mode, rolled in a spiral-wound fashion [140]. The module has an effective height of 40 cm and channel length of 1.5 m.

The pilot has two water loops - hot feed and cold permeate. The water circulation velocity was kept equal for the feed and the permeate and was varied in the range of 500 to 1500 l/hr, resulting in empty channel velocities of 3 to 9 cm/sec. The temperatures are measured using 3-wire PT-100 temperature sensors (Bürkert TR-30P, Germany). The flow rates were measured using flow rate meters (Bürkert type 8032, Germany) and a controller is altering the pump power in order to achieve a constant flow rate. Two buffer tanks are placed in the feed and on the permeate loops. As the distillate is permeating through the membrane, the level in the feed tank is decreasing and the level in the distillate tank is increasing. The distillate tank is then overflowing into a permeate buffer tank, which is supplied with a pressure meter (Bürkert type 8314, Germany). The pressure meter is used to measure the hydrostatic pressure in this tank, allowing the flux to be calculated, based on the time derivative of the hydrostatic pressure. When a certain level is reached a pump starts and pumps the distillate back into the feed tank, which avoids an increase in the feed salinity. A conductivity meter (Bürkert type 8222) was placed in the permeate loop in order to monitor the permeate quality.

4.3 Spacer characterization

4.3.1 Pressure drop measurement

The pressure drop of the spacer was measured inside the lab-scale MD cell at different velocities. The connections of the differential pressure drop meter were filled with water before each experiment to avoid measurement errors due to different hydrostatic pressure and were attached about 5 cm from the connections of the module. Before the pressure drop of the spacer can be measured, a calibration measurement must be performed in order to quantify the pressure drop inside the manifolds. In this way the spacer pressure drop measured on the lab-scale can be extrapolated linearly to the longer channel lengths used in the full-scale module. The calibration measurement is done with an empty channel and includes the pressure drop inside the manifolds as well as the empty channel. In order to calculate the pressure for the empty

channel part, the Hagen-Poiseuille equation for laminar flows was used - eq. 4.4 [141].

$$f = 16/Re \quad (4.1)$$

$$Re = \frac{vD_h\rho}{\mu} \quad (4.2)$$

$$D_h = 4(DW)/(2D + 2W) \quad (4.3)$$

$$\Delta P_{empty}^{calc} = 2f \frac{L}{D_h} \rho v^2 \quad (4.4)$$

Where f , Re , v , ρ , D_h , D , W , μ , Δp are the Fanning friction factor, Reynolds number, channel velocity, fluid density, hydraulic diameter, thickness of the channel, width of the channel, fluid viscosity and pressure drop, respectively. The pressure drop of the manifolds can then be calculated by subtracting the calculated pressure drop of the empty channel from the measured pressured drop with an empty channel - eq. 4.5

$$\Delta P_{manif} = \Delta P_{empty}^{meas} - \Delta P_{empty}^{calc} \quad (4.5)$$

After the pressure drop of the manifolds is known it can be subtracted from the spacer-filled channel measurements to obtain the pressure drop only for the spacer-filled region - eq. 4.6.

$$\Delta P_{spacer} = \Delta P_{spacer}^{meas} - \Delta P_{manif} \quad (4.6)$$

4.3.2 Heat and mass transfer characterization

The heat transfer was measured by inserting an aluminium foil with thickness of 153 μm inside the MD cell instead of a porous membrane, similarly to Phattaranawik et al. [15]. In this way, the system becomes a simple heat exchanger. The heat transfer is then measured under different flow velocities and the Nusselt equation (eq. 9.3) is calibrated in order to obtain best fit between the experimental and the calculated overall heat transfer coefficient. This is done by automatically adjusting the proportionality constant (a) and the Reynolds exponent (b) in the equation using a local optimization tool (fminsearch) in Matlab. This method was demonstrated thoroughly in chapter 3, where more detailed explanation can be found.

4.4 Lab-scale modelling

Figure 4.3 shows the resistances in the system and their respective arrangement.

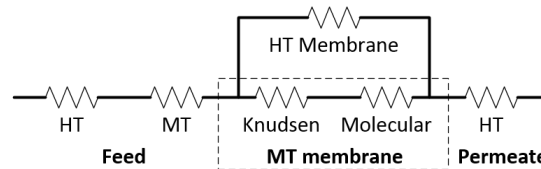


Figure 4.3: Heat (HT) and mass transfer (MT) resistances in the DCMD system

The lab-scale modelling structure was thoroughly explained in chapter 3, therefore the governing equations are compiled in an Appendix 9.2 and will only be briefly explained here.

4.4.1 Heat and mass transfer inside the channels

The temperature polarization inside the channels of the module was simulated using the Nusselt equation with the coefficients obtained during the spacer characterization. The salt concentration on the feed interface of the membrane will increase due to flux, also known as concentration polarization. To model this effect, a Sherwood equation was built using the Chilton-Colburn analogy [111], reusing the coefficients obtained during the heat transfer characterization of the spacer - eq. 9.10.

4.4.2 Heat and mass transfer inside the membrane

The thermal conductivity of the membrane κ_m was calculated using the Maxwell's lower bound equation [40] (eq. 9.14). The thermal conductivity of the membrane matrix is important for the calculation of the Energy Efficiency (EE), but also affects the flux due to the additional temperature polarization that the membrane conductivity introduces.

The membrane used in this study has a pore radius of $0.15 \mu\text{m}$ and a Knudsen number of 0.48, calculated at 50°C . Therefore, the vapour transport should be governed by both Knudsen and molecular diffusion [26]. In chapter 3 we recommended the use of the permeability constant as well as the Dusty Gas

model corrected for the Knudsen number of the membrane, proposed by Field et al. [75]. In this chapter we focus on the membrane properties, therefore, the Knudsen corrected Dusty Gas model (eq. 9.26) is used to model the membrane permeability.

4.4.3 *Lab-scale model calibration*

Since the channel heat and mass transfer resistances were already characterized using Nusselt and Sherwood equations specific to the particular spacer, the only resistances that are left for calibration are the heat and mass transfer resistance in the membrane. The calibration was done by simultaneously adjusting the membrane tortuosity and the membrane thermal conductivity κ_m while maximizing the goodness-of-fit of the simulated to the experimental flux and energy efficiency for all lab-scale experiments. The goal function used in the calibration and more detailed information about the lab-scale model calibration can be found in Hitsov et al. [139].

4.5 Model upscaling

4.5.1 *Model discretization*

In order to scale up the model, the geometry of the spiral wound module is virtually unwound and the channel is split into a number of small sections (Figure 4.4). Then, for each section the average temperature and flow rate are calculated based on the module geometry and the lab-scale model is applied to each section.

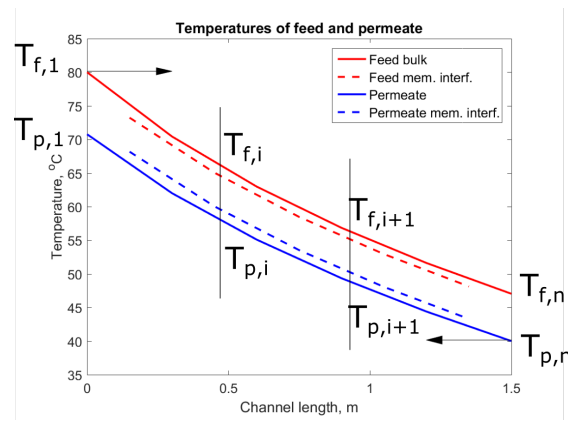


Figure 4.4: Discretization of the model, only 3 sections are considered in the particular example

The temperatures, flow rates and concentrations are solved from left to right, i.e. starting from the feed inlet/permeate outlet. Since the module is operated counter-currently, during the first iteration only feed inlet fluid properties are known, because they are in the user-defined, initial state. To tackle this problem, the model is solved iteratively. During the first iteration the model is initialized with a linear temperature profile along the channel length and the model is solved to obtain the flux and temperature profiles for the current iterations. During each next iteration, the unknown temperatures are taken from the previous iteration. During a new iteration the initial guess for the permeate outlet temperature ($T_{p,1}$) is corrected with the difference between the set and the calculated permeate inlet temperatures ($T_{p,n}$). The model is considered solved, once the difference between the calculated permeate inlet temperature ($T_{p,n}$) and the set inlet temperature are within 0.01 degrees for at least two iterations.

The inlet bulk velocity v , the length of each section L_X and the membrane surface area of each section A are given in the following equations:

$$v = \frac{Q_{mod}}{D_{ch}H_{mod}\frac{n_{ch}}{2}} \quad (4.7)$$

$$L_X = \frac{A_{mod}}{n_{sec}n_{ch}H_{ch}} \quad (4.8)$$

$$A = 2dXH_{ch} \quad (4.9)$$

In the equations above Q_{mod} and D_{ch} , H_{mod} and n_{ch} are the module flow rate, channel thickness, height of the module and the total number of parallel channels (hot plus cold). The tested module has 6 hot and six cold channels. Finally,

A_{mod} and n_{sec} are the total module area and the number of sections in which the module length is discretized.

4.5.2 Heat and mass balance in each section

The heat balance inside each section is described in Figure 4.5.

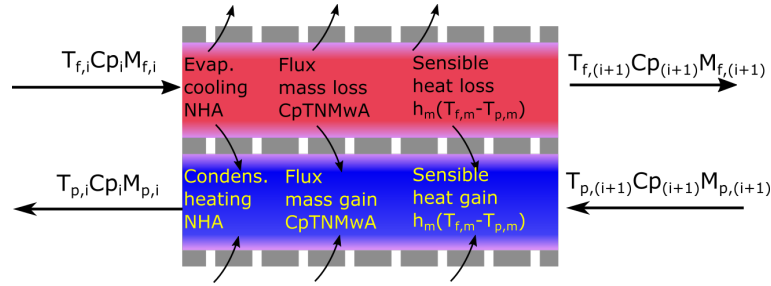


Figure 4.5: Heat transfer balance components for each section

When a heat balance is performed for the cold or the hot fluid in each section, the heat fluxes that are entering the section in Figure 4.5 have a positive sign and the exiting heat fluxes take a negative sign. The modelling is performed in steady state, therefore the accumulation term vanishes. The right hand side temperatures $T_{(f,i+1)}$ and $T_{(p,i+1)}$ for each of the sections can now be expressed as:

$$T_{f,(i+1)} = \frac{T_{f,i}Cp_{f,i}M_{f,i} - NHA - CpTNMwA - h_mA(T_{f,m} - T_{p,m})}{M_{(f,i+1)}Cp_{(f,i+1)}} \quad (4.10)$$

$$T_{p,(i+1)} = \frac{T_{p,i}Cp_{p,i}M_{p,i} - NHA - CpTNMwA - h_mA(T_{f,m} - T_{p,m})}{M_{p,(i+1)}Cp_{p,(i+1)}} \quad (4.11)$$

In these equations M is the water mass flow rate, Cp is the specific heat capacity, N is the flux, H is the specific heat of evaporation, Mw is the molecular weight of the water molecule and h_m is the local heat transfer coefficient of the membrane (eq. 9.15). In the cases where no subscript number is used for the flux, specific heat capacity, temperature and the specific heat of evaporation, the respective local average value for the current section is used.

The mass balance for each section is much simpler - the only component that exchanges through the walls of the membrane in each section is the water, driven by flux. From left to right the feed channel reduces its volume due to

this flux, whereas vice versa the permeate channel accumulates mass along the channel. The equations predicting the mass flow rates $M_{f,(i+1)}$ and $M_{p,(i+1)}$ can therefore be expressed as:

$$M_{f,(i+1)} = M_{f,i} - ANM\tau w \quad (4.12)$$

$$M_{p,(i+1)} = M_{p,i} - ANM\tau w \quad (4.13)$$

When an iteration is complete, the calculated inlet permeate flow rate $M_{p,n}$ (last section) is subtracted from the user-defined flow rate and the result is added to the initial guess for the permeate outlet flow rate $M_{p,1}$ (first section). The same correction is done for the guess of permeate outlet temperature. In the last iteration, the calculated inlet permeate temperature for the last section $T_{p,n}$ is subtracted from the user-defined temperature and the result is added to the initial guess for the permeate outlet temperature $T_{p,1}$ (first section).

By taking into account that the mass flow rate of salt inside the feed channel M_{NaCl} is constant, the salinity $C_{NaCl,(i+1)}$ in wt % for the outlet of the sections is calculated as:

$$C_{NaCl,(i+1)} = \frac{100M_{NaCl}}{M_{f,(i+1)}} \quad (4.14)$$

The thermophysical properties of the fluids are then updated for both channels as a function of the temperature and salinity using the Matlab functions supplied by Sharqawy et al. [118].

4.5.3 Membrane compaction at full-scale

Pressure drop modelling

The pressure drop modelling on lab-scale was done by interpolating the pressure measured with the spacer for the current velocity, including the pressure of the manifolds. Since the system is operated in counter-current mode, the pressure drop profiles are inversed. Therefore to find the compaction pressure exerted on the membrane, the measured pressure was divided by two to average it for the channel length.

In order to model the membrane compaction on full-scale, the pressure drop profile in the channels must be known first. From Section 4.3.1 we can predict the pressure drop that the spacer exert per meter of channel length, based on eq. 4.6. However, the manifolds and the internal flow distribution inside

the full-scale MD module also creates pressure drop. Therefore the pressure drop on full-scale was recorded and averaged for each of the three flow rates used in the experiments - 500, 1000 and 1500 l/hr. This allows to identify the pressure drop in the manifolds by subtracting the spacer pressure drop normalized for the channel length from the total measured pressure drop on full-scale. The pressure profiles for the feed and the permeate channels can then be reconstructed, assuming linear pressure drop in the channels (i.e. the channels remain with their nominal thickness) and equal pressure drop of the inlet and outlet manifolds.

Modelling membrane compaction effects

Membrane thickness The membrane thickness in the model is simply interpolated from its measurement as a function of pressure. The membrane thickness is affecting the mass transfer as well as the heat transfer equations (see Appendix 9.2).

Membrane porosity The following equations are used to recalculate the porosity in the compressed state ϵ , using the assumption that the polymer volume remains constant during compression.

$$V_{pol} = V_{mem,0} - \epsilon_0 V_{mem,0} \quad (4.15)$$

$$V_{mem} = V_{mem,0} \frac{\delta}{\delta_0} \quad (4.16)$$

$$\epsilon = \frac{V_{mem} - V_{pol}}{V_{mem}} = \frac{V_{mem,0} \frac{\delta}{\delta_0} - V_{mem,0} + \epsilon_0 V_{mem,0}}{V_{mem,0} \frac{\delta}{\delta_0}} = \frac{\frac{\delta}{\delta_0} - 1 + \epsilon_0}{\frac{\delta}{\delta_0}} \quad (4.17)$$

Where V_{mem} , V_{pol} and V_{air} are the total membrane, polymer and air volumes, respectively. The symbols with subscript of 0 are in their uncompressed or initial state. Similarly to the thickness the porosity affects both the heat and mass transfer (see Appendix 9.2).

Membrane tortuosity In order to recalculate the tortuosity during compression, a conceptual representation of a tortuous pore similar to Lawson et al. was used [74] (Figure 4.6).

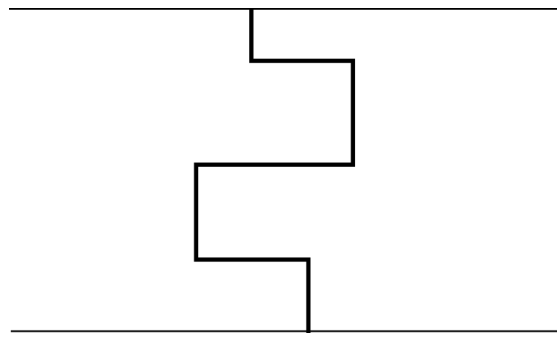


Figure 4.6: Conceptual representation of a tortuous pore

By its definition, the tortuosity (τ) is the ratio of the total path a fluid travels divided by the membrane thickness. The sum of the vertical sections of the pore in Figure 4.6 is always equal to the current membrane thickness (δ) and following the definition of tortuosity, the sum of the horizontal sections (or extra path) is equal to $(\tau-1)*\delta$. The tortuosity for an uncompressed membrane is:

$$\tau = \frac{\sum ([vertical] + [horizontal])}{thickness} = \frac{[\delta_0] + [(\tau_0 - 1) * \delta_0]}{\delta_0} = \tau_0 \quad (4.18)$$

When the membrane is compressed two cases exist. In the first case large macropores are compressed and the extra path that the fluid takes in the horizontal sections remains the same, resulting in:

$$\tau = \frac{[\delta] + [(\tau_0 - 1) * \delta_0]}{\delta} \quad (4.19)$$

In the second case, the compressed pores collapse and their length ($\delta_0 - \delta$) is added to the extra path, becoming:

$$\tau = \frac{[\delta] + [(\tau_0 - 1) * \delta_0 + (\delta_0 - \delta)]}{\delta} \quad (4.20)$$

To decide which equation to use for the tortuosity of a compressed membrane we need to look into the SEM pictures of the membrane (Figure 4.7)

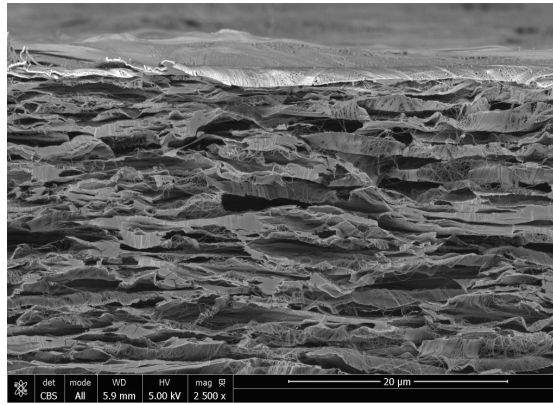


Figure 4.7: SEM cross-section micrograph of the membrane used in this study (uncompressed state).

The membrane has a layered structure with macropores between the layers with thickness of 1 to 2 μm , while the nominal pore size was measured to be 0.15 μm . During compression the distance between the layers will be decreased and the large macropores will be compressed, but not change their orientation. Hence, the extra path in the horizontal direction will remain the same, resembling the first case. Hence, eq. 4.19 is used to correct the tortuosity.

Membrane pore size As discussed in the part for tortuosity, the nominal size pores of 0.15 μm will remain with the same size while only the macropores will be compressed. This will not affect the permeability, since the macropores are much larger and are not limiting the mass transfer. Therefore, it was decided not to correct the pore size of the membrane as a function of pressure.

4.6 Results and discussion

4.6.1 Lab-scale model calibration

The results of the lab-scale calibration are presented as scatter plot in Figure 4.8.

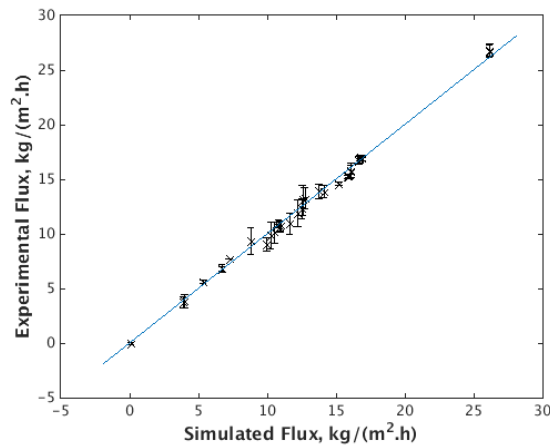


Figure 4.8: Lab-scale model calibration - simulated versus experimental flux. Error bars represent the difference between the measured flux based on the feed and permeate loops.

The experimental values for flux are taken as average between the calculated flux from the feed and the permeate tank weight balances and the error bars represent the difference between the feed and permeate fluxes as done in chapter 3. A large variety of experimental conditions was tested. The average feed and the permeate temperatures were ranged from 38 to 59 °C and 23 to 39 °C respectively. The empty channel velocity was ranged from 5 to 14 cm/s and the salinity was ranged from 0 to 24 wt % NaCl. Using only the tortuosity and the thermal conductivity of the membrane as calibration parameters, the average flux error was 0.06 kg/(m².h). R² values of 0.995 and 0.969 for the flux and the energy efficiency were achieved, respectively, suggesting very good agreement between the experiments and the model predictions over the entire range of conditions tested.

4.6.2 Full-scale experimental and modelling results

Experimental conditions and measured outputs

A design of experiments approach was performed in order to study the behavior of the full-scale installation. The conditions employed in the study as well as the measured outputs are given in Table 4.1.

Table 4.1: Experimental conditions and measured outputs on full-scale

$T_{f,in}, ^\circ\text{C}$	$T_{p,in}, ^\circ\text{C}$	Q, l/hr	Sal, g/l	$N_{exp}, \text{kg}/(\text{m}^2\text{h})$	P_{exp}, mbar	$T_{f,out}, ^\circ\text{C}$	$T_{p,out}, ^\circ\text{C}$
50.0	20.0	500	60	0.97	78	23.9	44.7
50.0	20.0	1000	60	2.03	255	25.4	43.0
50.0	20.0	1500	60	2.90	551	26.6	41.5
70.0	20.0	500	60	2.52	78	25.3	62.2
70.0	20.0	1000	60	4.69	255	27.3	59.2
70.0	20.0	1500	60	6.45	551	29.3	57.1
50.0	20.0	500	100	0.78	78	24.1	44.1
50.0	20.0	1000	100	1.24	255	25.5	42.6
50.1	20.0	1500	100	2.61	551	26.8	41.2
70.0	20.0	500	100	2.16	78	25.2	61.5
70.0	20.0	1000	100	4.30	255	27.6	58.9
68.6	20.0	1500	100	5.89	551	29.3	55.5
50.0	20.0	500	200	0.39	78	24.1	43.8
49.9	20.0	1000	200	1.32	255	26.0	42.0
50.0	20.0	1500	200	1.82	551	27.2	40.5
70.0	20.0	500	200	1.33	78	26.0	60.1
70.0	20.0	1000	200	3.50	255	28.2	57.6
69.5	20.0	1500	200	5.19	551	30.0	55.2

Three levels of salinity and flow rates were studied, while the feed temperature had only two levels and the permeate temperature was kept constant. All conditions exhibited positive fluxes ranging from 0.39 to 6.45 $\text{kg}/(\text{m}^2\text{h})$.

Pressure profiles along the module

In order to study the membrane compression, the pressures along the module were reconstructed as described in Section 4.5.3. The resulting pressure distribution along the channels for an example of 3 sections are presented in Figure 4.9.

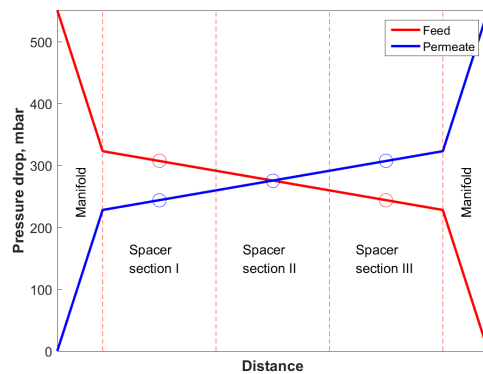


Figure 4.9: An example of the pressure profile along the module at 1500 l/hr. The markers represent the average pressure for each spacer section. Only three spacer sections are considered in this example. The distance on X axis is not to scale, since the length of the manifolds is unknown.

The pressure profiles of the feed and the permeate are inversed, since they are operated in counter current mode. The majority of the pressure drop is exhibited in the manifolds of the module, while the spacer pressure drop is about 20 % of the total, suggesting a margin for module design improvement in this particular case. The compression force exerted on the membrane is then the minimal of the feed and the permeate section pressures. For example if the average pressure for a feed section is 321 mbar and the average pressure for the corresponding permeate section is 230 mbar, the compression force on the membrane will be 230 mbar. The extra 91 mbar on the feed side will push the membrane towards the permeate channel, but will not compress it. When the membrane is pushed through the spacer openings, it will be stretched, however the stretching effect is not modelled in this chapter.

Membrane compaction as a function of pressure

The measurement of the membrane thickness as a function of pressure is given in Figure 4.10.

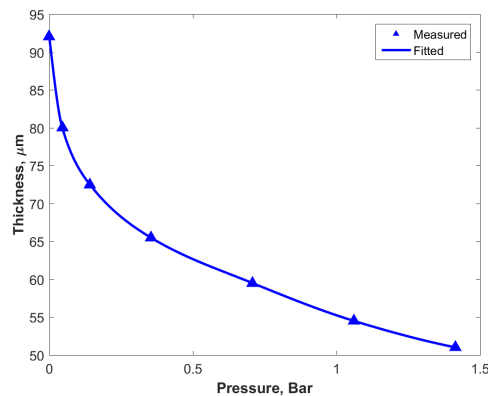


Figure 4.10: Measured membrane thickness as a function of pressure

The first point in the figure is in fact the SEM measurement of the uncompressed membrane sample at $92 \mu\text{m}$. As can be seen the membrane compresses quite significantly. The membrane compacts with 30 percent in the operational pressure regime of the module (up to 300 mbar), therefore this effect cannot be neglected. This measurement suggests that the layered structure of the membrane is quite weak in the short transverse (through) direction. For example, the thickness of the UF membranes studied by Persson et al. [143] is reduced by less than 10 % at 1 bar. However Zhang et al. [137] found similar compaction as a function of pressure for the stretched PTFE membrane with 22 % thickness reduction at 0.3 bar, while the phase inverted hollow membrane in their study was virtually non-compressible in the tested range up to 0.7 bar. This demonstrates that stretching can produce mechanically weak membranes in terms of compaction, since both the stretched PTFE membrane studied by Zhang et al. [137] and the stretched PE membrane studied in this work are prone to compaction.

Effect of membrane compaction

In order to study the effect of membrane compaction the local heat transfer coefficient of the membrane and permeability were recalculated as a function of applied pressure as shown in Figure 4.11.

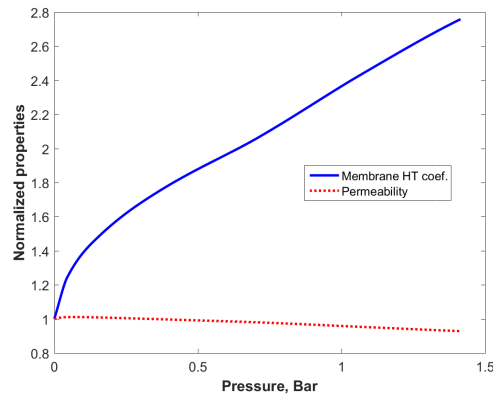


Figure 4.11: Modelled normalized local heat transfer (HT) coefficient of the membrane and permeability as a function of pressure

The normalized local heat transfer coefficient can be calculated as $h_m/h_{m,0}$ (eq. 9.15). The thermal conductivity sharply increases as a function of pressure. This is expected since the decreased porosity of the compacted membrane increases the thermal conductivity κ_m (eq. 9.14), while the decreased membrane thickness further increases the heat transfer through the membrane (eq. 9.15). The predicted value of the thermal conductivity has a complex shape, because it is a function of the highly non-linear compaction behavior of the membrane as a function of pressure (Figure 4.10).

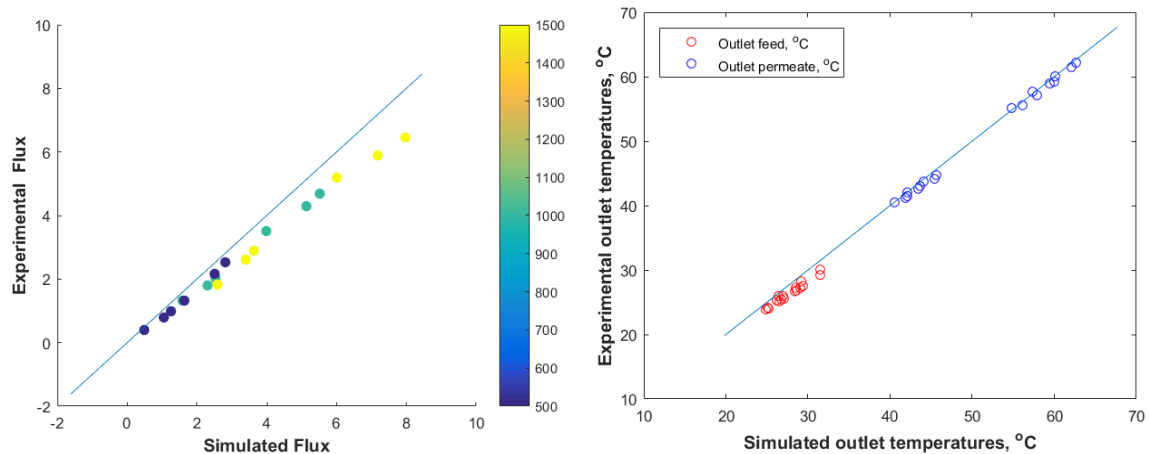
For depicting the normalized membrane permeability a simplification is taken. In the ordinary (molecular) diffusion the permeability is proportional to $\frac{\epsilon}{\tau\delta}$, whereas in the Knudsen regime it is proportional to $\frac{\epsilon R_p}{\tau\delta}$ [26]. Earlier we assumed that the macropores will collapse first and this will not affect the nominal pore size, therefore R_p will remain constant. This allows to calculate the normalized permeability for the Knudsen-molecular transition regime as $\frac{\epsilon}{\tau\delta} / \frac{\epsilon_0}{\tau_0\delta_0}$. This simplification is used only to depict the membrane permeability as a function of pressure (Figure 4.11). In the model, the membrane permeability is simply recalculated with the compacted properties obtained in Section 4.6.2. As can be seen in Figure 4.11, the permeability remains within 3 % of its original value in the operational range of the module and will not strongly affect the flux calculations. The effect of a slight membrane permeability increase, followed by a permeability decrease as a function of compaction is also described by Lawson et al. [74], although in their work a decrease in the pore size was also considered, which made the permeability decrease much more significant at high pressures. At the mild pressures exhibited in this module and in membrane distillation in general, the assumption that the pore size

remains constant probably holds true, however if one is to operate it at much higher pressures, the pore size might be reduced. The pressure drop modelling in this chapter, combined with the stress-strain measurements of various membranes performed in the PhD thesis of Lies Eykens [142] can be used to model this phenomenon in the future. The membrane deflection can be calculated and incorporated into the model in terms of channel thickness correction.

Full-scale model validation

The model is validated with and without the membrane compaction effects in order to show the importance of the membrane compaction modelling. These effects are incorporated both in the lab-scale calibration procedure as well as in the full-scale modelling.

Model results without considering membrane compaction When the model is not correcting for membrane compaction effects, the simulated fluxes are overestimating the experimental ones (Figure 4.12a). The prediction of the outlet temperatures is quite good (Figure 4.12b), meaning that the model predicts well how much energy is exchanged in total.



(a) Simulated versus experimental fluxes. Colorbar represents the flow rate of the experiment in l/hr. $R^2=0.884$.

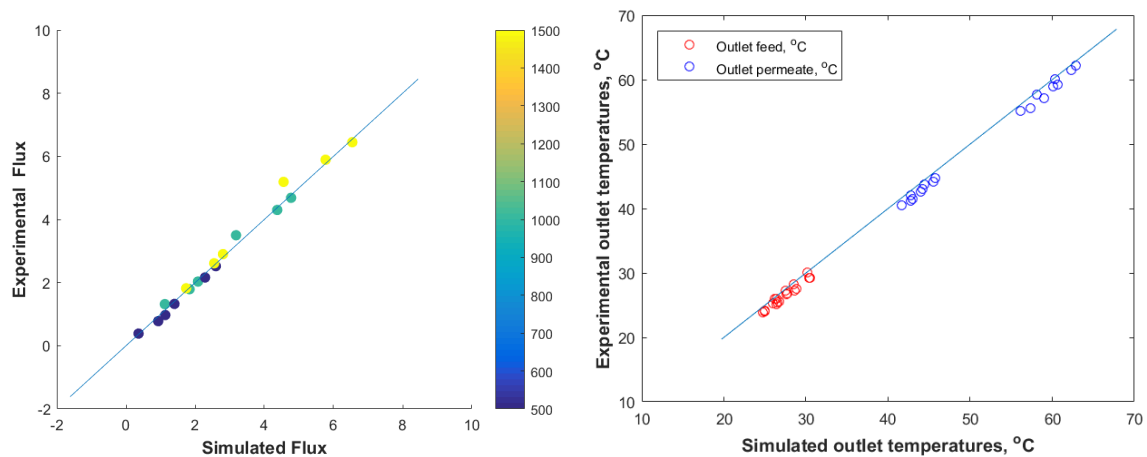
(b) Simulated versus experimental module outlet temperatures. $R^2=0.993$.

Figure 4.12: Simulated versus experimental module flux and outlet temperatures. Without membrane compaction effects included in the model.

It is noteworthy that the fluxes at the lowest flow rates are well predicted and only the fluxes at high flow rates are overestimated. It is therefore possible that the mismatch is due to compaction effects that would be more pronounced at high flow rates and thus high pressure drops along the channels.

The energy can be exchanged in two ways through the membrane - as flux energy or as sensible heat losses through the membrane. The total energy exchange is predicted well, but the flux is overestimated, suggesting that the parasitic losses through the membrane are underestimated, leaving more energy to be exchanged as flux, thus overestimating the flux prediction.

Model results including membrane compaction The model validation when the membrane compaction effects are taken into account can be seen in Figure 4.13.



(a) Simulated versus experimental fluxes. $R^2=0.986$. (b) Simulated versus experimental module outlet temperatures. $R^2=0.994$.

Figure 4.13: Simulated versus experimental module flux and outlet temperatures. With membrane compaction effects included in the model.

The prediction of the outlet temperatures is slightly improved. However, by including the compaction effects the fit for the flux is increased significantly with $R^2=0.986$. As shown in Section 4.6.2 the compaction effects do not strongly affect the membrane permeability, however, the local heat transfer coefficient of the membrane can be increased as much as 1.7 times as a function of pressure in the operational range of the module (Figure 4.11). The influence of the thermal conductivity of the membrane is quite significant at full-scale, since unlike lab-scale experiments, almost all of the energy that is flowing into the

module is exchanged through the membrane. Therefore, if less energy is exchanged due to sensible heat losses, the saved energy can be utilized for evaporation and, hence, increase the observed flux.

To further study how the membrane compaction affects the process, the powers exchanged along the membrane are plotted in Figure 4.14:

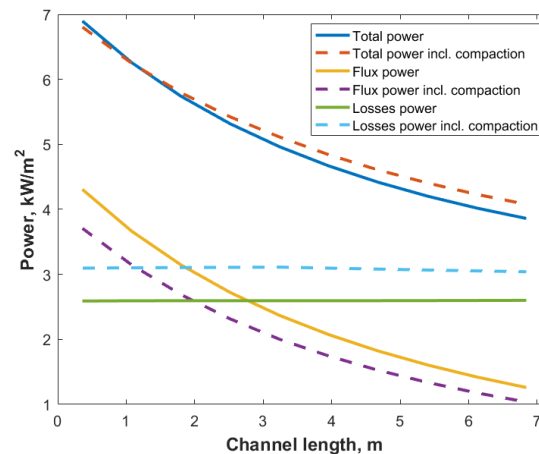


Figure 4.14: The power exchanged due to flux (latent heat of evaporation) and due to thermal losses through the polymer matrix of the membrane are plotted along the channel length. The feed and the permeate inlet temperature are set at 60 and 20 °, respectively, while the salinity and the recirculation velocity are set to 60 g/l and 1000 l/hr.

The thermal losses are nearly constant while the power exchanged due to flux decays along the channel length. The thermal losses are driven by the temperature difference across the membrane, which is almost constant, while the flux is driven by the vapor pressure of water, which is an exponential function of the temperature (eq. 2.22). As seen in Figure 4.14, the total energy exchanged along the channel is almost the same in both cases, which is also the reason why simulation of the membrane compression has little effect on the outlet temperatures of the module and only the ratio of power exchanged due to flux and losses changes.

It is noteworthy that the majority of the commercially available MD modules today utilize stretched membranes produced from PE or PTFE [6,144]. While the PTFE membranes were already proven to compact in the operational pressure relevant to MD [36,137], this study reveals the same for the PE membranes, therefore membrane compaction cannot be neglected when modelling.

4.6.3 *Influence of number of sections in which the model is discretized*

In order to study how many sections are needed in order to properly discretize the model the number of sections was changed and the validation for flux and outlet temperatures was performed (Table 4.2).

Table 4.2: Influence of the number of sections in which the model was discretized

Sections	1	2	3	4	5	6	7	8	9	10
R^2 Flux	0.987	0.985	0.986	0.986	0.986	0.986	0.986	0.986	0.986	0.986
$R^2 T_{out}$	0.993	0.993	0.993	0.993	0.993	0.993	0.993	0.993	0.994	0.994

The fit of the model does not change significantly if the model is discretized in 3 sections or more. Similarly, the fit for the outlet temperatures is almost not influenced by the number of sections in which the model is discretized. The temperature distribution along the length of the module is almost linear, which explains why a even a low number of sections results in a model that predicts the system well. Discretizing the model in great number of sections increases the computational time, since the flux needs to be calculated in each section. Therefore, the default number of sections is taken as 5.

4.6.4 *Module optimization based on the validated model*

In order to estimate which parameter of the system is most limiting for the flux, a variance-based Global Sensitivity Analysis (GSA) study was performed. A total of 10 000 samples were taken, using Sobol sampling and the design proposed by Saltelli et al. [127]. Further explanation of the method and its application is available in Mortier et al. [128]. The parameters used in the global

sensitivity analysis and how they affect the model can be seen below:

$$\tau = \tau_0 C1; \quad (4.21)$$

$$\kappa_m = \kappa_{m,0} C2 \quad (4.22)$$

$$Nu_{f,p} = Nu_{f,p,0} C3 \quad (4.23)$$

$$Sh = Sh_0 C4 \quad (4.24)$$

$$Q_{f,p} = Q_{f,p,0} C5 \quad (4.25)$$

$$Re_{f,p} = \frac{(v_{ch}/\epsilon_s) D_{ch} \rho}{\mu C5} \quad (4.26)$$

All parameters C1 through C5 are varied in the range of $\pm 20\%$. Parameter C1 alters the membrane tortuosity and hence the overall membrane permeability. Parameter C2 alters the thermal conductivity of the membrane and hence the losses through the polymer. Parameters C3 and C4 modify the Nusselt and Sherwood equations which boils down to linearly altering the heat and mass transfer coefficients, respectively. The last coefficient C5 alters the flow rates of the channels. However, it is also included in the denominator of the Reynolds equation. In this way the coefficient influences how much energy is flown in the channels, but will not affect the hydrodynamics. For example, a 20% higher flow rate will result in a 20% increased channel velocity, which will be counteracted by placing the parameter C5 in the denominator of the Reynolds equation, thus the hydrodynamic conditions will remain constant in the model. The results of the GSA are provided in Table 4.3.

Table 4.3: Total effect indices calculated from the global sensitivity analysis

Inflow Energy	Membrane permeability	Membrane thermal conductivity	Thermal con-polarization	Concentration polarization
0.579	0.215	0.209	0.002	0

The GSA was performed at 60 and 20 °C inflow temperatures of the feed and permeate respectively, a flow rate of 1000 l/hr and 100 g/l salinity. The flux was taken as output parameter. The study reveals that at full-scale the module flux is severely limited by the inflow energy. This also explains why the thermal conductivity has the same importance on full-scale as the membrane permeability. If a fraction of the inflow energy can be saved by having a membrane with lower thermal conductivity, this energy can be utilized to evaporate

more water and increase the flux. As a result, in this particular case the flux will be increased by employing a membrane with 20 % lower thermal conductivity, just as much as it would with a membrane which is 20 % more permeable. What is interesting to notice is that the heat and mass transfer coefficients have minimal effect on flux on full-scale. This can be explained by the relatively low flux at full-scale, which is the major driving force for the thermal polarization and the only driving force for the concentration polarization. Therefore, a full-scale MD module will not benefit greatly from a spacer with improved mixing. A better direction is to use a spacer with a lower pressure drop which will compact the membrane less and reduce the risk of membrane wetting. In order to study the influence of pressure on the flux, a model-based scenario analysis was performed. Results are shown in Figure 4.15.

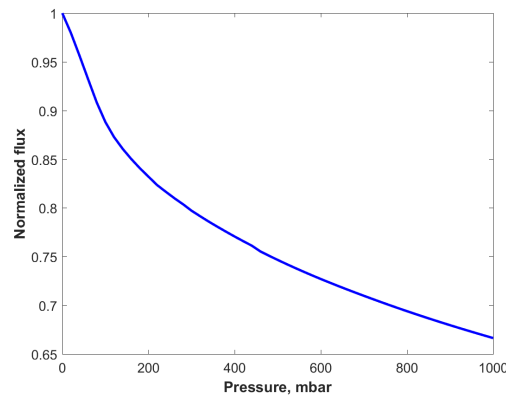


Figure 4.15: Normalized flux as a function of pressure performed at 60 and 20 °C inflow temperatures of the feed and permeate respectively, flow rate of 1000 l/hr and 100 g/l salinity.

The figure clearly reveals that the pressure has a negative impact on the flux for this particular membrane. The model predicts that the performance of the module can be vastly improved, if the membrane would be incompressible, or if the manifolds of the module can be improved, since they are the biggest source of pressure drop in the module (see Figure 4.9).

4.7 Conclusions

In this chapter the effect of membrane compaction is modelled and validated on a full-scale for the first time, using a commercially available module.

Moreover, a methodology for scaling up of a direct contact membrane distillation model from lab-scale to full-scale was demonstrated without the need of additional calibration of the full-scale model. This underlines that when the lab-scale calibration is performed properly, the model can be scaled-up with confidence, since all of the resistances in the system are identified correctly. By having such model, a sensitivity analysis was performed on the system and the influence of all major resistances was evaluated. The full-scale module flux is severely limited by the inflow energy and would benefit from a membrane with lower thermal conductivity just as much as a more permeable membrane. Because of the limited inflow energy, the influence of the thermal and concentration polarization is minimal.

It was demonstrated that the membrane used in the module compacts significantly, even though the operational pressures can be considered mild. The membrane compaction mainly increased the thermal conductivity of the membrane, while the permeability was almost unaltered within the tested range. When the model was extended to account for the membrane compaction, values of $R^2=0.99$ for both the flux and the outlet temperatures were achieved. All of the commercially available MD modules used today utilize PTFE or PE membranes that are produced by stretching. Previous papers have demonstrated the compressibility of the stretched PTFE membranes, while the current work reveals the same for the stretched PE membrane. Therefore, this effect should not be further neglected in MD modelling.

Acknowledgment

The authors would like to express their deepest gratitude towards Mr. Ko Schaap from Benelux Scientific B.V. (The Netherlands) for performing the measurement of the membrane thickness as a function of pressure.

The authors would also like to thank Aquastill for providing the membrane and spacer samples from the module.

CHAPTER 5

Full-scale validated Air Gap Membrane Distillation (AGMD) model without calibration parameters

Redrafted from: I. Hitsov, K. De Sitter, C. Dotremont, P. Cauwenberg, I. Nopens, 2017. Full-scale validated Air Gap Membrane Distillation (AGMD) model without calibration parameters, *Journal of Membrane Science* (533), p. 309-320

Abstract

Air gap membrane distillation (AGMD) is one of the most widely discussed membrane distillation configurations at the moment and has been regarded as more thermally efficient than direct contact membrane distillation (DCMD), due to the insulation properties of the air gap. Several AGMD models are available in the literature. However, most of the models developed to date are either missing validation or are only validated at lab-scale. A major hurdle in modelling membrane distillation is the lack of information about the condensation that is occurring inside the gap. Often, major parameters such as the average condensate thickness are taken from semi-empirical formulas or are simply estimated based on educated guesses. Moreover, some studies had shown that at certain conditions the gap can be completely flooded with condensate, which raises the question whether the module can be modelled as air gap altogether. In this study, a previously developed and thoroughly validated DCMD model is extended by adding the air gap compartment. In this way the

model only needs to be adjusted for the gap-related parameters. A simple technique is demonstrated for observing the condensation in real time, which also allows to experimentally obtain the value of the average condensate thickness parameter and the flooding of the gap. The model is subsequently thoroughly and simultaneously validated with experimental data from two commercially available modules with areas of 7.2 and 24 m², showing an excellent fit to the experimental data. Moreover, this work shows a direct comparison between AGMD and DCMD in terms of flux and thermal efficiency at full-scale using modules with identical geometries from the same manufacturer.

5.1 Introduction

Membrane distillation can be performed in various configurations [56]. The two most widely discussed configurations in the literature are the direct contact (DCMD) and the air gap (AGMD) configurations [144] - Figure 5.1.

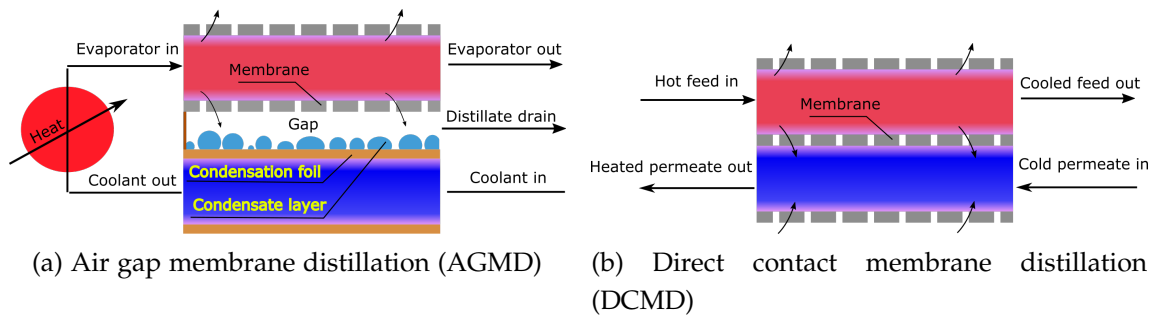


Figure 5.1: Direct contact and air gap membrane distillation configurations.

In AGMD (Figure 5.1a), a gap is present between the membrane and the coolant compartment, filled with air. This gap provides thermal insulation between the hot and the cold compartments, reducing the thermal losses through the membrane matrix. On the other hand the air gap is also a mass transfer resistance, since the water vapor needs to diffuse through the gap before condensing on a condensation foil that separates the gap from mixing with the coolant channel. In lab scale tests the air gap configuration shows clearly a much lower flux, compared to the DCMD configuration (Figure 5.1b) and a lower flux than the permeate gap configurations where the gap is completely filled with condensate [145]. However, a direct comparison between direct contact and air gap configurations at full-scale is currently missing. In this work, for the first time in the literature a DCMD module is compared directly with an AGMD module from the same manufacturer and the same geometry at identical conditions in terms of flux and gained output ratios (GORs).

In order to fully understand the process and its current bottlenecks, a mathematical model is built. Two air gap modules manufactured by Aquastill, B.V. (Sittard, The Netherlands) are used for validation in this study with areas of 7.2 m² and a 24 m². The structure of the previously developed DCMD model can be reused, since the flow spacers and the membrane are identical. However, the model had to be extended in order to model the heat and mass transfer inside the gap. The gap was considered as partially flooded, which is the only model to date to account for the gap flooding phenomenon. This means that

two models are solved simultaneously for the gap region - one where the condensate layer has a certain thickness on the condenser wall and one where the condensate has completely saturated the gap, effectively making it a permeate gap membrane distillation (PGMD). This model structure leads to the complication that two parameters are practically unknown - the average condensate thickness of the "dry" part of the gap and the fraction of the gap that is completely flooded. Previous attempts have tried to use semi-empirical models to estimate the thickness of the condensate layer [146,147], but experimental validation of this approach is currently missing. However, when the flooding fraction of the gap is regarded, there are neither experimental studies, nor theoretical models to describe the phenomenon. One can try to fit both parameters of the model in order to achieve a good fit to experimental data, however, as shown in previous work [139] sometimes the parameters can interact with one another and different combinations can lead to the same quality of fit (i.e. the parameters are not uniquely identifiable). If completely different combinations of parameters lead to the same quality of fit, the model cannot be used to study the importance of these parameters, since their exact value is unknown and the model would have a low predictive power.

5.2 Materials and Methods

5.2.1 *Full-scale membrane distillation setup*

The setup used to test the DCMD module in our previous work was now modified to accommodate AGMD modules. The system, supplied by Aquastill, was rerouted to use only the former feed side of the DCMD system (Figure 5.2).

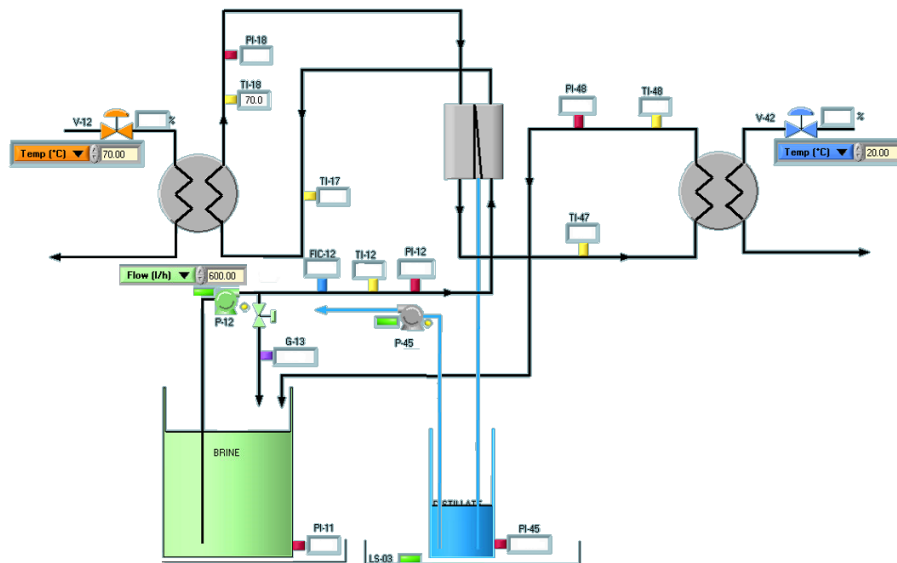


Figure 5.2: Schematic representation of the full-scale air gap system used in this study

The flow starts from the brine tank, goes through the coolant compartment of the DCMD module, gets additionally heated by a heat exchanger, after which it enters the evaporator compartment of the AGMD module. After leaving the module, the fluid is cooled by another heat exchanger and returns to the brine tank. The distillate is collected at the bottom of the module, driven by gravity and enters the distillate tank. When the distillate reaches a certain level it is pumped back into the brine tank, in order to keep the brine concentration constant over time. The flux can be calculated based on the time derivative of the hydrostatic pressure in the distillate tank. Further description of the system and the equipment is available elsewhere [148].

Two air gap modules supplied by Aquastill were tested in this work. The modules have a coolant and evaporator channel thickness of 2 mm, a module height of 0.4 m, a 92 μm thick polyethylene (PE) membrane and an air gap compartment of 0.8 mm, drained at the bottom side of the module. The condensing foil is a non-transparent polyethylene terephthalate (PET) film with thickness of 42 μm . The gap spacer is made from polypropylene, is 0.8 mm thick and has an 84 percent porosity, measured by submerging the spacer in water and measuring the volume of displaced water. The spacers in the evaporator and coolant channels are made of PET, have a thickness of 2 mm and porosity of 86 %, similarly measured by the water volume displacement method.

Both modules are spiral wound and have 6 hot and 6 cold parallel channels operated counter-currently. The larger module has a channel length of 5 m ,

while the smaller has a channel length of 1.5 m. The membrane areas are 24 m² and 7.2 m², respectively.

5.2.2 Setup for measurement of the condensate layer thickness

In order to visually observe the condensation inside the air gap a simple setup was constructed - Figure 5.3.

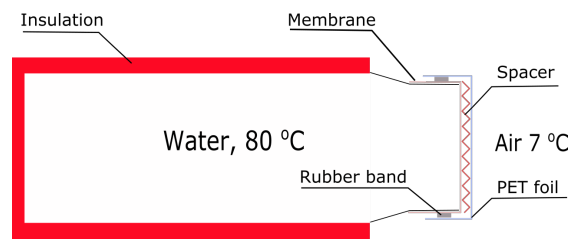


Figure 5.3: Schematic cross section of the smaller scale AGMD setup used for measuring the average condensate layer thickness

An insulated water bottle with an outlet diameter of 45 mm was filled with hot water (80 °C) and covered with a membrane. The membrane is then secured with a rubber band to prevent leakage and covered with a spacer, followed by a PET foil. Since the original condensation foil in the module is non-transparent a different, transparent PET foil was used. The contact angles of the original and the substitute foils were measured. The non-transparent PET foil used by Aquastill has a contact angle of $78.0^{\circ} \pm 0.8$, while the substitute PET foil has a $78.4^{\circ} \pm 0.8$, measured with OCA 15EC contact angle system of dataphysics (Filderstadt, Germany), using the static sessile drop method [138, 149]. The setup is then placed inside a refrigerator at a temperature of 7 °C, in such a way that the gap is vertical, similar to the full-scale case. The water evaporates on the vessel-side of the membrane, the vapors travel through the membrane and the gap spacer and then condense at the inner side of the condensing foil and continuously drain freely to the bottom. Pictures were taken using a Canon EOS 600D DSLR camera after equilibrating the system for at least 45 minutes. After each test the water mass inside the gap was weighed using an analytical balance (Mettler toledo AB204-S).

5.2.3 Setup for measurement of the gap flooding

In order to measure the fraction of the gap that is completely flooded a larger-scale setup was built from a PVC tube with diameter of 12.5 cm and total height of 50 cm. A membrane port was cut with dimensions of 10 cm width and 40 cm height, and a mesh was placed under the membrane for support. The membrane was sealed to the vessel with a water-resistant double sided tape. The gap spacer was placed on top of the membrane, followed by the clear PET foil discussed in the previous section. The assembly is pressed to the vessel by a PVC face plate, reinforced by aluminium profiles and secured with zip-ties. The setup can be seen in Figure 5.4.

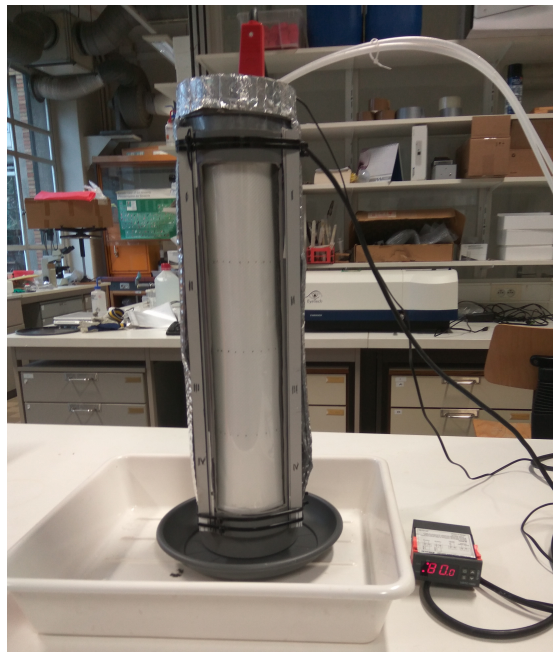


Figure 5.4: Gap flooding experiments using the larger-scale setup

A temperature-controlled immersion heater with nominal power of 1.5 kW is placed on the top side of the vessel. An external pump (Watson Marlow 505u) was used to circulate the water inside the vessel, ensuring good mixing. The vessel is then insulated with mylar-laminated bubble wrap, to prevent significant losses to the environment. The water inside the vessel can be heated to a maximum of 80 °C and a 40 W cooling fan is directed towards the air-gap in some of the experiments in order to intensify the flux. An excellent seal was achieved, which allowed to collect the distillate over a known time and, hence, measure the flux. Pictures of the flooding inside the gap were taken using

Canon EOS 600D DSLR camera after equilibrating the system for at least one hour.

5.3 Air gap model structure

5.3.1 *Model calibration at lab-scale*

The only calibration parameters in the model are membrane and channel spacer specific. However, these calibration parameters have already been obtained at lab-scale MD module as explained in previous work [139]. The flow channel spacer related parameters in both the Nu and Sh equations are obtained by replacing the membrane in the lab-scale setup by an aluminium foil (hence, the system becomes a heat exchanger), performing a number of heat transfer experiments at different flow rates and calibrating the parameters a and b in the Nusselt equation [139] in order to match the experimental heat transfer coefficients. Subsequently, the Chilton-Colburn analogy between heat and mass transfer is used to construct a Sh equation [111], which is responsible for the concentration polarization.

The membrane related parameters are also obtained at lab-scale by performing lab-scale experiments and calibrating the membrane tortuosity and thermal conductivity in order to match the experimental flux and energy efficiency [139]. The described calibration procedure can be performed to characterize another system which uses another membrane or flow spacer.

5.3.2 *Module discretization and solution method*

In order to clearly visualize the structure of the model and its solution, a step-wise diagram is provided (Figure 5.5).

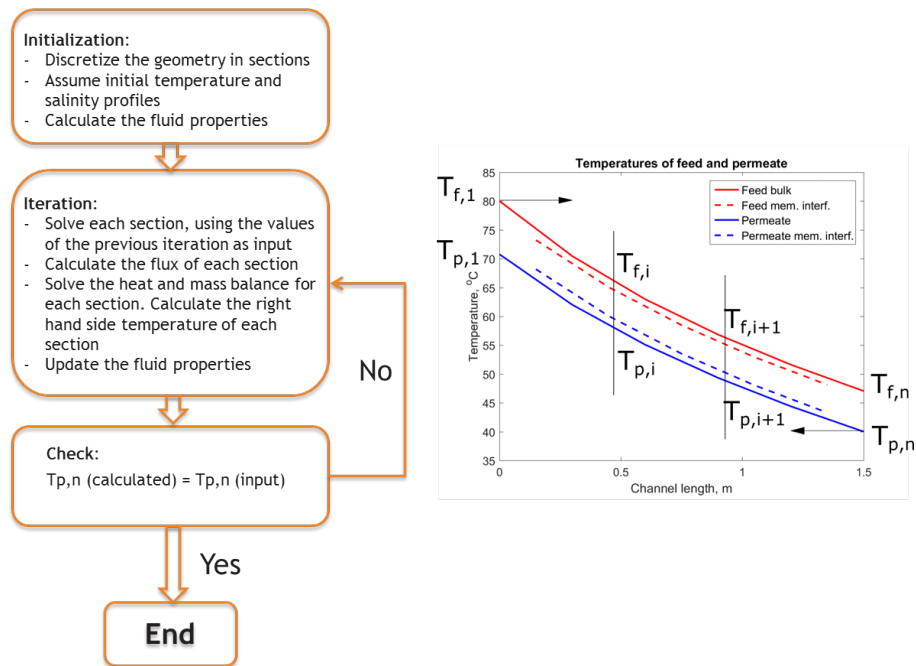


Figure 5.5: Solution diagram of the model (left) and the discretization of a single channel (right).

The model is solved iteratively from left to right. Initially, the model is discretized and initial values for the fluid temperature and properties are assumed. In every following iteration, the values obtained from the previous iteration are used as input for the heat and mass balances. The solution is considered converged, once the calculated permeate inlet temperature is predicted to be within 0.01 degrees of the temperature input by the user. The module is split into five virtual sections, for which the heat and mass transfer equations (Appendix A) are solved (Figure 5.6).

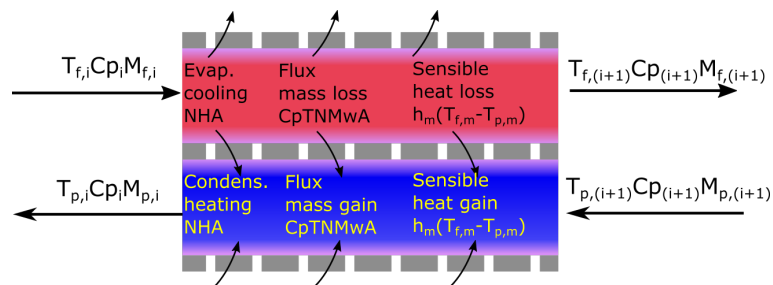


Figure 5.6: Heat transfer balance components for each section

The heat balance for each section is similar to the one for DCMD, with the exception that the cold channel is separated by an impermeable foil. Therefore

the mass flow rate M_c in each section is constant and the term for flux mass gain is removed. The right hand side temperatures of the evaporator ($T_{(e,i+1)}$) and coolant ($T_{(c,i+1)}$) channels for each of the sections can now be expressed as:

$$T_{e,(i+1)} = \frac{T_{e,i}Cp_{e,i}M_{e,i} - NHA - CpTNM\tau wA - h_m A(T_{m,e} - T_{m,c})}{M_{(e,i+1)}Cp_{(e,i+1)}} \quad (5.1)$$

$$T_{c,(i+1)} = \frac{T_{c,i}Cp_{c,i}M_c - NHA - h_m A(T_{m,e} - T_{m,c})}{M_c Cp_{c,(i+1)}} \quad (5.2)$$

The symbols Cp , N , H , A , Mw and h stand for specific heat capacity, flux, specific heat of evaporation, area, molecular weight and local heat transfer coefficient, respectively. The subscripts e, c, m and i represent the evaporation channel, coolant channel, membrane and section number, respectively. When a section number is missing, the average value for the section is used. The more common equations, used in the model, can be found in Appendix 9.3.

The equation predicting the mass flow rate ($M_{e,(i+1)}$) and salinity ($C_{NaCl,(i+1)}$) in the evaporator channel can be expressed as:

$$M_{e,(i+1)} = M_{e,i} - ANMw \quad (5.3)$$

$$C_{NaCl,(i+1)} = \frac{100M_{NaCl}}{M_{e,(i+1)}} \quad (5.4)$$

The mass flow rate and therefore salinity in the cold channel remain constant at their user defined values.

5.3.3 Heat and mass transfer in each section of the model

The temperature polarization inside the channels of the module was simulated using a Nusselt equation. To model the concentration polarization, a Sherwood equation was adopted. The coefficients a and b in the Nusselt and Sherwood equations (eq. 9.29 and 9.33) were reused from our previous work [148], since the channel spacers are the same in both modules.

5.3.4 Heat and mass transfer inside the membrane and the gap

Heat transfer inside the gap

The thermal conductivity of the membrane κ_m was calculated using the Maxwell's lower bound equation [40] (eq. 9.37). As shown in previous work [139], the models that calculate the thermal conductivity of the membrane cannot predict the exact value of the thermal conductivity, since they are developed for an idealized membrane structure. Moreover, the thermal conductivity of the base polymer is rarely known as an exact value, since it can change with the polymer orientation and manufacturing process. Therefore, the calibrated value of the thermal conductivity of the membrane was taken from a previous work [139].

In order to calculate the interfacial temperatures, a heat balance is solved for each layer of the system in Figure 5.6 for the case where the gap is not flooded, assuming a steady state system:

$$\begin{aligned}
 \underbrace{h_e(T_{b,e} - T_{m,e})}_{(1)} &= \underbrace{NH_v}_{(2)} + \underbrace{h_m(T_{m,e} - T_{m,g})}_{(3)} = \underbrace{NH_v}_{(2)} + \underbrace{h_{g,air}(T_{m,g} - T_{cond})}_{(4)} = \\
 &= \underbrace{h_{g,cond}(T_{cond} - T_{foil,g})}_{(5)} = \underbrace{h_{foil}(T_{foil,g} - T_{foil,c})}_{(6)} = \underbrace{h_c(T_{foil,c} - T_{b,c})}_{(7)}
 \end{aligned} \tag{5.5}$$

Where, the components 1 through 7 denote the heat flux in the evaporator channel boundary layer (1), the heat flux carried with water vapors (2), the sensible heat fluxes in the membrane (3), the gap air layer (4), the gap condensate layer (5) and the condensing foil (6). The last component is the heat flux in the coolant channel boundary layer (7). The subscripts b, e, m, c, g, cond and foil represent the bulk, evaporator, membrane, coolant, gap, condensate and foil temperatures, respectively. The same system of equations is built for the case where the gap is completely flooded, however in this case the "Gap, air" component of equation 5.5 vanishes. In order to explicitly solve equation 5.5 for the interfacial temperatures for the gap and the membrane, the *solve* function of Matlab was used, treating equation 5.5 as a system of equations, where each equality term is equal to the next. The resulting equations are not shown, since they are extremely large and can easily be replicated.

Mass transfer inside the membrane and the gap

The interfacial temperatures in the gap and the membrane need to be transformed to vapor pressure, accounting for the vapor pressure reduction on the feed side of the membrane caused by salinity, using equations 9.43 and 9.45.

The membrane used in this study has a pore radius of $0.15 \mu m$ and therefore the vapor transport is governed by both Knudsen and molecular diffusion [148]. In this work we are using the Dusty Gas model corrected for the Knudsen number of the membrane, proposed by Field et al. [75], (equation 9.53). The equation, together with the calibration for the tortuosity is reused from a previous work [139] and is divided by the water vapor pressure difference across the membrane ($p_{m,e} - p_{m,g}$) in order to obtain the permeability of the membrane B_{mem} .

The permeability of the air-filled part of the gap (B_{gap}) was calculated by dividing the flux equation for molecular diffusion (equation 9.55) by the water vapor pressure difference across the gap ($p_{m,g} - p_{cond}$). The resistance in series [150] approach can then be used in order to calculate the overall membrane and gap permeability for the non-flooded parts of the module (B_{non-fl}) - equation 5.6.

$$B_{non-fl} = \frac{1}{\frac{1}{B_{mem}} + \frac{1}{B_{gap}}} \quad (5.6)$$

The fluxes in the flooded (N_{fl}) and non-flooded (N_{non-fl}) areas of the module can be calculated by multiplying the permeability with the driving force

$$N_{fl} = B_{mem}(p_{m,e} - p_{m,g}) \quad (5.7)$$

$$N_{non-fl} = B_{non-fl}(p_{m,e} - p_{cond}) \quad (5.8)$$

In order to find the average flux for the flooded and the non-flooded parts of the module, the flux model is solved two times for both cases for each section. The average flux (N_{av}) for each section can now be averaged for each section, weighing the degree of flooding (X) using the following equation

$$N_{av} = N_{fl}X + (1 - X)N_{non-fl} \quad (5.9)$$

The degree of flooding X , ranging from 0 to 1, represents the fraction of the gap, flooded with water.

5.4 Results and discussion

5.4.1 Air-gap condensation

The small scale air gap condensation experiments with the insulated flask placed inside a refrigerator were performed two times. A representative picture can be seen in Figure 5.7.

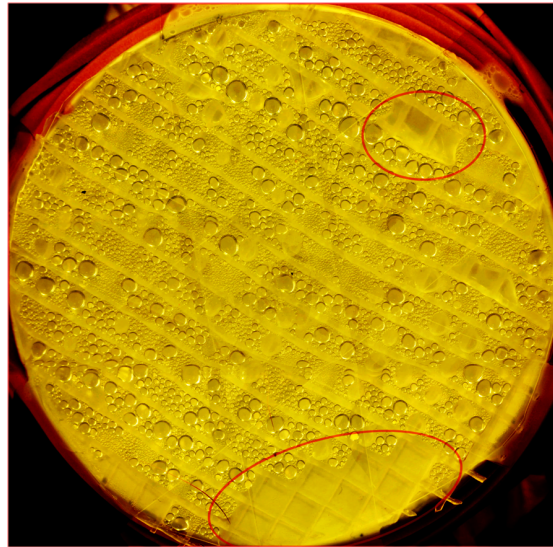


Figure 5.7: Small scale condensation experiments used to measure the average thickness of the condensate layer thickness, the wetted areas are circled in red. Video of the experiment can be seen at <http://bit.ly/2gppI0A>

It should be noted that some parts of the spacer was already flooded (circled in red in Figure 5.7). The flooded area (A_{fl}) was measured using the freeware software *ImageJ*, in order to exclude it from the total area of the sample. The average condensate layer thickness δ_{cond} can be derived using the following equations.

$$A = A_{tot} - A_{fl} \quad (5.10)$$

$$V_{gap} = A\delta_{gap}\epsilon_s \quad (5.11)$$

$$V_{fl} = A_{fl}\delta_{gap}\epsilon_s \quad (5.12)$$

$$V_{gap,meas} = A_{tot}\delta_{gap}\epsilon_s \quad (5.13)$$

$$\delta_{cond} = \frac{V_{gap,meas} - V_{fl}}{\epsilon_s A} \quad (5.14)$$

Where A is the non-flooded area, A_{tot} is the total area of the sample, A_{fl} is the flooded area, V_{fl} is the volume of water in the flooded area of the sample, ϵ_s is the gap spacer porosity, $V_{gap,meas}$ is the total volume of water measured inside the gap and δ_{gap} is the thickness of the gap. The condensate layer thickness can then be found by dividing the volume of water inside the gap by the area of the gap, while accounting for the spacer porosity. The resulting condensate layer thickness is $143.5 \pm 6.2 \mu m$, which is the first unknown gap-related parameter in the model.

The average condensate layer thickness appears not to be a strong function of the flux, which contradicts the semi-empirical formulas used in previous air gap modelling [146, 147], where the condensate layer thickness is directly proportional to the flux. In fact, the opposite trend was noticed - at higher fluxes the average droplet size of the non-flooded gap areas appeared smaller. When the droplets reach a certain size, they either form a wetted area of the gap or drain to the bottom, agglomerating with other droplets during draining in an avalanche fashion and releasing a new space for condensation. However the condensate droplets in the previously-flooded areas start from the smallest size, thus reducing the average thickness of the condensate layer. Therefore, although the method demonstrated in this article appears to perform satisfactory, it can probably be further improved in the future by measuring the condensate layer thickness as a function of the flux.

5.4.2 Measurement of gap flooding

In order to experimentally derive the value of the second gap-related parameter the larger-scale setup was used as described in Section 5.2.3 (Figure 5.4). After equilibration for at least 30 min, the condensate was collected at the bottom of the vessel over at least 1 hr and the flux was calculated. The flooding was measured by splitting the air gap area into 4 equal vertical sections and taking a picture for each section. The fraction of the flooded area is measured using *ImageJ* by manually selecting the flooded regions and is then averaged for the whole module (Figure 5.8).

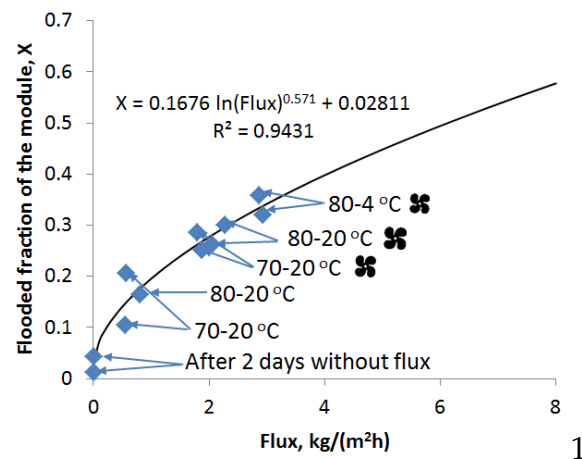


Figure 5.8: Flooded fraction measured as a function of flux at different conditions.

As seen in the figure, the flooding is clearly a function of the flux. In order to intensify the process some of the conditions were performed with a fan directed to the condensation foil. To further intensify the flux two of the experiments were performed in a cold storage room at 4 °C.

To test if the flooding is reversible, some of the experiments were done in a reverse order of the flux, from high flux conditions to lower flux conditions (Figure 5.8). The system was found to be completely reversible. This can be visually confirmed from the movie of the process, the wetted areas shift dynamically from one place to another and droplet condensation starts to occur in place of the previously wetted area. In fact, if the vessel is left full of water, but without heating the flooding almost completely disappears. It should be noted that in this case the flooding does not clear up due to evaporation, since the water in the vessel keeps the air inside the gap saturated with water vapors. The gap remains full of condensate droplets on the foil, but the flooding disappears.

In order to include the flooding parameter in the model a function can be fitted through the experimental data. A polynomial function fits the data well and levels off to a realistic value when extrapolated. The extrapolation capabilities of the function are important since the extrapolation is needed for some of the higher flux conditions in the small module. The large module produces lower fluxes which can be simulated without extrapolation of the flooding parameter. In order to give the reader a better overview of the condensation process inside the gap a time-lapse movie was taken during the 80-4 °C experiment with fan.

Each frame is taken 10 seconds apart and the movie corresponds to a 1 hour experiment, seen in Figure 5.9.



Figure 5.9: Movie still of the condensation process. Hyperlink: <http://bit.ly/2gIgoDg>

5.4.3 *Experimental comparison between air gap and direct contact membrane distillation*

Since the experimental conditions were the same for the DCMD and the smaller AGMD module (7.2 m²) a direct comparison of the flux and the Gained Output Ratio (GOR) can be made. GOR is a dimensionless number representing the thermal efficiency of the process and can be calculated using the following equation [56]:

$$GOR = \frac{NAH_v}{HX_{duty}} \quad (5.15)$$

Where A is the membrane area of the module in m², H_v is the specific heat of evaporation of water in $\frac{J}{mol}$ and HX_{duty} is the duty of the heat exchanger in W. The specific heat of evaporation is a weak function of the temperature and, therefore, it is calculated at the average temperature of the feed channel. A direct comparison between the two technologies is provided in Figure 5.10

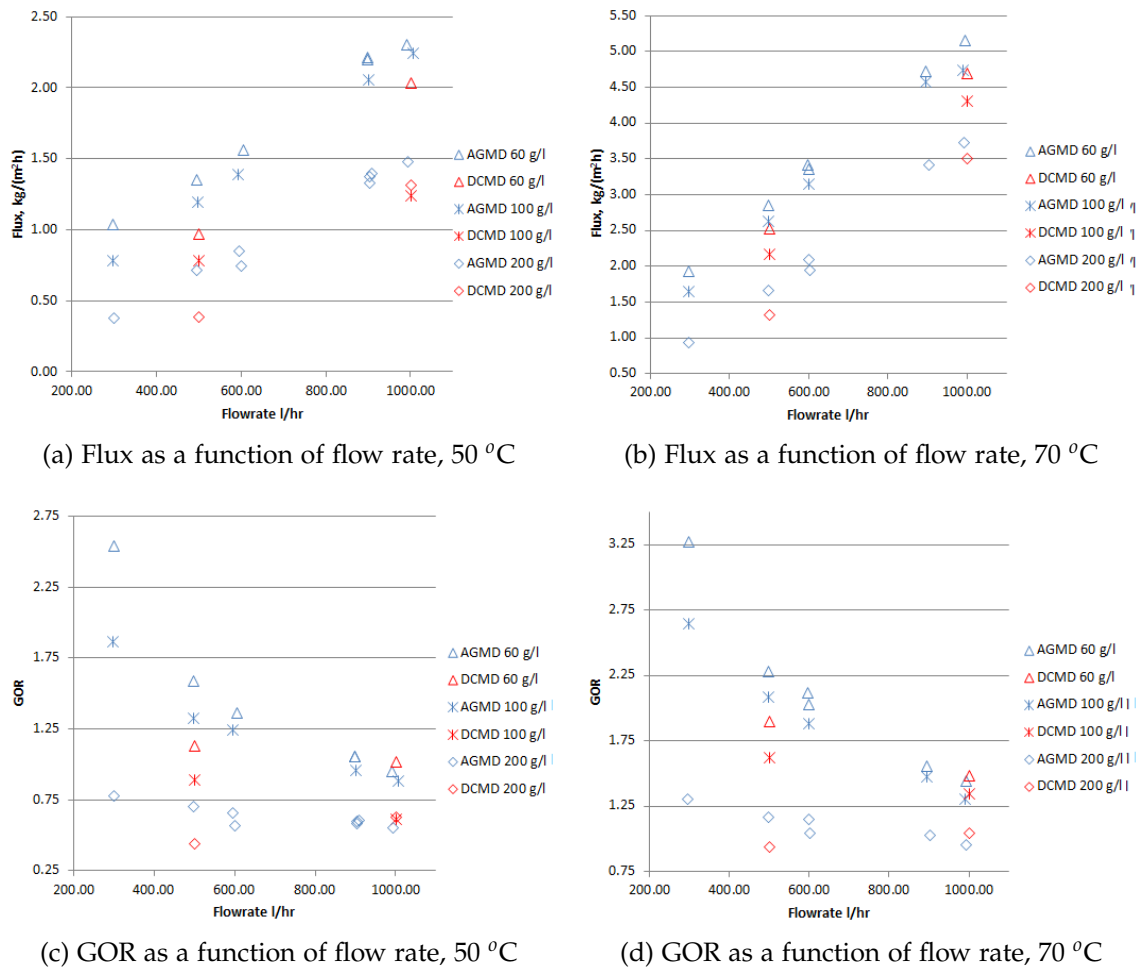


Figure 5.10: Experimental comparison between DCMD and AGMD at different conditions, 7.2 m² modules, permeate temperature kept at 20 °C. An 8 m² external recuperating heat exchanger was used in the DCMD system.

As can be clearly seen, the air gap module performs better than the DCMD module both in terms of flux and GOR under all tested conditions. This is quite surprising at first, since the air gap introduces additional mass transfer resistance and it is counter-intuitive that the AGMD will have higher flux, given that the flux should clearly be hindered by the gap diffusion. However, unlike the typical behavior of lab-scale modules, which reach an asymptotic value of flux as a function of flow rate [117, 151], at full-scale the flux linearly increases all the way up to 1000 l/hr (Figure 5.10a, 5.10b), which is the maximum permissible flow rate for the AGMD module due to the feed inlet pressure approaching the design maximum of 700 mBar. The linear increase of flux as a function of flow rate, confirms the result in our previous work, where it was demonstrated that the 7.2 m² DCMD module is severely limited

by the amount of energy fed into the module [148]. During the experiments, the highest recorded conductivity of the permeate was 0.35 mS.

There are two reasons why the air gap module performs better than DCMD. We first have to consider how the energy is exchanged in the module - part of it is exchanged as flux, used to evaporate water, and the other part is being lost as sensible energy via conduction through the membrane matrix as seen in Figure 5.6. If indeed the module is limited by inflow energy, an air gap will work more efficiently as the sensible losses are greatly reduced by the low thermal conductivity of air. Therefore, more energy will be left to evaporate water and thus the flux will be increased. This is an important conclusion, that a membrane with lower thermal conductivity will not only be more efficient, but will also exhibit a higher flux when applied at full-scale.

To demonstrate degree of limitation by inflow energy fed into the module the following equation can be used - eq. 5.16

$$G = \frac{M_e T_e C p_e - M_c T_c C p_c}{A} \quad (5.16)$$

Where G represents the ratio of the energy fed into the module to the module area. The typical values from the work of Eykens et al. [138] are used for the lab-scale dimensions, i.e. 60 and 45 °C for the evaporator (T_e) and coolant channel (T_c) inlets, 60 kg/h (M) and lab-scale module dimensions of 6x18 cm, resulting in an area (A) of 0.0108 m². For the full-scale AGMD the average values of the conditions are used, i.e. 60 and 20 °C for the evaporator and coolant channel inlets, 600 kg/hr feed flow rate and area of 7.2 m². As a result, after converting to SI units, on lab-scale the module exchanges 97.2 kW per m² of area, while at full-scale G is only 3.9 kW/m². This number quantifies that even the smaller 7.2 m² full-scale module is nearly 25 times more limited by inflow energy than a typical lab-scale module, hence the heat and mass transfer resistances inside the module are much less important, compared to lab-scale. If the flow rate of the lab-scale module is reduced 25 times to have the same energy to membrane area ratio, problems with measurement accuracy will arise. Additionally, the channel velocity will be reduced to 0.5 cm/s and the hydrodynamics of the module will not be representative for the full-scale, where the channel velocity is 3.5 cm/s. This demonstrates that one should be very careful when studying the behavior of a MD system at lab-scale, since the conditions are not representative to a full-scale system, unless the channel lengths and velocities are equal.

Logically, one can ask if the module design could be improved by reducing the area. While the flux will certainly be increased, less area will be available for internal heat recuperation and therefore the energy efficiency of the process will suffer. Therefore, an optimal module design exists, but will be specific for each application, depending on the requirements of higher flux, or higher energy efficiency of the process. Moreover, smaller modules will probably result in higher capital costs of the system, since each module needs to have an envelope, internal tubing and labor costs, which are not directly correlated to the membrane area.

The second reason why the air gap module is performing better on full-scale is probably related to the membrane compressibility. In previous work it was demonstrated that the stretched membrane used in these modules can compress as much as 30 percent under the operational pressure of the DCMD module [148]. The compression was shown to have a mostly negative effect, mainly due to the porosity and thickness reduction, which consequently severely increased the thermal losses through the membrane. However, in contrast, in the air gap configuration, the pressure in the distillate compartment is close to atmospheric, which means that the hydrostatic pressure in the feed channel will probably push it through the spacer and slightly stretch it, but it will not compress the membrane.

It should be noted that the higher flux and GOR of AGMD over DCMD is quite important for the overall system design of membrane distillation. For example an AGMD system uses only one loop instead of two, which halves the number of required components in terms of recirculation pump, sensors, piping and valves. Moreover, the AGMD module employs an internal heat recuperation and does not need an expensive recuperation heat exchanger as required in DCMD.

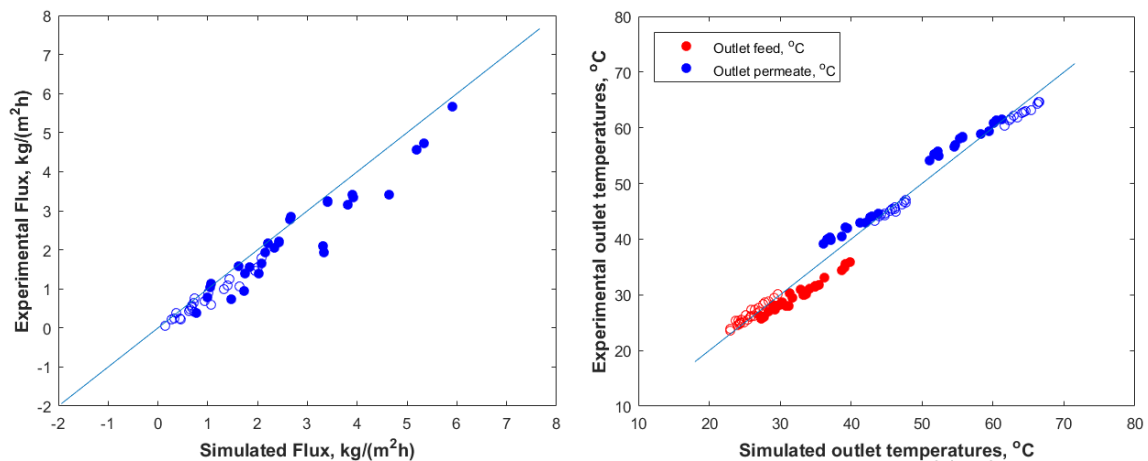
It is interesting to notice that the external recuperation heat exchanger used in DCMD transfers heat from the permeate outlet to the feed outlet channel of the module (See Figure 4.2). Hence, it is less effective in the cases where the temperature drop along the channels is small and one can arrive at a situation where the recuperation heat exchanger does not recover any heat. In fact, if the temperature drop is so small that the permeate outlet temperature is lower than the feed outlet temperature, the recuperation heat exchanger will have negative effect on GOR.

5.4.4 Model validation

The model prediction was validated against the experimental results from both the small (7.2 m²) and the large (24 m²) AGMD modules. The experimental conditions were chosen using a design of experiments scheme, where the permeate flow rate was always kept at 20 °C and the feed had two temperature levels, i.e. 50 and 70 °C. The flow rate had 3 levels, i.e. 300, 600 and 900 l/hr and the salinity also had 3 levels, 60, 100 and 200 g/l. Additional flow rate levels of 500 and 1000 l/hr were included for the small AGMD module in order to directly compare it to the DCMD module. In order to demonstrate the importance of the flooding inside the module the validation is done twice, once when the flooding is not taken into account and once with the flooding enabled in the model.

Model validation without taking the gap flooding into account

The flux and the outlet temperature for both modules for 55 different experimental conditions can be seen in Figure 5.11.



(a) Simulated versus experimental fluxes, $R^2=0.90$ (b) Simulated versus experimental outlet temperatures, $R^2=0.98$

Figure 5.11: Model validation for flux and outlet module temperatures when the gap flooding is not considered in the model. The solid markers represent the 7.2 m² module data points, while the non-filled markers represent the fit for the data points of the 24 m² module.

The model severely overestimates the flux when the gap flooding is ignored. The fit for the outlet temperatures seems to be reasonable for the large module, but becomes much worse for the small module.

Model validation with gap flooding included in the model structure

The validation of the model when the gap flooding is considered in the model can be seen in Figure 5.12.

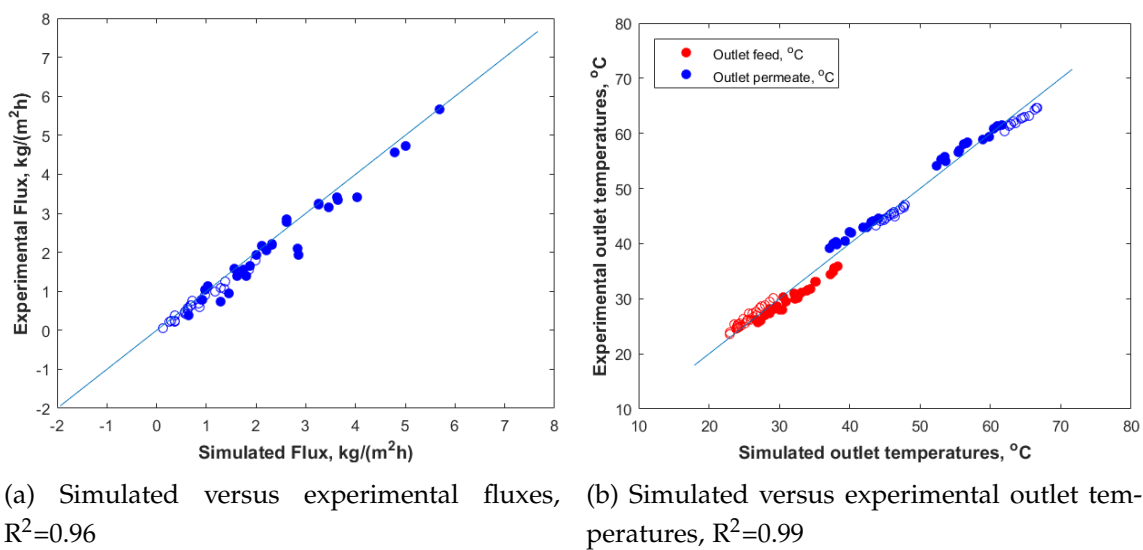


Figure 5.12: Model validation for flux and outlet module temperatures with flooding of the gap taken into account. The solid markers represent the 7.2 m² module data points, while the non-filled markers represent the fit for the data points of the 24 m² module.

As can be seen the model closely matches the experimental flux and outlet temperatures. The prediction for both the flux and the outlet temperatures is improved, when the gap flooding is included in the model.

While the flooding improves the flux on lab-scale [145] (i.e. PGMD performs better than AGMD), on full-scale the flooding has a negative effect according to the model. On the average, the flux is 8.5 % lower for the small module and 10 % lower for the large module when flooding is included in the model. While the flooding lowers the resistance of the gap and increases the driving force across the membrane, the flooded gap configuration does not have the insulating properties of an air gap. Considering that the resistances of the membrane and the gap are arranged in series (eq. 5.5), the conductive losses

will be limited by the highest resistance in the system. Therefore, in the case where the gap is flooded, the conductive losses are dictated by the thermal conductivity of the membrane, while in the non-flooded case the thermal losses are dictated by the thermal conductivity of air in the gap. Considering that the full-scale configuration is highly limited by inflow energy, the effect of the increased losses through the membrane becomes more important than the decreased mass transfer resistance, hence on full-scale AGMD performs better when there is no flooding of the gap. It should be noted that the model prediction is very good, although there are no adjustable parameters. Further improvement in the model prediction is expected if the method for measuring the degree of flooding as a function of flux is improved to avoid extrapolation at higher flux conditions.

5.4.5 Module optimization based on the validated model

A variance-based Global Sensitivity Analysis (GSA) study was performed, in order to investigate which parameter of the system is most limiting for the flux. A total of 10 000 samples were taken, using Sobol sampling and the design proposed by Saltelli et al. [127]. Further explanation of the method and its application is available in Mortier et al. [128]. The parameters used in the global sensitivity analysis and how they affect the model can be seen below:

$$\tau = \tau_0 C1; \quad (5.17)$$

$$\kappa_m = \kappa_{m,0} C2 \quad (5.18)$$

$$Nu_{f,p} = Nu_{f,p,0} C3 \quad (5.19)$$

$$Sh = Sh_0 C4 \quad (5.20)$$

$$Q_{f,p} = Q_{f,p,0} C5 \quad (5.21)$$

$$Re_{f,p} = \frac{(v_{ch}/\epsilon_s) D_{ch} \rho}{\mu} C5 \quad (5.22)$$

$$h_{gap,air} = h_{gap,air,0} C6 \quad (5.23)$$

$$B_{gap} = B_{gap,0} C7 \quad (5.24)$$

$$X = X_0 C8 \quad (5.25)$$

$$\delta_{cond} = \delta_{cond} C9 \quad (5.26)$$

All coefficients $C1$ through $C9$ are varied in the range of $\pm 20\%$. Coefficient $C1$ alters the membrane tortuosity and, hence, the overall membrane permeability. Coefficient $C2$ alters the thermal conductivity of the membrane and, hence, the losses through the membrane polymer. Coefficients $C3$ and $C4$ modify the Nusselt and Sherwood equations which translates to linearly altering the heat and mass transfer coefficients, respectively. The $C5$ coefficient alters the flow rates of the channels and, hence, the inflow energy that is entering the module. However, it is also included in the denominator of the Reynolds equation. In this way the coefficient influences how much energy is flown in the channels, but will not affect the hydrodynamics. Coefficients $C6$ and $C7$ alter the heat and mass transfer inside the air-filled gap, respectively. Coefficient $C8$ alters the flooded fraction of the gap and the coefficient $C9$ alters the thickness of the condensate layer inside the gap. The GSA was performed at the average experimental conditions - 60 and 20 °C inflow temperatures of the feed and permeate respectively, a flow rate of 600 l/hr and 120 g/l salinity. The flux was taken as output parameter. The results of the GSA are provided in Figure 5.13.

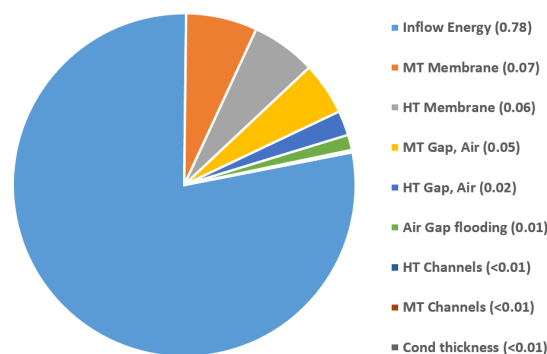


Figure 5.13: Total effect indices calculated from the global sensitivity analysis

The total effect indices in the figure directly represent the importance of the parameter on the output, relative to the importance of the other parameters. Similarly to our previous study, where GSA was performed on DCMD [148], at full-scale the module flux is severely limited by the inflow energy, which is completely saturating the GSA analysis. Because of this limitation, the thermal conductivity has the same importance on full-scale as the membrane permeability, since a more efficient process will leave more energy to be exchanged as flux, instead of losses through the membrane matrix. Therefore, based on the GSA study, the flux will be increased similarly by employing a membrane with

20 % lower thermal conductivity, as it would with a membrane which is 20 % more permeable.

Improving the mass transfer inside the gap is of similar importance to improving the membrane properties. Another field of improvement is reducing the heat losses inside the gap compartment, which are evaluated to be about 1/3 as important as the membrane properties. The last field of improvement is the gap flooding. While it is not as important as the membrane and the air gap properties, this parameter may have a greater potential for improvement and possibly the flooding of the gap can be completely avoided. Similarly to the DCMD study, the heat and mass transfer inside the channels have a very minor influence in a full-scale AGMD system. The least important parameter for the system is the condensate layer thickness. A thicker condensate layer will improve the mass transfer inside the air gap, since the vapors will diffuse through a thinner gap, but will increase the temperature drop across this thicker layer and, hence, reduce the driving force of the process. Therefore, this parameter has a controversial influence on the system, but based on the GSA we can conclude that it is not very important.

5.5 Conclusions

In this work for the first time a model without calibration parameters was created for air gap membrane distillation. A previously developed DCMD model was extended by adding the air gap compartment. For the first time in the literature the gap-related parameters were measured in relatively simple lab-scale experiments allowing to create an air gap model without calibration parameters. Moreover, the method allowed for the best visual observation to date of the condensation in the gap. By measuring, instead of calibrating the gap-related parameters the model can now be used for optimizing the module design. This is also the first model to date that considers the air gap configuration as partially flooded. Thorough validation using two commercially available modules with different areas was performed demonstrating that the model can predict both the flux and the outlet temperatures of the modules with high accuracy at various conditions.

For the first time in the literature an air gap and a direct contact module from the same manufacturer and geometries were directly compared at identical conditions. Furthermore, a global sensitivity analysis was performed, reveal-

ing that flux on full-scale is mostly limited by the amount of energy flown into the module, hence a module with higher liquid throughput will enhance the flux. Other promising areas of improvement are the optimization of heat and mass transfer inside the membrane, followed by optimization of the heat and mass transfer inside the gap, as well as reducing the gap flooding. Similarly to our previous study on DCMD [148], the heat and mass transfer inside the flow channels is of minor importance.

Contrary to the popular belief [144,152], both the flux and the energy efficiency were higher for the air gap modules. This was explained by the severe limitation of the full-scale MD modules in terms of inflow energy fed into the module and the lack of membrane compaction in the air gap configuration.

5.6 Acknowledgment

The full-scale module experiments were performed within the framework of the ECWRTI (Electro Coagulation for Water Recycling in Textile Industry) project funded by the European Union's Horizon 2020 research and innovation programme, contract No. 642494 (<http://ecwrti.eu>). The authors would also like to thank Aquastill for providing samples from the materials used in the AGMD modules.

CHAPTER 6

Model-based process and module optimization of membrane distillation

To be submitted as: I. Hitsov, K. De Sitter, C. Dotremont, I. Nopens, 2017. Model-based process and module optimization of membrane distillation

Abstract

Membrane distillation (MD) is a thermally driven separation process. One of the key advantages of MD is that it operates at moderate temperature, allowing for the use of waste heat as well as the high rejection for non-volatile components and the ability to operate with feeds with extreme concentrations. While the literature is saturated with lab-scale models, almost none exist for designing a complete MD system. This work demonstrates a tool, capable of designing a complete membrane distillation system, including all of the supporting equipment and able to predict the price of the obtained distillate for the most commonly studied and used membrane distillation configurations. A graphical user interface is developed, where all of the major simulation inputs can be easily altered. The user can also optimize the module geometry based on specific requirements. Several cases are discussed and the optimal system design for each case is demonstrated. Finally, the reader is presented with a simplified cost model that can be used to quickly estimate the price of the produced distillate at different production scales and concentration factors. At the heart of the decision support tool are the models developed in the previous chapters.

6.1 Introduction

Membrane distillation can be performed in various configurations [56]. The three most widely discussed configurations in the literature are the direct contact (DCMD), air gap (AGMD) and permeate gap membrane distillation (PGMD) [144] - Figure 6.1.

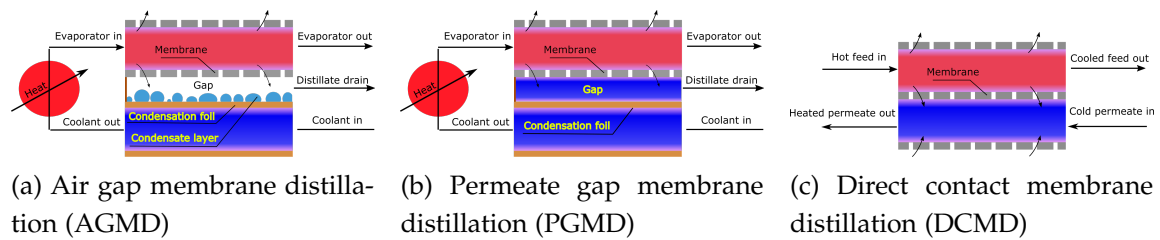


Figure 6.1: The most widely used membrane distillation configurations.

The DCMD configuration has the simplest design where two loops (hot feed and a cold permeate) are contacted directly via a porous hydrophobic membrane. In order to improve the thermal efficiency of the process, an external recuperating heat exchanger recovers the heat of the permeate outlet to the cooled feed outlet. In the AGMD and the PGMD configurations an extra gap compartment is formed by adding an impermeable foil between the hot feed and the permeate compartments. The AGMD and the PGMD configurations are identical in their designs, however the AGMD modules are assumed to have a gap, which is completely evacuated of distillate, while the PGMD modules are considered to have a completely flooded gap. The PGMD and the AGMD configurations have the advantage of an inherited internal heat recuperation, since the cold feed gets preheated while it flows through the coolant compartment.

In order to fully utilize the performance of MD, modelling can be applied to intensify the performance of the modules and to design tailor made complete MD systems. However, to date the majority of MD modelling is done almost exclusively on lab-scale and full-scale modelling is rarely performed. Moreover, to date there are only a few studies aimed at module optimization and even less studies where the economics of the process are discussed [6,8,153]. Ali et al. [153] performed an optimization of the membrane thickness and module length of a DCMD module and performed an economic calculation for a multistage DCMD system with extremely high operational capacity

(1 000 m³/h). This particular study, however, used an in-house developed hollow fibre module and the price is calculated only on one production scale. Winter et al. [6] performed a thorough economic analysis of systems with different modules and configurations using commercially available modules from Solarspring GMBH (Germany), but no multiple stages were considered.

In this chapter we are presenting a tool with a graphical user interface that is able to optimize an AGMD, PGMD or DCMD module, starting from the design of a commercially available modules from Aquastill BV (The Netherlands). The simulation of the commercially available modules is shown in Chapters 4 and 5, including a methodology that avoids calibration on full-scale.

Four case scenarios are simulated using the standard Aquastill modules, followed by a simulation using the optimized modules, validating the optimized module designs and demonstrating the potential gains of a system that uses optimized modules. The model can simulate a system with up to three salinity stages, which increases the efficiency of the system.

Finally, a simplified cost model is presented that allows the reader to quickly estimate the price of the distillate and the investment cost of a system, depending on the configuration, concentration factor, feed temperature and production scale. The use of this model does not require prior modelling experience, therefore it can be used easily in cost estimation studies.

6.2 Materials and Methods

The graphical user interface (GUI) allowing interaction with the model is developed in Matlab and then exported as a Microsoft Windows executable file. The GUI consists of two parts. The first part deals with module-specific design optimization, where different number of parallel channels, module geometry, membranes and membrane properties can be tested. The second part of the GUI deals with designing a complete MD system.

6.2.1 GUI for module optimization

The GUI dealing with module design (Figure 6.2) is composed of user-definable inputs in the first two columns, output in the middle section and graphical outputs at the right hand side. First, the user can select the recirculation flow rate and temperatures of both the feed and the permeate, as well as the salinity of

the feed.

In the section dealing with membrane and spacer, the user has the choice to select a calibration for a different membrane and spacer from drop-down menus. The choice of spacer affects the heat and mass transfer in the channels by employing a different Nusselt and Sherwood equation in each case as described in Chapter 3. However, each spacer will affect the pressure drop of the module, which is modelled by employing different coefficients in the polynomial fit for the pressure drop as a function of the mean channel velocity.

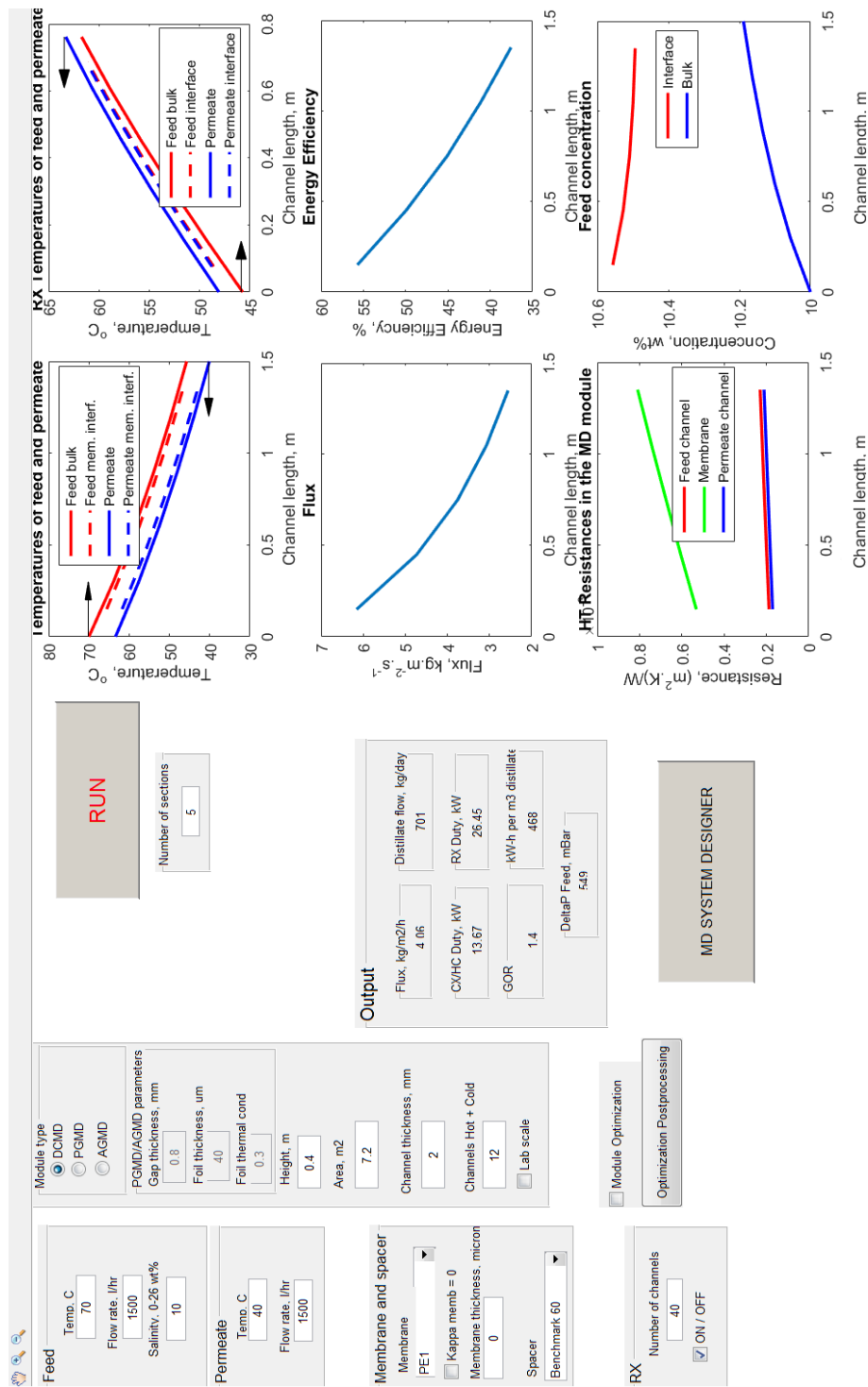


Figure 6.2: Module optimization GUI. The fields which are editable boxes (white) are inputs, the boxes which are with gray (inactive) background are outputs of the model.

If the check box $\kappa_{memb} = 0$ is selected, the model considers a membrane, having the thermal conductivity of air, i.e. one can study the maximum obtainable gain from reducing the thermal conductivity of the membrane and, hence, the thermal losses through the polymer matrix of the membrane. Further, the user can set a custom thickness of the membrane by directly setting its value in the editable box, or alternatively, leaving it to 0, will make the model use the default membrane thickness for the currently selected membrane. The membrane thickness affects both the heat and mass transfer in the membrane, while the model assumes that the membrane structure remains the same. This means that a two times thinner membrane will be twice as thermally conductive, but also two times more permeable. For the case of direct contact membrane distillation, the membrane is considered to compress, or compact as a function of pressure as shown in chapter 4. While this effect was studied only for the PE1 membrane, if another membrane is used, the same percentage of compaction is considered as a function of pressure. Therefore, care should be taken when analyzing the results in this case, unless the calibration for membrane compaction as a function of pressure is also updated (See Chapter 4, Section 4.6.2 for details).

For the case of a DCMD module, a recuperating heat exchanger (RX) is also simulated if the corresponding check box is enabled. The heat exchanger is simulated using the DCMD model, in which an impermeable titanium plate is simulated, instead of a membrane. The heat exchangers in the system are plate and frame with a height and width of 0.76 and 0.29 m, respectively, and a channel thickness of 5 mm. The user can change the number of plates in the heat exchanger in order to study how this would affect the overall performance of the DCMD system. It should be noted that by adding plates, both the area and the hydrodynamics of the RX are affected.

The type of MD module can be selected from a radio button. Three configurations are considered - direct contact membrane distillation, permeate gap and air gap membrane distillation. The direct contact and the air gap are thoroughly described in Chapters 4 and 5. The permeate gap membrane distillation is considered here only theoretically as the model was never validated. However, the permeate gap configuration is a logical extension since the configuration is identical to the air gap, but the gap is completely flooded with water, while in air gap the flooding is only partial and a function of the flux as demonstrated in Chapter 5.

When either air gap or permeate gap configuration is selected, the gap para-

meters such as gap thickness, thermal conductivity and thickness of the condensation foil can be changed, to evaluate their influence.

The parameters related to the module geometry can also be changed. The module height, area and total number of parallel channels can be altered, while the channel length is automatically re-calculated as a function of the aforementioned parameters. The channel thickness can also be changed, which will affect the hydrodynamics and pressure drop. The model can also be used to simulate the lab-scale module (described in Chapter 3) by selecting the *Lab-scale* check box, in which case the channel height and length will be selected as 6 and 18 cm, respectively, with two channels and a single membrane in between.

The middle section of the GUI (Figure 6.2) reveals the flux, distillate flow, duty of the heat exchangers, specific thermal energy and pressure drop of a system equipped with a single module.

The right hand side of the GUI displays how the temperatures, flux, single pass energy efficiency, feed concentrations and heat transfer resistances in the module evolve along the length of a single channel in the module.

In case the *Module Optimization* check box is selected, a sub-window will open - Figure 6.3.

The dialog box 'Input for optimization' contains the following parameters and their settings:

- Area (enabled, range, step), m²**: 1, 5 30, 5
- Membrane thickness (enabled, range, step), micron**: 1, 50 500, 50
- Channel thickness (enabled, range, step), mm**: 1, 1 3, 1
- Module height (enabled, range, step), cm**: 1, 20 50, 10
- Total number of parallel channels (enabled, range, step)**: 1, 8 16, 4
- Flow rate (enabled, range, step), l/hr**: 1, 500 2000, 500
- Gap thickness (enabled, range, step), micron**: 1, 500 2000, 300
- Assume no gap flooding if gap thickness is larger than, micron**: 1200

Buttons: OK, Cancel

Figure 6.3: Choice of module optimization parameters

Most of the fields in this window have three lines. The first line is either a 0 or 1, meaning that this parameter will either be included or omitted from the optimization. If a parameter is not included in the simulation, the parameter value will be taken from the main screen of the GUI. The second line is the range of values taken in the optimization and the last number is the step that the optimizer takes. For example, the first field means that the optimizer will study the influence of module area, with a range of values from 5 to 30 m², and a step of 5 m² or 6 levels in total for the area input parameter. The optimizer will then solve all of the possible combinations in a structured manner, i.e. all possible combinations of the input parameters will be solved. For example

if a, b and c are three levels of parameter A and d, e and f are 3 levels (or steps) of parameter B, the number of possible solutions will be the products of the number of levels of parameter A, multiplied with the number of levels of parameter B - equation 6.3

$$\text{Parameter } A = [a \quad b \quad c] \quad (6.1)$$

$$\text{Parameter } B = [d \quad e \quad f] \quad (6.2)$$

$$\text{Solutions}(A,B) = [ad, \quad ae, \quad af, \quad bd, \quad be, \quad bf, \quad cd, \quad ce, \quad cf] \quad (6.3)$$

It should be noted that including too many parameters and using small steps in the optimization can make obtaining the solution prohibitively slow as the number of solutions increases drastically. One possible approach is to obtain an initial guess for the optimal design using larger steps for the parameters (coarse grid), and then re-run the optimization with a finer grid and smaller parameter ranges. Each solution requires between 1 and 5 seconds of processing time, depending on the process conditions and the selected configuration.

It is noteworthy that the recirculation flow rate of the module is also included in the optimization. While it is not strictly a module design parameter, it affects both the flux and the energy efficiency of the module. Moreover, the geometry of the module can be designed for larger or smaller flow rates, therefore the flow rate should be included in the optimization.

The *Gap thickness* field is enabled only when an air or permeate gap configuration is enabled. In this case, an extra field appears which enables the user to specify a cut-off thickness of the gap. If the gap value is larger than the cut-off value, the model will assume that there is no flooding present in the air gap. This option can be used as a crude tool to demonstrate the influence of gap flooding, or disabled when set to a value outside of the tested gap thickness range.

6.2.2 System design model

In the case where a complete MD system needs to be designed, the user can click the *MD SYSTEM DESIGNER* button in Figure 6.2, which opens a new GUI - Figure 6.4.

inflow
inflow salinity, wt%
6

OPEX

Advanced Settings

Price of electricity, E/kW-h
0.11

Pretreatment cost, E/m³ inflow
0.05

Membrane module lifetime, years
5

Maintenance costs, % of system price without modules per year
2.5

Biom disposal E/m³
0

Insurance, % of Capital / yr (includes depreciation)
1

Man-hours and hourly rate
8 Hr/day 33 EUR/hr

CAPEX

Rack, where the installation is housed, kEUR
5

Price of one tank with plumbing
5

Price per pump, EUR
3000

Controller, cabling and programming, kEUR
15

Average price per sensor, EUR
250

Price of DCMD module
900 EUR, assembly 50 EUR/m²

Price of PGMD module
1950 EUR, assembly 75 EUR/m²

Price of Heat Exchangers, titanium
850 EUR, endplates 350 EUR/m²

Heating installation
Excluding heat exchangers including pipes, pumps, etc., kEUR
5

Cooling installation
Excluding heat exchangers including pipes, pumps, etc., kEUR
5

Scale-up coefficient
0.6

Base, modules
3

Scale-up coefficient
0.5

Base, modules
3

Scale-up coefficient
0.6

Base, modules
5

Scale-up coefficient
0.3

Base, modules
3

Stage 1 output

Flux, kg/m²/h
1.79

WH Flow m³/hr
197.4

CX/HC Duty, kW
5934.85

kW-HT per m³ distillate
167

Distillate flow, kg/hr
23969

Inflow, kg/hr
59298

Bleed flow, kg/hr
35333

Stage 2 output

Flux, kg/m²/h
1.51

WH Flow m³/hr
126

CX/HC Duty, kW
3593.92

kW-HT per m³ distillate
204

Distillate flow, kg/hr
11869

Inflow, kg/hr
35368

Bleed flow, kg/hr
23500

Stage 3 output

Flux, kg/m²/h
1.2

WH Flow m³/hr
82.7

CX/HC Duty, kW
2178.04

kW-HT per m³ distillate
249

Distillate flow, kg/hr
5903

Inflow, kg/hr
23495

Bleed flow, kg/hr
17591

Operational parameters

Hot feed, C
80

Cold permeate, C
20

l/hr/module
950

Number of modules
227

Enable RX if DCMD

Operational parameters

Hot feed, C
80

Cold permeate, C
20

l/hr/module
950

Number of modules
365

Enable RX if DCMD

Operational parameters

Hot feed, C
80

Cold permeate, C
20

l/hr/module
950

Number of modules
620

Enable RX if DCMD

Operational parameters

Hot feed, C
80

Cold permeate, C
20

l/hr/module
950

Number of modules
227

Enable RX if DCMD

Calculate

Size the system for, m³/day distillate
1000

Total distillate, m³/day
1001.5

System Price kEUR
2278

CAPEX E/m³ Distillate
0.62

OPEX E/m³ Distillate
1.51

Total E/m³ Distillate
2.13

View

View

View

Figure 6.4: GUI of the system design tool. The fields which are editable boxes (white) are inputs, the boxes which are with gray (inactive) background are outputs of the model.

The purpose of this program is to be able to quickly size, design and predict the distillate price of a MD system. The left side of the GUI is designated to input related to the feed salinity, operational expenditures (OPEX) and capital expenditures (CAPEX) parameters. This will now be discussed in more detail.

OPEX parameters in the system design GUI

The price of electricity is used in the model for calculation of the pumping cost. The shaft power of each pump is calculated using 60 % efficiency. The pretreatment cost is calculated in € per m³ of inflow. This can reflect on the price of pretreatment, acid dosing for pH regulation, or if needed, the total OPEX price of a pretreatment system, which can be calculated separately by the user in each specific case. The *Membrane module lifetime* field is used to calculate the OPEX cost of module replacement and is set to 5 years by default. The lifetime of reverse osmosis elements is frequently stated between 2 and 5 years [154], therefore, considering that MD is not a pressure driven process the chosen value of 5 years seem realistic, but more solid data is still needed. The maintenance cost can be entered as a percentage of the capital cost that is spent each year for repairs and maintenance of equipment. It is noteworthy that the maintenance cost excludes membrane cleaning and the replacement of the membrane modules, since they are scheduled for complete replacement at the end of their lifetime. In other sources the maintenance cost of pipes and pumps are quoted as 1 and 4 percent of the investment cost [155], respectively. Therefore, in this work a default value of 2.5 percent is utilized. The brine disposal field can be used in those cases where the brine cannot be discharged freely and conveniently in a nearby water body, but needs to be transported to a disposal location. In such cases it may be advantageous to design a system with higher water recovery rate in order to minimize the brine disposal cost, which can be quite substantial in some cases [156]. The insurance cost can also be calculated by the model. The calculation is done as a percentage of the value of the system, assuming linear depreciation over the depreciation period (useful lifetime of the system). The salaries of the personnel can be calculated by entering the man-hours per day as well as the personnel payment rate in € per hour.

The model can be used to calculate the financing of a loan to build the MD system, using a compound interest rate over a given period. The last value of the

OPEX list is a system downtime, which can be dictated by interruptions of the supply of waste heat, or due to yearly maintenance and unavoidable accidents. During a downtime period, the system will not have operational expenditures. However, also no distillate will be produced during the downtime, which will increase the CAPEX-related price of the distillate as the MD system will have to be oversized to compensate for the downtime.

CAPEX parameters in the system design GUI

The model takes an approach where scale-up factors are used to extrapolate for the price of the major components in the system. The scale-up factors are a common approach used in engineering calculations [157], seen in Equation 6.4

$$CostA = CostB \left(\frac{CapA}{CapB} \right)^X \quad (6.4)$$

Where $CostA$, $CostB$, $CapA$, $CapB$ and X are the unknown and known cost, capacity A, capacity B and the scale factor, respectively. The rule is also known as the six-tenths-factor, because commonly X is taken as 0.6, which means that the equipment becomes relatively cheaper at the larger scale, reflecting the economy of scale. For the common equipment such as pumps and heat exchangers the typical factor of 0.6 was taken [157], while for most of the other equipment a more modest scale-up factor of 0.8 was employed. Smaller scale-up factors were chosen for the controller and cabling and for the tanks and plumbing - 0.3 and 0.5, respectively. These factors are taken much lower than the rest, since the price of the controller and the cabling will remain almost constant with respect to the rest of the installation size. Similarly, the tank price remains almost constant and only the plumbing will have to be up-scaled.

The known (base) price is entered at a known (base) capacity (Figure 6.4). In this example the base capacities are used the same as the ones utilized in the pilot-scale module. The base prices are chosen based on discussion with engineers and experts in the field of MD. For the heat exchangers and the pumps, the base capacity is in m^2 of heat exchange area and m^3/hr , respectively. The heating and the cooling installations are also referenced in m^3/hr , since they essentially consist of pumps and pipes. The rest of the equipment is based on number of modules. In this way the base price of the equipment used in a pilot-sized system can be extrapolated to a larger-scale installation with more modules.

Since membrane distillation is not widely adopted so far, the production of the MD modules is done at small production scale and is not fully automated yet. Hence, a large fraction of the price of one module is the price of assembly and testing. Therefore, the price of one module in the model is formed by adding the price of the assembly to the price of the membrane area. By using this price formulation, the price of a module is not a very strong function of the membrane area of the module (Figure 6.5).

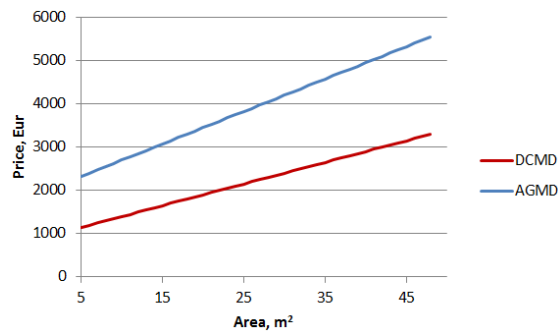


Figure 6.5: The price of DCMD and AGMD modules as a function of membrane area assumed in this study

A base price of the AGMD module was taken as almost two times more expensive, because of the higher complexity of adding a gap compartment to the system.

A similar approach was used in forming the price of the plate and frame heat exchangers. In this type of heat exchangers, corrugated heat exchange plates are stacked and then pressed firmly together by thick cast iron end plates. Since the price of the end plates is substantial, it is added to the price of the heat exchange area to form the total price of the heat exchanger.

Advanced CAPEX and OPEX settings

By clicking on the *Advanced Settings* another page with user-definable model parameters is displayed (Figure 6.6).

The screenshot shows a software interface for setting CAPEX and OPEX parameters. It is organized into four main panels:

- Waste Heat:**
 - Pricing:** Two input fields for 'Eur/m3' (0.02) and 'Eur/kW-h' (0.003).
 - Waste heat availability, m3/h:** Input field (100) with checkboxes for 'Unlimited' (checked) and 'Comes With Inflow' (unchecked).
 - Waste heat temperature, C:** Input field (85).
 - Head of the pump, Bar:** Input field (1).
- Cooling:**
 - Cooling, Eur/m3:** Input field (0).
 - Cooling availability, m3/h:** Input field (100) with checkboxes for 'Unlimited' (checked) and 'Comes With Inflow' (unchecked).
 - Cooling temperature, C:** Input field (15).
 - Head of the pump, Bar:** Input field (1).
- Heat Exchangers:**
 - Approach temp of Heat Exchangers, C:** Input field (3).
 - Number of plates per module CX and HX:** Input field (15).
 - Number of plates per module, RX:** Input field (40).
- Cleaning and flux decline:**
 - System needs cleaning every, Days:** Input field (5).
 - Every cleaning event costs, E/module:** Input field (1).
 - Flux has declined to (value) before cleaning, Percent:** Input field (60).
 - Flux recovers to (value), Percent:** Input field (90).

On the right side, there are two buttons: 'Save the new values' and 'Restore values'.

Figure 6.6: Advanced CAPEX and OPEX settings

The first section defines the parameters related to the waste heat source. The price of waste heat can be calculated based on € per cubic meter or as € per kW-h, while the inactive box is grayed out. The waste heat availability in m³/h can be entered, which will trigger a warning dialog in case the waste heat availability is exceeded. If the waste heat comes with the inflow, the heat exchanger is omitted in the first stage of the system. The waste heat temperature can also be entered in the model. This number is used to calculate the flow rate of waste heat - Equation 6.5

$$M_{WH} = \frac{HXDuty}{(T_{WH,in} - T_{WH,out})Cp} \quad (6.5)$$

Where M_{WH} , $HXDuty$, $T_{WH,in}$, $T_{WH,out}$, Cp are the waste heat mass flow rate, heat exchanger duty, inlet temperature of the waste heat, outlet temperature of the waste heat and specific heat capacity, respectively. The waste heat outlet temperature can be calculated by adding the approach temperature to the temperature of the feed that enters the heat exchanger. Finally, the head pressure of the pump can be entered and later used in the pumping power calculations. The section regarding the cooling is identical, except for the pricing scheme, which can be based only in € per m³ in the case for the coolant.

The sections regarding the heat exchangers define approach temperature of the Heating (HX) and Cooling (CX) heat exchangers. The approach temperature of the heat exchanger is an engineering simplification used to reduce the com-

putational load, describing the minimal possible difference between the two fluids that the heat exchanger can achieve. The recuperation heat exchanger used to recover the heat in the case of DCMD does not use this simplification. The user can set the number of plates (and thus heat exchanger area) per module for each type of heat exchanger. It is noteworthy that increasing or reducing the number of heat exchanger plates also has an effect on the pressure drop of the heat exchanger.

In the section *Cleaning and flux decline* the cleaning frequency and the cost of each cleaning event can be entered. Additionally, the model includes a simplified calculation for the flux decline, the user can set the value to which the flux has declined before cleaning and the average value to which the flux recovers after cleaning. In the displayed example the flux declines to 60 percent before cleaning is required and then recovers to 90 percent of the initial flux. Therefore, assuming a linear flux decline profile, the average flux at which the system will operate is the average of the two numbers or 75 % of the initially calculated flux. Although this approach oversimplifies the flux decline effect, it is useful to study the impact of flux decline on the overall price of the distillate.

6.2.3 Pressure drop modelling

In order to model the pressure drop in the system an empirical approach was taken. The major pressure drop components such as the heat exchangers and MD modules are modelled, while the pressure drop in the pipes is neglected. The pressure drop inside the modules is modelled as two components - pressure drop exerted by the spacer and pressure drop exerted by the vertical (axial) manifolds in the module. A polynomial expression was fitted to the measured pressure drop of the spacer (dP_{Spacer} obtained in Chapter 4). Similarly, another polynomial expression was fitted for the manifolds of the module, by subtracting the predicted pressure drop of the spacer from the measured pressure drop of the module (experimental data available in Chapter 4). The resulting pressure drop equations are presented in eq. 6.6 and 6.7:

$$dP_{Spacer} = (507v^2 + 75.5v) \frac{L}{L_0} \quad (6.6)$$

$$dP_{Manif} = (0.0070Q_{manif}^2 + 0.1513Q_{manif}) \frac{L}{L_0} \quad (6.7)$$

Where dP_{Spacer} , dP_{Manif} and v are the pressure drop in the spacer, manifold and average flow channel velocity in the module. The pressure drops of the spacer and the module manifolds are recalculated for the current length by multiplying with the ratio of the current and the calibrated length ($\frac{L}{L_0}$), where the calibrated length L_0 is 0.18 and 0.4 m, for the spacer and the manifold, respectively. All pressure drops are calculated in mBar, channel velocity is in m/s and the flow rates are in l/hr.

The model uses the assumption that the two major pressure drops in the module are in the spacer-filled channels and the vertical manifolds that distribute the water along the module length. The pressure drop of distributing the water from the main tube to the vertical manifolds is considered negligible. The second assumption is that the pressure drop in the channels and the manifolds linearly scales with the length ($\frac{L}{L_0}$). This assumption almost certainly holds for the spacer-filled channels, but needs further experimental investigation for the manifolds, which is impossible at this stage, since the commercially available modules cannot be disassembled for legal reasons.

Similarly, pressure drop experiments were performed with a heat exchanger with 15 plates using flow velocities up to 2600 l/hr and a polynomial equation was fitted for the pressure drop - eq. 6.8

$$dP_{HeatEx} = 0.00013552(Q_{HeatEx} \frac{N_{Ch,0}}{N_{Ch}})^2 + 0.0084Q_{HeatEx} \frac{N_{Ch,0}}{N_{Ch}} \quad (6.8)$$

Where dP_{HeatEx} , Q_{HeatEx} , $N_{Ch,0}$ and N_{Ch} are pressure drop, total flow rate, calibrated and current number of heat exchanger plates. It is noteworthy that the flow rate (Q_{HeatEx}) is recalculated for the currently used number of plates. For example if we take a heat exchanger with doubled number of plates, the flow rate and, hence, fluid velocity in each plate will be twice lower (accounted for by the $Q_{HeatEx} \frac{N_{Ch,0}}{N_{Ch}}$ term). This approach has not been validated and therefore further investigation is needed.

The presented pressure drop correlations are simple to use and have very low computational burden. However, if another, new type of flow spacers, manifolds or a heat exchanger is used, experimental data must first be collected and then these correlations must be updated to fit the pressure drop behavior of the new equipment.

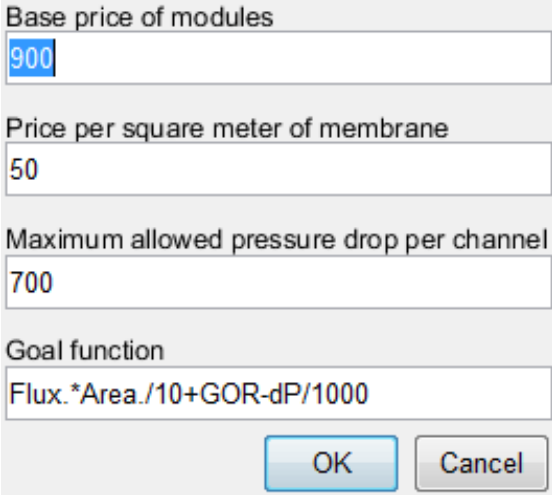
6.3 Results and discussion

6.3.1 Module design optimization

Two cases are optimized in each configuration, 80 °C feed, 20°C permeate and salinity of 20 or 10 wt %. For the case of direct contact membrane distillation an external heat exchanger with 40 channels or total of 8 m² was always used. In order to study the influence of each of the major module design parameters, the optimization of each module is done in steps, with each step including more module parameters, starting from a readily available commercial module design.

DCMD optimization

After defining the range of the parameters included in the optimization (Figure 6.3) and performing the required simulations, the results can be revealed by pressing the *Optimization Postprocessing* button. The user is presented with an input window where the goal function can be dynamically defined (Figure 6.7). The goal function is a mathematical expression which is defined by the user in order to quantify the goodness of the solution, i.e. the higher the value of the goal function is, the better the solution is considered to be.



The screenshot shows a dialog box with the following fields and values:

Base price of modules	900
Price per square meter of membrane	50
Maximum allowed pressure drop per channel	700
Goal function	Flux.*Area./10+GOR-dP/1000

At the bottom of the dialog box are two buttons: "OK" and "Cancel".

Figure 6.7: Definition of the goal function

The base price and the price per square meter of membrane are not currently included in the goal function, but this can be done by including the *ModPrice*

variable in the equation, in case this is desired. The maximum pressure cut-off value will exclude the solutions which yield pressure drops higher than the cutoff value. The cut-off values are defined as 700 mBar for DCMD and 350 mBar for the gap configurations, due to design specifications of the membrane, preventing the membrane from wetting. This means that solutions with predicted pressure drops higher than the cut-off value will be excluded from the optimization.

The goal function currently can be constructed in many different ways, for example giving more or less weight on the energy efficiency (GOR), or flux, or punishing more the solutions with higher pressure drop. The results from the optimization for DCMD can be seen in Table 6.1

Table 6.1: Optimization of DCMD module. Parameters colored in green are included in the optimization, while the ones in yellow are optimized previously.

	Mem. Area, m ²	Mem. Thickness, μm	Channel thickness, mm	Module height, cm	Number of channels	Flow rate, l/h	Flux, GOR kg/(m ² h)	Pressure drop, mBar	Dist product, l/hr	Goal Fn	
Salinity, 20 wt%	7.2	92	2	40	12	1700	0.84	6.16	698	44.4	4.58
	6	92	2	40	12	1700	0.79	7.54	683	45.2	4.63
	7.2	92	3	30	16	2600	0.65	8.86	687	63.8	6.34
	8	92	3	30	16	2600	0.68	7.98	697	63.8	6.36
	8	130	3	30	16	2600	0.64	8.17	697	65.4	6.49
Salinity, 10 wt%	7.2	92	2	40	12	1700	1.28	8.95	698	64.5	7.03
	7	92	2	40	12	1700	1.27	9.20	695	64.4	7.01
	7.2	92	3	30	16	2600	0.94	12.48	687	89.8	9.23
	8	92	3	30	16	2600	0.99	11.37	697	90.9	9.39
	8	60	3	30	16	2600	1.09	11.44	697	91.6	9.55

During the first optimization (first line for each salinity) only the flow rate is included (in green), which yields the optimal solution being at the highest possible flow rate, where the maximal permissible pressure drop is achieved. This is logical, since the biggest contributor for the goal function is the distillate production rate (the product of the area and the flux) and flux is most limited at full-scale by the amount of energy flown in the module (see Table 4.3). By including the area in the optimization, the goal function and the distillate production rates are not improved in both cases, because the starting value of 7.2 m² is already close to the optimal value.

During the next optimization iteration the module parameters which are directly responsible for the flow design were optimized together. Three levels of channel thicknesses (1,2 and 3 mm) were studied, together with three levels of module height (20, 30 and 40 cm) and 3 levels for the total number of flow channels (8, 12 and 16) simultaneously with optimizing the flow rate with a

step of 100 l/hr. This optimization yielded a large increase in the flux, distillate production rate and the goal function. It is noteworthy that the optimal module design is at the upper limit for the channel thickness and the number of parallel channels. The thick channels decrease the channel pressure drop at the expense of reduced heat transfer. Similarly, the increased number of parallel channels reduces the flow rate for each channel and its associated axial manifold, reducing the pressure drop both inside the spacer filled channels and the manifolds inside the module, at the expense of reducing the heat transfer inside the channels due to the lower channel velocity.

The module height on the other hand has a more complex influence. Reducing the module height from 40 to 30 cm reduces the pressure drop inside the vertical manifolds since they become shorter (eq. 6.7). However, reducing the module height results in longer channels and higher channel velocity, improving the heat transfer inside the channels.

Further optimizing the module area with the new flow parameters yields a small increase in the goal function.

Interestingly, optimizing the membrane thickness yields only a minor improvement in the distillate production rate as well as the GOR of the module. In contrast to our previous study [117], where the optimal membrane thickness was key to optimizing the flux and the energy efficiency at lab-scale, this parameter seems of negligible importance at full-scale DCMD. This can be due to a number of reasons. The optimal membrane thickness depends on the level of driving force across the membrane. Therefore, one possibility is to tune the membrane thickness to the average driving force across the membrane, or take the opposite approach and tune the driving force for the current membrane. For example, modules with smaller membrane area will have a higher driving force across the membrane, similarly the driving force across the membrane is a function of the hydrodynamics inside the channels.

At full-scale the driving force reduces along the channel length as the fluid cools down. Therefore, what is found to be the optimal membrane thickness for the beginning of the channel can be different at the end of the channel, thus changing the membrane thickness just changes the flux profile along the channel length, but the average flux remains similar. Moreover, the full-scale modules are severely limited by the amount of energy flown inside the module and the influence of optimal membrane thickness is reduced.

Overall, the module optimization for DCMD yields excellent results. Even if the membrane thickness remains at its original value, the optimization results

in 44 and 29 % increase in the distillate production and flux, respectively, while the GOR is only slightly reduced by 19 percent in comparison to the standard module geometry. The reduction in GOR is due to the increased recirculation flow rate, while the external recuperating heat exchanger area is kept constant. Similarly, for the 10 wt% salinity case a 41 and 27 % increase in the distillate production and flux is achieved, respectively, while the GOR is only slightly reduced by 22 %. Interestingly, the optimal module design for both salinity cases is the same, which is a very important consideration for the system design.

PGMD optimization

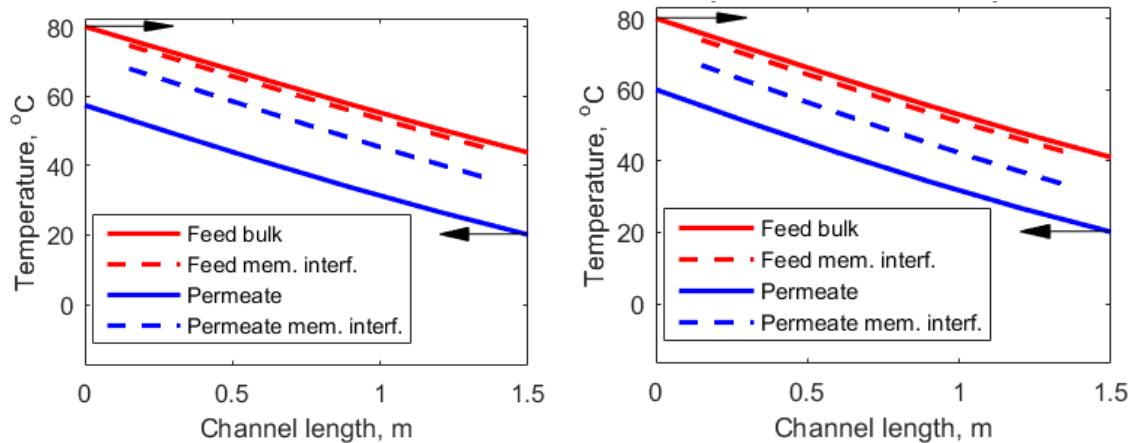
The optimization for the PGMD module is done in a similar way as the DCMD optimization (Table 6.2)

Table 6.2: Optimization of PGMD module. Parameters colored in green are included in the optimization, while the ones in yellow are optimized previously.

	Mem. Area, m ²	Mem. Thickness, μm	Channel thickness, mm	Module height, cm	Number of channels	Flow rate, l/h	Gap thickness, μm	GOR	Flux, kg/(m ² h)	Pressure drop, mBar	Goal Fn	Dist product. rate, l/hr
Salinity, 20 wt%	7.2	92	2	40	12	1100	800	0.91	4.49	310	3.83	32.30
	9	92	2	40	12	1100	800	1.02	3.52	322	3.87	31.71
	7.2	92	3	20	16	1800	800	0.70	7.27	344	5.59	52.37
	9	92	3	20	16	1700	800	0.84	5.67	345	5.60	51.05
	13	230	3	20	16	1500	800	1.11	4.14	340	6.16	53.85
	9	92	3	20	16	1700	500	1.02	6.07	345	6.14	54.62
	11	190	3	20	16	1600	500	1.12	5.22	345	6.52	57.44
Salinity, 10 wt%	7.2	92	2	40	12	1100	800	1.25	6.82	310	5.86	49.13
	20	92	2	40	12	1000	800	2.83	2.30	329	7.09	45.91
	7.2	92	3	20	16	1800	800	0.87	10.14	344	7.83	73.03
	11	92	3	20	16	1600	800	1.62	6.92	345	8.90	76.17
	13	110	3	20	16	1500	800	1.57	5.46	340	8.33	70.97
	13	92	3	20	16	1500	500	1.93	5.62	340	8.90	73.09
	13	110	3	20	16	1500	500	1.87	5.67	340	8.90	73.70

The goal function remains the same as for the DCMD case. During the optimization of the standard module geometry, the optimal solution is obtained at the highest permissible recirculation flow rate. Similar to the DCMD case, the biggest impact on the module optimization is brought about the flow-related module parameters - the channel thickness, module height and the number of parallel channels, allowing more water to be processed in the module.

An extra degree of freedom in this configuration is the thickness of the gap. Two gap thicknesses were studied - the default 800 μm and a thinner 500 μm gap. The influence of the gap thickness in PGMD can be studied by plotting the temperature profile along a single channel (Figure 6.8).



(a) Temperature profile along a single PGMD channel, 800 μm gap (b) Temperature profile along a single PGMD channel, 500 μm gap

Figure 6.8: Comparison of the temperature profiles in PGMD with different gap thicknesses

The smaller gap configuration exhibits a higher flux, since the resistance in the gap is decreased and the driving force across the membrane (the distance between the dashed lines) is increased. Moreover, the configuration with the smaller gap also exhibits a higher GOR. This is because in this configuration the difference between the bulk temperatures is decreased (solid lines) and thus the heating heat exchanger needs to put less energy into the stream (the permeate outlet temperature needs to be heated to the feed inlet temperature). Therefore, theoretically lower gap values are always desirable. In practice however, making the gap extremely small obstructs the drainage of the permeate. D. Winter [6] observed experimentally that making the gap smaller does not yield the improvements predicted by the model which was explained by swelling of the gap compartment due to the accumulation of permeate. Another possible explanation is that when the gap compartment pressure rises, the membrane will be compressed, which was shown to be detrimental due to the increased thermal conductivity of the membrane [148]. However, the modules used by Winter et al. have a height of 1 m, while the optimized modules here have long channels with height of only 0.2 m, reducing the flow velocity of distillate in the gap in the vertical (axial) direction. Therefore, the problem with pressure build-up in the gap compartment will be mitigated.

Similar to the DCMD case, optimizing the membrane thickness does not yield a significant improvement to the module design, and only a marginal improvement in the GOR is observed.

The optimal module designs for both salinities are very similar for both salinity cases - without including the gap and the membrane thickness in the optimization, the optimal membrane area is 9 or 11 m² for the 20 and the 10 wt% salinity cases, respectively. By optimizing the PGMD system, without including the membrane thickness in the optimization, an improvement of 49 and 54 % was obtained for the distillate production and the GOR, while the flux was reduced by only 18 % for the 10 % salinity case. For the 20 % salinity case the distillate production rate, flux and the GOR were all improved by 69, 35 and 12 %, respectively.

AGMD optimization

The optimization of the AGMD module was carried out in a similar way to the PGMD optimization (Table 6.3).

Table 6.3: Optimization of AGMD module. Parameters colored in green are included in the optimization, while the ones in yellow are optimized previously. The case with 1200 micron gap considers completely dry gap. The 800 micron gap uses the gap-flooding function described in Chapter 5

	Mem. Area, m ²	Mem. Thickness, μ m	Channel thickness, mm	Module height, cm	Number of channels	Flow rate, l/h	Gap thickness, μ m	GOR	Flux, kg/(m ² h)	Pressure drop, mBar	Dist Goal Fn	Dist product. rate, l/hr
Salinity, 20 wt%	7.2	92	2	40	12	1100	800	1.07	5.64	310	3.86	40.63
	13	92	2	40	12	1100	800	1.69	3.48	347	4.35	45.28
	15	92	3	30	16	1600	800	1.37	4.19	324	6.09	62.79
	19	92	3	30	16	1600	800	1.65	3.42	347	6.32	64.99
	19	170	3	30	16	1600	800	1.54	3.56	347	6.56	67.56
	25	92	3	30	16	1500	1200	2.15	3.15	341	7.76	78.87
	19	30	3	30	16	1600	1200	1.86	4.38	347	8.16	83.23
Salinity, 10 wt%	7.2	92	2	40	12	1100	800	1.27	7.35	310	5.11	52.94
	23	92	2	40	12	1000	800	3.64	2.60	345	6.00	59.77
	24	92	3	30	16	1500	800	2.63	3.57	336	8.49	85.67
	19	92	3	30	16	1600	800	2.06	4.60	347	8.59	87.36
	19	90	3	30	16	1600	800	2.07	4.60	347	8.59	87.35
	25	92	3	30	16	1500	1200	2.38	3.79	341	9.37	94.76
	25	30	3	30	16	1500	1200	2.712	3.96	341	9.83	99.03

Two cases were considered for the air gap. One where the value is kept at 800 micron and the gap-flooding is a function of the flux as calibrated in Chapter 5. In the other case the gap is considered 50 % thicker (1200 μ m), but without gap flooding. The gap flooding decreases the resistance of the gap as the water is more conductive than air. However, at full-scale, modules are limited by inflow energy, and the insulating properties of the gap make far more efficient use of the inflow energy and can potentially increase the overall flux.

The goal function here was slightly different compared to the previous configurations:

$$GoalFn = Flux. * Area./10 + GOR/10 - dP/1000 \quad (6.9)$$

AGMD can achieve extreme GORs at low fluxes. This is due to the flooding of the channels - low fluxes lead to low gap flooding, making the process very thermally efficient due to the insulation properties of the air inside the gap. Therefore, to avoid optimization of the module geometry for extremely low fluxes and high GORs, the importance of GOR was decreased in the goal function by dividing the value of GOR by 10.

As with the previous optimizations the largest effect is contributed by improving the flow-related parameters of the module. Similarly to the DCMD and PGMD case the optimal solution is with the thickest channels (3 mm) and the highest number of flow channels (16). Also in this configuration, optimizing the membrane thickness does not yield any appreciable improvements in the flux, GOR or the distillate production rate, when the gap is kept at the original value.

When the gap is increased to 1200 μm (line 6) the GOR and distillate production rate increased, while the flux is slightly reduced. Overall the case with larger, but dry gap yields better module performance. Interestingly, if the membrane thickness is optimized with a dry gap, the optimal membrane thickness is with the thinnest possible membrane. The heat and mass transfer are both resistances in series in the membrane-gap assembly. A thin membrane will minimize the resistance of the membrane, increasing the overall mass transfer of the gap-membrane assembly. On the other hand, a thin membrane will be very conductive, but in a completely dry gap, the limiting resistance for the heat transfer is going to be the resistance of the air inside the gap, hence the heat losses will not be increased appreciably with a thin membrane.

As with the previous configurations the optimal module design is the same for both salinities. Overall the optimization of the AGMD module yields 94 and 102 percent increase in the distillate production and the GOR, while the flux is reduced by 44 percent at the 20 % salinity case (line 6). In the 10 % salinity case the distillate production rate and GOR are increased by 79 and 87 % respectively, while the flux is reduced by 48 %. While the reduced flux is a drawback in the module optimization, the doubled distillate production rate is more important as the price for production and testing of the module will remain the same and only a few additional square meters of membrane and spacers will have to be added. It is also important to notice that the doubled

distillate production rate happens at only 36 % higher flow rate, which will also reduce the pumping costs.

6.3.2 Full-scale system optimization

In this section several case scenarios are studied and in each case a complete MD system is designed. This allows to study how parameters such as production scale, equipment costs, price of waste heat and personnel cost affects the final distillate price. Unless explicitly specified, the input parameters responsible for the capex and opex are listed in section 6.2.2, Figures 6.4 and 6.6.

Case 1: Small pilot scale, 2 m³/day

In this case an extremely small production scale is studied with distillate flow rate of 2 m³/day. The conditions are presented in Table 6.4

Table 6.4: Simulation inputs, Case 1

Distillate, m ³ /day	Waste heat, €/m ³	Personnel, hr/day	Feed, °C	Permeate, °C	Inlet Sa- linity, wt %	Final Sa- linity, wt %
2	0.02	0	80	20	6	20

It should be noted that the personnel was set to 0 man-hrs/day, otherwise this setting would oversaturate the distillate cost. If even one man-hr/day is considered, at 33 €/man-hr and distillate production of 2 m³/day, the opex price related to personnel would be 16.5 €/m³. Therefore, it is prohibitively expensive to include personnel cost at such small scale and the production must be as automated as possible. On the other hand, the membrane distillation systems are extremely automated and could be operated in an unmanned way, including the cleaning events, with only the maintenance being done manually. The simulation for this case with both AGMD and DCMD modules can be seen in Table 6.5.

Table 6.5: Simulation of the case scenario with AGMD and DCMD modules

	AGMD			DCMD		
	Stage 1	Stage 2	Stage 3	Stage 1	Stage 2	Stage 3
Sal, wt %	20			20		
Feed, °C	80			80		
Permeate, °C	20			20		
Q, l/module/hr	950			1500		
N Modules	4			4		
Area, m ²	24			7.2		
Flux, kg/m ² /hr	1.23			4.13		
WH flow, m ³ /hr	1.4			2.5		
Duty, kW	37.5			118.4		
kW-hr T /m ³	238			746		
Capex, €/m ³		6.3			8.5	
Opex, €/m ³		4.3			5.4	
Total, €/m ³		10.6			13.9	
System ,k€		58			79	

In both configurations a 7.2 and a 24 m², commercially available modules from Aquastill were considered. The lowest distillate price was achieved at the highest operational flow rates (950 and 1500 l/hr for the AGMD and DCMD respectively). It is interesting to notice that even though the salinity is extremely high, a better distillate price was achieved using the larger, 24 m² module for the AGMD case, whereas the smaller 7.2 m² module was selected for the DCMD case.

The price of waste heat in all case scenarios is set to 0.02 €/m³ as an example value, however it can easily be recalculated at the new price. In case that the waste heat is sold in €/m³, the opex price can be recalculated using the simulation output for thermal energy per cubic meter of distillate (kW-hr T /m³), given in Table 6.5.

The single pass recovery of a membrane distillation module is in the order of 3 to 5 percent [158]. Therefore, in order to achieve higher recovery, the water needs to be recirculated several times through the modules, by means of having a recirculation buffer tank. However, this also means that the modules will operate with the concentration inside the recirculation tank, which is also the final concentration. The driving force in membrane distillation is reduced at high salinities due to the decreased activity of the feed [105,117] and, therefore, it could be beneficial to operate the system in several stages with different salinities. The model is built in such a way that it can simulate up to three stages

connected in a "feed and bleed" configuration, where each stage bleeds part of the fluid to the next one. However, under the *Case scenario 1* conditions, the financial overhead of the additional equipment of more than 1 stage cannot be justified because of the small production scale and a cheaper price of the distillate is achieved with a single stage operating at the final salinity of 20 wt %.

It should be noted that in all case scenarios, the displayed fluxes are reduced, using the values listed in the cleaning and flux decline section (seen in Figure 6.6), i.e. the flux is reduced to 75 % of the simulated value in order to account for the short and long term flux decline due to fouling during the lifetime of the MD system. The AGMD based system performs better, achieving a lower capex and opex price of the distillate. The capex of DCMD is higher because the DCMD system has two separate loops, hence, two tanks and pumps instead of one in the case of AGMD. Moreover, the two loops require more sensors and the DCMD has an external recuperating heat exchanger. Additionally, the DCMD modules operate at higher flow rate, which increases the pumping costs, and the higher system price means higher costs for maintenance and insurance. Moreover, even though the DCMD modules work with an external recuperating heat exchanger, the thermal energy requirement is several times higher than the one of AGMD. Therefore, unless DCMD is needed due to a specific application (e.g. to use the DCMD modules not only for evaporation, but also as contactors [159] and possibly as reactors), the AGMD system is always more advantageous, due to its lower capex, opex and simplicity.

It should be noted that in our previous full-scale experimental practice the distillate conductivity was typically between 20 and 50 $\mu\text{S}/\text{cm}$, even when the feed salinity was as high as 200 g/l. This means that MD has a high potential to produce ultrapure water ($<5 \mu\text{S}/\text{cm}$), considering careful process operation and increase the revenue.

Detailed breakdown of the capex, opex and system price of the case scenario can be found in Appendix 9.4.

Case 2: Small production scale, 10 m³/day

In this case a small production scale is studied with a distillate flow rate of 10 m³/day. The conditions are presented in Table 6.6.

Table 6.6: Simulation inputs, Case 2

Distillate, m ³ /day	Waste heat, €/m ³	Personnel, hr/day	Feed, °C	Permeate, °C	Inlet Salinity, wt %	Final Salinity, wt %
10	0.02	0	80	20	6	20

In this case the personnel was also set to 0 man-hrs/day, since at this scale MD is likely to be an additional technology to an existing plant and the maintenance can be taken care of by pre-existing personnel. The simulation for this case with both AGMD and DCMD modules can be seen in Table 6.7.

Table 6.7: Simulation of the case scenario with AGMD and DCMD modules

	AGMD			DCMD		
	Stage 1	Stage 2	Stage 3	Stage 1	Stage 2	Stage 3
Sal, wt %	20			20		
Feed, °C	80			80		
Permeate, °C	20			20		
Q, l/module/hr	950			1500		
N Modules	16			16		
Area, m ²	24			7.2		
Flux, kg/m ² /hr	1.23			4.13		
WH flow, m ³ /hr	5.7			10		
Duty, kW	149.9			473.4		
kW-hr T /m ³	238			746		
Capex, €/m ³		3.3			4.4	
Opex, €/m ³		3.0			4.0	
Total, €/m ³		6.4			8.4	
System ,k€		124			166	

At this scale, similarly to the 2 m³/day case, the cheapest distillate was obtained by a system with a single stage operating at the highest salinity. The total distillate price is predicted to be almost two times lower compared to the 2 m³/day case, which is logical because only a few more modules and heat exchanger plates will be added to the existing system and a slightly higher capacity pump will have to be selected. The reduced system price also reduces the opex price because the maintenance and insurance prices will be lower. Detailed breakdown of the capex, opex and system price of the case scenario can be found in Appendix 9.5.

Case 3: Production scale, 100 m³/day

In this case a small production scale is studied with distillate flow rate of 100 m³/day. The conditions are presented in Table 6.8.

Table 6.8: Simulation inputs, Case 3

Distillate, m ³ /day	Waste heat, €/m ³	Personnel, hr/day	Feed, °C	Permeate, °C	Inlet Salinity, wt %	Final Salinity, wt %
100	0.02	1	80	20	6	20

In this case the personnel was set to 1 man-hrs/day. The simulation for this case with both AGMD and DCMD modules can be seen in Table 6.9

Table 6.9: Simulation of the case scenario with AGMD and DCMD modules

	AGMD			DCMD		
	Stage 1	Stage 2	Stage 3	Stage 1	Stage 2	Stage 3
Sal, wt %	13	20		13	20	
Feed, °C	80	80		80	80	
Permeate, °C	20	20		20	20	
Q, l/module/hr	950	950		1500	1500	
N Modules	90	37		89	36	
Area, m ²	24	24		7.2	7.2	
Flux, kg/m ² /hr	1.65	1.2		5.6	4.13	
WH flow, m ³ /hr	29.5	13.5		55.2	22.5	
Duty, MW	0.86	0.35		2.52	1.07	
kW-hr T /m ³	181	249		527	746	
Capex, €/m ³		1.3			1.7	
Opex, €/m ³		2.1			2.7	
Total, €/m ³		3.4			4.4	
System ,k€		484			633	

At this scale the equipment starts to become significantly cheaper due to scale factors (also known as economy of scale). This significantly reduces the capital expenditures of the system per m³ of produced distillate. The MD modules also become cheaper at this scale, since they would have been produced in a more automated way, better contracts can be negotiated for the membranes, spacers, etc.

The opex price of the distillate is also significantly reduced. The larger scale justifies the use of two stages operating at different salinity, instead of only one.

This means that the modules operate more efficiently, hence, less modules and supporting equipment is needed as well as the thermal efficiency is increased, which directly translates to using less waste heat.

Detailed breakdown of the capex, opex and system price of the case scenario can be seen in Appendix 9.6.

Case 4: Large production scale, 1000 m³/day

In this case a very large production scale is studied with distillate flow rate of 1000 m³/day. The conditions are presented in Table 6.10.

Table 6.10: Simulation inputs, Case 4

Distillate, m ³ /day	Waste heat, €/m ³	Personnel, hr/day	Feed, °C	Permeate, °C	Inlet Salinity, wt %	Final Salinity, wt %
1000	0.02	8	80	20	6	20

In this case the personnel was set to 8 man-hrs/day, i.e. one person at full time employment. The simulation for this case with both AGMD and DCMD modules can be seen in Table 6.11.

Table 6.11: Simulation of the case scenario with AGMD and DCMD modules

	AGMD			DCMD		
	Stage 1	Stage 2	Stage 3	Stage 1	Stage 2	Stage 3
Sal, wt %	10	15	20	10	15	20
Feed, °C	80	80	80	80	80	80
Permeate, °C	20	20	20	20	20	20
Q, l/module/hr	950	950	950	1500	1500	1500
N Modules	620	365	227	605	350	220
Area, m ²	24	24	24	7.2	7.2	7.2
Flux, kg/m ² /hr	1.79	1.51	1.2	6.1	5.2	4.13
WH flow, m ³ /hr	197	126	82.7	373	218	137
Duty, MW	5.93	3.59	2.18	17.0	10.0	6.5
kW-hr T /m ³	167	204	249	479	571	746
Capex, €/m ³		0.6			0.8	
Opex, €/m ³		1.5			2.1	
Total, €/m ³		2.1			2.9	
System ,M€		2.28			2.76	

At this scale, the cheapest distillate is obtained when three stages of salinity are used. This makes the system operate much more efficient, using even less modules, additional equipment and waste heat for the same volume of produced distillate. The modules are also becoming much cheaper due to the scale factor. For example the price of the 24 m² AGMD in the *Case 1* was 2975 €, while in this case, the same module costs only 950 € or about 40 €/m² of membrane in-module price. While this price is much lower than in *Case 1*, the in-module price is still roughly two times higher than the currently available RO modules. The module price accounts for about 50 % of the system price at this scale (Appendix 9.7) and the capex accounts only for about 1/3 of the price of the distillate. Therefore, if the modules cannot be produced so cheaply, the final price of the produced distillate will not be much higher.

It should be noted that the power required to desalinate water at this scale is extremely large - 9.7MW and 33.5 MW for the AGMD and DCMD system, respectively. Possible supplies of waste heat at this production scale are power generation plants. While the supply of waste heat can be a potential problem, it can also be considered as an advantage. The efficiency of a typical power plant is typically between 40 and 70 % and the remaining thermal energy is released as heat to the environment, which can have a significant environmental impact [160]. Typically power plants are required to build cooling ponds, before discharge is permitted. With MD it is possible to use the system as a heat sink for power plants and reduce the environmental impact of waste heat. In fact, one possibility is to use a DCMD system without an external recuperating heat exchanger, which will utilize a tremendous amount of heat and reduce the system price of MD and avoid the building of cooling ponds.

Detailed breakdown of the capex, opex and system price of the case scenario can be found in Appendix 9.7.

Simulation of the case scenarios using the optimized modules

In this section, the AGMD and DCMD modules optimized in section 6.3.1 are used in order to simulate Cases 1-4 and check the impact of the optimization. The optimized modules have the following dimensions (Table 6.12).

Table 6.12: Properties of the optimized AGMD and DCMD modules

	Area, m ²	Mem. Thickness, μ m	Channels thickness, mm	Module Height, cm	Number of channels	Flow rate, l/hr	Gap thickness, μ m
AGMD	25	92	3	30	16	1500	1200
DCMD	8	92	3	30	16	2600	

When the optimized modules are used to simulate the Cases 1-4, the following results are obtained (Table 6.13)

Table 6.13: Simulation of the case scenarios using the optimized DCMD and AGMD modules

	Commercial AGMD			Optimized AGMD			Reduction of total price, %
	Capex, €/m ³	Opex, €/m ³	Total, €/m ³	Capex, €/m ³	Opex, €/m ³	Total, €/m ³	
Case 1	6.3	4.3	10.6	4.8	3.1	7.9	25
Case 2	3.3	3	6.4	2.5	2.2	4.7	27
Case 3	1.3	2.1	3.4	1	1.9	2.8	18
Case 4	0.6	1.5	2.1	0.4	1.5	1.9	11
	Commercial DCMD			Optimized DCMD			
	Capex, €/m ³	Opex, €/m ³	Total, €/m ³	Capex, €/m ³	Opex, €/m ³	Total, €/m ³	
Case 1	8.5	5.4	13.9	8.4	5.5	13.9	0
Case 2	4.4	4	8.4	3.9	3.9	7.8	7
Case 3	1.7	2.7	4.4	1.4	2.9	4.4	0
Case 4	0.8	2.1	2.9	0.7	2.3	3	-3

It should be noted that more heat exchanger plates were used in the simulations with the optimized modules in order to keep the pressure drop of the heat exchangers to their previous levels. In the case of AGMD 23 instead of 15 plates per module were used and for the DCMD 26 plates per module were used in the cooling and heating heat exchanger and 60 instead of 40 plates per module were used in the recuperating heat exchanger.

The results of the simulation with optimized modules suggests that for AGMD the optimized modules can reduce the price of distillate by up to 27 percent and the influence becomes lower at larger scale, since the share of the capital cost is decreased at larger scale.

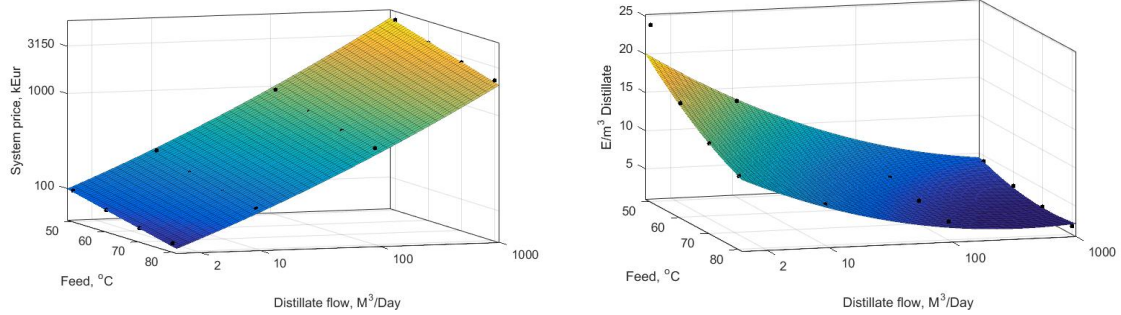
However, for DCMD the effect of using optimized modules has mixed results. While the optimized modules reduce the capital costs, the higher flow rate increases the pumping cost and the overall distillate price remains similar. A

better crafted goal function is probably needed in order to improve the module design optimization.

More importantly the optimized modules have the same dimension for both 10 and 20 wt % salinity, meaning that the systems can be built and operated in a batch mode. This has the advantage that the modules will work extremely efficient (equates to a system with infinite number of stages). Such a system can be applied for the lower-production scales where more than one stage cannot be justified due to the financial overhead of the supporting equipment in each stage. The batch operation would mean that an extra buffer tank must be installed to allow for continuous operation, however it is likely that this price will be justified.

Simplified cost model, influence of feed temperature and final salinity

In this section, the Case scenarios 1-4 were simulated at 50, 60, 70 and 80 °C feed temperatures. Furthermore, two cases of final recovery were tested. In the first case the final salinity was 20 wt%, while in the second case a final salinity of only 12 wt % was achieved. In the 12 wt % case there was only one salinity stage, since this configuration achieved the lowest distillate price. By simulating all of these conditions, a simplified cost model for the system price and the total distillate price can be built by constructing a polynomial fit to the data which can be utilized as a simple cost estimation tool. The cost estimation plane for AGMD at 20 wt % final concentration can be seen (Figure 6.9).



(a) System price as a function of feed temperature and production scale, 20 wt % final concentration, AGMD

(b) Distillate price as a function of feed temperature and production scale, 20 wt % final concentration, AGMD

Figure 6.9: System and distillate price as a function of feed temperature and production scale, 20 wt % final concentration, AGMD. Notice that the axes for the distillate production and system price are logarithmic.

Two polynomial equations were constructed for the system price and the distillate price:

$$DistPrice = C1 + C2T_f + C3 \log Q_{Dist} + C4T_f \log Q_{Dist} + C5(\log Q_{Dist})^2 \quad (6.10)$$

$$SystemPrice = 10^{(C1+C2T_f+C3 \log Q_{Dist}+C4T_f \log Q_{Dist}+C5(\log Q_{Dist})^2)} \quad (6.11)$$

Where $DistPrice$, $SystemPrice$, T_f and Q_{Dist} are the price of distillate (€/m³), system price (k€), feed temperature (°C) and distillate production (m³/day). The constants C1-C5 are listed below (Table 6.14).

Table 6.14: Constants used in the simplified cost model

	AGMD				DCMD			
	System Price		Distillate Price		System Price		Distillate Price	
	12 wt %	20 wt %	12 wt %	20 wt %	12 wt %	20 wt %	12 wt %	20 wt %
C1	2.083	2.247	25.79	37.26	2.244	2.518	42.37	62.54
C2	-0.00689	-8.091E-03	-0.1907	-0.3046	-0.00684	-9.966E-03	-0.3584	-0.5697
C3	0.5341	0.5186	-10.18	-14.95	0.544	0.5084	-16.35	-24.36
C4	-0.001163	-8.548E-04	0.04512	0.08487	-0.001682	-5.85E-04	0.09448	0.1599
C5	0.04565	0.04323	1.238	1.521	0.04252	0.03541	1.697	2.293
Fit	R ² =0.99	R ² =0.99	R ² =0.98	R ² =0.98	R ² =0.99	R ² =0.99	R ² =0.97	R ² =0.96

6.4 Conclusions

In this chapter, for the first time in literature a complete tool for module and system design of MD has been presented. Modules of the three most popular MD configurations (AGMD, PGMD and DCMD) can be optimized based on a user-defined goal function.

It was demonstrated that on full-scale, the membrane thickness is less important than it is on lab-scale. In previous work the optimal membrane thickness was shown to be a function of the intermembrane driving force [117]. However, it can be problematic to tune the membrane thickness for an already existing commercially available membrane. Instead, the module design can be tuned on full-scale to create the optimal driving force for the current membrane thickness.

For all 3 configurations the optimal module design was shown to be the same, or very similar for both 12 and 20 wt % salinities. This means that the same module can be used in a batch operated system, operating the system extremely efficiently. Batch operation is expected to be extremely beneficial for small scale systems, where building multiple stages of salinity is not economically feasible.

The modelling tool was also used to design complete systems and performed a detailed cost analysis for four different case scenarios, predicting the system and the distillate price. The AGMD system was shown to outperform the DCMD system in terms of distillate and system price. The price of the MD distillate was demonstrated to vary from 25 €/m³ of distillate on small scale and low feed temperatures to as low as 2.1 €/m³ on large scale and high feed temperatures. The price of waste heat is an important factor. Therefore, in each of the 4 case scenarios the thermal consumption per m³ of distillate was presented, allowing the reader to re-calculate the distillate price.

The four different case scenarios were also simulated using the optimized modules, revealing that up to 27 % lower price of the distillate can be achieved using the optimized modules. This suggests that the module design can be a very important factor for the cost of the distillate.

A simplified cost model was presented, allowing the reader to quickly estimate the price of a AGMD or DCMD system at different production scales, recovery ratios and feed temperatures.

CHAPTER 7

Conclusions and perspectives

7.1 General conclusions

Throughout this thesis modelling of membrane distillation was performed both on lab- and full-scale. The thesis revealed various insights both regarding the model build up as well as bottlenecks in the process. Finally, a decision support tool was demonstrated for automated system and module optimization. The main conclusions that can be drawn from the work are summarized here.

7.1.1 *Lab-scale modelling*

The literature review in Chapter 2 revealed that the mass transfer modelling of the membrane region has been covered by many different mechanistic and statistical models that can predict the flux with varying accuracy. More recent models such as the ballistic transport model and the structural network models are innovative and could be used for building knowledge relevant to membrane synthesis, but have not yet been thoroughly tested and validated. Some of the physical phenomena that occur inside the membrane such as the surface diffusion has always been neglected in MD modelling which can prove to be important for membrane synthesis studies.

Computational fluid dynamics (CFD) can be useful for the development of novel spacers as well as overall improvement of the module design. However, to date there are only a handful of studies utilizing CFD in membrane distillation modelling.

In Chapter 3 a series of supported and unsupported membranes were simulated and the model structure was examined using a Monte Carlo filtering method. The study concluded that the Nusselt equations can predict the heat transfer in the system with satisfactory accuracy, however these equations need to be properly calibrated for each particular flow spacer and transferral between different systems needs to be done with care.

A three dimensional interaction between the pore size, tortuosity and porosity was found in the dusty gas model if all three parameters are simultaneously calibrated. Whereas, the fit is not really improved, a unique calibration set cannot be produced if all 3 are adjusted simultaneously. Since the tortuosity is the most uncertain of the 3 and cannot be measured trivially, it was left as the only calibration parameter concerning the membrane permeability.

The choice of mass transfer model for the membrane permeability is of little importance for the predictive power. The permeability constant was found to give rise to the same quality of fit as the most sophisticated models and is therefore recommended. Yet, this model cannot be used to study the importance of the structural parameters of the membrane and when this is the modelling goal, a more sophisticated model such as the newly proposed Kn corrected DGM equation by Field et al. (eq. 3.33) is a good candidate. This model also predicts more realistically the membrane tortuosity and is therefore recommended over the traditional DGM model.

The thermal conductivity of the membrane proved to be a very important calibration parameter but its value can only be identified if both the errors of flux and the energy efficiency are evaluated during the calibration, unlike the traditional approach where only the flux error is evaluated.

7.1.2 *Full-scale MD modelling*

Full-scale DCMD modelling

The commercially available, spiral wound, direct contact membrane distillation modules from Aquastill were modeled in Chapter 4. The channels are virtually unwound and discretized in small sections in which the lab-scale model proposed in Chapter 3 is applied in each section.

The effect of membrane compaction was modelled and validated on a full-scale for the first time, using a commercially available module. Moreover, a methodology for scaling up of a direct contact membrane distillation model from

lab-scale to full-scale was demonstrated without the need of additional calibration of the full-scale model. This underlines that when the lab-scale calibration is performed properly, the model can be scaled-up with confidence, since all of the resistances in the system are identified correctly. In this way the model can be used for optimization of the bottlenecks in the system.

The full-scale module flux is severely limited by the inflow energy and would benefit from a membrane with lower thermal conductivity just as much as a more permeable membrane. Because of the limited inflow energy, the influence of the thermal and concentration polarization inside the flow channels is minimal.

It was demonstrated that the membrane used in the module compacts significantly, even though the operational pressures can be considered mild. The membrane compaction mainly increased the thermal conductivity of the membrane, while the permeability was almost unaltered within the tested range.

When the model was extended to account for the membrane compaction, values of $R^2=0.99$ for both the flux and the outlet temperatures were achieved. All of the commercially available MD modules used today utilize PTFE or PE membranes that are produced by stretching. Previous papers have demonstrated the compressibility of the stretched PTFE membranes, while the current work reveals the same for the stretched PE membrane. Therefore, this effect should not be further neglected in MD modelling.

Full-scale AGMD modelling

In Chapter 5 for the first time a model without calibration parameters was created for air gap membrane distillation. A previously developed DCMD model (Chapter 4) was extended by adding the air gap compartment. For the first time in the literature the gap-related parameters were measured in relatively simple lab-scale experiments allowing to create an air gap model without calibration parameters. Moreover, the method allowed for the best visual observation to date of the condensation in the gap.

By measuring, instead of calibrating the gap-related parameters the model can now be used for optimizing the module design. This is also the first model to date that considers the air gap configuration as partially flooded. Thorough validation using two commercially available modules with different areas was performed demonstrating that the model can predict both the flux and the outlet temperatures of the modules with high accuracy at various conditions.

For the first time in the literature an air gap and a direct contact module from the same manufacturer and geometries were directly compared at identical conditions. In contrast to the popular belief, both the flux and the energy efficiency were higher for the air gap modules. This was explained by the severe limitation of the full-scale MD modules in terms of inflow energy fed into the module and the lack of membrane compaction in the air gap configuration.

7.1.3 *Process and module optimization of membrane distillation*

In Chapter 6, for the first time in literature a complete tool for module and system design of MD has been presented. Modules of the three most popular MD configurations (AGMD, PGMD and DCMD) can be optimized automatically based on a user-defined goal function.

It was demonstrated that on full-scale, the membrane thickness is less important than it is on lab-scale. In previous work the optimal membrane thickness was shown to be a function of the intermembrane driving force [117]. However, it can be problematic to tune the membrane thickness for an already existing commercially available membrane. Instead, the module design can be tuned on full-scale to create the optimal driving force for the current membrane thickness.

For all 3 configurations the optimal module design was shown to be the same, or very similar for both 12 and 20 wt % salinities. This means that the same module can be used in a batch operated system, operating the system extremely efficiently. Batch operation is expected to be extremely beneficial for small scale systems, where building multiple stages of salinity is not economically feasible.

The modelling tool was also used to design complete systems and performed a detailed cost analysis for four different case scenarios, predicting the system and the distillate price. The AGMD system was shown to outperform the DCMD system in terms of distillate and system price. The price of the MD distillate was demonstrated to vary from 25 €/m³ of distillate on small scale and low feed temperatures to as low as 2.1 €/m³ on large scale and high feed temperatures.

The four different case scenarios were also simulated using the optimized modules, revealing that up to 27 % lower price of the distillate can be achieved using the optimized modules. This suggests that the module design can be a very

important factor for the cost of the distillate.

A simplified cost model was presented, allowing the reader to quickly estimate the price of a AGMD or DCMD system at different production scales, recovery ratios and feed temperatures.

7.2 Perspectives

Different knowledge gaps, promising areas of future research are listed below:

7.2.1 *Improvements and gaps in the experimental measurements*

- As demonstrated in this thesis the existing module designs are severely limited by the inflow energy flown into the modules. Consequently, the thermal conductivity of the membrane is of equal importance as the membrane permeability for DCMD. However, to date there is no reliable method to measure this parameter beforehand. The problem is that when the membrane is clamped between two disks to measure its thermal conductivity, if the applied pressure is too high, the membrane is likely to get compressed and the thermal conductivity overestimated. On the other hand if the clamping force is too low, the contact resistances will be too high and the thermal conductivity will be underestimated. One possible way to measure it is to use a laser flash technique [41], but to date this is rarely done.
- The membrane used in the Aquastill module was shown to compact under the typical pressures exhibited in the modules. The compressibility was shown to have a significant effect on the performance of the full-scale DCMD module and therefore the membrane compressibility should be included in the membrane characterization routine. Moreover, the membrane compaction effect should be tested for hysteresis, i.e. to see if the compaction is reversible or permanent. As a follow up of this study the stretching effect of the membrane should be tested. If the membrane stretches, it will bulge inside the spacer opening, effectively changing the thickness of the channels, which will affect the heat and mass transfer properties.

- The main effect of the membrane compressibility is on the thermal conductivity of the membrane. When the membrane is compacted, it becomes less porous, hence, more thermally conductive. Therefore, ideally, the thermal conductivity measurement should be combined with the compressibility measurement, however, the problem with the contact resistances at light pressures should still be avoided.
- The thermal conductivity currently is derived on lab-scale by fitting both the flux and the energy efficiency of the model to the experimentally obtained values. However, the experimental calculation of the energy efficiency requires an accurate measurement of the temperature drop along the flow channels. The lab-scale module has membrane area of only 0.0108 m² and at the typical flow rates of 60 l/hr, the measured temperature drops along a single channel of the module are only 1-3 °C. This means that small inaccuracies in the temperature measurement due to sensor drifting, sensor positioning in the tube and losses to the environment include extremely high uncertainties in the measurement of energy efficiency. One possible approach is to perform the experiments at lower flow rates, which will increase the temperature drop, but will worsen the problem with sensor positioning. Another approach is to use a larger lab-scale module, where the temperature drop will also be larger. The better accuracy in the measurement of the energy efficiency will improve the calibration of the thermal conductivity of the membrane.
- Currently, apart from the spacer-filled spacers there is no knowledge how the pressure drop evolves in the full-scale modules. The model suggests that the manifolds inside the module are creating pressure drops up to 3-4 times higher than the spacer-filled channels. The pressure drop is unwanted in membrane distillation since it increases the pumping costs, creates risk conditions for membrane wetting and in DCMD can lead to membrane compaction which has a negative impact on the process. Therefore, the internal flow organization inside the full-scale modules need to be studied and optimized. Computational fluid dynamics can serve as an extremely helpful tool in this optimization.

7.2.2 *Process and module optimization gaps and promising research paths*

- The experimental methods shown in Chapter 5 can be used for further analysis of the condensation process inside the air gap compartment. The method can be used to test different combinations of gap spacers and condensation foils and directly measure the degree of flooding inside the gap.
- Out of the three tested configurations (DCMD, PGMD and AGMD), the AGMD configuration seems to be the most promising. One way to intensify AGMD is to apply light vacuum in the air gap compartment. It should be clearly distinguished that, in such case, the vacuum will not be the driving force in the system and will only be applied to evacuate the air from the air gap compartment. Although applying vacuum is considered expensive, the volume of the non-condensable gases from the air gap is small due to the low solubility of nitrogen and oxygen in water, therefore a relatively small pump is required for this purpose. Applying vacuum immensely intensifies the mass transfer inside the gap, since the mechanism of vapor travel will no longer be diffusion of water vapors through a stagnant layer of air. Instead, the transport mechanism in such a system will be viscous flow, which is tremendously more efficient than diffusion. Applying vacuum to an air gap configuration has previously been demonstrated, amongst others, by D. Winter [6] and lead to intensification of both flux and GOR.
- Since the full-scale modules in MD are limited by inflow energy, the influence of heat and mass transfer inside the flow channels is much less important, compared to lab-scale. Therefore it is possible that the system can benefit from another spacer that has different mixing or pressure drop properties. The current optimization of the module design did not attempt different spacers and therefore it could be interesting to study this aspect of module design in future works.
- Building multiple stages, each with increasing salinity makes membrane distillation operate more efficiently when high recovery ratios are required. However, on small production scales it is not economically feasible to build more than 1 stage. Operating such system in batch mode can be extremely beneficial, since batch operation equates to a system with infinite number of stages at the expense of a slightly more complicated system and the need for a buffer tank to enable continuous operation. In order to simulate such

system, a time dependent MD model is needed. Therefore, it could be interesting to extend the current model and explore the possible savings in such a configuration.

- The current model is limited to simulation of NaCl feeds. However, membrane distillation is becoming a niche market technology, applied on complex feed streams and not only limited to desalination. Therefore, it would be beneficial to attempt to model the performance of MD with such streams too. Different feeds, however, would have different activity, thermal conductivity, specific heat capacity, density, viscosity, etc., and measuring and integrating all of these fluid parameters as a function of temperature and concentration inside the model can be extremely complex and time consuming. Most of the time such feeds have a complex composition and the fluid properties cannot be easily looked up from tables. From the process knowledge obtained with modelling it was found that the heat and mass transfer inside the channels are not as important on full-scale, compared to lab-scale. It is therefore possible that a good fit will be obtained even if the changes in fluid properties responsible for heat and mass transfer in the channels are neglected.

CHAPTER 8

Bibliography

Bibliography

- [1] USGS, International desalination association - IDA.
URL <https://water.usgs.gov/edu/earthhowmuch.html>
- [2] J. Glater, The early history of reverse osmosis membrane development, *DESALINATION* 117 (1) (1998) 297 – 309. doi:[http://dx.doi.org/10.1016/S0011-9164\(98\)00122-2](http://dx.doi.org/10.1016/S0011-9164(98)00122-2).
URL <http://www.sciencedirect.com/science/article/pii/S0011916498001222>
- [3] International desalination association - IDA.
URL <http://idadesal.org/publications/fact-sheets/>
- [4] Water desalination: When and where will it make sense?
URL https://ec.europa.eu/jrc/sites/jrcsh/files/jrc_aaas2011_energy_water_koschikowski.pdf
- [5] M. Elimelech, W. A. Phillip, The future of seawater desalination: Energy, technology, and the environment, *SCIENCE* 333 (6043) (2011) 712–717. arXiv:<http://science.sciencemag.org/content/333/6043/712.full.pdf>, doi:10.1126/science.1200488.
URL <http://science.sciencemag.org/content/333/6043/712>
- [6] D. Winter, Membrane distillation: A thermodynamic, technological and economic analysis, Dissertation. doi:10.2370/9783844037067.
- [7] A. Ali, F. Macedonio, E. Drioli, S. Aljlil, O. Alharbi, Experimental and theoretical evaluation of temperature polarization phenomenon in direct contact membrane distillation, *CHEM ENG RES DES* 91 (2013) 1966–1977.
- [8] S. Al-Obaidani, E. Curcio, F. Macedonio, G. Di Profio, H. Al-Hinai, E. Drioli, Potential of membrane distillation in seawater desalination: Thermal

- efficiency, sensitivity study and cost estimation, *J MEMBRANE SCI* 323 (2008) 85–98.
- [9] B. R. Bodel, Silicone rubber vapor diffusion in saline water distillation, United States Patent Serial No. 285,032 (1963).
- [10] A. Tamburini, G. Micale, M. Ciofalo, A. Cipollina, Experimental analysis via thermochromic liquid crystals of the temperature local distribution in membrane distillation modules, *CHEM ENG TRANS* 32 (2013) 2041–2046.
- [11] A. Tamburini, P. Pitò, A. Cipollina, G. Micale, M. Ciofalo, A thermochromic liquid crystals image analysis technique to investigate temperature polarization in spacer - filled channels for membrane distillation, *J MEMBRANE SCI* 447 (2013) 260–273.
- [12] V. U. Kakade, M. Lock, G. D. Wilson, J. M. Owen, J. Mayhew, Accurate heat transfer measurements using thermochromic liquid crystal. Part 1: Calibration and characteristics of crystals, *INT J HEAT FLUID FL* 30 (2009) 939–949.
- [13] M. Gryta, M. Tomaszewska, M. A. W., Membrane distillation with laminar flow, *SEP PURIF TECHNOL* 11 (1997) 93–101.
- [14] M. Gryta, M. Tomaszewska, Heat transport in the membrane distillation process, *J MEMBRANE SCI* 144 (1998) 211–222.
- [15] J. Phattaranawik, R. Jiraratananon, A. Fane, Heat transport and membrane distillation coefficients in direct contact membrane distillation, *J MEMBRANE SCI* 212 (2003) 177–193.
- [16] M. Khayet, A. Velazques, J. Mengual, Modelling mass transport through a porous partition: Effect of pore size distribution, *J NON-EQUIL THERMODY* 29 (2004) 279–299.
- [17] X. Yang, H. Yu, R. Wang, A. G. Fane, Analysis of the effect of turbulence promoters in hollow fiber membrane distillation modules by computational fluid dynamics (CFD) simulations, *J MEMBRANE SCI* 415-416 (2012) 758–769.
- [18] X. Yang, H. Yu, R. Wang, A. G. Fane, Optimization of microstructured hollow fiber design for membrane distillation applications using CFD modelling, *J MEMBRANE SCI* 421-422 (2012) 258–270.

- [19] H. Yu, X. Yang, R. Wang, A. G. Fane, Numerical simulation of heat and mass transfer in direct membrane distillation in a hollow fiber module with laminar flow, *J MEMBRANE SCI* 384 (2011) 107–116.
- [20] H. Yu, X. Yang, R. Wang, A. G. Fane, Analysis of heat and mass transfer by CFD for performance enhancement in direct contact membrane distillation, *J MEMBRANE SCI* 405-406 (2012) 38–47.
- [21] M. Shakaib, A. Iqbal, R. M. Yunus, CFD modeling for fluid flow and heat transfer in membrane distillation, in: *2nd International Conference on Environmental Science and Technology*, 2011, pp. 265–268.
- [22] M. Shakaib, S. Hasani, I. Ahmed, R. M. Yunus, A CFD study on the effect of spacer orientation on temperature polarization in membrane distillation modules, *DESALINATION* 284 (2012) 332–340.
- [23] M. Khayet, Membranes and theoretical modeling of membrane distillation: A review, *ADV COLLOID INTERFAC* 164 (2011) 56–88.
- [24] F. Lagana, G. Barbieri, E. Drioli, Direct contact membrane distillation: modelling and concentration experiments, *J MEMBRANE SCI* 166 (2000) 1–11.
- [25] K. W. Lawson, D. R. Lloyd, Membrane distillation. II. direct contact MD, *J MEMBRANE SCI* 120 (1996) 123 – 133.
- [26] K. W. Lawson, D. R. Lloyd, Membrane distillation, *J MEMBRANE SCI* 124 (1997) 1–25.
- [27] L. Martínez, J. Rodríguez-Maroto, On transport resistances in direct contact membrane distillation, *J MEMBRANE SCI* 295 (2007) 28–39.
- [28] R. W. Schofield, A. G. Fane, C. J. D. Fell, Gas and vapor transport through microporous membranes. I. knudsen-poiseuille transition, *J MEMBRANE SCI* 53 (1990) 159–171.
- [29] R. W. Schofield, A. G. Fane, C. J. D. Fell, Gas and vapor transport through microporous membranes. II. membrane distillation, *J MEMBRANE SCI* 53 (1990) 173–185.
- [30] A. Imdakm, T. Matsuura, A monte carlo simulation model for membrane distillation process: direct contact (MD), *J MEMBRANE SCI* 237 (2004) 51–59.

- [31] A. Imdakm, T. Matsuura, Simulation of heat and mass transfer in direct contact membrane distillation (MD): The effect of membrane physical properties, *J MEMBRANE SCI* 262 (2005) 117–128.
- [32] A. Imdakm, M. Khayet, T. Matsuura, A monte carlo simulation model for vacuum membrane distillation process, *J MEMBRANE SCI* 306 (2007) 341–348.
- [33] M. Khayet, A. Imdakm, T. Matsuura, Monte carlo simulation and experimental heat and mass transfer in direct contact membrane distillation, *INT J HEAT MASS TRAN* 53 (2010) 1249–1259.
- [34] M. Qtaishat, T. Matsuura, B. Kruczek, M. Khayet, Heat and mass transfer analysis in direct contact membrane distillation, *DESALINATION* 219 (2008) 272–292.
- [35] E. Curcio, D. E., Membrane distillation and related operations - A Review, *SEPAR PURIF REV* 34 (2005) 35–86.
- [36] J. Zhang, S. Gray, J. Li, Modelling heat and mass transfers in DCMD using compressible membranes, *J MEMBRANE SCI* 387-388 (2012) 7–16.
- [37] K. K. Sirkar, L. Song, Pilot-scale studies for direct contact membrane distillation-based desalination process, U.S. department of the interior bureau of reclamation, Report No. 134 (2009).
URL <http://www.usbr.gov/research/AWT/reportpdfs/report134.pdf>
- [38] L. Martínez-Díez, M. Vázquez-González, F. J. Florido-Díaz, Study of membrane distillation using channel spacers, *J MEMBRANE SCI* 144 (1998) 45–56.
- [39] A. Jonsson, R. Wimmerstedt, A. Harrysson, Membrane distillation - a theoretical study of evaporation through microporous membranes, *DESALINATION* 56 (1985) 237–249.
- [40] M. C. Garcia-Payo, M. A. Izquierdo-Gil, Thermal resistance technique for measuring the thermal conductivity of thin microporous membranes, *J PHYS D* 37 (21) (2004) 3008–3016.
- [41] L. F. Dumée, S. Grey, M. Duke, K. Sears, J. Schültz, N. Finn, The role of membrane surface energy on direct contact membrane distillation performance, *DESALINATION* 323 (2013) 22–30.

- [42] M. Izquierdo-Gil, M. Garcia-Payo, C. Fernandez-Pineda, Air gap membrane distillation of sucrose aqueous solutions, *J MEMBRANE SCI* 155 (1999) 291–307.
- [43] A. Bahmanyar, M. Asgharia, N. Khoobi, Numerical simulation and theoretical study on simultaneously effects of operating parameters in direct contact membrane distillation, *CHEM ENG PROCESS* 61 (2012) 42–50.
- [44] A. Saleem, L. Frommann, A. Iqbal, High performance thermoplastic composites: Study on the mechanical, thermal, and electrical resistivity properties of carbon fiber-reinforced polyetheretherketone and polyethersulphone, *POLYM COMPOSITE* 28 (2007) 785–796.
- [45] L. Martínez-Díez, Vázquez-González, Temperature and concentration polarization in membrane distillation of aqueous salt solutions, *J MEMBRANE SCI* 156 (1999) 265–273.
- [46] M. N. Chernishov, G. W. Meidersma, A. B. de Haan, Modelling of temperature and salt concentration distribution in membrane distillation feed channel, *DESALINATION* 157 (2003) 315–324.
- [47] M. Gryta, Fouling in direct contact membrane distillation process, *J MEMBRANE SCI* 325 (2008) 383–394.
- [48] S. Srisurichan, R. Jiratananon, A. Fane, Mass transfer mechanisms and transport resistances in direct contact membrane distillation process, *J MEMBRANE SCI* 277 (2006) 186–194.
- [49] Y. Yun, R. Ma, W. Zhang, A. G. Fane, J. Li, Direct contact membrane distillation mechanism for high concentration nacl solutions, *DESALINATION* 188 (2006) 251–262.
- [50] J. Gilron, Y. Ladizansky, E. Korin, Silica fouling in Direct Contact Membrane Distillation, *IND ENG CHEM RES* 52 (2013) 10521–10529.
- [51] J. W. Chew, W. B. Krantz, A. G. Fane, Effect of a macromolecular- or bio-fouling layer on membrane distillation, *J MEMBRANE SCI* 456 (2014) 66–76.
- [52] L. Martínez, F. Florido-Díaz, Theoretical and experimental studies on desalination using membrane distillation, *DESALINATION* 139 (2001) 373–379.

- [53] C. Fernández-Pineda, M. A. Izquierdo-Gil, M. C. García-Payo, Gas permeation and direct contact membrane distillation experiments and their analysis using different models, *J MEMBRANE SCI* 198 (1) (2002) 33 – 49.
- [54] A. Sereno, M. Hubinger, J. Comesana, A. Correa, Prediction of water activity of osmotic solutions, *J FOOD ENG* 49 (2011) 103–114.
- [55] R. Schofield, A. Fane, C. Fell, Heat and mass transfer in membrane distillation, *J MEMBRANE SCI* 33 (3) (1987) 299 – 313.
- [56] M. Khayet, T. Matsuura, *Membrane distillation principles and applications*, Elsevier, 2011.
- [57] A. J. J. Fontana (Ed.), *Water Activity in Foods: Fundamentals and Applications*, Wiley, 2007, appendix B.
- [58] Food, drug administration, *Bad bug book, foodborne pathogenic microorganisms and natural toxins*. Second Edition, USFDA, 2012, appendix 3.
- [59] D. Kitic, D. C. P. Jardim, F. G. J., S. M. Resnik, C. Jorge, Theoretical prediction of the water activity of standard saturated salt solutions at various temperatures, *J FOOD SCI* 51 (1986) 1037–1041.
- [60] J. Chirife, S. L. Resnik, Unsaturated solutions of sodium chloride as reference sources of water activity at various temperatures, *J FOOD SCI* 49 (1984) 1486–1488.
- [61] K. S. Pitzer, G. Mayorga, Thermodynamics of electrolytes. ii. activity and osmotic coefficients for strong electrolytes with one or both ions univalent, *J PHYS CHEM* 77 (1973) 2300–2308.
- [62] H. Renon, J. M. Prausnitz, Estimation of parameters for the NRTL equation for excess Gibbs energies of strongly nonideal liquid mixtures, *IND ENG CHEM PROCESS DES DEV* 8 (1969) 413–419.
- [63] E. Mason, A. Malinauskas, Gas transport in porous media: the dusty-gas model, in: *Chemical engineering monographs*, Vol. 17, 1983.
- [64] R. Krishna, Problems and pitfalls in the use formulation for intraparticle of the Fick diffusion, *CHEM ENG SCI* 48 (1993) 845–861.

- [65] E. Close, E. Sorensen, Modelling of direct contact membrane distillation for desalination, in: 20th European Symposium on Computer Aided Process Engineering - ESCAPE20, 2010.
- [66] C. Rieckmann, F. J. Keil, Multicomponent diffusion and reaction in three-dimensional networks: general kinetics†, *IND ENG CHEM RES* 36 (8) (1997) 3275–3281.
- [67] M. Matsumoto, K. Yosuke, Study on liquid-vapor interface of water. I. simulation results of thermodynamic properties and orientational structure, *J CHEM PHYS* 88 (1988) 3233–3245.
- [68] K. W. Lawson, D. R. Lloyd, Membrane distillation. I. module design and performance evaluation using vacuum membrane distillation, *J MEMBRANE SCI* 120 (1996) 111 – 121.
- [69] C. Guijt, Rácz, T. Reith, A. B. de Haan, Determination of membrane properties for use in the modelling of a membrane distillation module, *DESALINATION* 132 (2000) 255–261.
- [70] F. Gao, X. Chen, G. Yu, C. Asumana, Compressible gases transport through porous membrane: A modified dusty gas model, *J MEMBRANE SCI* 379 (2011) 200–206.
- [71] Z. Lei, B. Chen, Z. Ding, Membrane distillation, in: *Special Distillation Processes*, Elsevier Science, 2005.
- [72] J. Zhang, Theoretical and experimental investigation of membrane distillation, Ph.D. thesis, Victoria University (2011).
- [73] J. Zhang, J.-D. Li, M. Duke, M. Hoang, Z. Xie, A. Groth, C. Tun, S. Gray, Modelling of vacuum membrane distillation, *J MEMBRANE SCI* 434 (2013) 1–9.
- [74] K. W. Lawson, M. S. Hall, D. R. Lloyd, Compaction of microporous membranes used in membrane distillation. I. effect on gas permeability, *J MEMBRANE SCI* 101 (1994) 99 – 108.
- [75] R. W. Field, H. Y. Wu, J. J. Wu, Multiscale modeling of membrane distillation: Some theoretical considerations, *IND ENG CHEM RES* 52 (2013) 8822–8828.

- [76] J. Phattaranawik, R. Jiratananon, A. Fane, Effect of pore size distribution and air flux on mass transport in direct contact membrane distillation, *J MEMBRANE SCI* 215 (2003) 75–85.
- [77] R. Schofield, A. Fane, C. Fell, R. Macoun, Factors affecting flux in membrane distillation, *DESALINATION* 77 (1990) 279–294.
- [78] C. Z. Mooney, *Monte Carlo Simulation*, Vol. 116, SAGE Publications, Inc, 1997.
- [79] S. Soukane, S. Chelouche, M. Naceur, A ballistic transport model for vacuum membrane distillation, *J MEMBRANE SCI* 450 (2014) 397–406.
- [80] A. Ajith, *Artificial Neural Networks*, John Wiley and Sons Ltd, 2005, ISBN 0-470-02143-8.
- [81] T. Hill, L. Marquez, O. Marcus, W. Remus, Artificial neural network models for forecasting and decision making, *INT J FORECASTING* 10 (1994) 5–15.
- [82] M. Khayet, C. Cojocar, Artificial neural network modelling and optimization of desalination by air gap membrane distillation, *SEP PURIF TECHNOL* 86 (2012) 171–182.
- [83] M. Khayet, C. Cojocar, Artificial neural network model for desalination by sweeping gas membrane distillation, *DESALINATION* 308 (2013) 102–110.
- [84] D. C. Montgomery, *Design and analysis of experiments*, third edition Edition, John Wiley and Sons, 1991.
- [85] M. Khayet, C. Cojocar, C. Garcia-Payo, Application of response surface methodology and experimental design in direct contact membrane distillation, *IND ENG CHEM RES* 46 (2007) 5673–5685.
- [86] P. Onsekizoglu, K. Savas Bahceci, J. Acar, The use of factorial design for modeling membrane distillation, *J MEMBRANE SCI* 349 (2010) 225–230.
- [87] T. Mohammadi, M. A. Safavi, Application of taguchi method in optimization of desalination by vacuum membrane distillation, *DESALINATION* 249 (2009) 83–89.

- [88] M. Khayet, C. Cojocaru, A. Baroudi, Modeling and optimization of sweeping gas membrane distillation, *DESALINATION* 287 (2012) 159–166.
- [89] J. D. Anderson, G. Degrez, J. Degroote, E. Dick, R. Grundmann, J. Vierendeels, *Computational Fluid Dynamics, An Introduction*, 3rd Edition, Springer, 2009.
- [90] S. Al-Sharif, M. Albeirutty, A. Cipollina, G. Micale, Modelling flow and heat transfer in spacer-filled membrane distillation channels using open source CFD code, *DESALINATION* 311 (2013) 103–112.
- [91] A. Cipollina, A. Di Miceli, J. Koschikowski, G. Micale, L. Rizzuti, CFD simulation of a membrane distillation module channel, *DESALIN WATER TREAT* 6 (2009) 177–183.
- [92] K. Charfi, M. Khayet, M. Safi, Numerical simulation and experimental studies on heat and mass transfer using sweeping gas membrane distillation, *DESALINATION* 259 (2010) 84–96.
- [93] Z. Xu, Y. Pan, Y. Yu, CFD simulation on membrane distillation of NaCl solution, *FRONT CHEM ENG CHINA* 3 (2009) 293–297.
- [94] H. J. Hwang, K. He, S. Gray, J. Zhang, S. Moon, Direct contact membrane distillation (DCMD): Experimental study on the commercial PTFE membrane and modelling, *J MEMBRANE SCI* 371 (2011) 90–98.
- [95] N. Tang, H. Zhang, W. Wang, Computational fluid dynamics numerical simulation of vacuum membrane distillation for aqueous NaCl solution, *DESALINATION* 274 (2011) 120–129.
- [96] G. A. Fimbres-Weihs, D. E. Wiley, Review of 3D CFD modeling of flow and mass transfer in narrow spacer-filled channels in membrane modules, *CHEM ENG PROCESS* 49 (2010) 759–781.
- [97] R. Nichols, *Turbulence models and their application to complex flows* (2012).
URL http://people.nas.nasa.gov/~pulliam/Turbulence/Turbulence_Guide_v4.01.pdf
- [98] D. Zhongwei, L. Liying, M. Runyu, Study on the effect of flow maldistribution on the performance of the hollow fiber modules used in membrane distillation, *J MEMBRANE SCI* 215 (2013) 11–23.

- [99] V. Chen, M. Hlavacek, Application of voronoi tessellation for modeling randomly packed hollow-fiber bundles, *AIChE J* 40 (1991) 606–612.
- [100] F. Banat, F. A. Al-Rub, K. Bani-Melhem, Desalination by vacuum membrane distillation: sensitivity analysis, *SEP PURIF TECHNOL* 33 (2003) 75–87.
- [101] F. A. A. Al-Rub, F. Banat, K. Beni-Melhim, Parametric sensitivity analysis of direct contact membrane distillation, *SEP PURIF TECHNOL* 37 (2001) 3245–3271.
- [102] M. M. A. Shirazi, A. Kargari, D. Bastani, L. Fatehi, Production of drinking water from seawater using membrane distillation (MD) alternative: Direct contact MD and sweeping gas MD approaches, *DESALIN WATER TREAT* 52 (2014) 2372–2381.
- [103] *Comprehensive Membrane Science and Engineering*, Volume 1, Elsevier, 2010, ISBN: 978-0-444-53204-6.
- [104] M. M. A. Shirazi, A. Kargari, A review on application of membrane distillation (MD) process for wastewater treatment, *J MEMBRANE SCI AND RES* 1 (2015) 101–112.
- [105] I. Hitsov, T. Maere, K. De Sitter, C. Dotremont, I. Nopens, Modelling approaches in membrane distillation: A critical review, *SEP PURIF TECHNOL* 142 (2015) 48–64.
- [106] A. Alkhudhiri, N. Darwish, N. Hilal, Membrane distillation: A comprehensive review, *DESALINATION* 287 (2012) 2 – 18, special Issue in honour of Professor Takeshi Matsuura on his 75th Birthday.
doi:<http://dx.doi.org/10.1016/j.desal.2011.08.027>.
URL <http://www.sciencedirect.com/science/article/pii/S0011916411007284>
- [107] M. M. A. Shirazi, A. Kargari, F. A. Ismail, T. Matsuura, Computational fluid dynamic (CFD) opportunities applied to the membrane distillation process: State-of-the-art and perspectives, *DESALINATION* 377 (2016) 73–90.
- [108] A. Tamburini, M. Renda, A. Cipollina, G. Micale, M. Ciofalo, Investigation of heat transfer in spacer-filled channels by experiments and direct numerical simulations, *INT J HEAT MASS TRANSF* 93 (2016) 1190–1205.

- [109] M. El-Bourawi, Z. Ding, R. Ma, M. Khayet, A framework for better understanding membrane distillation separation process, *J MEMBRANE SCI* 285 (1-2) (2006) 4 – 29. doi:<http://dx.doi.org/10.1016/j.memsci.2006.08.002>.
URL <http://www.sciencedirect.com/science/article/pii/S0376738806005230>
- [110] W. Winston Ho, K. Sirkar, *Membrane Handbook, Volume I*, Springer Science + Business Media, LLC, 1992.
- [111] C. Geankoplis, *Transport Processes and Separation Process Principles (Includes Unit Operations) Fourth Edition, 4th Edition*, Prentice Hall Press, Upper Saddle River, NJ, USA, 2003.
- [112] A. Saltelli, S. Tarantola, F. Campolongo, M. Ratto, *Sensitivity Analysis in Practice: A Guide to Assessing Scientific Models*, Halsted Press, New York, NY, USA, 2004.
- [113] A. Saltelli, M. Ratto, T. Andres, F. Campolongo, J. Cariboni, D. Gatelli, M. Saisana, S. Tarantola, *Global Sensitivity Analysis, The Primer*, John Wiley & Sons Ltd, 2008.
- [114] K. J. Beven, *Environmental Modelling: An Uncertain Future?*, Taylor & Francis, 2008.
- [115] A. Efstratiadis, D. Koutsoyiannis, One decade of multi-objective calibration approaches in hydrological modelling: a review, *J MEMBRANE SCI* 55:1 (2010) 58:78.
- [116] J. Nocedal, S. Wright, *Numerical Optimization*, Springer-Verlag New York, New York, 2006.
- [117] L. Eykens, I. Hitsov, K. De Sitter, C. Dotromont, L. Pinoy, I. Nopens, B. Van der Bruggen, Influence of membrane thickness and process conditions on direct contact membrane distillation at different salinities, *J MEMBRANE SCI* 498 (2016) 353–364.
- [118] M. H. Sharqawy, J. H. Lienhard V, S. M. Zubair, Thermophysical properties of seawater: a review of existing correlations and data, *DESALIN WATER TREAT* 16 (2010) 354–380.
URL <http://web.mit.edu/seawater/>

- [119] K. Beven, A. Binley, The future of distributed models: Model calibration and uncertainty prediction, *HYDROL PROCESS* 6 (1992) 279–298.
- [120] P. Bratley, B. L. Fox, Algorithm 659 implementing sobol’s quasirandom sequence generator, *Mathematical Software. ACM* 14 (1988) 88–100.
- [121] C. Zopounidis, P. M. Pardalos, *Handbook of Multicriteria Analysis*, 1st Edition, Springer Publishing Company, Incorporated, 2010.
- [122] J. C. Lagarias, J. A. Reeds, M. H. Wright, P. E. Wright, Convergence properties of the nelder–mead simplex method in low dimensions, *SIAM J OPTIM* 9 (1) (1998) 112–147. doi:10.1137/S1052623496303470.
URL <http://dx.doi.org/10.1137/S1052623496303470>
- [123] J. Fernández-Seara, F. J. Uhía, S. Jaime, A. Campo, A general review of the wilson plot method and its modifications to determine convection coefficients in heat exchange devices, *APPL THERM ENG* 27 (2007) 2745–2757.
- [124] N. Ratkovich, I. Nopens, Heat-and-mass transfer relationship to determine shear stress in tubular membrane systems, *INT J HEAT MASS TRAN* 55 (21–22) (2012) 6152 – 6162. doi:<http://dx.doi.org/10.1016/j.ijheatmasstransfer.2012.06.035>.
URL <http://www.sciencedirect.com/science/article/pii/S0017931012004632>
- [125] E. Eckert, H. Sakamoto, T. Simon, The heat/mass transfer analogy factor, nu/sh , for boundary layers on turbine blade profiles, *INT J HEAT MASS TRAN* 44 (6) (2001) 1223 – 1233. doi:[http://dx.doi.org/10.1016/S0017-9310\(00\)00175-7](http://dx.doi.org/10.1016/S0017-9310(00)00175-7).
URL <http://www.sciencedirect.com/science/article/pii/S0017931000001757>
- [126] C. L. Choi, Thermal conductivity of polymers, *POLYMER* 18 (1977) 984–1004.
- [127] A. Saltelli, P. Annoni, I. Azzini, F. Campolongo, M. Ratto, S. Tarantola, Variance based sensitivity analysis of model output. design and estimator for the total sensitivity index, *COMPUT PHYS COMMUN* 181 (2) (2010) 259 – 270. doi:<http://dx.doi.org/10.1016/j.cpc.2009.09.018>.
URL <http://www.sciencedirect.com/science/article/pii/S0010465509003087>

- [128] S. T. F. C. Mortier, K. V. Gernaey, T. De Beer, I. Nopens, Global sensitivity analysis applied to drying models for one or a population of granules, *AIChE J* 60 (5) (2014) 1700–1717. doi:10.1002/aic.14383.
URL <http://dx.doi.org/10.1002/aic.14383>
- [129] P. A. Vanrolleghem, M. V. Daele, D. Dochain, Practical identifiability of a biokinetic model of activated sludge respiration, *WATER RES* 29 (11) (1995) 2561 – 2570. doi:[http://dx.doi.org/10.1016/0043-1354\(95\)00105-T](http://dx.doi.org/10.1016/0043-1354(95)00105-T).
URL <http://www.sciencedirect.com/science/article/pii/S004313549500105T>
- [130] D. Dochain, P. A. Vanrolleghem, M. V. Daele, Structural identifiability of biokinetic models of activated sludge respiration, *WATER RES* 29 (11) (1995) 2571 – 2578. doi:[http://dx.doi.org/10.1016/0043-1354\(95\)00106-U](http://dx.doi.org/10.1016/0043-1354(95)00106-U).
URL <http://www.sciencedirect.com/science/article/pii/S004313549500106U>
- [131] M. Friedman, The use of ranks to avoid the assumption of normality implicit in the analysis of variance, *AMER STATIST ASSOC* 32:200 (1936) 675–701.
- [132] Goodfellow - Polyethylene Terephthalate.
URL <http://www.goodfellow.com/E/Polyethylene-terephthalate.html>
- [133] Goodfellow - Polyethylene - U.H.M.W.
URL <http://www.goodfellow.com/E/Polyethylene-UHMW.html>
- [134] L. D. Tijning, Y. C. Woo, J.-S. Choi, S. Lee, S.-H. Kim, H. K. Shon, Fouling and its control in membrane distillation-a review, *J MEMBRANE SCI* 475 (2015) 215 – 244. doi:<http://dx.doi.org/10.1016/j.memsci.2014.09.042>.
- [135] D. M. Warsinger, J. Swaminathan, E. Guillen-Burrieza, H. A. Arafat, J. H. L. V, Scaling and fouling in membrane distillation for desalination applications: A review, *DESALINATION* 356 (2015) 294 – 313. doi:<http://dx.doi.org/10.1016/j.desal.2014.06.031>.
URL <http://www.sciencedirect.com/science/article/pii/S0011916414003634>

- [136] R. D. Gustafson, J. R. Murphy, A. Achilli, A stepwise model of direct contact membrane distillation for application to large-scale systems: Experimental results and model predictions, *DESALINATION* 378 (2016) 14 – 27. doi:<http://dx.doi.org/10.1016/j.desal.2015.09.022>.
URL <http://www.sciencedirect.com/science/article/pii/S0011916415300837>
- [137] J. Zhang, J. Li, S. Gray, Effect of applied pressure on performance of PTFE membrane in DCMD, *J MEMBRANE SCI* 369 (1–2) (2011) 514 – 525. doi:<http://dx.doi.org/10.1016/j.memsci.2010.12.033>.
URL <http://www.sciencedirect.com/science/article/pii/S037673881001001X>
- [138] L. Eykens, K. D. Sitter, C. Dotremont, L. Pinoy, B. V. der Bruggen, Characterization and performance evaluation of commercially available hydrophobic membranes for direct contact membrane distillation, *DESALINATION* 392 (2016) 63 – 73. doi:<http://dx.doi.org/10.1016/j.desal.2016.04.006>.
URL <http://www.sciencedirect.com/science/article/pii/S001191641630159X>
- [139] I. Hitsov, L. Eykens, K. De Sitter, C. Dotromont, L. Pinoy, I. Nopens, B. Van der Bruggen, Calibration and analysis of a direct contact membrane distillation model using Monte Carlo filtering, *J MEMBRANE SCI* 515 (2016) 63–78.
- [140] B. Nelemans, H. Van Sonsbeek, Device suitable for treating a fluid, as well as a method suitable for manufacturing such a device, US Patent 8,728,317 (May 20 2014).
URL <https://www.google.be/patents/US8728317>
- [141] D. W. Green, R. H. Perry, *Perry's Chemical Engineers' Handbook*, McGraw-Hill, New-York, NY, 1934.
- [142] L. Eykens, A comprehensive study of membrane distillation: Membrane development, configuration assessment and applications, Dissertation.
- [143] K. M. Persson, V. Gekas, G. Trägårdh, Study of membrane compaction and its influence on ultrafiltration water permeability, *J MEMBRANE SCI* 100 (2) (1995) 155 – 162. doi:[http://dx.doi.org/10.1016/0376-7388\(94\)00263-X](http://dx.doi.org/10.1016/0376-7388(94)00263-X).

- URL <http://www.sciencedirect.com/science/article/pii/S037673889400263X>
- [144] L. M. Camacho, L. Dumée, J. Zhang, J. de Li, M. Duke, J. Gomez, S. Gray, Advances in membrane distillation for water desalination and purification applications, *WATER* 5 (2013) 94–196.
- [145] L. Eykens, T. Reyns, K. D. Sitter, C. Dotremont, L. Pinoy, B. V. der Bruggen, How to select a membrane distillation configuration? process conditions and membrane influence unraveled, *DESALINATION* 399 (2016) 105 – 115. doi:<http://dx.doi.org/10.1016/j.desal.2016.08.019>.
URL <http://www.sciencedirect.com/science/article/pii/S0011916416302533>
- [146] A. Alsaadi, N. Ghaffour, J.-D. Li, S. Gray, L. Francis, H. Maab, G. Amy, Modeling of air-gap membrane distillation process: A theoretical and experimental study, *J MEMBRANE SCI* 445 (2013) 53 – 65. doi:<http://dx.doi.org/10.1016/j.memsci.2013.05.049>.
URL <http://www.sciencedirect.com/science/article/pii/S0376738813004705>
- [147] A. Alklaibi, N. Lior, Transport analysis of air-gap membrane distillation, *J MEMBRANE SCI* 255 (1–2) (2005) 239–253. doi:<http://dx.doi.org/10.1016/j.memsci.2005.01.038>.
URL <http://www.sciencedirect.com/science/article/pii/S0376738805001171>
- [148] I. Hitsov, L. Eykens, W. D. Schepper, K. D. Sitter, C. Dotremont, I. Nopens, Full-scale direct contact membrane distillation (DCMD) model including membrane compaction effects, *J MEMBRANE SCI* 524 (2017) 245 – 256. doi:<http://dx.doi.org/10.1016/j.memsci.2016.11.044>.
URL <http://www.sciencedirect.com/science/article/pii/S0376738816317677>
- [149] C. Huh, R. Reed, A method for estimating interfacial tensions and contact angles from sessile and pendant drop shapes, *J COLLOID INTERFACE SCI* 91 (2) (1983) 472 – 484. doi:[http://dx.doi.org/10.1016/0021-9797\(83\)90361-2](http://dx.doi.org/10.1016/0021-9797(83)90361-2).
URL <http://www.sciencedirect.com/science/article/pii/S0021979783903612>

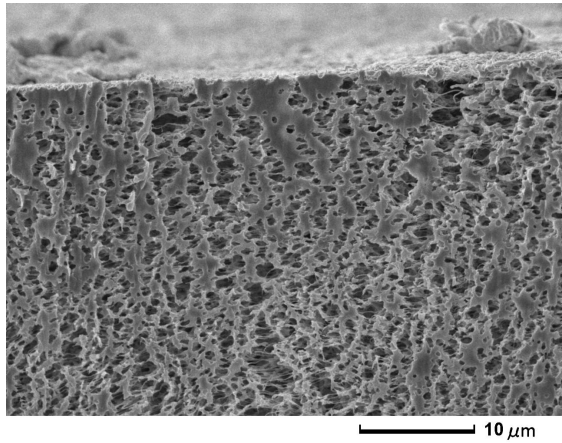
- [150] A. Cipollina, M. D. Sparti, A. Tamburini, G. Micale, Development of a membrane distillation module for solar energy seawater desalination, *CHEM ENG RES DES* 90 (12) (2012) 2101–2121. doi:<http://dx.doi.org/10.1016/j.cherd.2012.05.021>.
URL <http://www.sciencedirect.com/science/article/pii/S0263876212002444>
- [151] M. El-Bourawi, Z. Ding, R. Ma, M. Khayet, A framework for better understanding membrane distillation separation process, *J. MEMBRANE SCI* 285 (1-2) (2006) 4 – 29. doi:<http://dx.doi.org/10.1016/j.memsci.2006.08.002>.
URL <http://www.sciencedirect.com/science/article/pii/S0376738806005230>
- [152] P. Wang, T.-S. Chung, Recent advances in membrane distillation processes: Membrane development, configuration design and application exploring, *J MEMBRANE SCI* 474 (2015) 39 – 56. doi:<http://dx.doi.org/10.1016/j.memsci.2014.09.016>.
URL <http://www.sciencedirect.com/science/article/pii/S0376738814007091>
- [153] A. Ali, C. Quist-Jensen, F. Macedonio, E. Drioli, Optimization of module length for continuous direct contact membrane distillation process, *Chemical Engineering and Processing: Process Intensification* 110 (2016) 188 – 200. doi:<http://dx.doi.org/10.1016/j.cep.2016.10.014>.
URL <http://www.sciencedirect.com/science/article/pii/S0255270116305220>
- [154] S. Avlonitis, K. Kouroumbas, N. Vlachakis, Energy consumption and membrane replacement cost for seawater ro desalination plants, *DESALINATION* 157 (1) (2003) 151 – 158. doi:[http://dx.doi.org/10.1016/S0011-9164\(03\)00395-3](http://dx.doi.org/10.1016/S0011-9164(03)00395-3).
URL <http://www.sciencedirect.com/science/article/pii/S0011916403003953>
- [155] A. Bick, L. Gillerman, Y. Manor, G. Oron, Economic assessment of an integrated membrane system for secondary effluent polishing for unrestricted reuse, *WATER* 4 (1) (2012) 219–236. doi:10.3390/w4010219.
URL <http://www.mdpi.com/2073-4441/4/1/219>

- [156] M. Marufuzzaman, S. D. Ekşioğlu, R. Hernandez, Truck versus pipeline transportation cost analysis of wastewater sludge, *Transportation Research Part A: Policy and Practice* 74 (2015) 14 – 30. doi:<http://dx.doi.org/10.1016/j.tra.2015.02.001>.
URL <http://www.sciencedirect.com/science/article/pii/S096585641500018X>
- [157] M. S. Peters, K. D. Timmerhaus, *Plant design and economics for chemical engineers*, 4th Edition, McGraw-Hill, New York, USA, 1991.
- [158] A. Ruiz-Aguirre, D.-C. Alarcón-Padilla, G. Zaragoza, Productivity analysis of two spiral-wound membrane distillation prototypes coupled with solar energy, *DESALINATION WATER TREAT* 55 (10) (2015) 2777–2785. arXiv:<http://dx.doi.org/10.1080/19443994.2014.946711>, doi: 10.1080/19443994.2014.946711.
URL <http://dx.doi.org/10.1080/19443994.2014.946711>
- [159] L. L. Tun, D. Jeong, S. Jeong, K. Cho, S. Lee, H. Bae, Dewatering of source-separated human urine for nitrogen recovery by membrane distillation, *J MEMBRANE SCI* 512 (2016) 13 – 20. doi:<http://dx.doi.org/10.1016/j.memsci.2016.04.004>.
URL <http://www.sciencedirect.com/science/article/pii/S0376738816302150>
- [160] L. Rybach, T. Kohl, *Waste heat problems and solutions in geothermal energy*, Geological Society, London 236 (2004) 369–380.

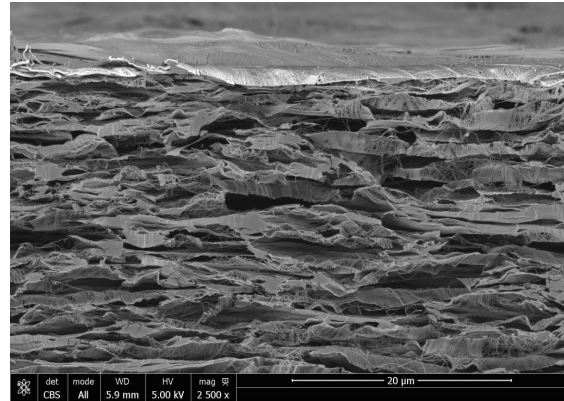
APPENDIX 9

Appendices

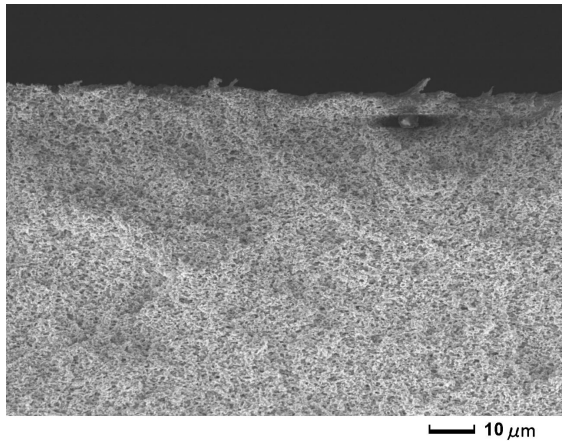
9.1 SEM crossections of the membranes studied in Chapter 3



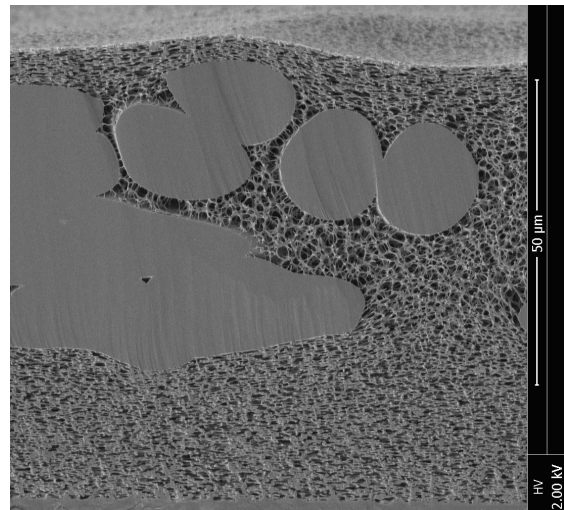
(a) PP (Phase inversion)



(b) PE (Stretching)

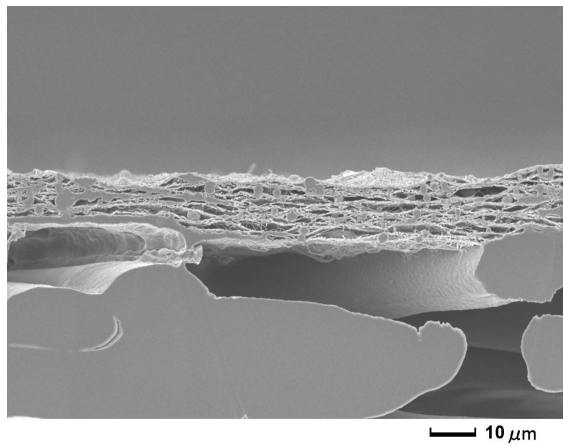


(c) PVDF (Phase inversion)

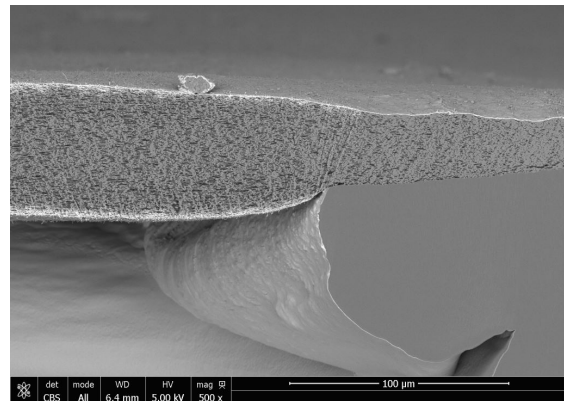


(d) PES (Phase inversion with internally embedded non-woven support)

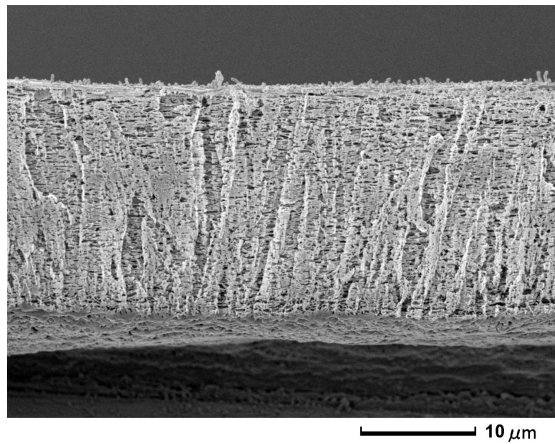
Figure 9.1: SEM micrographs of the unsupported membranes used Chapter 3



(a) ePVDF (Electrospinning with non-woven support)



(b) PTFE1 (Stretching with scrim support)



(c) PTFE2 (Stretching with non-woven support)

Figure 9.2: SEM micrographs of the supported membranes used Chapter 3

9.2 Equations used in Chapter 4

Region	Equation
Heat transfer in the channels	$Re = \frac{(v_{ch}/\epsilon_s)D_{ch}\rho}{\mu} \quad (9.1)$
	$Pr_{b,w} = \mu_{b,w}Cp_{b,w}/\kappa_{b,w} \quad (9.2)$
	$Nu_{f,p} = a(Re_{f,p})^b(Pr_{b,f,p})^{0.13}(Pr_{b,f,p}/Pr_{w,f,p})^{0.25} \quad (9.3)$
	$h_{f,p} = Nu_{f,p}\kappa_{f,p}/D_{ch,f,p} \quad (9.4)$
	$h_m = \kappa_m/\delta \quad (9.5)$
	$T_{m,f} = \frac{T_{b,f}h_f + T_{m,p}h_m - NH_V}{h_f + h_m} \quad (9.6)$
	$T_{m,p} = \frac{T_{b,p}h_p + T_{m,f}h_m + NH_V}{h_p + h_m} \quad (9.7)$
Mass transfer inside the channels	$c_{m,f} = c_{b,f}e^{MwN/\rho K} \quad (9.8)$
	$K = \frac{ShD}{d_h} \quad (9.9)$
	$Sh = a(Re_f)^b(Sc_{b,f})^{0.13}(Sc_{b,f}/Sc_{w,f})^{0.25} \quad (9.10)$
	$Sc = \frac{\mu}{\rho D} \quad (9.11)$
Heat transfer inside the membrane	$\kappa_g = 2.72 \times 10^{-3} + 7.77 \times 10^{-5}T_m \quad (9.12)$
	$\beta = (\kappa_s - \kappa_g)/(\kappa_s + 2\kappa_g) \quad (9.13)$
	$\kappa_m = c_m \frac{\kappa_g(1 + 2\beta(1 - \epsilon))}{1 - \beta(1 - \epsilon)} \quad (9.14)$
	$h_m = \frac{\kappa_m}{\delta} \quad (9.15)$
Mass transfer inside the membrane	$p_0 = \exp\left(23.5377 - \frac{4016.3632}{T - 38.6339}\right) \quad (9.16)$
	$p_i = p_0 a_w \quad (9.17)$
	$a_w = 1 - 0.03112m - 0.001482m^2 \quad (9.18)$
	$y_{af} = (P - p_{m,f})/P \quad (9.19)$
	$y_{ap} = (P - p_{m,p})/P \quad (9.20)$
	$K_0 = \frac{2\epsilon R_p}{3\tau} \quad (9.21)$
	$K_1 = \epsilon/\tau \quad (9.22)$
	$D_{aw} = 1.895 \times 10^{-5}Tm^{2.072}K_1 \quad (9.23)$
	$\bar{v} = \sqrt{\frac{8RT}{\pi M}} \quad (9.24)$
	$D_c^K = K_0\bar{v} \quad (9.25)$
	$N = \frac{D_{aw}(1 + Kn)}{\delta RT_m} \ln\left(\frac{D_c^K y_{ap} + D_{aw}(1 + Kn)}{D_c^K y_{af} + D_{aw}(1 + Kn)}\right) \quad (9.26)$
	Lab-scale derived calibration parameters

9.3 Equations used in Chapter 5

Region	Equation
Heat transfer in the channels	$Re = \frac{(\mathbf{v}_{ch}/\epsilon_s)D_{ch}\rho}{\mu} \quad (9.27)$
	$Pr_{b,w} = \mu_{b,w}Cp_{b,w}/\kappa_{b,w} \quad (9.28)$
	$Nu_{f,p} = a(Re_{e,c})^b(Pr_{b,e,c})^{0.13}(Pr_{w,e,c}/Pr_{b,e,c})^{0.25} \quad (9.29)$
	$h_{e,c} = Nu_{e,c}\kappa_{e,c}/D_{ch,e,c} \quad (9.30)$
Mass transfer inside the channels	$c_{m,f} = c_{b,e}e^{MwN/\rho K} \quad (9.31)$
	$K = \frac{ShD}{d_h} \quad (9.32)$
	$Sh = a(Re_e)^b(Sc_{b,e})^{0.13}(Sc_{w,e}/Sc_{b,e})^{0.25} \quad (9.33)$
	$Sc = \frac{\mu}{\rho D} \quad (9.34)$
Heat transfer inside the membrane	$\kappa_{air} = 2.72 \times 10^{-3} + 7.77 \times 10^{-5}T_m \quad (9.35)$
	$\beta = (\kappa_s - \kappa_{air})/(\kappa_s + 2\kappa_{air}) \quad (9.36)$
	$\kappa_m = c_m \frac{\kappa_{air}(1 + 2\beta(1 - \epsilon))}{1 - \beta(1 - \epsilon)} \quad (9.37)$
	$h_m = \frac{\kappa_m}{\delta} \quad (9.38)$
Heat transfer inside the gap	$\kappa_{gap,air} = \epsilon_{spacer}\kappa_{air} + (1 - \epsilon_{spacer})\kappa_{pol} \quad (9.39)$
	$h_{gap,air} = \frac{\kappa_{gap,air}}{\delta_{gap} - \delta_{cond}} \quad (9.40)$
	$\kappa_{gap,cond} = \epsilon_{spacer}\kappa_w + (1 - \epsilon_{spacer})\kappa_{pol} \quad (9.41)$
	$h_{gap,cond} = \frac{\kappa_{gap,cond}}{\delta_{cond}} \quad (9.42)$

Region	Equation
Mass transfer inside the membrane	$p_0 = \exp\left(23.5377 - \frac{4016.3632}{T - 38.6339}\right) \quad (9.43)$
	$p_i = p_0 a_w \quad (9.44)$
	$a_w = 1 - 0.03112m - 0.001482m^2 \quad (9.45)$
	$y_{a,\epsilon} = (P - p_{m,\epsilon})/P \quad (9.46)$
	$y_{ap} = (P - p_{m,p})/P \quad (9.47)$
	$K_0 = \frac{2\epsilon R_p}{3\tau} \quad (9.48)$
	$K_1 = \epsilon/\tau \quad (9.49)$
	$D_{aw} = 1.895 \times 10^{-5} T m^{2.072} K_1 \quad (9.50)$
	$\bar{v} = \sqrt{\frac{8RT}{\pi M w}} \quad (9.51)$
	$D_\epsilon^k = K_0 \bar{v} \quad (9.52)$
	$B_{mem} = \frac{D_{aw}(1 + Kn)}{\delta RT_m} \ln\left(\frac{D_\epsilon^k y_{ap} + D_{aw}(1 + Kn)}{D_\epsilon^k y_{af} + D_{aw}(1 + Kn)}\right) \frac{1}{(p_{m,f} - p_{m,p})} \quad (9.53)$

Mass transfer inside the gap

$$D = 4.46 \times 10^{-6} T_{gap}^{2.334} \quad (9.54)$$

$$B_{gap} = \frac{D}{\delta_{gap} RT_{gap}} \ln\left(\frac{P - p_{cond}}{P - p_{m,p}}\right) \frac{1}{(p_{m,p} - p_{cond})} \quad (9.55)$$

	Symbol	Value	Unit
Model inputs and constants	δ	9.20E-05	m
	δ_{cond}	1.44E-04	m
	δ_{gap}	8.00E-04	m
	ϵ	0.76	-
	ϵ_s	0.79	-
	ϵ_{spacer}	0.84	-
	κ_s	0.49	W/(m.K)
	κ_{pol}	0.2	W/(m.K)
	D_{ch}	2.00E-03	m
	Mw	18.015E-03	kg/mol
	P	1013255	Pa
	Rp	0.150E-06	m

Parameters calibrated at lab-scale

$$a = 0.22, b = 0.69 \quad eq.9.29, 9.33$$

$$c_m = 0.93, \quad eq.9.37$$

$$\tau = 2.27, \quad eq.9.49$$

Region	Equation
Mass transfer inside the membrane	$p_0 = \exp\left(23.5377 - \frac{4016.3632}{T - 38.6339}\right) \quad (9.56)$
	$p_i = p_0 a_w \quad (9.57)$
	$a_w = 1 - 0.03112m - 0.001482m^2 \quad (9.58)$
	$y_{a,\epsilon} = (P - p_{m,\epsilon})/P \quad (9.59)$
	$y_{ap} = (P - p_{m,p})/P \quad (9.60)$
	$K_0 = \frac{2\epsilon R_p}{3\tau} \quad (9.61)$
	$K_1 = \epsilon/\tau \quad (9.62)$
	$D_{aw} = 1.895 \times 10^{-5} T m^{2.072} K_1 \quad (9.63)$
	$\bar{v} = \sqrt{\frac{8RT}{\pi M_{aw}}} \quad (9.64)$
	$D_\epsilon^k = K_0 \bar{v} \quad (9.65)$
	$B_{mem} = \frac{D_{aw}(1 + Kn)}{\delta RT_m} \ln\left(\frac{D_\epsilon^k y_{ap} + D_{aw}(1 + Kn)}{D_\epsilon^k y_{af} + D_{aw}(1 + Kn)}\right) \frac{1}{(p_{m,f} - p_{m,p})} \quad (9.66)$

Mass transfer inside the gap

$$D = 4.46 \times 10^{-6} T_{gap}^{2.334} \quad (9.67)$$

$$B_{gap} = \frac{D}{\delta_{gap} RT_{gap}} \ln\left(\frac{P - p_{cond}}{P - p_{m,p}}\right) \frac{1}{(p_{m,p} - p_{cond})} \quad (9.68)$$

	Symbol	Value	Unit
Model inputs and constants	δ	9.20E-05	m
	δ_{cond}	1.44E-04	m
	δ_{gap}	8.00E-04	m
	ϵ	0.76	-
	ϵ_s	0.79	-
	ϵ_{spacer}	0.84	-
	κ_s	0.49	W/(m.K)
	κ_{pol}	0.2	W/(m.K)
	D_{ch}	2.00E-03	m
	Mw	18.015E-03	kg/mol
	P	1013255	Pa
	Rp	0.150E-06	m

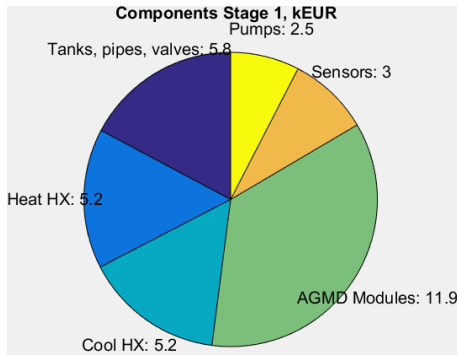
Parameters calibrated at lab-scale

$$a = 0.22, b = 0.69 \quad eq.9.29, 9.33$$

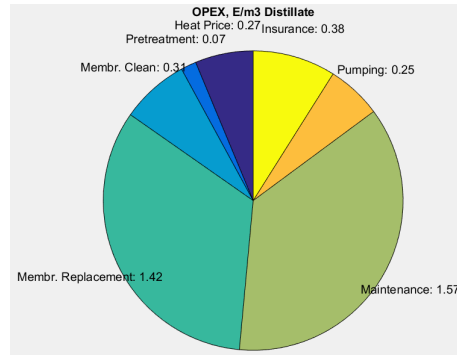
$$c_m = 0.93, \quad eq.9.37$$

$$\tau = 2.27, \quad eq.9.49$$

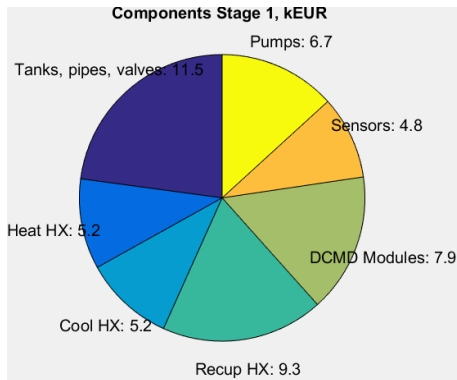
9.4 Case scenario 1, pilot scale 2 m³ distillate per day, Chapter 6



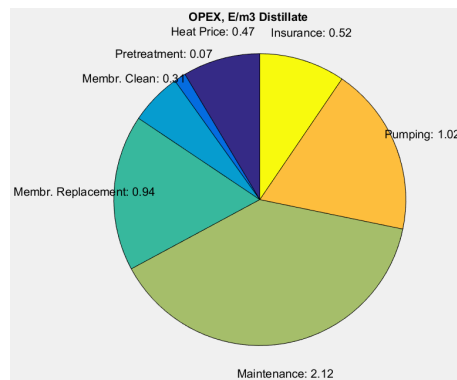
(a) Components, AGMD



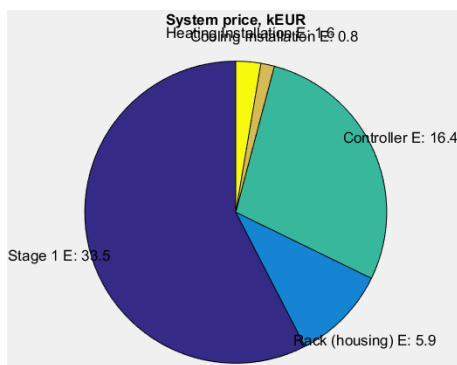
(b) Operational expenditures, AGMD



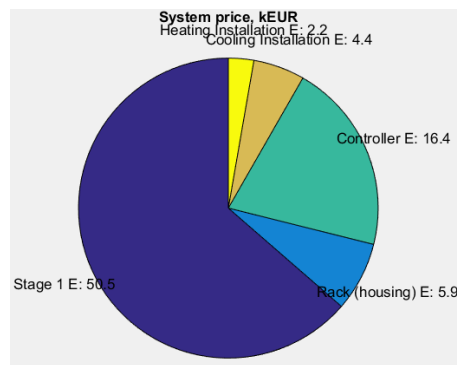
(c) Components, DCMD



(d) Operational expenditures, DCMD



(e) System price AGMD



(f) System price DCMD

Figure 9.3: Capex, opex and system price for AGMD and DCMD, case scenario 1

9.5 Case scenario 2, small production scale, 10 m³ distillate per day, Chapter 6

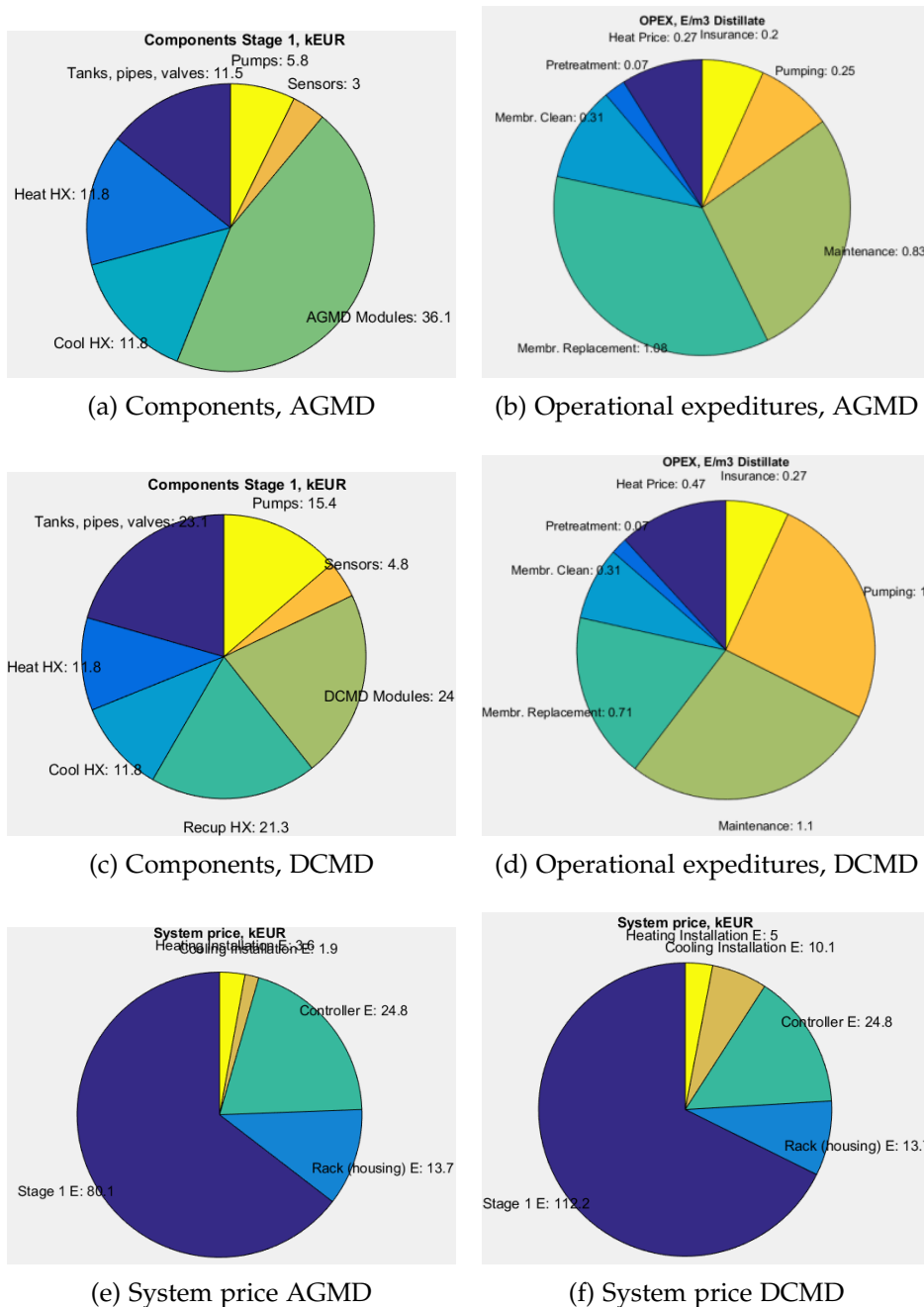


Figure 9.4: Capex, opex and system price for AGMD and DCMD, case scenario 2

9.6 Case scenario 3, production scale, 100 m³ distillate per day, Chapter 6

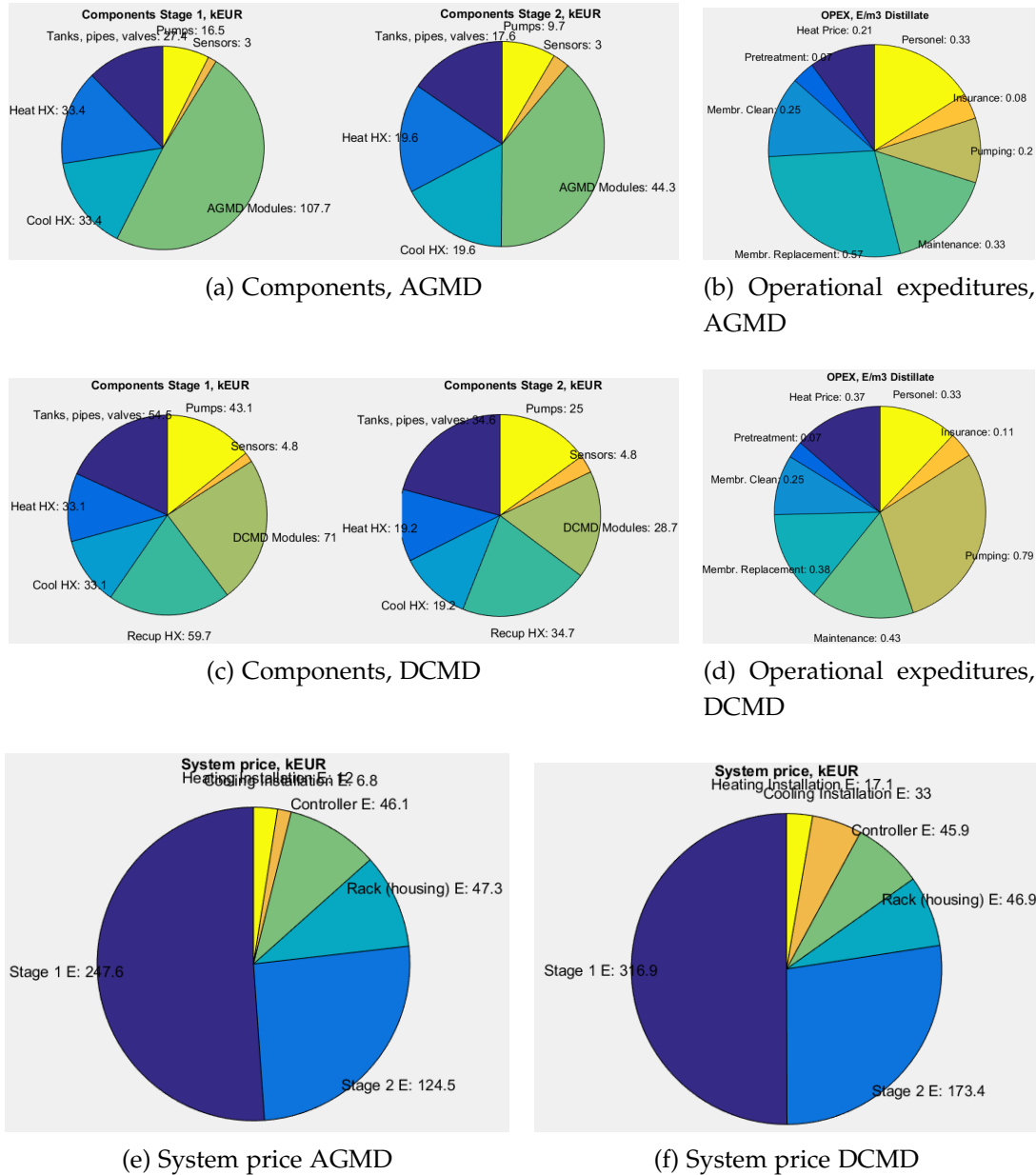


Figure 9.5: Capex, opex and system price for AGMD and DCMD, case scenario 3

9.7 Case scenario 4, large production scale, 1000 m³ distillate per day, Chapter 6

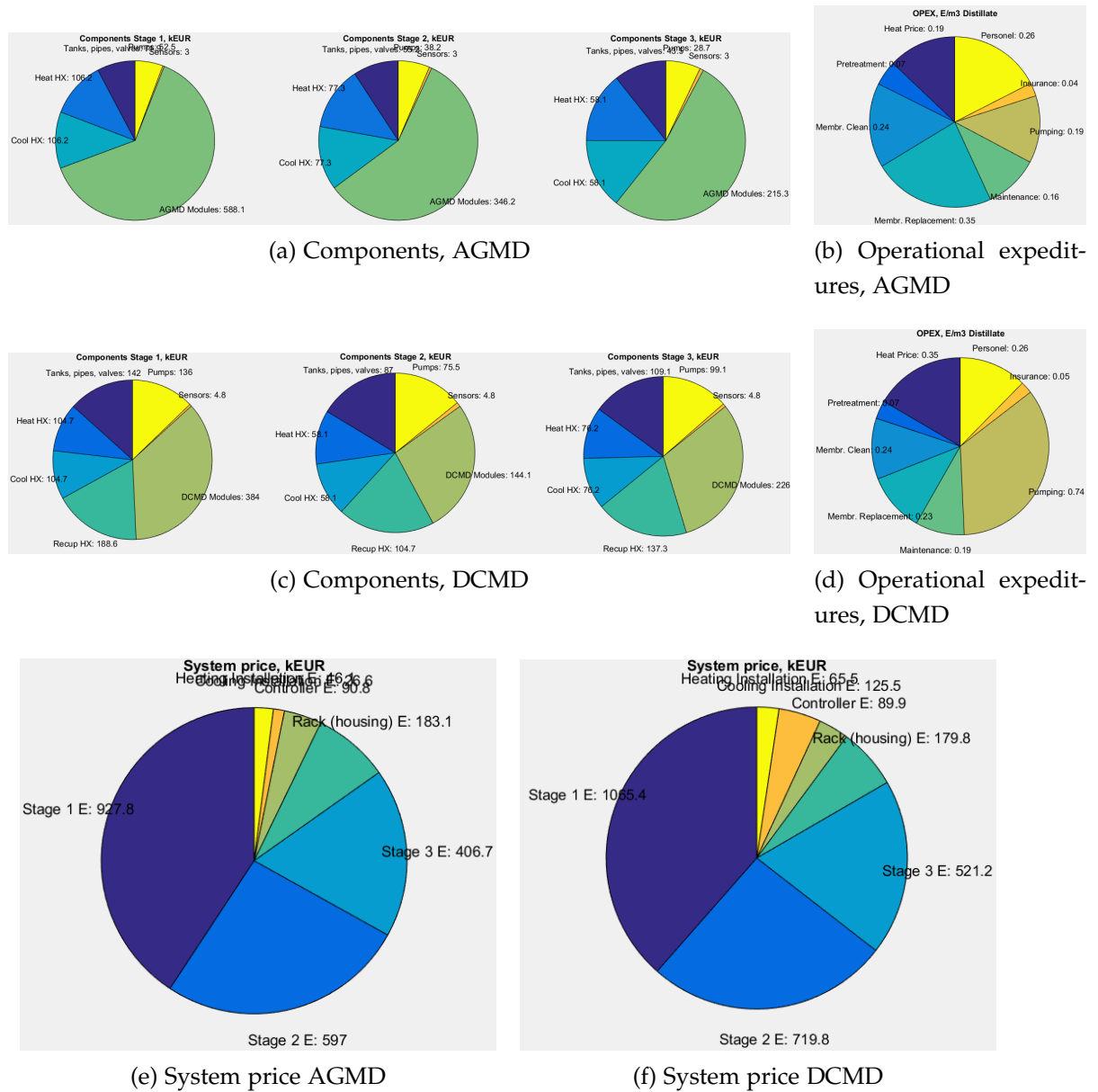


Figure 9.6: Capex, opex and system price for AGMD and DCMD, case scenario 4

Nomenclature

δ	Membrane thickness	m
ϵ	Porosity	—
γ	Activity coefficient	—
κ	Thermal conductivity	$\frac{W}{m.K}$
λ_i	Mean free path of a the molecule	m
$ p_a _{ln}$	Logarithmic mean pressure of air across the membrane	Pa
μ	Dynamic viscosity	Pa.s
\bar{P}	Average pressure	Pa
ρ	Density	$\frac{kg}{m^3}$
σ	Standard deviation	—
σ_i	Water vapor collision diameter	Å
τ	Tortuosity	—
D	Diffusive (Superscript)	
V	Viscous (Superscript)	
w	Wall (Subscript)	
avg	average (Subscript)	
a	air (Subscript)	
b	bulk (Subscript)	
ch	channel (subscript)	—
c	coolant (Subscript, Superscript)	
e	evaporator (Subscript, Superscript)	
f	feed (Subscript, Superscript)	
g	gap (Subscript)	
m	membrane (Subscript)	

<i>p</i>	permeate (Subscript, Superscript)	
<i>s</i>	solid; spacer (Subscript)	
<i>w</i>	water (Subscript)	
<i>AGMD</i>	Air Gap Membrane Distillation	
<i>ANN</i>	Artificial neural network	
<i>c</i>	concentration	$\frac{\text{mol}}{\text{m}^3}$
<i>C_p</i>	Specific heat capacity	$\frac{\text{J}}{\text{kg}\cdot\text{K}}$
<i>CFD</i>	Computational Fluid Dynamics	
<i>D</i>	Diffusion coefficient	$\frac{\text{m}^2}{\text{s}}$
<i>d</i>	Characteristic size of channel	m
<i>D_{aw}</i>	Molecular diffusion coefficient	$\frac{\text{m}^2}{\text{s}}$
<i>D_e^K</i>	Effective Knudsen diffusion coefficient	$\frac{\text{m}}{\text{s}}$
<i>D_{ij,e}^m</i>	Effective molecular diffusion coefficient	$\frac{\text{m}^2}{\text{s}}$
<i>D_{ij}^K</i>	Effective Knudsen diffusion coefficient	$\frac{\text{m}}{\text{s}}$
<i>DCMD</i>	Direct Contact Membrane Distillation	
<i>DGM</i>	Dusty Gas Model	
<i>DoE</i>	Design of experiments	
<i>EE</i>	Energy Efficiency	%
<i>GSA</i>	Global Sensitivity Analysis	
<i>h</i>	Local heat transfer coefficient	$\frac{\text{W}}{\text{m}^2\text{K}}$
<i>H_v</i>	Specific heat of evaporation	$\frac{\text{J}}{\text{mol}}$
<i>HT</i>	Heat Transfer	
<i>K</i>	Mass transfer coefficient	$\frac{\text{m}}{\text{s}}$
<i>K_B</i>	Boltzmann constant	$\frac{\text{m}^2\text{kg}}{\text{s}^2}$
<i>KTG</i>	Kinetic Theory of Gasses	
<i>M</i>	Molar weight	$\frac{\text{kg}}{\text{mol}}$
<i>m</i>	Molality	$\frac{\text{mol}}{\text{kg}}$
<i>MT</i>	Mass transfer	
<i>Mw</i>	Molar weight	$\frac{\text{kg}}{\text{mol}}$
<i>N</i>	Flux	$\frac{\text{mol}}{\text{m}^2\cdot\text{s}}$
<i>NF</i>	Nano filtration	
<i>NW</i>	Non-woven	

P	Pressure	Pa
p	partial pressure	Pa
P_a	Average pressure of air inside the membrane	Pa
PE	Polyethylene	
$PGMD$	Permeate Gap Membrane Distillation	
PP	Polypropylene	
Pr	Prandtl Number	—
Pr_{wall}	Prandtl number at the membrane interface	—
$PTFE$	Polytetrafluoroethylene	
$PVDF$	Polyvinylidene fluoride	
q	Heat flux	$\frac{W}{m^2}$
R	Universal gas constant	$\frac{J}{mol.K}$
r	Pore radius	m
R_p	Pore radius	m
Re	Reynolds Number	—
$RMSD$	Root Mean Square Deviation	$\frac{kg}{m^2h}$
RO	Reverse osmosis	
R_p	Pore radius	m
RSM	Response surface methodology	
SNM	Structural Network Model	
T	Temperature	K
U	Overall heat transfer coefficient	$\frac{W}{m^2K}$
$UHMW$	Ultra high molecular weight	
v	Velocity	$\frac{m}{s}$
VMD	Vacuum Membrane Distillation	
x	Molar fraction	—

APPENDIX 10

Curriculum Vitae

Ivaylo Hitsov

GHENT UNIVERSITY
BIOMATH, BW10
Coupure links 653
Ghent, Belgium

Phone: +32 48 3640894
Email: hitsov@gmail.com

Education

- 2013-pres **Ph.D. Candidate** in bioscience engineering, Ghent University, Belgium
2010-2012 **M.Sc.** Chemical engineering, Twente University in collaboration with Wet-sus Academy, The Netherlands
2005-2009 **B.Sc.** Chemical engineering, university of chemical technology and metal-lurgy (UCTM), Bulgaria

Publications

- | | |
|------|---|
| 2017 | I. Hitsov, K. De Sitter, C. Dotremont, P. Cauwenberg, I. Nopens. Full-scale validated Air Gap Membrane Distillation (AGMD) model without calibration parameters. <i>Journal of Membrane Science</i> 533, 533, p. 309–320 (I.F. 5.56) |
| 2016 | I. Hitsov, L. Eykens, W. De Schepper, K. De Sitter, C. Dotremont, I. Nopens. Full-scale direct contact membrane distillation (DCMD) model including membrane compaction effects. <i>Journal of Membrane Science</i> 524, p. 245–256 (I.F. 5.56) |

- 2016 I. Hitsov, L. Eykens, K. De Sitter, C. Dotremont, L. Pinoy, B. Van der Bruggen, I. Nopens. Calibration and analysis of a direct contact membrane distillation model using Monte Carlo filtering. *Journal of Membrane Science* 515, p. 63–78 (I.F. 5.56)
- 2016 L. Eykens, I. Hitsov*, K. De Sitter, C. Dotremont, L. Pinoy, I. Nopens, B. Van der Bruggen. Influence of membrane thickness and process conditions on direct contact membrane distillation at different salinities. *Journal of Membrane Science* 498, p. 353–364 (I.F. 5.56)
*Shared first authorship
- 2015 I. Hitsov, T. Maere, K. De Sitter, C. Dotremont, , I. Nopens. Modelling approaches in membrane distillation: A critical review. *Separation and Purification Technology* 142, p. 48–64 (I.F. 3.31)

Abstracts

- 2017 I. Hitsov, K De Sitter, C. Dotremont, I Nopens. Full-scale Air Gap Membrane Distillation (AGMD) model. *Membranes in Drinking and Industrial Water Production (MDIW)*, Leeuwarden, The Netherlands. **Oral presentation**
- 2016 I. Hitsov, K De Sitter, C. Dotremont, I Nopens. Decision support tool for the optimization of Membrane Distillation modules and systems. 15th Poster Day Membrane Technology, Apeldoorn, The Netherlands. **Poster presentation**
- 2015 L. Eykens, I. Hitsov, K. De Sitter, C. Dotremont, L. Pinoy, I. Nopens. B. Van der Bruggen. Operation of direct contact membrane distillation at high salinities: evaluation of membrane properties and process conditions. Singapore. **Oral presentation**
- 2015 I. Hitsov, L. Eykens, K. De Sitter, C. Dotremont, I. Nopens. Successful model validation of flux and energy efficiency at full-scale using a model calibrated at lab-scale. Singapore. **Poster presentation**
- 2015 I. Hitsov, L. Eykens, K. De Sitter, C. Dotremont, I. Nopens. Calibration and analysis of a direct contact membrane distillation model using the GLUE method. Desalination for clean water and energy. Palermo, Italy. **Oral presentation**
- 2015 I. Hitsov, L. Eykens, K. De Sitter, C. Dotremont, L. Pinoy, B. Van der Bruggen, I.Nopens. Calibration And Analysis Of A Direct Contact Membrane Distillation Model Using Monte Carlo Filtering. *Mathematics in (bio)Chemical Kinetics and Engineering 2015*. Ghent, Belgium. **Oral presentation**

- 2015 I. Hitsov, L. Eykens, W. De Schepper, K. De Sitter, C. Dotremont, I. Nopens. Full-scale model validation of flux and energy efficiency for a direct contact membrane distillation module. Euromembrane 2015. Aachen, Germany. **Oral presentation**
- 2015 L. Eykens, I. Hitsov, K. De Sitter, C. Dotremont, L. Pinoy, I. Nopens, B. Van der Bruggen. How to operate direct contact membrane distillation at high salinities: Evaluation of membrane properties and process conditions. Sicily Italy. **Poster presentation**
- 2015 I. Hitsov, L. Eykens, K. De Sitter, C. Dotremont, I. Nopens. Calibration And Analysis Of A Direct Contact Membrane Distillation Model Using The GLUE Method. 2nd International Workshop on Membrane Distillation and Innovating Membrane Operations in Desalination and Water Reuse. Ravello, Italy. **Poster presentation**
- 2014 I. Hitsov, L. Eykens, K. De Sitter, C. Dotremont, L. Pinoy, B. Van der Bruggen, I. Nopens. Evaluation of optimal membrane thickness for DCMD via modelling and experiments. IV International Scientific Conference on Pervaporation, Vapor Permeation and Membrane Distillation. Torun, Poland. **Oral presentation given by Wim De Schepper**
- 2014 I. Hitsov, L. Eykens, K. De Sitter, C. Dotremont, L. Pinoy, B. Van der Bruggen, I. Nopens. Evaluation of optimal membrane thickness for DCMD via modelling and experiments. Membrane Distillation – the next DME-Seminar S-005-2014. Freiburg, Germany. **Oral presentation**
- 2014 I. Hitsov, T. Maere, L. Eykens, K. De Sitter, C. Dotremont, I. Nopens. Analysis of salinity and membrane thickness influence on a Direct Contact Membrane Distillation module using the Dusty Gas model. Desalination for the Environment: Clean Water and Energy. Limassol, Cyprus. **Oral presentation**
- 2014 I. Hitsov, S. Van Hoey, L. Eykens, T. Maere, K. De Sitter, C. Dotremont, I. Nopens. Calibration and analysis of a Direct Contact Membrane Distillation (DCMD) model using the GLUE method. Lisbon, Portugal. **Poster presentation**

